An Approach To Ground Moving Target Indication Using Multiple Resolutions of Multilook Synthetic Aperture Radar Images

Geoffrey A. Akers

Submitted to the graduate degree program in
Electrical Engineering & Computer Science and the
Graduate Faculty of the University of Kansas
School of Engineering in partial fulfillment of the
requirements for the degree of Doctor of Philosophy

Dissertation Committee:

Chairperson: James Stiles

Shannon Blunt

Tyrone Duncan

David Petr

Glenn Prescott

Date Defended

The Dissertation Committee for Geoffrey A. Akers certifies that this is the approved version of the following dissertation:

An Approach To Ground Moving Target Indication Using Multiple Resolutions of Multilook Synthetic Aperture Radar Images

Committee:

Chairperson: James Stiles

Shannon Blunt

Tyrone Duncan

David Petr

Glenn Prescott

Date Approved

The views expressed in this proposal are those of the author and do not reflect the official policy or position of the United States Air Force, Department of Defense, or the United States Government.

Contents

Acceptance Page **i**

Acknowledgements **x**

Abstract **xi**

1 Introduction **1**

1.1 GMTI 2
1.2 SAR 6
1.3 Proposed Approach 8
1.4 Scope of Application 9
1.5 Document Overview 9
1.6 Notation and Terminology 11

2 Ground Moving Target Indication **13**

2.1 Radar Model 14
2.1.1 Radar Geometry 14
2.1.2 Transmit Signal 16
2.1.3 Space-Time Measurement Vector 17
2.2 Ground Moving Target Indication Processing 22
2.2.1 Form of Interference Covariance Matrix 26
2.2.2 Displaced Phase Center Antenna 30
2.2.3 Generalized DPCA 32
2.2.4 Space-Time Adaptive Processing 36
2.2.5 Structured Covariance Estimation Techniques 39
2.2.6 Nonhomogeneity Detector Preprocessors 45
2.2.7 Direct Data Domain 46
2.2.8 Other Techniques 47
2.2.9 Knowledge-Based Processing 47
2.2.10 SAR-Based GMTI 48

3 Synthetic Aperture Radar **49**
3.1 SAR Processing 49
3.2 Iterative SAR Processing 51
3.3 Multiresolution Filtering of SAR Images Using Filter Banks 57
3.4 The SAR Image and GMTI Clutter 61
3.4.1 Fading Statistics 65
3.4.2 Scattering Function Heterogeneity 68
3.4.3 Measurement Degrees of Freedom 69

4 Multiple Look SAR Using Subapertured Eigensensors **73**
4.1 Multilook SAR as Power Spectral Estimation 74
4.1.1 Power Spectral Estimation Math 74
4.1.2 Incremental Multiresolution Spectral Estimates 77
4.1.3 Power Spectral Estimation and Heterogeneous Spectra 79
4.1.4 Subaperturing Space-Time Data 81
4.1.5 Extension to Multilook Imaging 84
4.2 Subaperturing Using Eigensensors 87
4.2.1 Eigensensor Math 88
4.2.2 Ambiguity and Resolution 92
4.2.3 Under-Determined Estimation 99
4.2.4 Matched Filtering 105

5 Multiple Resolution GMTI **107**
5.1 Estimating the Interference Covariance Matrix 108
5.1.1 Heterogeneous Clutter and the Interference Covariance Matrix 109
5.1.2 Moving Target and the Interference Covariance Estimate . . . 110
5.2 Updating the Inverted Interference Covariance Matrix 111
5.3 Receiver Operating Characteristic Curves 115
5.4 Accounting for Range-Spread Energy 116
5.4.1 Optimal Processor for Multiple Range Cells 117
5.4.2 SMI for Multiple Range Cells 120
5.5 Final Detection From Detection Vector 122

6 Results **125**
6.1 Experimental Design 126
6.1.1 MATLAB Radar Model 126
6.1.2 Monte Carlo Simulations 127
6.2 GMTI Using Multilook SAR Images as Estimate of $\mathbf{R}_\gamma$ 131
6.2.1 Multilook SAR Images 131
6.2.2 Interference Covariance Matrix Estimates 138
6.3 GMTI Using DWT-Smoothed SAR Images as Estimate of $\mathbf{R}_\gamma$ 138
6.4 SMI Estimates of Interference Covariance Matrix 142
6.5 Effect of SAR Resolution on GMTI Performance 144
6.6 Multiresolution GMTI Performance 148

7 Conclusions **156**

A ROC Curves From Multilook SAR GMTI **158**

B ROC Curves From Voting Algorithms **168**

References **175**

List of Figures

1.1 Notional clutter scene 5
1.2 SAR image of bridge over Rio Grande 7

2.1 Radar geometry for a side-looking airborne platform 15
2.2 Coherent pulse train 17
2.3 Space-time radar data cube 21
2.4 MTI detector architecture 23
2.5 DPCA phase center progression 31
2.6 MTI radar noise and signal plus noise PDFs 34
2.7 Eigenspectra of clutter and generalized DPCA approximation 35
2.8 Space-time adaptive processor architecture 36
2.9 Fully-adaptive space-time processor 37
2.10 Expected and realized scattering spectrum 64x16 road scene 40
2.11 Eigenspectra comparison of SMI-estimated $\mathbf{R}_I$ for different scattering regions 41
2.12 Eigenspectra comparison of SMI-estimated $\mathbf{R}_I$ for homogeneous scene 42
2.13 Effect of heterogeneous clutter on SMI STAP ROC 42
2.14 Knowledge-aided STAP architecture 43

3.1 Iterative MMSE estimation architecture 52
3.2 Simplifications relating Kalman filtering, iterative MMSE, RLS, and back projection 56
3.3 DWT synthesis filter bank tree 57
3.4 Haar scaling function and wavelet 58
3.5 Haar wavelet, compressed wavelet, and compressed and translated wavelet 59
3.6 One-dimensional DWT demo using sine wave 60
3.7 One-dimensional DWT reconstruction of sine wave at multiple resolutions 61
3.8 Iterative MMSE-estimated 64x64 SAR image of road scene and DWT filtered image 62

3.9 Lower-resolution DWT output of 64x64 SAR image of road scene . . 63
3.10 Comparison of expected and realized SAR images 64
3.11 Boat off wake illustrating azimuth offset in SAR image 70
3.12 GMTI measurement degrees of freedom 70

4.1 One-dimensional PSE of unit-variance, white-Gaussian noise 80
4.2 One-dimensional PSE for nonuniform power spectrum 82
4.3 Subaperture size effect on spectral transition region 83
4.4 Expected intensity SAR image for a synthetic scene 85
4.5 Multiple spatial resolutions of one realization of 256x256 intensity image 86
4.6 Dyadically increasing spatial resolutions 87
4.7 Synthetic array sensor locations for a receive array of 12 elements . . 93
4.8 Synthetic sensor array locations for 4 azimuth subapertures 95
4.9 Azimuth subapetures 95
4.10 Range subapetures 97
4.11 Eigensensor subapetures 98
4.12 Circular synthetic sensor array 100

5.1 Eigenspectra for two different expected clutter scenes 110
5.2 Eigenanalysis of estimated $\mathbf{R}_I$ for single range of WGN scene with and without moving target 112
5.3 Eigenanalysis of estimated $\mathbf{R}_I$ for 3 ranges of WGN scene with and without moving target 113
5.4 Eigenspectrum of residual moving target energy 114
5.5 Example ROC curve 116
5.6 Measurement energy from moving target with respect to range 118
5.7 ROC comparison for the optimum GMTI processor using measurements from one and three range cells 119
5.8 Eigenspectra comparison for SMI using measurements from one and three range cells of WGN scene 121
5.9 ROC comparison for SMI using measurements from one and three range cells of WGN and road scenes 123

6.1 Graphical user interface for MATLAB radar model 127
6.2 Intensity-squared realizations of 64x64 demonstration scenes 130

6.3 Histograms of the locations and radial velocities moving targets for Monte Carlo simulations 132
6.4 16-look, 64x64 SAR image of homogeneous, unit-variance Gaussian scene 134
6.5 1024-look, 64x64 SAR image of homogeneous, unit-variance Gaussian scene 135
6.6 16-look, 64x64 SAR image of homogeneous, road scene 136
6.7 1024-look, 64x64 SAR image of homogeneous, road scene 137
6.8 Eigenanalysis of clutter subspace for clairvoyant and ML estimated $\mathbf{R}_I$ 139
6.9 Eigenanalysis of clutter subspace for clairvoyant and ML estimated $\mathbf{R}_I^{-1}$ 140
6.10 Eigenanalysis of clutter subspace for clairvoyant and MF estimated $\mathbf{R}_I^{-1}$ 141
6.11 Eigenanalysis of clutter subspace for $\mathbf{R}_I^{-1}$ estimated using DWT-smoothed image 143
6.12 Eigenanalysis of WGN clutter subspace for SMI estimated $\mathbf{R}_I^{-1}$ for one and three ranges 145
6.13 Eigenanalysis of road clutter subspace for SMI estimated $\mathbf{R}_I^{-1}$ for one and three ranges 146
6.14 ROCs for MVM GMTI detector using ML to estimate multiple multi-look SAR images 149
6.15 ROCs for MVM GMTI detector using MF to estimate multiple multi-look SAR images 150
6.16 ROCs for MVM GMTI detector using DWT-smoothed SAR images with 0 dB SCR moving target 151
6.17 ROCs for MVM GMTI detector using voting fusion algorithm for WGN scene, SCR = 0 dB 152
6.18 ROCs for MVM GMTI detector using voting fusion algorithm for WGN scene, SCR = -3 dB 153
6.19 ROCs for MVM GMTI detector using voting fusion algorithm for road scene, SCR = 0 dB 154
6.20 ROCs for MVM GMTI detector using voting fusion algorithm for road scene, SCR = -3 dB 155

A.1 ROCs for MVM GMTI detector using ML to estimate multiple multi-look SAR images of WGN scene 159

A.2 ROCs for MVM GMTI detector using ML to estimate multiple multilook SAR images of road scene 160
A.3 ROCs for MVM GMTI detector using ML to estimate multiple multilook SAR images, SCR = -3 dB 161
A.4 ROCs for MVM GMTI detector using MF to estimate multiple multilook SAR images of WGN scene 162
A.5 ROCs for MVM GMTI detector using MF to estimate multiple multilook SAR images of road scene 163
A.6 ROCs for MVM GMTI detector using MF to estimate multiple multilook SAR images, SCR = -3 dB 164
A.7 ROCs for MVM GMTI detector using DWT-smoothed SAR images, SCR = 3 dB 165
A.8 ROCs for MVM GMTI detector using DWT-smoothed SAR images, SCR = 0 dB 166
A.9 ROCs for MVM GMTI detector using DWT-smoothed SAR images, SCR = -3 dB 167

B.1 ROCs for MVM GMTI detector using voting fusion algorithm and ML estimated multilook SAR images of WGN scene 169
B.2 ROCs for MVM GMTI detector using voting fusion algorithm and MF estimated multilook SAR images of WGN scene 170
B.3 ROCs for MVM GMTI detector using voting fusion algorithm and DWT-smoothed SAR images of WGN scene 171
B.4 ROCs for MVM GMTI detector using voting fusion algorithm and ML estimated multilook SAR images of road scene 172
B.5 ROCs for MVM GMTI detector using voting fusion algorithm and MF estimated multilook SAR images of road scene 173
B.6 ROCs for MVM GMTI detector using voting fusion algorithm and DWT-smoothed SAR images of road scene 174

Acknowledgements

As with most endeavors in life, this document and the research it represents cannot be attributed to a single individual. This accomplishment was made possible by the direct and indirect assistance of many more individuals than can be acknowledged in a single page. The bibliography contains the names of many scientists and engineers whose work provided the foundation for this research. Additionally, many instructors and fellow students throughout my academic career at three universities have helped hone my knowledge and understanding of technical subjects, including radar. As said in the Bible, in Proverbs 27:17[1], "As iron sharpens iron, so one man sharpens another."

My advisor, Dr. Jim Stiles, is an exceptional teacher, and I'm grateful for his patience and perseverance. On several topics he had to explain the same concept several different times. On each occasion he explained it with the same vigor and detail without belittling my lack of understanding. As I look toward my next military assignment at the Air Force Institute of Technology, Dr. Stiles provided many qualities of an advisor I plan to emulate.

No major accomplishment in my life, including this dissertation, would be possible without the love, support, and prayer of my wife, Karey. The peace she keeps in our home of four children allows me to focus on the task at hand when I am at work and anticipate coming home in the evenings.

Finally, there are two truths that I believe more and more as I mature; 1) God exists, and 2) He as revealed Himself to us through the Holy Bible. These facts are central to everything good I do. Academically, two verses keep my grounded. The first motivates diligence, 2 Timothy 2:15[1], "Do your best to present yourself to God as one approved, a workman who does not need to be ashamed and who correctly handles the word of truth." The second encourages balance, Ecclesiastes 12:12[1], "...Of making many books there is no end, and much study wearies the body."

Abstract

Ground moving target indication (GMTI) using multiple resolutions of synthetic aperture radar (SAR) images to estimate the clutter scattering statistics is shown to outperform conventional sample matrix inversion space-time adaptive processing GMTI techniques when jamming is not present. A SAR image provides an estimate of scattering from nonmoving targets in the form of a clutter scattering covariance matrix for the GMTI optimum processor. Since the homogeneity of the scattering statistics are unknown, using SAR images at multiple spatial resolutions to estimate the clutter scattering statistics results in more confidence in the final detection decision.

Two approaches to calculating the multiple SAR resolutions are investigated. Multiple resolution filter bank smoothing of the full-resolution SAR image is shown to outperform an innovative approach to multilook SAR imaging. The multilook SAR images are calculated from a single measurement vector partitioned base on synthetic sensor locations determined via eigenanalysis of the radar measurement parameters.

Chapter 1

Introduction

It has been over 120 years since Hertz first observed reflected electromagnetic waves. In 1922 the Naval Aircraft Radio Laboratory at Anacostia, D.C. experimentally confirmed Marconi's idea to capitalize on Hertz's observation by detecting reflected waves to "immediately reveal the presence and bearing of the other ship in fog or thick weather" [1]. Since then radar has become indispensable in defense, intelligence, transportation safety, scientific, and many other military and civilian applications.

The word radar originated as an acronym for *RAdio Detection And Ranging* and was initially employed to detect scattering objects and determine their azimuth and range with respect to the radar's location. The advent of coherent radar systems allowed radars to capitalize on the Doppler shift of electromagnetic (EM) waves reflected by objects with a relative velocity with respect to the radar. Christian Johann Doppler (1803-1853) first described how the frequency of light and sound is changed by the relative velocity between the source and observer. Likewise, the relative velocity between the radar and a scattering object results in a shift in frequency between the transmitted and reflected EM waves, and the shift in frequency is called the Doppler shift. Detecting the Doppler shift allows radar to determine the relative velocity of scattering objects.

Detecting moving objects using radar is appropriately termed moving target indi-

cation (MTI). When the MTI radar is hosted on an airborne or spaceborne platform and used to detect moving objects on the ground it is called a ground moving target indication (GMTI) system. In addition to the desired signal due to the transmitted EM waves scattering off a moving object on the ground, referred to as the target, the measured signal contains interference, which reduces the detectability of the target. The three general interference sources are jamming, clutter, and noise. Jamming is due to incoherent transmitters external to the radar system transmitting within the radar receiver's bandwidth. Noise is internal and external to the radar electronics, and is typically considered to have known statistical properties.

Clutter is self-induced interference. In addition to the transmitted EM waves scattering off a moving object on the ground, the EM waves scatter off terrain, buildings, and other nonmoving objects. These nonmoving objects are clutter sources in GMTI, and the clutter return can be larger in magnitude than the moving target return. Radar clutter is usually the most complicated form of interference in GMTI, since it is distributed in angle and range as well as spread in Doppler due to the radar platform's motion. The statistics of the clutter energy are unknown a priori, so it is difficult to distinguish the desired signal (radar return from the moving object) from the clutter. The basic goal of GMTI is to determine whether or not the measurements contain energy from a moving target. Because clutter can obscure the scattering from a moving target, detecting the presence of a moving target is challenging.

1.1 GMTI

Klemm [2] discusses the optimum processor for the discrete, linear radar model. Because the interference statistics are unknown, approximations to the optimum processor must be made. He calls processors that include interference statistics in the

covariance matrix as adaptive processors. Additionally, the covariance matrix of spectral estimation techniques contain the desired signal and interference.

There are three basic categories of GMTI processors. A matched filter approach attempts to maximize the radar's response to the target with respect to the internal and external noise. This approach is not commonly used in GMTI, because it ignores the clutter, which is typically the larger source of interference.

The second category of GMTI approaches is orthogonal projection. Orthogonal projection techniques deterministically project the measurements into a subspace orthogonal to the subspace occupied by the clutter. Displaced phase center antenna (DPCA) [3–5], eigencancellers [6–8], maximum likelihood [9] are distinctly different techniques, which are included in this category. The drawback to orthogonal projection approaches is that the target and clutter subspaces often overlap, to some extent. This is especially true for slow-moving targets. The target energy contained in the clutter subspace is lost during the projection resulting in less target energy for the detector.

The most commonly used GMTI techniques fall into the adaptive suppression category of processors. These approaches attempt to suppress the clutter and simultaneously maximize the radar's response to the target. Rather than project the measurements into a subspace orthogonal to the entire clutter subspace, an estimate of the interference is used to suppress its effect on the measurements without suppressing the target energy. The key to successful interference suppression is an accurate estimate of the expected interference statistics in the form of an estimated interference covariance matrix.

A revolution in the GMTI world began in 1973, when Brennan and Reed [10] introduced what came to be known as optimal space-time adaptive processing (STAP).

STAP is based on estimating the interference covariance matrix from the measurements of a multiple antenna element array. However, the problem with using measurements to suppress the interference is that any moving target energy in the measurement would corrupt the interference estimate and therefore be suppressed. Optimal, or fully-adaptive STAP is computationally intractable. To increase the practical usefulness of STAP, Reed et al. [11] introduced sample matrix inversion (SMI) as a method to increase the convergence rate of the detector. SMI is a direct method of adaptive weight computation by estimating the interference covariance matrix of the region-of-interest with measurements of an area nearby. This nearby area is assumed to not contain any target energy and to have the same interference characteristics as the region of interest. Additionally, SMI requires a large amount of measurements from these nearby areas to converge on an interference covariance estimate.

While STAP based on SMI is adaptive, assuming the clutter in two different areas have the same statistical properties is often invalid. Melvin [12] shows that significant losses can occur from using this assumption. Figure 1.1 is a cartoon illustrating how a region of interest, in this case, the region around the moving car, as indicated by the red lines, could be drastically different than the surrounding regions, which are the washed-out regions in the figure.

The inability of STAP to directly estimate the interference in the region of interest and the large amount of sample support required are well-known limitations, and many approaches to overcome these deficiencies have been proposed. Structured covariance methods [9,13,14] take advantage of the inherent structure of the measurement covariance matrix to improve detection performance. An extension of structured covariance methods is knowledge-aided (KA) GMTI methods which attempt to improve detection performance by using a priori knowledge sources to improve STAP

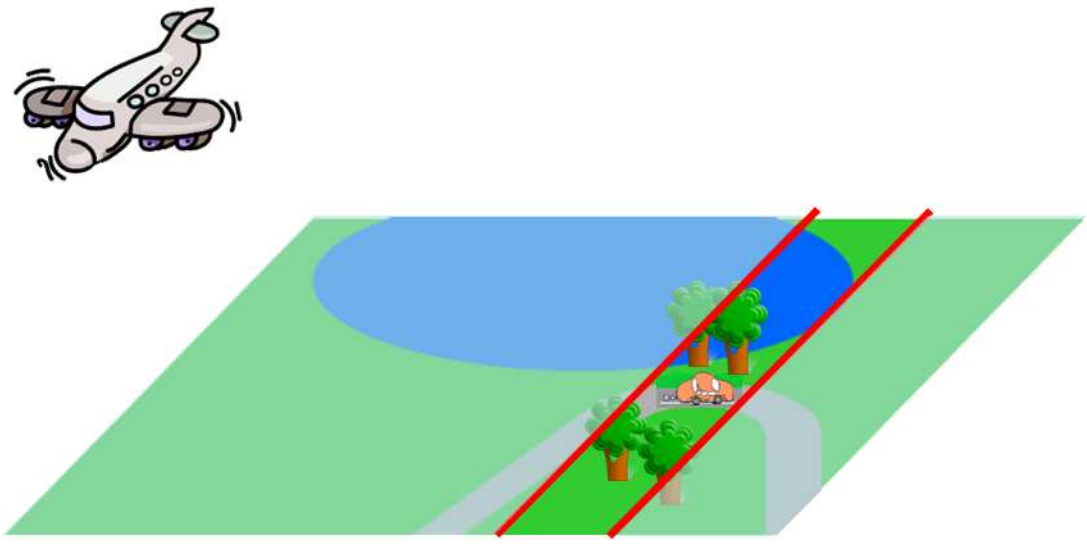

Figure 1.1. Cartoon illustrating difference in clutter scene between potential target region and other regions used to estimate clutter statistics in STAP

performance. Through a variety of techniques, KA methods exploit knowledge of the platform location, velocity, and radar parameters [15–17] and/or scattering characteristics of the scene [18–21]. The sources of knowledge and how the knowledge is incorporated into the processor are the primary distinguishing characteristics of different KA-STAP approaches. The two purposes of KA-STAP are to increase the processor's detection performance and/or to reduce the amount of secondary data required to estimate the interference covariance matrix. KA-STAP approaches have demonstrated great improvements over STAP; however, they have drawbacks. In addition to the possibility of errors in the knowledge source, to employ these knowledge-aided tools, ownship location, and motion must be known precisely [22]. Mischaracterizing the actual statistics with incorrect or poorly applied knowledge has the potential to do more harm than good.

Many other GMTI approaches have been proposed, including nonhomogeneity detectors [23–25], direct data domain (D^3) [26], and joint domain localized processors

[22, 27]. These and the previously mentioned methods are not exclusive. Techniques to blend or autonomously choose a certain algorithm to fit a give scenario have been called knowledge-based [28, 29] processors.

1.2 SAR

Another application of airborne and spaceborne radar is synthetic aperture radar (SAR) imaging of the Earth. A SAR image is a two-dimensional map of the scattering intensity of an area on the Earth, also called the image scene.

SAR processing exploits the Doppler shift between pulses of the received radar signal of a pulsed-Doppler radar system to determine the relative velocity between stationary objects on the ground and the moving radar platform. Sampling the received signal within a single pulse enables the range between the radar platform and the scattering objects to be determined. The SAR processor registers the scattered energy in azimuth and range resulting in a two-dimensional intensity image of the illuminated scene generally called a SAR image. Fine range resolution is achieved by transmitting a wide bandwidth signal, and fine azimuth resolution is a result of processing many sequential pulses. The SAR image is a fine spatial resolution estimate of the scattering intensity using the hypothesis that all scatterers have zero velocity with respect to ground. Figure 1.2 is an example of a SAR image with many distinctly different scattering characteristics.

A SAR image, therefore, is a high spatial resolution estimate of the GMTI clutter scene. Using a high spatial resolution estimate of the clutter is not necessarily a good estimate of the expected scattering scene. A phenomenon called fading results in speckle in the SAR image. Speckle is the intensity variance in what would otherwise be a homogeneous region within a scene. Fading is due to small path length differences

Figure 1.2. X-Band SAR image of bridge over Rio Grande near Los Lunas, NM, (used with permission from Sandia National Laboratory)

between similar scatterers within a resolution cell, which is larger than the wavelength of the radar's transmitted signal. Speckle is clearly evident in what appears to be a field in lower, center of Figure 1.2.

Statistically, speckle is a result of a SAR image being a single statistical realization of the expected scattering characteristics of an imaged scene. The optimum GMTI processor requires the expected scattering characteristics, or expected clutter spectrum. Multilook SAR processing reduces the effect of speckle by incoherently averaging independent SAR images of the same scene. Multilook SAR may be accomplished by processing SAR images from subsets of the measurement vector. A SAR image may be calculated from each measurement subset, and these SAR images

can then be incoherently averaged for the multilook image. The number of measurements and how they are selected from the measurement vector determine how well the resulting multilook image approximates the expected clutter spectrum of the observed scene.

The potential of using real-time SAR or SAR-like data to adaptively estimate the clutter covariance matrix has been recognized by authors including Minardi, et al. [30], Minardi and Zelnio [31], Gierull [32], and Chapin and Chen [33]. The advantage to a real-time estimate of the clutter is coregistered with the GMTI measurements, which is noted a weakness in knowledge-aided GMTI approaches that use a priori information.

1.3 Proposed Approach

This dissertation discusses using multiple resolutions of a SAR image from long coherent processing interval (CPI), wide bandwidth, multiple aperture radar measurements, to estimate the interference covariance matrix used in ground moving target indication (GMTI). These space-time measurements allow real-time clutter estimation in the form of SAR images that are coregistered with the GMTI data. Calculating detection coefficients from progressively higher resolution estimates of the clutter, in the form of multilook SAR images, promises to increase the probability of detection and reduce the probability of false alarm.

Additionally, a novel approach to multilook SAR imaging is proposed. This approach is based on partitioning the measurements according to the space-time locations of the measurements, rather than the traditional approach of segmenting the measurements according to azimuth subbands.

1.4 Scope of Application

Regarding structured covariance matrix estimation techniques, such as will be used in this research, Burton and Smith [13] give the following cautions: 1) make sure that the assumption of block Toeplitz structure is valid (e.g., array errors and multipath reflections ruin spatial and temporal stationarity, respectively); and 2) structured covariance matrix estimation performs better than SMI but is more computationally intense. Additionally, The proposed approach to GMTI assumes clutter is the most significant interference source. Specifically, other techniques must be incorporated to suppress jammers, when present.

1.5 Document Overview

The following chapters of this dissertation present the proposed approach to multiresolution GMTI in the following order:

Chapter 2 introduces the linear, discrete radar model used throughout this document. This chapter also presents the background necessary to understand the strengths and weaknesses of GMTI presented in literature. The key component in the optimum processor is termed the interference covariance matrix in GMTI and the data covariance matrix in SAR. The interference covariance matrix estimation approaches of many GMTI approaches will be covered in detail. Specifically, Chapter 2 will show the shortfalls of popular approaches to GMTI, including sampled matrix inversion STAP, which assumes homogeneous clutter statistics.

In Chapter 3 the development of the SAR image equation will be presented, then the results are compared to the GMTI clutter spectrum. SAR imagery is shown to be a high spatial resolution estimate of one realization of the desired GMTI clutter spectrum. The source of speckle in the SAR image and its effect on the clutter

spectrum estimate are discussed.

Chapter 4 covers an iterative MMSE-based approach to calculating multilook SAR images at multiple resolutions. These multilook SAR images can then be used to provide the GMTI processor with multiple estimates of the clutter spectrum. The multiple resolutions of the SAR image are calculated in the data domain via multilook SAR, rather than smoothing a full-resolution image. Additionally, a novel approach to partitioning the measurements for multilook SAR is presented. This novel approach is termed eigensensor subaperturing and results in multilook SAR images with better estimation accuracy in homogeneous scattering regions at the expense of spatial resolution. Additionally, computational efficiency is addressed in Chapter 4. SAR processors are computationally complex. While this research does not attempt to optimize processing time, a technique loosely based on wavelet theory is presented to reduce computational complexity for low spatial resolution multilook SAR processing.

Chapter 5 presents a GMTI technique that uses multiple spatial resolutions of the clutter covariance matrix to calculate a final detection coefficient. A simple voting scheme is used to calculate the final detection coefficient from a vector of detection decisions. Each element of the detection vector represents a detection decision based on a single orthogonal projection estimate of the proposed moving target's scattering coefficient using one multilook SAR image to estimate the scattering covariance matrix.

Chapter 6 demonstrates the efficacy of the approach presented in Chapter 5. Simulations for several different scenarios are presented. The results of the proposed multiple resolution approach to GMTI using multilook SAR images to estimate the clutter spectrum is compared and contrasted to traditional SMI STAP.

Finally, the author's conclusions about the proposed approach to multilook SAR

and multiple resolution GMTI are detailed in Chapter 7. These conclusions include ideas for future research in this area.

1.6 Notation and Terminology

- The letter j is defined as $\sqrt{-1}$
- Scalars are denoted by uppercase or lowercase letters (e.g., t in (2.1))
- Vectors are denoted by bold, lowercase letters (e.g., $\mathbf{r}_s$ in (2.1))
- Matrices are denoted by bold, uppercase letters (e.g., $\mathbf{P}$ in (2.14))
- Complex conjugation is denoted by $(\cdot)^*$
- $(\cdot)^\dagger$ denotes the vector or matrix transpose operation
- $(\cdot)^H$ denotes the complex conjugate, or Hermitian vector or matrix transpose
- The symbol $*$ denotes convolution
- Vertical bars $|\cdot|$ denote the modulus of a complex number or magnitude of real number. When around a vector, the vertical bars denote the Euclidean norm

Some terms will be used throughout this document, and should be introduced. The terms, *target*, *scatterer*, resolution cell, and *scene* all represent objects that scatter electromagnetic energy in the direction of the radar. The scene is an area on Earth that is illuminated by the transmitted electromagnetic energy from the radar. Based on the resolution of the radar, the scene is segmented into smaller sections called resolution cells. These sections are larger are much larger than the wavelength of the radar's carrier frequency. In general, a target is a moving or nonmoving scatterer. Specifically, when discussing GMTI, a target is a moving scatterer.

Other terms that warrant mentioning are *range*, *along track*, *cross track*, *velocity*, and *relative velocity*. Range is the distance from the radar to the target or resolution cell of interest. Along track is the direction of travel of the radar platform, and conversely, cross track is perpendicular to along track. A resolution cell is defined by its along-track and cross-track position and area. Velocity refers to the speed and direction of the radar platform, while relative velocity is the difference speed between the radar platform and a target, along the range vector.

Chapter 2

Ground Moving Target Indication

By definition, the goal of a moving target indication (MTI) system is to detect scattering objects that are moving, otherwise known as moving targets, and determine their relative radial velocities with respect to the radar. For airborne MTI systems, specifically those detecting moving targets on the ground, or GMTI systems, strong ground clutter returns complicate detecting energy scattered from moving targets. Significantly reducing the clutter energy in the received airborne and spaceborne GMTI measurements has been a challenge for radar engineers for more than thirty years. Many solutions have been proposed, including the displaced phase center antenna (DPCA), generalized DPCA, many variations of space-time adaptive processing (STAP), direct data domain (D3), and a variety of other methods. Of these techniques, STAP-based approaches have been the most popular in terms of the number of books, papers, and presentations generated. However, STAP has two inherent weaknesses: 1) STAP lacks the ability to characterize the clutter in the local area of the moving target, and 2) STAP requires a large amount of supporting data.

This chapter begins with a description of the linear, discrete radar model used throughout this research. An overview of GMTI is presented to provide the background necessary to understand the problem faced by radar engineers and the many approaches to GMTI that have been proposed. A survey of these approaches and their limitations is presented.

2.1 Radar Model

Before discussing any signal processing techniques, a common understanding of the structure of the received signal model used in this research must be developed. This section presents a concise description of the discrete, linear, multiple aperture, range Doppler radar observation equation that will be used in this research. For a comprehensive background of this equation and the assumptions required to arrive at this equation, the reader is referred to any of a number of radar textbooks, including Curlander [34], Franceschetti [35], and Skolnik [36]. Specifically, the notation used and the radar model developed closely follows that of Goodman's dissertation [37], Jenshak's dissertation [38], and a paper by Stiles, et al. [39].

Some of the common assumptions used in developing this model are:

- Fixed transmit pattern over coherent pulse interval (CPI),
- Radar transmits coherent burst of M pulses at constant pulse repetition interval (PRI),
- Receiver for each element has down converter and analog-to-digital (A/D) converter, and
- Radar platform and any moving scatterers have constant velocity over a CPI.

2.1.1 Radar Geometry

The radar geometry is shown in Figure 2.1, where the radar host platform is an aircraft. In general, the host platform could be airborne or spaceborne. The platform is traveling in the positive x-direction, also referred to as the along-track direction, with velocity v. The array phase reference is located at the origin of the coordinate

system. Assuming a flat-Earth, the z-coordinate of the illuminated area on the Earth, referred to as the scene, is -h, where h is the altitude of the array phase reference. At $t = 0$ the transmitter is located at the array phase reference.

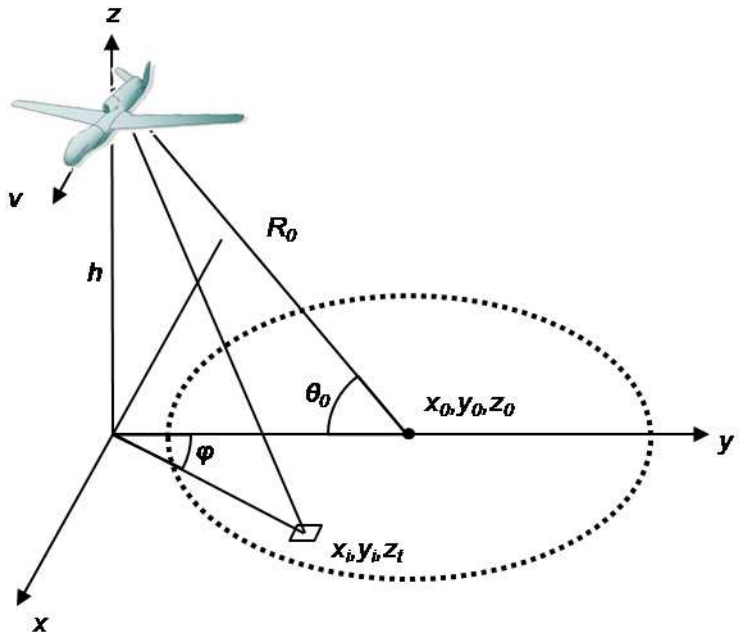

Figure 2.1. Radar geometry for a side-looking airborne platform with flat-Earth approximation

Using Figure 2.1, the location vectors of the transmitter, receivers, and locations within the scene may be defined. The vector defining the location of a spot within the scene is $\mathbf{r}_s = [x \; y \; -h]^\dagger$, where $(\cdot)^\dagger$ denotes the matrix or vector transpose operation. Since the transmitter is located at the array phase reference, which passes through the origin at $t = 0$, the transmitter location at an arbitrary time may be defined as $\mathbf{r}_t = \mathbf{v}t$, where $\mathbf{v}$ is the radar platform velocity vector, $\mathbf{v} = [v \; 0 \; 0]^\dagger$. Similarly, at $t = 0$, the location of a receiver is defined as $\mathbf{r}_r = [r_x \; r_y \; r_z]^\dagger$.

Using these location vectors, the range from the transmitter to an arbitrary loca-

tion in the scene at time t is

$$R_{tx}\left(\mathbf{r}_s, t\right) = |\mathbf{v}t - \mathbf{r}_s|. \tag{2.1}$$

Likewise, the range from the arbitrary location in the scene to a receiver is

$$R_{rx}\left(\mathbf{r}_s, \mathbf{r}_r, t\right) = |\mathbf{r}_r + \mathbf{v}t - \mathbf{r}_s|. \tag{2.2}$$

The round-trip delay from the time the signal is transmitted to the time it is received is then

$$\tau\left(\mathbf{r}_s, \mathbf{r}_r, t\right) = \frac{1}{c}\left[R_{tx}\left(\mathbf{r}_s, t\right) + R_{rx}\left(\mathbf{r}_s, \mathbf{r}_r, t\right)\right], \tag{2.3}$$

where c is the speed of light in freespace.

2.1.2 Transmit Signal

The general radar model used in this research has one transmitter and an arbitrary number of receivers N. The transmit signal is a superposition of weighted temporal basis functions $\psi_l\left(t\right)$, where the weights are s_l, such that

$$s\left(t\right) = \sum_m \sum_l s_l \psi_l\left(t - mT_0\right) \tag{2.4}$$

where T_0 is the PRI.

For simplicity, throughout this research the transmit signal $s\left(t\right)$ is assumed to be a coherent pulse train. Therefore, $s_l = 1,\ \forall l$, and $\psi_l\left(t\right)$ is assumed to be a time-limited pulse defined as

$$\psi_l\left(t\right) = \text{rect}\left(\frac{t - l\tau}{\tau}\right) \tag{2.5}$$

where

$$\text{rect}\left(\frac{t}{\tau}\right) = \begin{cases} 1, & -\frac{\tau}{2} < t < \frac{\tau}{2} \\ 0, \text{ elsewhere} \end{cases} \tag{2.6}$$

where τ is the time width of the transmit pulse, or chip. Note, the pulse width τ in (2.5) and (2.6) is not the same as delay $\tau(\mathbf{r}_s, \mathbf{r}_r, t)$ in (2.3) and later in (2.8) and (2.9).

The ideal coherent pulse train is illustrated in Figure 2.2. The entire timewidth of the transmit signal is $T = MT_0 + \tau$. Since $T_0 \gg \tau$,

$$T \approx MT_0. \tag{2.7}$$

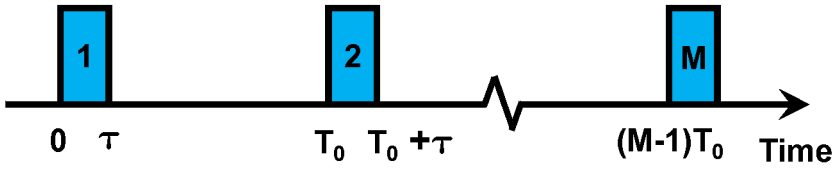

Figure 2.2. Coherent pulse train

2.1.3 Space-Time Measurement Vector

The transmitted signal propagates from the transmitter and illuminates an area on the Earth referred to as the scene. Let the gains of the transmitter and receiver in the direction of the scatterer be $G(\mathbf{r}_s)$, and the carrier frequency be ω_0. For one unit-response, point scatterer at location $\mathbf{r}_s$, the received signal measured at position $\mathbf{r}_r$ and time t is

$$\rho(\mathbf{r}_s, \mathbf{r}_r, t) = \frac{G(\mathbf{r}_s)}{R_{tx}(\mathbf{r}_s, t) R_{rx}(\mathbf{r}_s, \mathbf{r}_r, t)} \int_T e^{-j\omega_0 t'} \delta[t - t' - \tau(\mathbf{r}_s, \mathbf{r}_r, t)] s(t') dt', \tag{2.8}$$

where T is the transit signal length defined in (2.7), and $\delta(\cdot)$ is the delta function.

The difference between $R_{tx}(\mathbf{r}_s, t)$ and $R_{rx}(\mathbf{r}_s, \mathbf{r}_r, t)$ has an insignificant impact on the amplitude of $\rho(\mathbf{r}_s, \mathbf{r}_r, t)$ over the time and space of the processing interval. Therefore, the denominator may be approximated as $R_{tx}(\mathbf{r}_s, t) R_{rx}(\mathbf{r}_s, \mathbf{r}_s, t) \approx R_{tx}(\mathbf{r}_s, 0) R_{rx}(\mathbf{r}_s, \mathbf{0}, 0) = R(\mathbf{r}_s)^2$. Using this approximation and the sifting property of integrating the delta function results in

$$\rho(\mathbf{r}_s, \mathbf{r}_r, t) = \frac{G(\mathbf{r}_s)}{R(\mathbf{r}_s)^2} e^{-j\omega_0 \tau(\mathbf{r}_s, \mathbf{r}_r, t)} s(t - \tau(\mathbf{r}_s, \mathbf{r}_r, t)). \tag{2.9}$$

Equation (2.9) is the radar response function for a point target at $\mathbf{r}_s$ at time t. It is analogous to an impulse response. When the point scatterer is not unit-response, the radar response function is scaled by a scattering coefficient γ proportional to the radar cross section (RCS) of the scatterer. Without any interference, the resulting measurement at time t from a scatterer with scattering coefficient γ located at $\mathbf{r}_s$ would be

$$d(\mathbf{r}_r, t) = \gamma \rho(\mathbf{r}_s, \mathbf{r}_r, t). \tag{2.10}$$

In general, the scene is more complex than a single point scatterer. How the transmitted energy is reradiated, or scattered from nonmoving scatterers in a scene can be described by a scattering function $\gamma(\mathbf{r}_s)$. Incorporating the entire scene of nonmoving scatterers into (2.10) and including the radar system noise $n(\mathbf{r}_r, t)$ results in

$$d(\mathbf{r}_r, t) = \int_A \gamma(\mathbf{r}_s) \rho(\mathbf{r}_s, \mathbf{r}_r, t) \, d\mathbf{r}_s + n(\mathbf{r}_r, t), \tag{2.11}$$

where A is the area of the scene.

The function $\gamma(\mathbf{x}_s)$ is the scattering response for all illuminated scatterers, distributed and point scatterers. The scattering response may be described by a super-

position of basis functions,

$$\gamma\left(\mathbf{x}_s\right) = \sum_{n=1}^{N_t} \gamma_n \psi_n\left(\mathbf{x}_s\right). \tag{2.12}$$

The scene is assumed to consist of distributed scatterers and is pixelated into ground patches or along-track and cross-track resolution cells. The bandwidth, coherent processing interval (CPI), pulse repetition frequency (PRF), and antenna array characteristics determine the number and size of the resolution cells. In the case of resolution cells, the basis functions $\psi_n\left(\mathbf{x}_s\right)$ each represent the spatial area of the n^{th} resolution cell. The scalar γ_n in (2.12) is the complex scattering coefficient representing the composite scattering from all scatterers within the n^{th} resolution cell. Each scattering coefficient may be placed lexiconographically by cross track and then along track in a vector $\boldsymbol{\gamma}$.

Similarly, the radar response functions $\rho\left(\mathbf{r}_s, \mathbf{r}_r, t\right)$ correspond to the resolution cells. Additionally, the functions are sampled with a total of BT samples, where B is the bandwidth of the transmitted signal, and T is the timewidth, the response functions become response vectors $\boldsymbol{\rho}\left(\mathbf{r}_s, \mathbf{r}_r, t_k\right)$, for $k = 1, 2, \ldots, BT$. The continuous receive function becomes measurement vector $\mathbf{d}$, which can be represented as a sum of response vectors weighted by their corresponding scattering coefficients, as shown below:

$$\mathbf{d} = \sum_{i=1}^{N_t} \boldsymbol{\rho}_i \gamma_i + n_i + \varepsilon_i. \tag{2.13}$$

By organizing the response vectors $\boldsymbol{\rho}_i$ into a matrix called the array manifold $\mathbf{P}$, and the scattering coefficients γ_i lexiconographically by cross track and then along

track in a vector $\boldsymbol{\gamma}$, (2.13) becomes the linear, discrete radar model

$$\mathbf{d} = \mathbf{P}\boldsymbol{\gamma} + \mathbf{n} + \boldsymbol{\varepsilon}. \tag{2.14}$$

Equation (2.14) implicitly assumes the scattering from all the resolution cells are independent, in other words, there is no coupling nor mutlipath between resolution cells. However, without changing the form of (2.14), a response vector $\boldsymbol{\rho}_i$ and scattering coefficient γ_i a moving or non-moving scatterer may be added to the sum in (2.13) and equivalently, to $\mathbf{P}$ and $\boldsymbol{\gamma}$ in (2.14). To accommodate moving scatterers, commonly called targets in GMTI, a new notation for the scatterer parameters is introduced. The vector $\mathbf{x}_s$ is composed of the location parameters $\mathbf{r}_s$ and relative velocity with respect to ground v_s of a moving target. The vector $\mathbf{x}_s$ is defined as

$$\mathbf{x}_s = \left[\mathbf{r}_s^{\dagger}\ v_s\right]^{\dagger}. \tag{2.15}$$

From this point forward, the subscripts s, r, and t will not be used on the location vectors. The vector $\mathbf{x}$ will refer to the location and relative velocity with respect to ground of a scatterer, as in (2.15). The vector $\mathbf{r}$ will signify the spatial location of the receiver.

Given a receive array of N antenna elements, there are L fast-time samples for each returned pulse within a coherent processing interval (CPI), and sets of L fast-time samples are separated by the PRI, which equates to the slow-time sampling period. Assuming there are M pulses in a CPI, the sampled data vector would contain K elements, where K is the product of number of fast-time samples, the number of

slow-time samples, and the number of receive elements in the array, i.e., K=LMN.

$$\mathbf{d} = [d(\mathbf{r}_1, t_1) \ \cdots \ d(\mathbf{r}_N, t_1) \ \cdots \ d(\mathbf{r}_N, t_K)]^\dagger, \tag{2.16}$$

$$\mathbf{P} = [\boldsymbol{\rho}_1 \ \boldsymbol{\rho}_2 \cdots \ \boldsymbol{\rho}_{N_t}], \tag{2.17}$$

$$\boldsymbol{\gamma} = [\gamma_1 \ \gamma_2 \ \cdots \ \gamma_{N_t}]^\dagger, \tag{2.18}$$

$$\mathbf{n} = [n(\mathbf{r}_1, t_1) \ \cdots \ n(\mathbf{r}_N, t_K)]^\dagger, \tag{2.19}$$

$$\boldsymbol{\rho}_i = [\rho(\mathbf{x}_i, \mathbf{r}_1, t_1) \ \cdots \ \rho(\mathbf{x}_i, \mathbf{r}_N, t_K)]^\dagger, \tag{2.20}$$

and

$$\gamma_i = \gamma(\mathbf{x}_i). \tag{2.21}$$

Figure 2.3 is a graphical representation of the sampled measurement parameters.

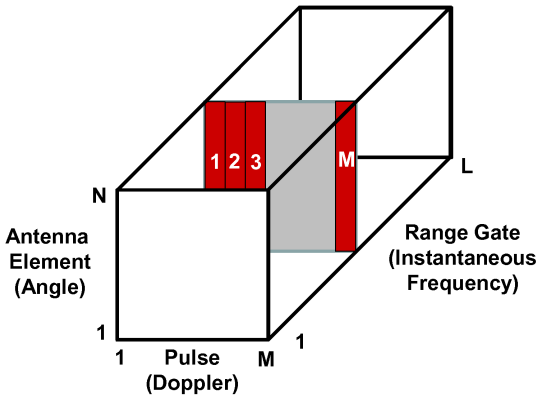

Figure 2.3. Space-time radar data cube

2.1.3.1 Interference

In addition to the energy received from scatterers, the received data includes Gaussian and nonGaussian noise and interference. In systems operating at microwave

frequencies, the noise is dominated by internal receiver noise, as noted in Chapter 1 of Skolnik [36]. Therefore, the elements of the complex noise vector $\mathbf{n}$ are assumed to be independent and identically distributed (iid) zero-mean, white Gaussian noise (WGN) with known variance σ_n^2.

The final component of the measurement vector $\boldsymbol{\varepsilon}$ contains all of the nonGaussian interference and any errors associated with the array manifold. Jammers; intrinsic clutter motion, such as windblown trees; aircraft crab angle; range walk; and calibration errors are included in $\boldsymbol{\varepsilon}$.

2.2 Ground Moving Target Indication Processing

Moving target detection depends on determining whether or not the measurements contain any energy due to at least one moving scatterer. Specifically, detecting moving scatterers on the ground requires a processor to determine whether or not the measurements contain energy from a moving object on the ground in the presence of a large reflection of radar energy from the ground itself. There are many approaches to detecting the energy from a moving scatterer and estimating its characteristics. This section will present a survey of GMTI techniques, beginning with the general GMTI detector architecture. The goal of the survey is to show the common heritage of progressively complex approaches and to lay the foundation for the multiple resolution approach to GMTI presented in Chapter 5.

In GMTI, moving scatterers are called targets, and scatterers that are not moving with respect to ground are considered to be clutter sources. In detection theory, the

GMTI detection problem becomes one of determining the correct hypothesis,

$$H_0 : \mathbf{d}_{H_0} = \mathbf{P}_C \boldsymbol{\gamma}_C + \mathbf{n} + \boldsymbol{\varepsilon}$$
$$H_1 : \mathbf{d}_{H_1} = \gamma_t \boldsymbol{\rho}_t + \mathbf{d}_{H_0} \tag{2.22}$$

where the null hypothesis H_0 is the interference only case, and the alternative hypothesis H_1 is the signal plus interference case. The signal in GMTI is due to a moving target with unknown scattering coefficient γ_t and space-time radar response vector $\boldsymbol{\rho}_t$.

Since the presence of a moving target is unknown, it follows that the scattering characteristics of the potential moving target are also unknown; therefore, a space-time radar response vector $\boldsymbol{\rho}_t$ is hypothesized and a detection coefficient must be calculated. By hypothesizing $\boldsymbol{\rho}_t$, the problem becomes detecting a known signal in interference, which is accomplished by comparing the magnitude of an estimated scattering coefficient to a predetermined threshold. The general MTI detector architecture in Figure 2.4 below will be developed as the different approaches to GMTI are presented.

As described in Chapter 1 of Klemm [2], the well-known linear weighting, or

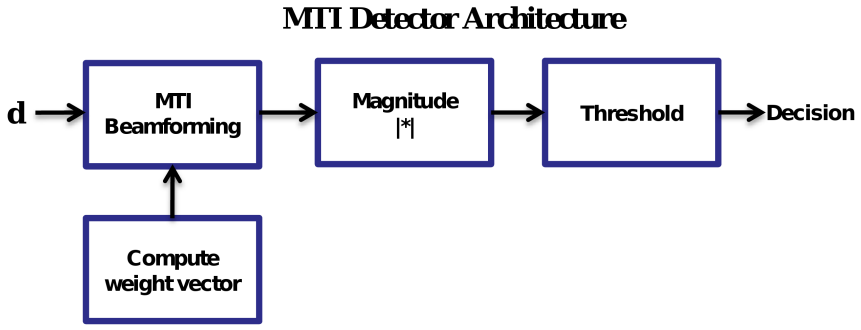

Figure 2.4. MTI detector architecture

beamformer for a discrete, linear model such as in the alternate hypothesis H_1 in (2.22), is

$$\mathbf{w}_{opt} = \mu \mathbf{R}_I^{-1} \boldsymbol{\rho}_t. \tag{2.23}$$

The symbol μ is a criterion-based scalar, and $\mathbf{R}_I$ is the interference correlation matrix, which is defined as

$$\mathbf{R}_I = E\left\{ \left(\mathbf{P}_C \boldsymbol{\gamma}_C + \mathbf{n} + \boldsymbol{\varepsilon} \right) \left(\mathbf{P}_C \boldsymbol{\gamma}_C + \mathbf{n} + \boldsymbol{\varepsilon} \right)^H \right\}. \tag{2.24}$$

The operator $E\{\cdot\}$ is the expectation operator, and $(\cdot)^H$ is the Hermitian (or complex conjugate) transpose operator. Assuming the interference is zero mean, $\mathbf{R}_I$ is then the covariance matrix of the interference. The estimate of the moving target's scattering coefficient is then

$$\hat{\gamma}_t = \mathbf{w}_{opt}^H \mathbf{d}. \tag{2.25}$$

An important observation of (2.25) is that the interference covariance matrix $\mathbf{R}_I$ *whitens* the measurements prior to the measurements being *matched* to the space-time radar response vector $\boldsymbol{\rho}_t$. These terms will be used throughout this document, particularly when discussing simplifications to the optimum processor.

Klemm [2] observes that the linear processor in (2.23) is optimal under several criteria:

1. Maximum likelihood performance measure, where $\mathbf{w}_{ML}$ maximizes the likelihood function of $\mathbf{d}_{H_1} = \gamma_t \boldsymbol{\rho}_t + \mathbf{P}_C \boldsymbol{\gamma}_C + \mathbf{n} + \boldsymbol{\varepsilon}$ with respect to γ_t. The constant in (2.23) becomes $\mu = \left(\boldsymbol{\rho}_t^H \mathbf{R}_d^{-1} \boldsymbol{\rho}_t \right)^{-1}$, and the signal plus interference covariance

matrix is:

$$\mathbf{R}_d = E\left\{\left(\gamma_t\boldsymbol{\rho}_t + \mathbf{P}_C\boldsymbol{\gamma}_C + \mathbf{n} + \boldsymbol{\varepsilon}\right)\left(\gamma_t\boldsymbol{\rho}_t + \mathbf{P}_C\boldsymbol{\gamma}_C + \mathbf{n} + \boldsymbol{\varepsilon}\right)^H\right\}. \tag{2.26}$$

2. Maximum signal-to-noise ratio (SNR), where the constant μ has no influence on the SNR and may be chosen arbitrarily.

3. Linearly constrained minimum noise variance, where the output power is minimized subject to the constraint $\mathbf{w}^H\boldsymbol{\rho}_t = g$. The constraint prevents the trivial solution $\mathbf{w} = \mathbf{0}$. The constant μ then becomes $\mu = g/\left(\boldsymbol{\rho}_t^H\mathbf{R}_I^{-1}\boldsymbol{\rho}_t\right)$.

4. Minimum mean square error (MMSE)[1] criterion, where the measured data vector $\mathbf{d}$ is weighted so that the squared difference between the output and γ_t is minimized. The result is

$$\mathbf{w}_{MMSE} = \mu\mathbf{R}_d^{-1}\boldsymbol{\rho}_t, \tag{2.27}$$

where $\mathbf{R}_d$ is given in (2.26) and the constant μ is then the variance of γ_t, which is σ_t^2.

It is important to note difference between the linear processors resulting from Klemm's third and fourth observations. The linearly constrained minimum noise variance processor, hereafter denoted the minimum variance method (MVM), whitens the data with the interference covariance matrix $\mathbf{R}_I^{-1}$, while the MMSE processor whitens the data with the data covariance matrix $\mathbf{R}_d^{-1}$. The difference being whether or not the outer product of the steering vector weighted by the target variance is included in the covariance matrix. As a foreshadow, the MVM processor will be used in the proposed approach to GMTI, while the MMSE processor will be used in SAR

[1]Klemm calls this criterion the least mean square error

image computations.

Since the interference in GMTI is unknown, the interference covariance matrix must be estimated. This estimation is complicated by the fact that none of the constituent parameters of the interference is completely known, and assumptions must be made about their statistical distributions. These assumptions and how they are implemented separate the many approaches to GMTI.

2.2.1 Form of Interference Covariance Matrix

By definition, a covariance matrix is a matrix of expected values. Assuming the constituent statistical parameters have zero mean, the covariance matrix equals the correlation matrix. Correlation is a statistical measurement of relationship. Therefore, if one vector is correlated with another, then knowledge of one vector reveals information about the correlated vector. In this sense, the interference covariance matrix is a matrix with elements measuring the interrelationships of the constituent parameters of the interference.

Returning to the definition of the received data vector in (2.14), the interference consists of the energy from scatterers other than the desired target, as well as noise, and other errors. In GMTI, nonmoving scatterers are referred to as clutter, and the clutter array manifold $\mathbf{P}_C$ consists of space-time radar response vectors corresponding to the clutter in the along-track, cross-track resolution cells. The vector of complex scattering coefficients associated with the scattering from clutter in the resolution cells are $\boldsymbol{\gamma}_C$. Together, the multiplication $\mathbf{P}_C\boldsymbol{\gamma}_C$ represents the received energy due

to the clutter scattering. Expanding (2.24), the interference covariance matrix is then

$$\begin{aligned}\mathbf{R}_I &= E\left\{\left(\mathbf{P}_C\boldsymbol{\gamma}_C+\mathbf{n}+\boldsymbol{\varepsilon}\right)\left(\mathbf{P}_C\boldsymbol{\gamma}_C+\mathbf{n}+\boldsymbol{\varepsilon}\right)^H\right\} \\ &= E\left\{\left(\mathbf{P}_C\boldsymbol{\gamma}_C\right)\left(\mathbf{P}_C\boldsymbol{\gamma}_C\right)^H+\left(\mathbf{P}_C\boldsymbol{\gamma}_C\right)\mathbf{n}^H+\left(\mathbf{P}_C\boldsymbol{\gamma}_C\right)\boldsymbol{\varepsilon}^H\right\} \\ &\quad + E\left\{\mathbf{n}\left(\mathbf{P}_C\boldsymbol{\gamma}_C\right)^H+\mathbf{n}\mathbf{n}^H+\mathbf{n}\boldsymbol{\varepsilon}^H\right\}+E\left\{\boldsymbol{\varepsilon}\left(\mathbf{P}_C\boldsymbol{\gamma}_C\right)^H+\boldsymbol{\varepsilon}\mathbf{n}^H+\boldsymbol{\varepsilon}\boldsymbol{\varepsilon}^H\right\}.\end{aligned} \tag{2.28}$$

The noise is expected to be zero-mean, complex, white Gaussian, which means the noise elements are uncorrelated with each other. As white complex Gaussian noise, $\mathbf{n}$ is also uncorrelated with the clutter and errors. Because the error vector contains errors associated with the array manifold and calibration errors, in general, $\boldsymbol{\varepsilon}$ may be correlated with itself and with the clutter energy. Using these assumptions, the interference covariance matrix reduces to

$$\begin{aligned}\mathbf{R}_I &= E\left\{\left(\mathbf{P}_C\boldsymbol{\gamma}_C\right)\left(\mathbf{P}_C\boldsymbol{\gamma}_C\right)^H\right\}+E\left\{\mathbf{n}\mathbf{n}^H\right\}+E\left\{\boldsymbol{\varepsilon}\boldsymbol{\varepsilon}^H\right\} \\ &\quad + E\left\{\boldsymbol{\varepsilon}\left(\mathbf{P}_C\boldsymbol{\gamma}_C\right)^H\right\}+E\left\{\left(\mathbf{P}_C\boldsymbol{\gamma}_C\right)\boldsymbol{\varepsilon}^H\right\} \\ &= E\left\{\left(\mathbf{P}_C\boldsymbol{\gamma}_C\right)\left(\mathbf{P}_C\boldsymbol{\gamma}_C\right)^H\right\}+E\left\{\mathbf{n}\mathbf{n}^H\right\}+E\left\{\boldsymbol{\varepsilon}\boldsymbol{\varepsilon}^H\right\}+\mathbf{P}_CE\left\{\boldsymbol{\gamma}_C\boldsymbol{\varepsilon}^H\right\} \\ &\quad + E\left\{\boldsymbol{\varepsilon}\boldsymbol{\gamma}_C^H\right\}\mathbf{P}_C^H.\end{aligned} \tag{2.29}$$

NonGaussian interference including jammers, intrinsic clutter motion such as windblown trees, aircraft crab angle, range walk, and calibration errors are included in $\boldsymbol{\varepsilon}$. The error sources are a valid concern and will need to be considered for any operational system; however, the nonGaussian interference is assumed to be negligible for the purposes of this research. Many researchers have considered techniques to account for error sources in GMTI. Guerci [40] introduced the covariance matrix taper as a method to account for the effects of nonstationary interference, and other error

sources, such as aircraft velocity vector errors. One effect of the covariance matrix taper is to reduce the minimum detectable velocity of moving targets. Additionally, many approaches to mitigating the effects of jammers have been proposed. However, SAR implicitly assumes the array manifold is known and no jammers exist; therefore, this research will consider the interference to consist of noise and stationary clutter only, which leads to

$$\mathbf{R}_I = E\left\{\left(\mathbf{P}_C\boldsymbol{\gamma}_C\right)\left(\mathbf{P}_C\boldsymbol{\gamma}_C\right)^H\right\} + E\left\{\mathbf{n}\mathbf{n}^H\right\} = \mathbf{R}_C + \mathbf{R}_n. \tag{2.30}$$

where $\mathbf{R}_C$ is the clutter covariance matrix and $\mathbf{R}_n$ is the noise covariance matrix. Since the noise is assumed to be zero-mean, white Gaussian, the noise covariance matrix can be represented by the average noise power per measurement σ_n^2 multiplied by an identity matrix

$$\mathbf{R}_n = \sigma_n^2\mathbf{I}. \tag{2.31}$$

The array manifold of the clutter is assumed to be known; otherwise, SAR images could not be created. $\mathbf{P}_C$ is then deterministic, and the clutter covariance matrix may be written

$$\mathbf{R}_C = \mathbf{P}_C E\left\{\boldsymbol{\gamma}_C\boldsymbol{\gamma}_C^H\right\}\mathbf{P}_C^H = \mathbf{P}_C\mathbf{R}_\gamma\mathbf{P}_C^H, \tag{2.32}$$

where $\mathbf{R}_\gamma$ is the clutter scattering coefficient covariance matrix, or simply the scattering covariance matrix, for N_C range-azimuth resolution cells has the form

$$\mathbf{R}_\gamma = E\left\{\boldsymbol{\gamma}_C\boldsymbol{\gamma}_C^H\right\} = \begin{bmatrix} E\left|\gamma_1\right|^2 & E\left\{\gamma_1\gamma_2^*\right\} & \cdots & E\left\{\gamma_1\gamma_{N_C}^*\right\} \\ E\left\{\gamma_2\gamma_1^*\right\} & E\left|\gamma_2\right|^2 & & \vdots \\ \vdots & & \ddots & \\ E\left\{\gamma_{N_C}\gamma_1^*\right\} & \cdots & & E\left|\gamma_{N_C}\right|^2 \end{bmatrix}. \tag{2.33}$$

Assuming the scattering coefficients from individual resolution cells are uncorrelated with each other, $E\left\{\gamma_i \gamma_j^*\right\} = 0, \quad \forall\, i \neq j$. This assumption is valid, in general, since each resolution cell is much larger than a wavelength in both dimensions, the scattering from any individual range cell is an aggregate of the scattering from many small scatterers in that area. Assuming that the scatterers within a resolution cell are independent and identically distributed (iid), the central limit theorem [41] may be invoked resulting in a Gaussian distribution with zero-mean. Therefore, even though the magnitudes of the scattering coefficients for two adjacent resolution cells may be similar the scattering coefficients themselves can be assumed to be independent and thus, uncorrelated. Therefore, the scattering intensity covariance matrix may be approximated as

$$\mathbf{R}_\gamma \approx \begin{bmatrix} E|\gamma_1|^2 & 0 & \cdots & 0 \\ 0 & E|\gamma_2|^2 & & \vdots \\ \vdots & & \ddots & 0 \\ 0 & \cdots & 0 & E|\gamma_{N_C}|^2 \end{bmatrix} = diag(\mathbf{\Gamma}), \tag{2.34}$$

where

$$\mathbf{\Gamma} = \left[E\left|\gamma_1\right|^2 \; E\left|\gamma_2\right|^2 \; \cdots \; E\left|\gamma_{N_C}\right|^2\right]^T. \tag{2.35}$$

Fuhrmann et al. [42] have shown that $\boldsymbol{\gamma}$ is the expected spectrum of the clutter scattering function. Since the values of $E\left|\gamma_i\right|^2$ are unknown, they must be estimated to estimate $\boldsymbol{\gamma}$ and thus $\mathbf{R}_I$. An important observation is that the clutter spectral values are expected values, and

$$E\left|\gamma_i\right|^2 \neq \left|\gamma_i\right|^2, \tag{2.36}$$

where γ_i is a sample of one statistical realization of the random variable $\boldsymbol{\gamma}$.

2.2.2 Displaced Phase Center Antenna

Displaced phase center antenna (DPCA) processing is a fixed space-time approach to GMTI. In the 1950's the DPCA technique was applied to airborne early warning radars (AEW) for the defense of North America against intercontinental ballistic missiles. A history of the development of the DPCA technique and operational deployment, including AEW and the Joint Surveillance and Target Attack Radar System (Joint STARS) was published by Muehe and Labitt [5]. The heart of the DPCA processor is a coherent difference of measurements taken at the same spatial location at a slightly different time. The coherent difference requires a strict relationship between the PRF, array spacing, and platform velocity, which is often difficult to achieve in practice. DPCA is actually a family of techniques, and this discussion will focus on the type of DPCA described by Staudaher [43] and in Appendix C of Ward [44].

Figure 2.5 below is adapted from Ward [44] and illustrates the DPCA concept for four receive elements and three transmitted pulses. The measurements at antenna elements one through three at the second time increment (Pulse #1) are subtracted from measurements at the first time increment (Pulse #0) at elements two through four. By subtracting the measurements in this way, the phase center of the array at Pulse #1 is effectively shifted back (or displaced) in space to match the phase center at Pulse #0. Therefore, the phase centers of the array are collocated in space, but not time, for the two pulses.

Coherent subtraction of measurements from collocated phase centers allows the energy from nonmoving scatterers to be subtracted out of the measurements, and theoretically, all the remaining energy is from scatterers that have moved in the time

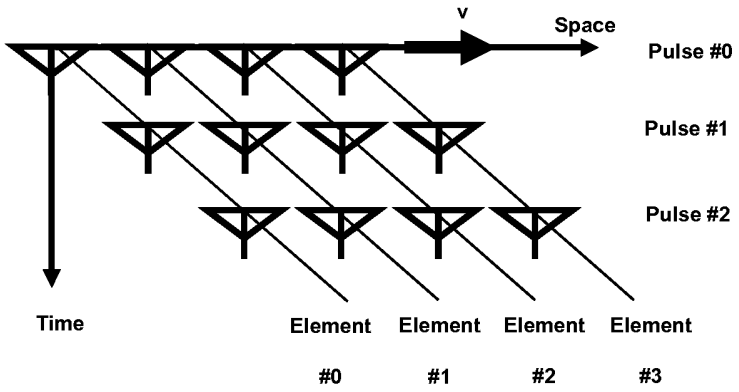

Figure 2.5. DPCA phase center progression

between the two measurements. For a given array element spacing d_x, the platform velocity v and PRF T_0 are chosen such that each subsequent pulse at the receive array has the same physical phase center as the previous pulse, resulting in the following relationship:

$$d_x = 2vT_0. \tag{2.37}$$

Given this heuristic approach of the DPCA technique, it is not immediately obvious that the process conforms to the general MTI detector architecture in Figure 2.4 or the GMTI estimator in (2.23). This realization is easily identified in the discrete measurement model below. Drawing from the mathematical description of the observation in (2.14), the measured data is projected into the subspace orthogonal to the clutter via the projection matrix $\mathbf{w}_{DPCA}$. Using a single two-pulse subCPI measurement, Ward [44] has shown the weight vector to be a simple canceler, which fits the form seen in (2.23)

$$\hat{\gamma}_t = \mathbf{w}_{DPCA}^H \mathbf{d}, \tag{2.38}$$

where

$$\mathbf{w}_{DPCA} = \begin{bmatrix} 0 \\ 1 \\ -1 \\ 0 \end{bmatrix} \boldsymbol{\rho}_t. \tag{2.39}$$

DPCA is a simple GMTI processor that may be implemented in hardware. However, it has poor minimum detectable velocity (MDV) performance, and the restrictions on velocity and PRI are difficult to maintain in practice.

2.2.3 Generalized DPCA

DPCA is analogous to specifying a radar system to meet the processor's requirements. On the other hand, generalized DPCA is a processor conforming to the design of a given radar system. Generalized DPCA is aptly named in that the technique is generalized to work without requiring the strict relationship between the antenna spacing, PRI, and platform velocity. Rather than a direct subtraction of measured data elements, generalized DPCA is a projection based on eigenspectral analysis. Richardson [4] has shown that for conditions in sideways looking airborne radar applications STAP can result in weight solutions equivalent to those required to perform DPCA. The following discussion shows the relationship between DPCA and generalized DPCA and highlights the deficiencies of generalized DPCA performance that more rigorous techniques attempt to improve upon.

In generalized DPCA, the eigenspectrum of the interference covariance matrix in (2.24) is calculated while approximating the clutter spectrum as uniform, resulting in the scattering covariance matrix $\mathbf{R}_\gamma$ equal to an identity matrix. This means the estimate of the interference covariance matrix is not adaptive, because it depends

solely on the array manifold. Therefore, the estimated interference covariance matrix is

$$\begin{aligned}\hat{\mathbf{R}}_I &= \mathbf{P}_C\mathbf{R}_\gamma\mathbf{P}_C^H + \sigma_n^2\mathbf{I} \\ &= \mathbf{P}_C\mathbf{I}\mathbf{P}_C^H + \sigma_n^2\mathbf{I} \\ &= \mathbf{P}_C\mathbf{P}_C^H + \sigma_n^2\mathbf{I} \\ &= \mathbf{E}_C\mathbf{\Lambda}\mathbf{E}_C^H + \sigma_n^2\mathbf{I},\end{aligned} \tag{2.40}$$

where $\mathbf{R}_\gamma = \mathbf{I}$. $\mathbf{E}_C$ is the unitary eigenmatrix of $\mathbf{P}_C\mathbf{P}_C^H$ and $\mathbf{\Lambda}$ is a matrix with the eigenvalues of $\mathbf{P}_C\mathbf{P}_C^H$ along the diagonal, and the eigenvalues are ordered, such that $\lambda_1 \geq \lambda_2 \geq \cdots \geq \lambda_K$. Assuming the noise energy is insignificant, the interference covariance matrix may be approximated by the estimated interference covariance matrix,

$$\hat{\mathbf{R}}_I \approx \mathbf{E}_C\mathbf{\Lambda}\mathbf{E}_C^H. \tag{2.41}$$

The eigenvectors corresponding to the *significant* eigenvalues are determined by the desired fraction of the clutter energy to reject F_E. While one would desire all of the clutter energy to be rejected, in reality, the subspace of the clutter energy and target energy overlap as illustrated in Figure 2.6. For simplicity, the clutter is assumed to have the same distribution as noise, which is a zero-mean, white Gaussian distribution. Rejecting all of the clutter energy would also reject some amount of the target energy. The significant eigenvectors of the clutter covariance matrix are then determined by choosing the N' largest eigenvalues such that

$$\frac{\sum_{i=1}^{N'}\lambda_i}{\sum_{i=1}^{N_t}\lambda_i} \geq F_E, \tag{2.42}$$

which leads to approximating the eigenvector matrix $\mathbf{E}_C$ with

$$\tilde{\mathbf{E}}_c \approx [\mathbf{e}_1 \, \mathbf{e}_2 \, \cdots \, \mathbf{e}_{N'}] \, . \tag{2.43}$$

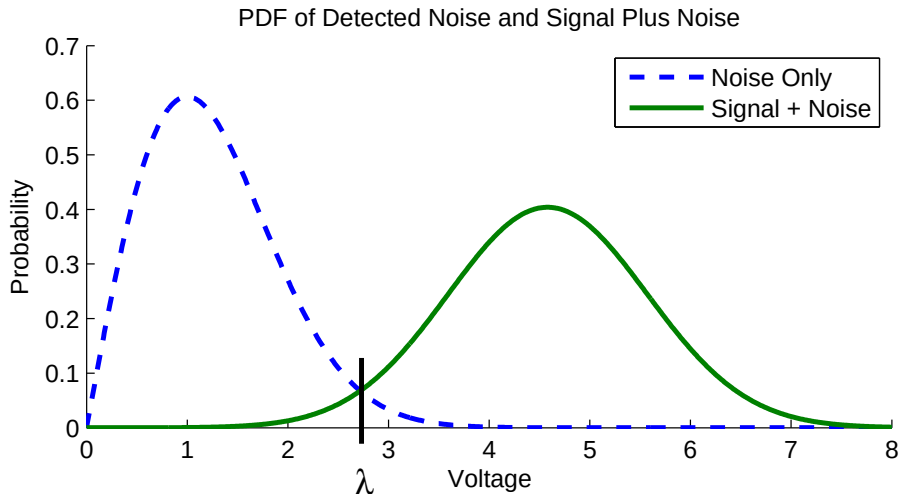

Figure 2.6. MTI radar noise and signal plus noise PDFs

The estimate of the interference covariance matrix for generalized DPCA is then composed of the eigenvectors corresponding to the larger eigenvalues of the interference covariance matrix. For simplicity, the significant eigenvalues are assumed to be unity, and the insignificant eigenvalues equal zero, by default. The resulting estimate of the interference matrix is then

$$\tilde{\mathbf{R}}_I = \tilde{\mathbf{E}}_C \tilde{\mathbf{E}}_C^H . \tag{2.44}$$

This generalized DPCA approach is an improvement over DPCA, in that it does not require strict relationships between the PRI and aircraft velocity. However, in reality the eigenvalues of the interference covariance matrix are not ones and zeros, as shown in Figure 2.7. Whitening the data with equally weighted eigenvectors of the

interference covariance matrix results in less computational complexity than using the true eigenvectors at the expense of estimation accuracy. Because the eigenvectors representing the clutter are all weighted equally, some of the clutter areas are undernulled, while other areas of the clutter are overnulled. This is evident in the difference between the true eigenspectrum and the unity spectrum assumed by generalized DPCA in Figure 2.7. The clutter for the indices less than around 200 will be undernulled by generalized DPCA, the clutter for indices above 200 will be overnulled, and the clutter spectrum above 510 will not be suppressed at all.

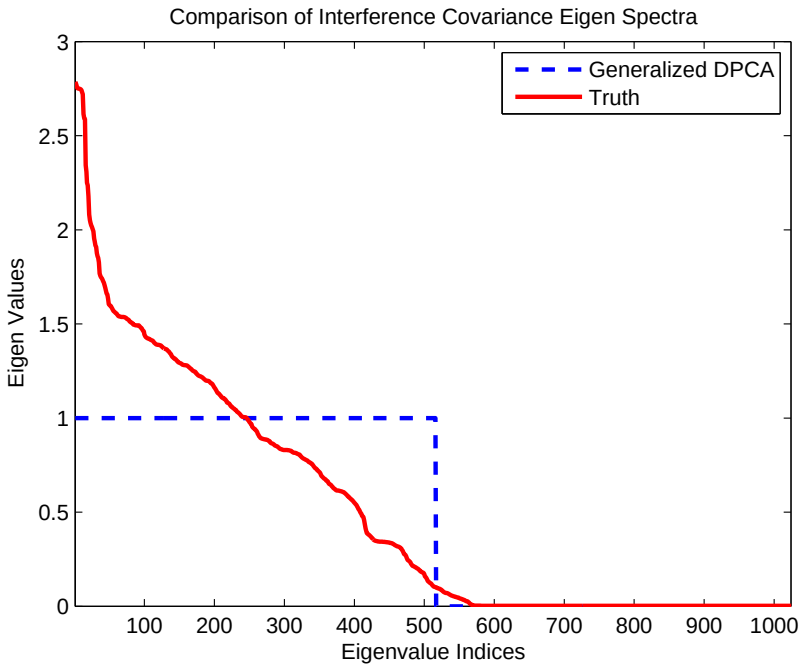

Figure 2.7. Eigenspectra of clutter and generalized DPCA approximation

Generalized DPCA is an intermediate step between DPCA and STAP that does not require the strict DPCA relationship in (2.37). As shown by Richardson [4], in sideways-looking airborne radar STAP, and thus generalized DPCA, can lead to a DPCA type solution when the array satisfies the DPCA relationship in (2.37).

Generalized DPCA is based on projecting the data into the target subspace, yet the uniform weighting of the clutter covariance eigenvectors results in suboptimum projection.

2.2.4 Space-Time Adaptive Processing

Brennan and Reed [10] introduced STAP based on estimating the interference covariance matrix from the collected data. The data are called space-time data, where space refers to the spatial sampling of the incoming electromagnetic radiation by spatial apertures, or receive elements, and time refers to the temporal sampling of the data. The process is adaptive because real-time measurements are used to estimate the interference covariance matrix in turn used to estimate the hypothesized target's scattering coefficient.

The general STAP detector architecture is shown in Figure 2.8. While very similar to the general MTI architecture in Figure 2.4, the primary difference is that STAP uses the measurements to calculate the weight vector. However, Figure 2.9 illustrates why fully-adaptive STAP is not practical. The processor must calculate a scalar weight for every measurement sample. This requirement led radar engineers to pursue reduced-rank approaches to approximate fully-adaptive STAP.

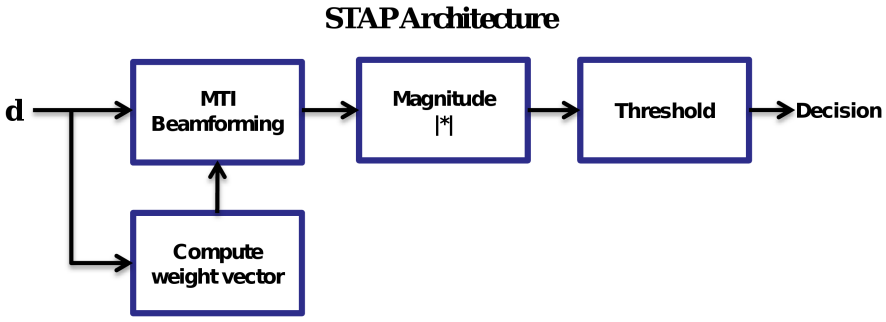

Figure 2.8. Space-time adaptive processor architecture

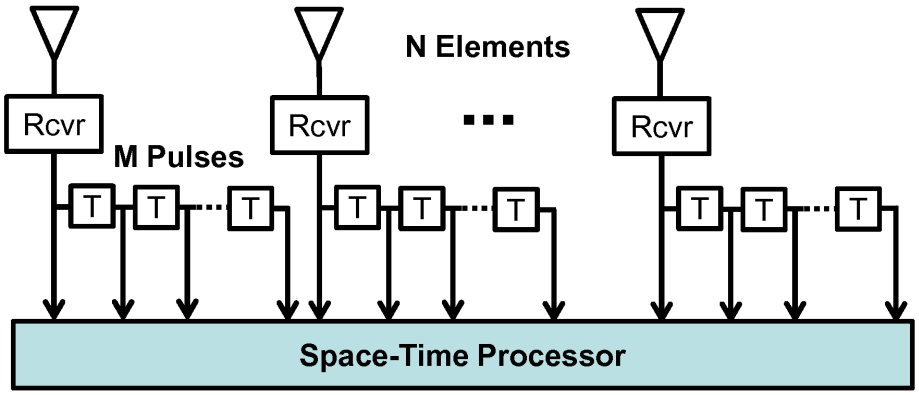

Figure 2.9. Fully-adaptive space-time processor

To increase the practical usefulness of STAP, Reed et al. [11] introduced sample matrix inversion (SMI) as a method to increase the convergence rate of the detector. SMI is a direct method of adaptive weight computation by estimating the interference covariance matrix with the received data. Measurements from only one range at a time are tested for the presence of a moving target, and measurements from that range are called the primary data. The primary data and one range cell on either side, called guard ranges, are assumed to contain the energy of the hypothesized target and are not included in the estimate of the interference covariance matrix. The measurements collected from other ranges are called *secondary data*, and are assumed to contain no energy from the moving target. The secondary data are then used in the SMI estimation of the interference covariance matrix. Recalling there are L range cells, the estimate of the interference covariance matrix (2.24) is then

$$\hat{\mathbf{R}}_I = \frac{1}{L-3}\left(\sum_{l=1}^{L}\mathbf{d}_l\mathbf{d}_l^H - \sum_{l=l_t-1}^{l_t+1}\mathbf{d}_l\mathbf{d}_l^H\right), \tag{2.45}$$

where l_t is the index for the primary range.

The SMI approach implicitly assumes the clutter statistical mean and covariance

from all the secondary ranges are identical to the clutter statistical mean and covariance of the primary range. In statistical terms, the clutter statistics are considered to be wide-sense stationary in range. The effect of heterogeneous clutter on the performance of STAP is covered in some detail by Melvin [12]. He states that simulation results reveal loss in signal-to-interference plus noise ratio (SINR) ranging between a few tenths of a decibel to greater than 16 dB for specific cases.

The amount of data required to estimate the interference covariance matrix using SMI depends on the rank of the interference covariance matrix. Brennan's rule originally introduced by Brennan and Staudaher [45] is an approximate rule for the rank of the clutter covariance matrix. Ward [44] proves Brennan's rule for the special case when the interpulse motion per half-element spacing, $\beta = 2vT_0/d_x$, is an integer less than or equal to N. Note, that $\beta = 1$ for DPCA. The rank of the interference covariance matrix is directly dependent on the number of spatial elements N, the number of pulses in a CPI M, the velocity of the radar platform v, the interelement spacing in along track d_x, and the PRI T_0, with the following relation:

$$r_C = N + (M - 1)\,\beta. \tag{2.46}$$

In Section 4.2 of his dissertation [37], Goodman discusses Brennan's rule and references work by Slepian, Landau, and Pollak [46–48], and other works in optics to conclude the time-bandwidth product is a more general estimate of the clutter rank, specifically

$$r_C = BT + 1, \tag{2.47}$$

where B is the bandwidth of the transmit signal, and T is the length of the CPI.

Both (2.46) and (2.47) support the claim that much secondary data is necessary

to estimate the clutter covariance matrix. The assumption of wide-sense stationary clutter with respect to range and large sample support are well-known drawbacks to STAP. Many approaches to overcoming these deficiencies by modifying STAP, or with alternative techniques, have been proposed with some success.

The effect of heterogeneous clutter may be demonstrated using a clutter scene with more than twice the number of range cells as azimuth cells, satisfying Brennan's Rule and the more stringent clutter rank in (2.47). Figure 2.10 shows a heterogeneous scene, and Figure 2.11 compares the eigenspectra of the estimates of the interference covariance matrix for two different ranges of heterogeneous scene. The eigenspectra of the SMI estimates are nearly identical for both ranges, as expected. However, the eigenspectra for the clairvoyantly estimates are very different, because the scattering from the upper and lower sections of the scene in Figure 2.10 have very different variance. In contrast, the eigenspectra of the clairvoyant and SMI estimates of the interference covariance matrix are similar, as shown in Figure 2.12. The resulting rece receiver operating characteristics (ROC) curves in Figure 2.13 illustrate how SMI performance can be degraded by clutter that is heterogeneous in range.

2.2.5 Structured Covariance Estimation Techniques

Many techniques have been proposed that take advantage of the structure of the interference covariance matrix. Knowledge-aided STAP (KA-STAP) represents the largest category of these techniques. A U.S. Defense Advanced Research Projects Agency (DARPA) program called Knowledge Aided Sensor Signal Processing and Expert Reasoning (KASSPER) from 2002-2005 contributed a large body of research in this area. Some of the results of the KASSPER program are included in the following sections.

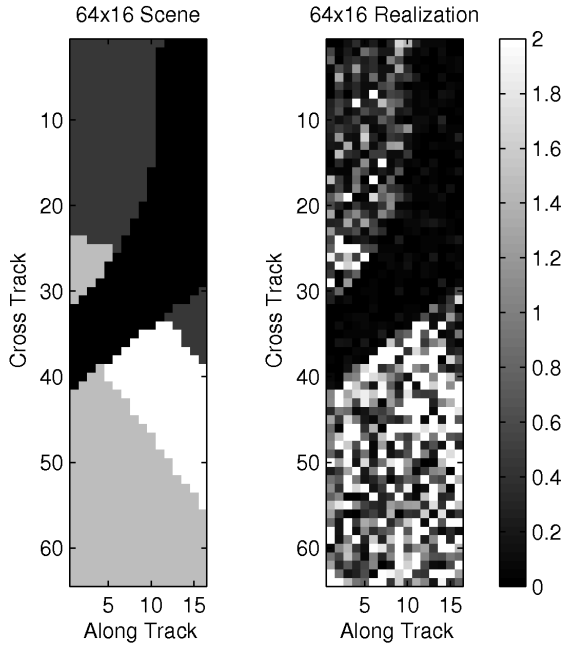

Figure 2.10. Expected and realized scattering spectrum for a simulated 64x16 heterogeneous scattering scene

2.2.5.1 Knowledge-Aided STAP (KA-STAP)

Returning to the description of STAP in Section 2.2.4, KA-STAP attempts to improve the interference covariance estimate by using a priori information about the interference statistics. The sources of knowledge and how the knowledge is incorporated into the processor are the primary distinguishing characteristics of different KA-STAP approaches. The two purposes of KA-STAP are to increase the processor's detection performance and to reduce the amount of secondary data required to estimate the interference covariance matrix. Figure 2.14 illustrates the general KA-STAP detector architecture, for comparison to Figures 2.4 and 2.8.

Papers by Bergin et al. [19, 49] are good examples of KA-STAP. They present a framework for incorporating knowledge sources directly into the space-time beamformer. They report that *blending* the information contained in the observed radar

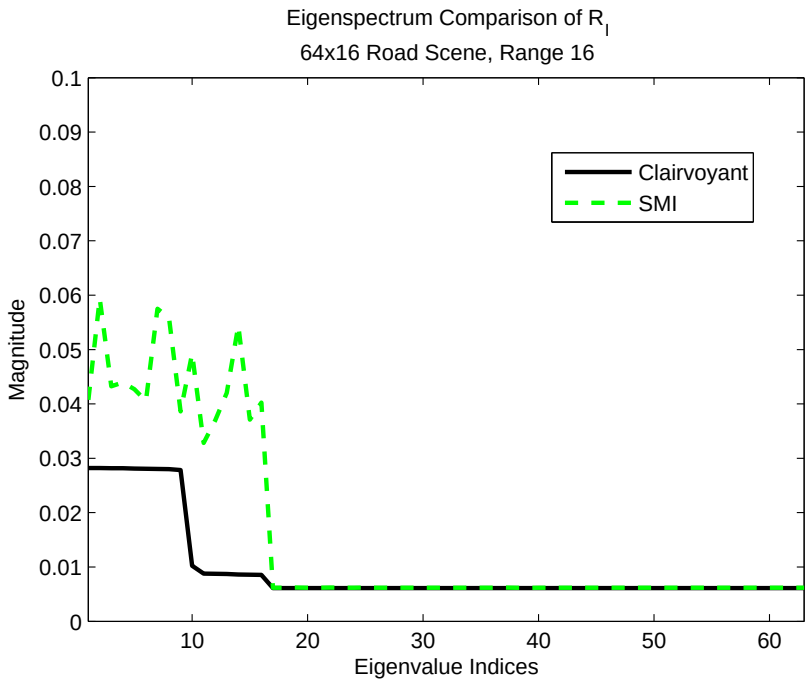

(a)

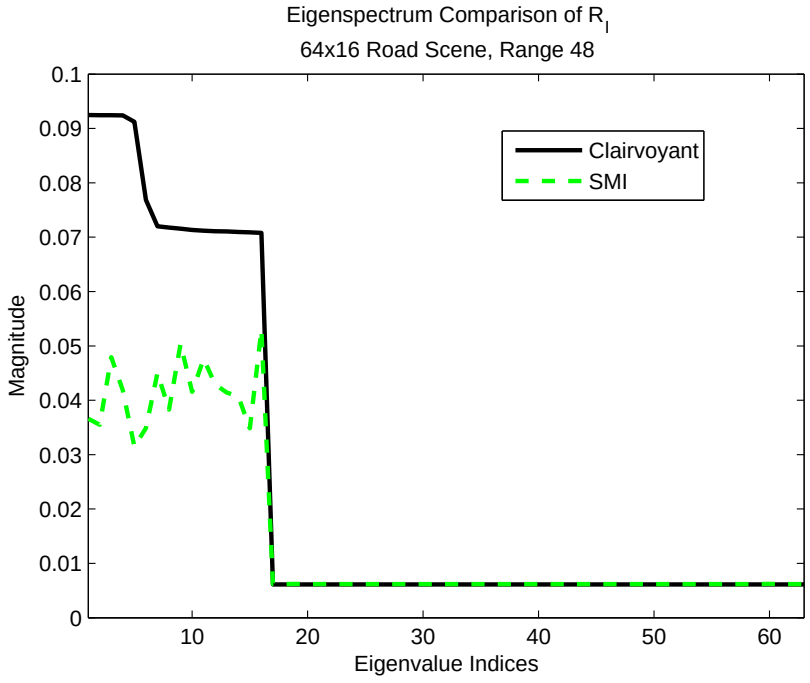

(b)

Figure 2.11. Comparison of eigenspectra for clairvoyant and SMI estimated interference covariance matrices, (a) low variance range of road scene, (b) high variance range of road scene

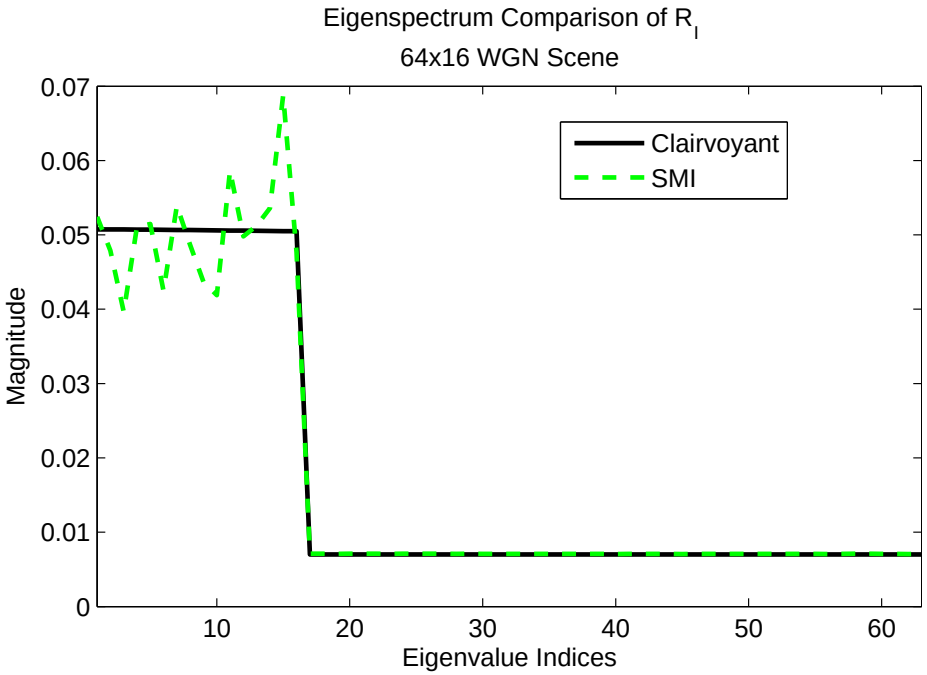

Figure 2.12. Comparison of eigenspectra for clairvoyant and SMI estimated interference covariance matrices for homogeneous, unit-variance scene

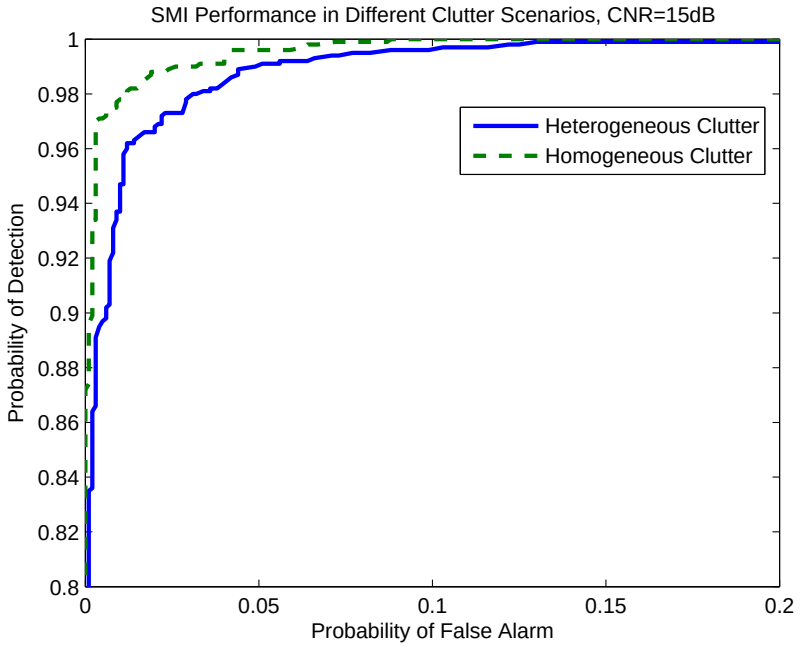

Figure 2.13. Effect of heterogeneous clutter on receiver operating characteristics of SMI STAP

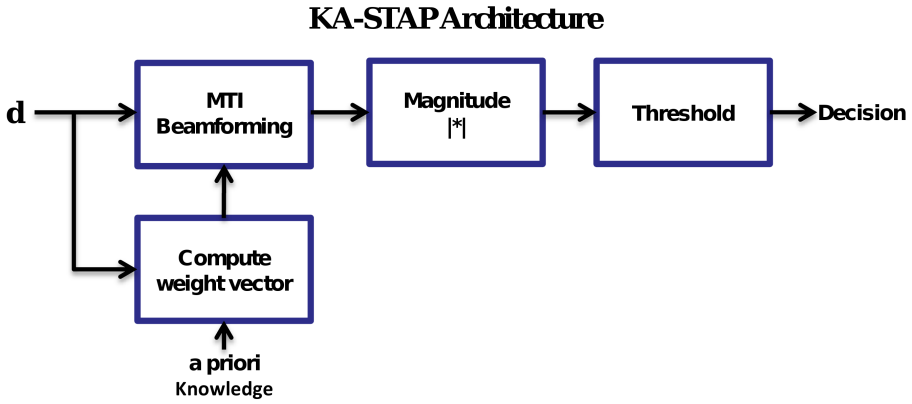

Figure 2.14. Knowledge-aided space-time adaptive processor architecture

data with the a priori knowledge sources reduces the sample support (number of secondary range bins) required by the STAP processor. The blending occurs by loading the standard SMI estimate of the interference covariance matrix with a scaled *colored* loading term consisting of the estimated clutter covariance matrix based on the a priori knowledge source.

Another example which suggests using previously collected SAR images as knowledge sources is presented by Gurram and Goodman [18]. They use the a priori knowledge to classify homogeneous regions of clutter, then minimum-variance spectral estimation is used to arrive at a spectral-domain clutter estimate.

These examples are just a few of the many different KA-STAP techniques to estimate the clutter covariance matrix that have been published. As in all MMSE-based estimators, incorrect knowledge of the constituent parameters of the estimator can lead to significant detection errors. Melvin and Showman [21] demonstrate a technique to reduce covariance estimation errors by using knowledge sources to better characterize the space-time response vectors of the cell under test.

KA-STAP has demonstrated great improvements over STAP; however, these ap-

proaches have drawbacks. In addition to the possibility of the knowledge source being out of date, to employ these knowledge-aided tools, ownship location, and motion must be known precisely [22] to properly register the a priori knowledge with the real time measurements. As previously stated, mischaracterizing the actual statistics with incorrect or poorly applied knowledge can do more harm than good.

2.2.5.2 Covariance Estimation Using Expectation-Maximization

Fuhrmann et al. [14] use the expectation-maximization algorithm to estimate the expected values of the clutter spectrum. The expectation-maximization algorithm is iterative, beginning with an initial estimate of the the clutter spectrum $\boldsymbol{\gamma}$ and updating that estimate with each iteration. The expected values of the sufficient statistics for the complete-data, log-likelihood, conditioned on the observed GMTI data $\mathbf{d}$ and assumed parameter values $\mathbf{P}_C$, are computed. In this case, the sufficient statistics are the squared magnitudes $|\hat{\gamma}_i|^2$. These sufficient statistics are then used to find the closed-form maximum likelihood (ML) estimate for $\boldsymbol{\gamma}$, and the process is repeated using another set of measurements collected from the same scene.

Fuhrmann et al. [14] conclude that their approach to estimating the clutter covariance allows one to carry out adaptive GMTI in situations where 1) the clutter is heterogeneous and therefore there is no "secondary data" from other range bins to estimate $\mathbf{R}_I$, and 2) the clutter covariance can be estimated from data at other platform positions and orientations. However, the authors also point out that their expectation-maximization approach has very high computational requirements.

2.2.6 Nonhomogeneity Detector Preprocessors

A nonhomogeneity detector (NHD) attempts to identify data outliers in order for the outliers to be excised from the data prior to GMTI processing. NHD may be applied to nearly any GMTI technique, including the approach presented in this research. As applied to STAP, NHD is used to eliminate nonhomogeneous range bins from the training data [28]. In addition to applying NHD prior to predetermined statistical algorithms, Adve et al. [22,27] use an NHD prior to choosing a STAP algorithm. The STAP stage can either draw from traditional algorithms in homogeneous environments or on the presented hybrid algorithm in nonhomogeneous environments. Their approach required at least two passes over the environment. The first pass is for NHD followed by the second pass with appropriate STAP processing.

Khanpour-Ardestani et al. [15] build on the approach of Adve et al. [22,27]. Since the location of the clutter ridge is known based on the radar platforms motion with respect to the ground, use a bandstop filter to reject clutter prior to the initial NHD step of the technique in [22, 27]. Khanpour-Ardestani's preprocessor is relatively simple and demonstrates reasonable clutter reduction on data from the Multi-Channel Airborne Measurements (MCARM) program [50].

One of the most popular NHD techniques is based on the generalized inner-product (GIP). GIP and modified sample matrix inverse (MSMI) are presented in significant mathematical detail by Chen [51]. A multistage NHD approach by Ogle et al. [24] interleaves the GIP with a multistage Wiener filter. According to Ogle, this approach provides a signal-dependent GIP intended to detect only those inhomogeneities that degrade the estimation of the colored noise and interference that passes through the steering vector. This approach is shown to more accurately identify moving targets than the signal-independent application of the GIP.

Guerci and Steinhardt [52] present an extension to NHD. The authors state that acute sources of clutter interference are resolved via quasi-SAR processing and then combined with STAP GMTI to reduce minimum detectable velocities, reduce the required degrees-of-freedom, increase available training set size, and lower SINR loss and false alarms. Specifically, their method uses the high resolution clutter estimate to isolate the larger discrete scatterers in order to prewhiten (as an NHD) the data prior to calculating one detection coefficient using STAP.

2.2.7 Direct Data Domain

Unlike stochastic GMTI methods Direct Data Domain (D^3) techniques process the measurements from only the range cell of interest. D^3 method are particularly useful when large amounts of support data are unavailable or the interference environment is not statistically stationary. Adve, et. al. [27] present D^3 concise manner and note that the presented D^3 algorithm differes from other non-statistical algorithms by maximizing the mainbeam gain in the look direction, as opposed to maintaining the gain at some chosen level.

Choi, et. al. [53] and Burintramart and Sarkar [54] compare fully-adaptive and reduced-rank statistical-based STAP methods and D^3-least squares (D^3LS) method as the amount of support data is varied. The D^3LS processor performance is stable without respect to the rank of the covariance matrix. When the amount of support data is less than the rank of the covariance matrix (1/2 in their simulation), the performance is severely degraded for all of the statistical-based STAP methods.

Sarkar, et. al. [55] introduce three D^3LS techniques that may be independently applied to the signal of interest to increase the confidence level of the processed results.

2.2.8 Other Techniques

Blunt et al. [16] presents another approach to improve STAP performance which blends knowledge-aided covariance estimation, the enhanced FRACTA algorithm [56], and a Doppler-sensitive adaptive coherence estimate detector. The enhanced FRACTA algorithm excises outliers that closely resemble targets. The knowledge-aided covariance estimation technique is based on the simplified general clutter model developed by Gerlach and Picciolo [17] which builds on the diagonal loading technique published by Carlson [57].

2.2.9 Knowledge-Based Processing

Fully optimal STAP and some of the most popular lower computational load statistical algorithms are discussed by Wicks et al. [58]. They provide an overview of GMTI processing techniques, including the joint domain localized (JDL) processing algorithm, the parametric adaptive matched filter (PAMF), the multistage Weiner filter (MWF), and factored STAP methods. The use of nonhomogeneity detectors (NHD) and direct data domain (D3) methods are discussed as well as a hybrid approach using D3 and JDL.

Wicks et al. [58] conclude there is no one best processor and each of the algorithms above have advantages and disadvantages depending on the target/clutter scenario. They develop the argument for a knowledge-based system to best match the adaptive processing algorithm to the interference scenario. In this sense, knowledge-based processing differs from KA-STAP in that a knowledge-based system uses a priori and/or real-time knowledge to choose an algorithm to fit the problem, while a KA system uses a priori knowledge to improve performance of an algorithm, in this case STAP.

The approach presented in later chapters of this dissertation could be one of the algorithms available to a knowledge-based GMTI processor.

2.2.10 SAR-Based GMTI

There are also many approaches to GMTI using single-aperture and multipass SAR data. These approaches are based on change detection, velocity mapping, and/or interferometrics. Change detection compares SAR images separated in time, and subsequently space. All changes in the images are assumed to be from scatterers that have moved from one pixel to another in the time separating the two images. Perry et al. [59, 60] discuss SAR imaging of moving targets using a technique they call *keystoning.* Keystoning compensates for the range migration which occurs as the moving target crosses resolution cell boundaries during a CPI. Sanyal, Zasada and Perry [61] extend the keystoning concept to detect moving targets using SAR imaging.

Minardi et al. [30,31] have shown that velocity mapping can be used in conjunction with change detection to determine the presence of moving targets and their velocities. Their SAR-MTI technique requires forming a stack of SAR images assuming different sensor ground speeds. Each image captures a different set of target velocities. They report that SAR-GMTI does not have a clutter notch, which eliminates about 15% of the moving targets for standard GMTI.

SAR along-track interferometry (ATI) as been used extensively in remote sensing. Several, including Gierull [32] and Chapin and Chen [33] have investigated, and even demonstrated using the multipass method for detecting slow-moving and low reflectivity ground targets. The Doppler bandwidth of this technique limits the maximum target velocity detectable.

Chapter 3

Synthetic Aperture Radar

The similarity between the form of the clutter spectrum in (2.35) and the values composing a SAR image is striking. The same discrete, linear radar model (2.14) used in the GMTI analysis can be used in SAR, though the array manifolds can be significantly different. In this section the development of the SAR image equation will be presented, then the results are compared to the GMTI clutter spectrum.

3.1 SAR Processing

To the remote sensing engineer, nonmoving scatterers are the targets, while the same nonmoving targets are considered clutter in GMTI. A SAR image is an estimate of the spectrum of the nonmoving scatterers of the illuminated area on the ground. For reference, the discrete, linear radar model (2.14) without the nonGaussian error term is stated here,

$$\mathbf{d} = \sum_{i=1}^{N_t} \boldsymbol{\rho}_i \gamma_i + n_i = \mathbf{P}\gamma + \mathbf{n}. \tag{3.1}$$

GMTI requires an estimate of one scattering coefficient for each potential moving target. SAR, on the other hand, requires an estimate of the entire scattering scene, which is divided into resolution cells. As in GMTI, each resolution cell is associated with a location on the earth and has an associated space-time radar response vector $\boldsymbol{\rho}_i$ in the array manifold $\mathbf{P}$ and scattering coefficient γ_i in the vector $\boldsymbol{\gamma}$. Recognizing

equation (3.1) as a Bayesian general linear model, Theorem 10.3 of Kay [62] may be restated using the notation from this proposal. Given the observed data model in equation (3.1) where $\mathbf{d}$ is a $K \times 1$ data vector, $\mathbf{P}$ is a known $K \times N_t$ matrix, $\boldsymbol{\gamma}$ is a N_t random vector with a Gaussian prior probability density function (PDF) $N(\mu_\gamma, \mathbf{R}_\gamma)$, and $\mathbf{n}$ is a $K \times 1$ noise vector with PDF $N(0, \mathbf{R}_n)$ and independent of $\boldsymbol{\gamma}$, then the posterior PDF $p(\boldsymbol{\gamma}|\mathbf{d})$ is Gaussian with mean

$$E(\boldsymbol{\gamma}|\mathbf{d}) = \mu_\gamma + \mathbf{R}_\gamma \mathbf{P}^H \left(\mathbf{P}\mathbf{R}_\gamma \mathbf{P}^H + \mathbf{R}_n\right)^{-1} (\mathbf{d} - \mathbf{P}\mu_\gamma) \tag{3.2}$$

and covariance

$$\mathbf{R}_{\gamma|d} = \mathbf{R}_\gamma - \mathbf{R}_\gamma \mathbf{P}^H \left(\mathbf{P}\mathbf{R}_\gamma \mathbf{P}^H + \mathbf{R}_n\right)^{-1} \mathbf{P}\mathbf{R}_\gamma. \tag{3.3}$$

Equation (3.3) is the tap weight matrix for the minimum mean squared error (MMSE), or Wiener estimate of the vector $\boldsymbol{\gamma}$. Given our assumption of zero-mean, the MMSE estimator is then

$$\mathbf{W}_{MMSE} = \left(\mathbf{P}\mathbf{R}_\gamma \mathbf{P}^H + \mathbf{R}_n\right)^{-1} \mathbf{P}\mathbf{R}_\gamma. \tag{3.4}$$

Consequently, this estimator is the vector version of the MMSE filter in equation (2.27) used to estimate the scattering coefficient of the moving target in GMTI. The definitions of the scattering covariance matrix and noise covariance matrix are the same as equations (2.32) and (2.31).

A intensity-squared SAR image is an estimate of the squared magnitude of the scattering coefficients of the resolution cells plotted on a two-dimensional grid with respect to the location on the earth of the associated resolution cells. The squared magnitudes of the scattering coefficients are analogous to the squared intensity of the

scattered energy from their respective resolution cells. Thus, the values of a SAR image in column vector form are

$$\hat{\boldsymbol{\gamma}}_{SAR} = \left[|\hat{\gamma}_1|^2 \ |\hat{\gamma}_2|^2 \ \cdots \ \left|\hat{\gamma}_{N_C}\right|^2 \right]^{\dagger}. \tag{3.5}$$

Using this notation it is obvious that SAR has the same form as the estimate of the expected GMTI clutter spectrum in (2.35). The difference is that (2.35) is a vector of expected values, while (3.5) is an estimate of one statistical realization of the expected values.

3.2 Iterative SAR Processing

The problem with the estimator in equation (3.4) is the matrix inversion. The volume of data necessary to create a SAR image precludes the calculation in one operation. Iterative approaches enable the estimates of the scattering coefficients to be refined as new sections of the data are included in the calculation. Kalman is a popular approach to iterative processing and has a vast background in literature. This section contains a brief tutorial three special cases of Kalman filtering, namely iterative MMSE estimation, recursive least-squares (RLS) estimation, and back projection. For a more complete discourse on Kalman filtering and RLS estimation, the reader is referred to any number of books on adaptive filtering, including Grewal and Andrews [63], Haykin [64], and Van Trees [65]. The information presented below on the approach to Kalman filtering and iterative MMSE estimation is largely from Section 13.3 of Moon [66] and an unpublished tutorial by Stiles [67]. The discussion on RLS draws from Chapter 5 of Haykin [64], and the back projection information parallels Chapter 5 of Soumekh [68].

In this research the energy scattered from the observed scene is assumed to be invariant within the observation time. While this is not strictly valid, it does greatly simplify the SAR image calculations. Time variance of the state vector ($\boldsymbol{\gamma}$ in the case of (3.1)) is assumed within the Kalman filter structure but is considered outside the scope of this research. Specifically, iterative MMSE estimation assumes the state system in the Kalman filter to be statistically stationary, which implies the state noise is zero.

Figure 3.1 is adapted from Fig 4.1 of Grewal [63] and shows the block diagram of the iterative MMSE estimator used to estimate the scattering coefficient vector $\boldsymbol{\gamma}$ given a subset $\mathbf{d}_k$ of the discrete measurement vector $\mathbf{d}$. Other than notation, the significant difference between Figure 3.1 and Fig 4.1 of Grewal is that Grewal's dynamical state system $\boldsymbol{\gamma}_{t+1} = \mathbf{A}\boldsymbol{\gamma}_t + \mathbf{w}$ in Fig 4.1 [63] has been replaced with a stationary *system* $\boldsymbol{\gamma}$. Please note that in Grewal's notation the subscript t refers to the time index and is not the same as the scattering coefficient for a moving target, as used in (2.14) and elsewhere in this document.

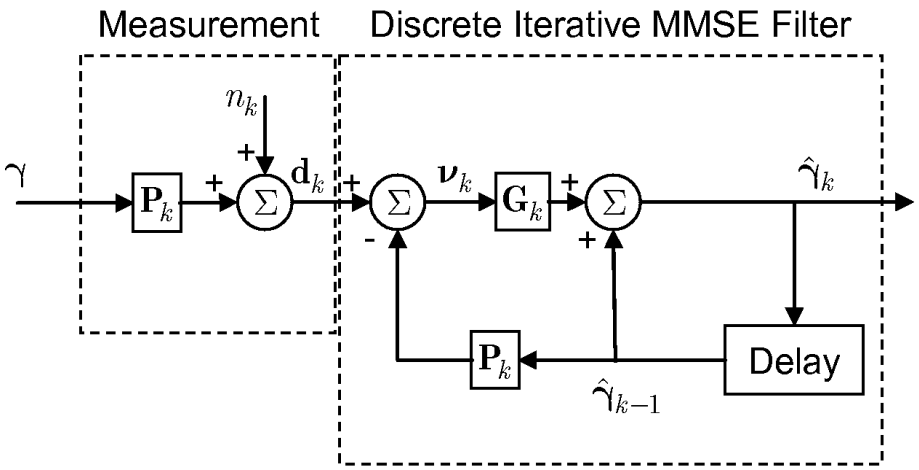

Figure 3.1. Iterative MMSE estimation architecture

Given the discrete, linear radar model in (3.1) we can partition the model into K' subapertures (note that $\frac{K'}{N_t}$ should be a factor of two for computational efficiency) such that

$$\mathbf{d}_k = \mathbf{P}_k\boldsymbol{\gamma} + \mathbf{n}_k \quad k = 0, 1, ...K' - 1, \tag{3.6}$$

where

$$\mathbf{d} = \begin{bmatrix} \mathbf{d}_0 \\ \mathbf{d}_1 \\ \vdots \\ \mathbf{d}_{K'-1} \end{bmatrix}, \quad \mathbf{P} = \begin{bmatrix} \mathbf{P}_0 \\ \mathbf{P}_1 \\ \vdots \\ \mathbf{P}_{K'-1} \end{bmatrix}, \quad \text{and } \mathbf{n} = \begin{bmatrix} \mathbf{n}_0 \\ \mathbf{n}_1 \\ \vdots \\ \mathbf{n}_{K'-1} \end{bmatrix}. \tag{3.7}$$

Each iteration of the iterative MMSE estimator then operates on one subaperture $\mathbf{d}_k$ of the data to update the estimate of the scattering coefficients and the scattering covariance matrix, as follows:

$$\hat{\boldsymbol{\gamma}}_{k+1} = \hat{\boldsymbol{\gamma}}_k + \mathbf{G}_{k+1}\boldsymbol{\nu}_{k+1} \tag{3.8}$$

where $\mathbf{G}_{k+1}$ is called the gain, and $\boldsymbol{\nu}_{k+1}$ is the innovation. The gain is then

$$\mathbf{G}_{k+1} = \mathbf{R}_{\hat{\gamma}_k}\mathbf{P}_{k+1}^H \left(\mathbf{P}_{k+1}\mathbf{R}_{\hat{\gamma}_k}\mathbf{P}_{k+1}^H + \mathbf{R}_n\right)^{-1}, \tag{3.9}$$

and the innovation is

$$\boldsymbol{\nu}_{k+1} = \mathbf{d}_{k+1} - \mathbf{P}_{k+1}\hat{\boldsymbol{\gamma}}_k. \tag{3.10}$$

The update to the scattering covariance matrix is

$$\mathbf{R}_{\hat{\gamma}_{k+1}} = \left(\mathbf{I} - \mathbf{R}_{\hat{\gamma}_k}\mathbf{P}_{k+1}^H \left(\mathbf{P}_{k+1}\mathbf{R}_{\hat{\gamma}_k}\mathbf{P}_{k+1}^H + \mathbf{R}_n\right)^{-1}\right)\mathbf{R}_{\hat{\gamma}_k}. \tag{3.11}$$

By design, the updates to the scattering coefficient vector are orthogonal to the

previous estimate.

The Kalman filter and the iterative MMSE estimator require initialization. Generally, the initial estimate for the scattering coefficient vector is a vector of zeros. The diagonal values of the initial scattering covariance matrix $\mathbf{R}_{\hat{\gamma}_0}$ are set to larger than any anticipated values of the estimate matrix. The diagonal values of the scattering covariance matrix are essentially limits, and if they are too small, the filters will not search outside those limits, therefore the filter error will never go to zero.

Recursive least squares (RLS) estimation with unity exponential weighting factor (stationary state vector) is a special case of the iterative MMSE estimator, which is essentially an iterative maximum likelihood (ML) estimator. Recall the MMSE estimator (3.4). If the signal-to-noise ratio (SNR) is assumed to be large, the noise variance σ_n^2 in (3.4) is assumed to be zero, so the noise covariance matrix in (3.11) becomes insignificant, i.e. $\mathbf{R}_n = \mathbf{0}$. Additionally, the scattering spectrum is assumed to be uniform, which leads to the scattering covariance matrix being an identity matrix, i.e., $\mathbf{R}_\gamma = \mathbf{I}$. The stochastic MMSE estimator reduces to the maximum likelihood estimator

$$\mathbf{W}_{ML} = \left(\mathbf{P}\mathbf{P}^H\right)^{-1}\mathbf{P}, \tag{3.12}$$

which is a completely deterministic estimator.

Extending this logic to simplifying the iterative MMSE estimator results in the following RLS gain vector

$$\mathbf{G}_{k+1} = \mathbf{P}_{k+1}^H\left(\mathbf{P}_{k+1}\mathbf{P}_{k+1}^H\right)^{-1}, \tag{3.13}$$

and the innovation (3.10) is unchanged, resulting in the following update to the state

estimate

$$\hat{\boldsymbol{\gamma}}_{k+1} = \hat{\boldsymbol{\gamma}}_k + \mathbf{G}_{k+1}\boldsymbol{\nu}_{k+1} \tag{3.14}$$

In Section 5 of the Background and Preview in [64], Haykin lists three distinct categories of RLS filtering algorithms:

1. The *standard RLS algorithm* has been discussed above and has the same virtues and vices of the Kalman filter. Namely, the largest drawback to the standard RLS algorithm is the computational complexity, which has prompted the development of the other two categories of RLS filtering algorithms.

2. *Square-root RLS algorithms* are based on QR-decomposition of the incoming data matrix. *Householder* and *Givens rotation* are two well-known data-adaptive QR-decomposition techniques. Square-root RLS algorithms are known to be stable and robust.

3. *Fast RLS algorithms* exploit the inherent redundancy in the Toeplitz structure of the input data matrix through the use of linear least-squares prediction in both the forward and backward directions. Fast RLS algorithms achieve computational complexities of $O(M)$, as compared to the standard and square-root RLS algorithms which are $O(M^2)$, where $O(\cdot)$ abbreviates *order of*.

Using the same relationships illustrated in Figure 3.2 and the Soumekh's [68] description of the back projection filter, further simplification of the Kalman filter may be made by assuming the radar response vectors from the resolution cells are orthogonal, and thus uncorrelated. The whitening matrix in (3.4) is further simplified from (3.12) to an identity matrix, reducing the processor to the deterministic matched filter estimator

$$\mathbf{W}_{MF} = \mathbf{P}. \tag{3.15}$$

Again, extending this logic to simplifying the RLS estimator results in the following back projection gain vector

$$\mathbf{G}_{k+1} = \mathbf{P}_{k+1}^{H}, \tag{3.16}$$

and the innovation (3.10) remains unchanged, resulting in the following update to the state estimate

$$\hat{\boldsymbol{\gamma}}_{k+1} = \hat{\boldsymbol{\gamma}}_{k} + \mathbf{G}_{k+1}\boldsymbol{\nu}_{k+1} \tag{3.17}$$

The relationship between Kalman filtering, iterative MMSE, and RLS estimation with unity exponential weighting factor is illustrated in Figure 3.2.

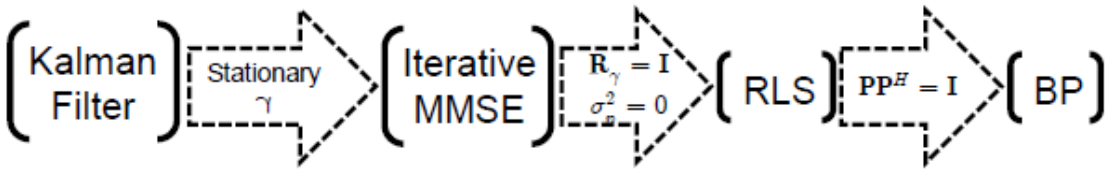

Figure 3.2. Simplifications relating Kalman filtering, iterative MMSE, RLS, and back projection

Matched filtering is much simpler computationally than either MMSE or maximum likelihood, because only one Hermitian transpose is required as opposed to a multiple matrix operations, including a matrix inverse. As an example, the calculating 370 full-resolution 64x64 SAR images (as described in Chapter 6) would take 14 days. Using back projection took only 14 minutes using a 3.0 GHz Quad Core Xeon processor. While MMSE does, by definition, result in lower estimation errors for properly determined systems, underdetermined systems do not have the same MMSE guarantee. For that reason, and the radical difference in computation costs, multilook SAR images estimated using the matched filter, regularized iterative MMSE, and RLS are compared in this research in Chapter 6.

3.3 Multiresolution Filtering of SAR Images Using Filter Banks

Wavelets and filter banks are extensively used in image compression, such as in JPEG 2000. In Section 1.6 of their book on wavelets and filter banks, Strang and Nguyen [69] note that the discrete wavelet transform (DWT) (referred to by Strang as the fast wavelet transform (FWT)) is a logarithmic tree of filters called the Mallat algorithm after its discoverer Stéphane Mallat. Figure 3.3 is adapted from Figure 1.12 [69] and illustrates a synthesis filter tree. Each filter bank (or stage) of the DWT is composed of a lowpass filter, which performs a moving average, and a highpass filter, which performs a difference. The matrix $\mathbf{L}^T$ is the lowpass filter and the highpass filter is the matrix $\mathbf{H}^T$ at each level. Using this explanation, the multiple resolution structure of the DWT can be easily recognized. Each lowpass/highpass pair moving from left to right in Figure 3.3 represents a progressively higher spatial resolution estimate of the scattering coefficient vector $\boldsymbol{\gamma}$.

Many choices for the lowpass and highpass filters exist. The contribution of wavelets and filter banks is to provide new bases to transform the data into. The object of wavelets is to efficiently localize a signal in time and frequency, as much as

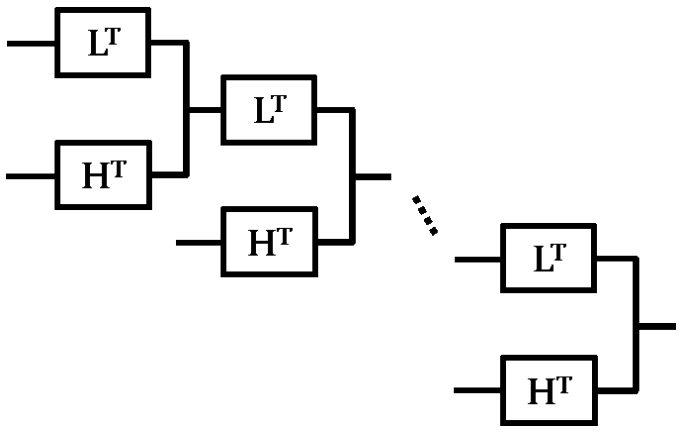

Figure 3.3. DWT synthesis filter bank tree

possible. By definition, the filters are finite-impulse response (FIR) filters, as opposed to infinite impulse response (IIR) filters, e.g., Fourier-based filters.

Strang [70] provides a conceptual description of Haar wavelets, the DWT, and the more elegant Daubechies wavelets. In [71], Strang emphasizes the general construction of wavelets through dilation and translation. Haar wavelets are the most fundamental wavelets and will be used here to demonstrate how the DWT filter bank tree are used for multiresolution processing of real signals. The notation of Strang and Nguyen [69] will be followed, in that the concept of filter banks applies to discrete time and scaling functions and wavelets are continuous time concepts.

Haar filter banks are box filters and are best illustrated in continuous time, as wavelets. Figure 3.4 is adapted from Figure 2 in Chapter 8 of Hubbard's book on wavelets [72] and illustrates the unity scaling function and the Haar wavelet function. The same wavelet function is used at every resolution (filter bank) of the DWT. In terms of the lowpass and highpass filters in Figure 3.3, the scaling function and wavelet in Figure 3.4 represent the lowpass highpass filters, respectively. The only difference is the function is dilated (or compressed) and translated (shifted) in time. Figure 3.5 shows the compression and translation of the next higher resolution.

The Haar wavelets in Figures 3.4 and 3.5 can be naturally related to the DWT

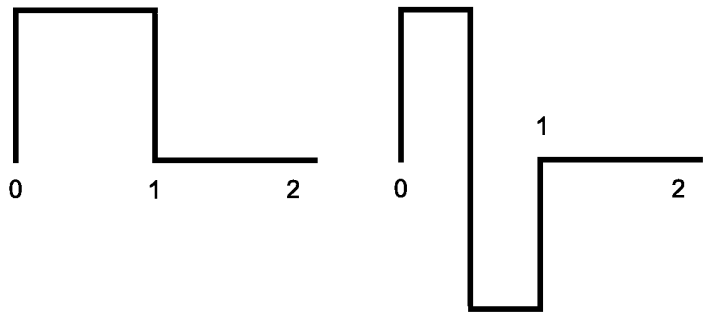

Figure 3.4. Haar scaling function and wavelet

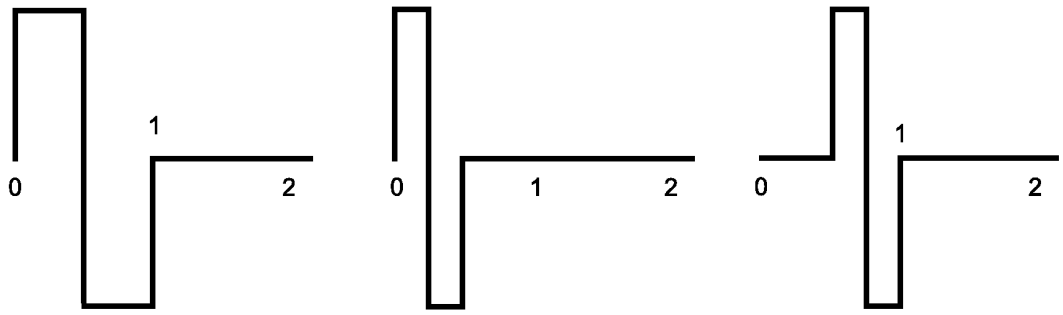

Figure 3.5. Haar wavelet, compressed wavelet, and compressed and translated wavelet

synthesis filter bank tree in Figure 3.3 by letting $\hat{\boldsymbol{\gamma}}^{(1)}$ be a vector of K wavelet coefficients representing the real, full-resolution signal. The first stage of the DWT synthesis filter bank tree can be expressed as a lowpass filter

$$\mathbf{L}_1^T = \sum_{i=1}^{K} \hat{\boldsymbol{\gamma}}^{(1)} \Rightarrow \hat{\boldsymbol{\Gamma}}^{(1)} \tag{3.18}$$

and a highpass filter

$$\mathbf{H}_1^T = \frac{1}{2}\sum_{i=1}^{K/2} \hat{\boldsymbol{\gamma}}^{(1)} - \frac{1}{2}\sum_{i=1}^{K} \hat{\boldsymbol{\gamma}}^{(1)}. \tag{3.19}$$

The next stage of the DWT synthesis filter bank tree operates on the output of the first stage by another lowpass filter

$$\mathbf{L}_2^T = \frac{1}{2}\mathbf{L}_1^T + \frac{1}{2}\mathbf{H}_2^T \Rightarrow \hat{\boldsymbol{\gamma}}^{(2)} \tag{3.20}$$

and takes into account the finer scale wavelet coefficients in the vector $\hat{\boldsymbol{\gamma}}^{(1)}$ via another highpass filter

$$\mathbf{H_2^T} = \frac{\mathbf{1}}{\mathbf{4}}\sum_{\mathbf{i=1}}^{\mathbf{\frac{K}{4}}} \hat{\boldsymbol{\gamma}}^{(\mathbf{1})} - \frac{\mathbf{1}}{\mathbf{4}}\sum_{\mathbf{i=\frac{K}{4}+1}}^{\mathbf{\frac{K}{2}}} \hat{\boldsymbol{\gamma}}^{(\mathbf{1})} + \frac{\mathbf{1}}{\mathbf{4}}\sum_{\mathbf{i=\frac{K}{2}+1}}^{\mathbf{\frac{3K}{4}}} \hat{\boldsymbol{\gamma}}^{(\mathbf{1})} - \frac{\mathbf{1}}{\mathbf{4}}\sum_{\mathbf{i=\frac{3K}{4}+1}}^{\mathbf{K}} \hat{\boldsymbol{\gamma}}^{(\mathbf{1})}. \tag{3.21}$$

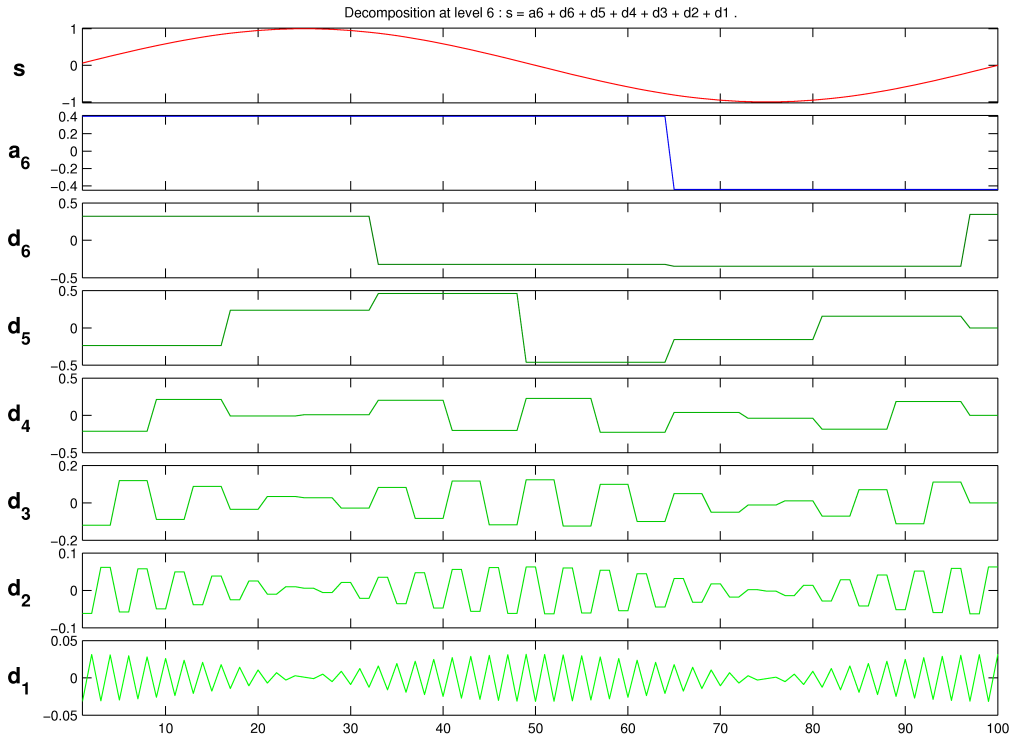

Figure 3.6. One-dimensional DWT demo using sine wave

The finest spectral, or spatial, resolution is achieved when each element in $\hat{\boldsymbol{\gamma}}^{(1)}$ is multiplied by a filter and summed. This concept can be demonstrated visually in one dimension using a sine wave as the desired signal.

The multiresolution characteristics of the DWT may be clearly seen in Figure 3.7. While the reconstructed sine wave in Figure 3.6 is visually identical to a perfect sine wave, the output from coarser scale stages of the DWT filter bank are clearly discretized. Including more stages dyadically includes more finer scale filters, and thus finer resolution.

The multiresolution approach using the two-dimensional DWT is a clear extension of the one-dimensional DWT. In the simplest form, two one-dimensional filter banks are applied to the image, one to the horizontal dimension and one to the vertical. Figure 3.8 shows a 64x64 resolution cell SAR image of a simulated road scene estimated

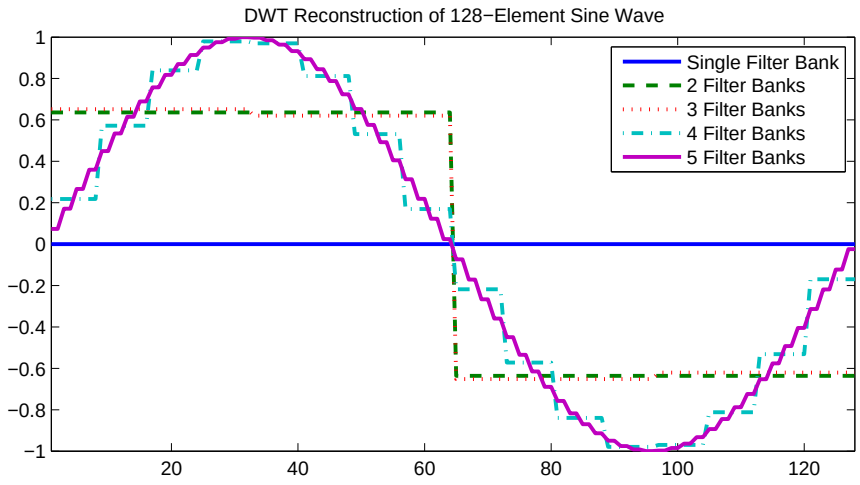

Figure 3.7. One-dimensional DWT reconstruction of sine wave at multiple resolutions

using iterative MMSE. It also shows the output of the low-scale filter at the 64th stage of a 256-stage Haar DWT filter bank. Similarly, Figure 3.9 shows the outputs of the 4th and 2nd stages of the same 256-stage Haar DWT filter bank. Many more sophisticated wavelets and filter banks exist, but the Haar DWT is the simplest and is sufficient to illustrate the multiresolution aspects of filter banks.

3.4 The SAR Image and GMTI Clutter

As previously stated, a SAR image is an estimate of the spectrum of the scattered energy from an illuminated area on the earth with high spatial resolution. The SAR image in Figure 3.10 illustrates how the scattering statistics can vary within an illuminated area or scene. The dark areas, which could represent bodies of water, roads, or other large flat areas, return very little scattered energy toward the receiver; therefore, they appear dark. The returns from areas with slightly more texture, such as fields, return more scattered energy and are lighter gray. Other regions that appear quite light vary significantly in returned energy intensity corresponding to a large

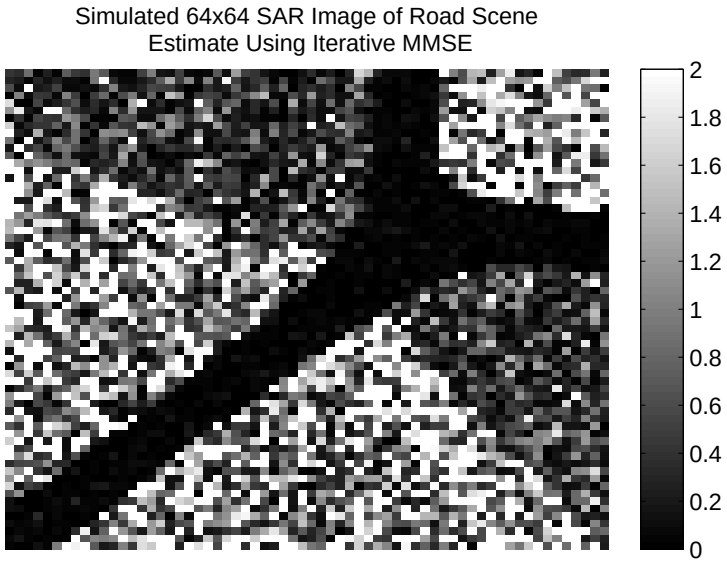

Figure 3.8. 64x64 SAR image of road scene Two resolutions of 64x64 SAR image of road scene (a) iterative MMSE-estimated (b) mid- to fine-scale image using 64 separable two-dimensional DWT based on Haar wavelets

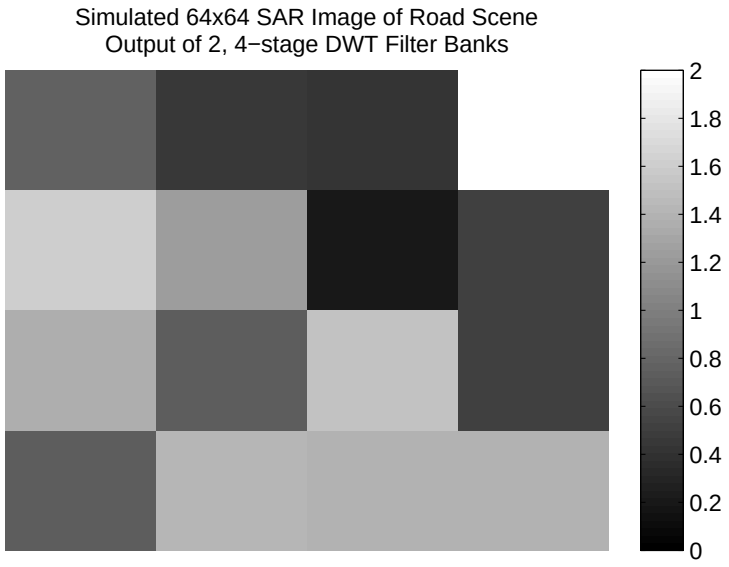

(a)

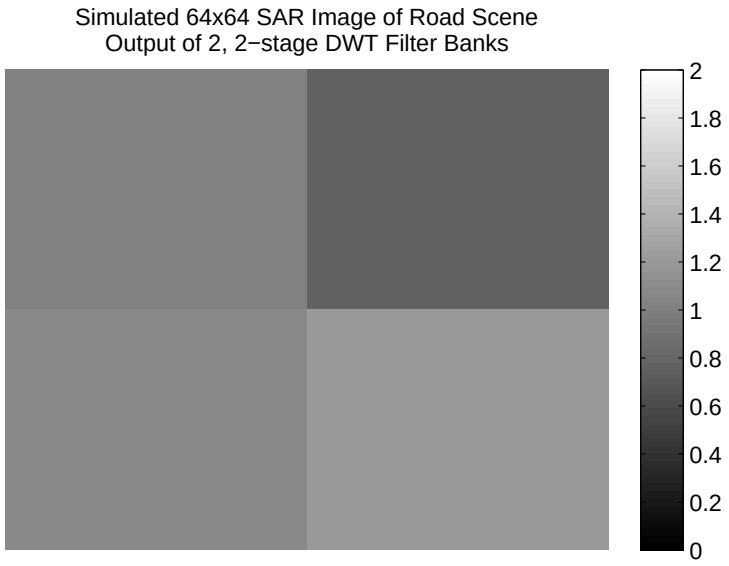

(b)

Figure 3.9. Two resolutions of 64x64 SAR image of road scene using separable two-dimensional DWT based on Haar wavelets, (a) mid-scale image using four separable two-dimensional DWT based on Haar wavelets (b) low-scale image using two separable two-dimensional DWT based on Haar wavelets

variance in the scattered energy from areas such as rocky terrain or forests. Building complexes and urban areas have many small regions with distinctly different scattering statistics. Each of these phenomena are intended to be represented in Figure 3.10, including a simulated building complex in the left-center of the image.

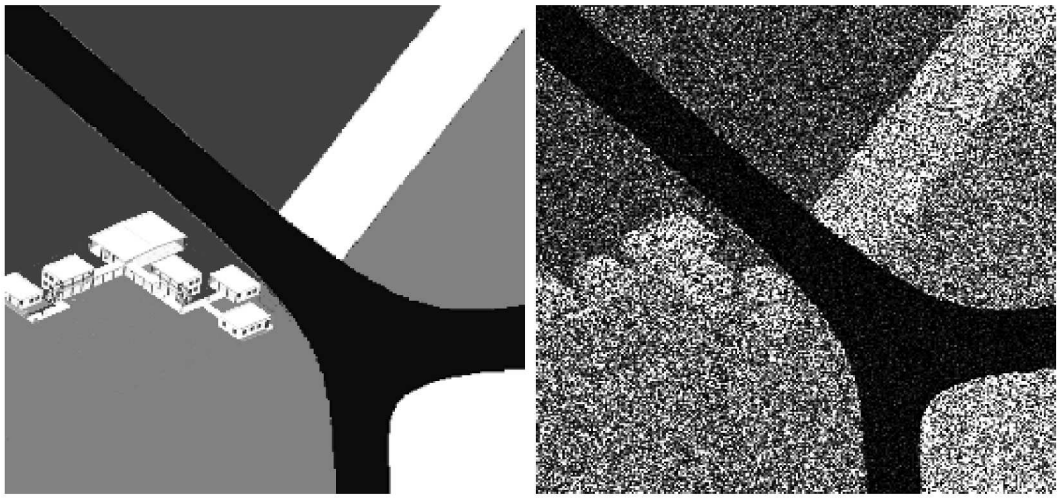

Figure 3.10. Side-by-side comparison of expected SAR image and SAR image realization

The scattering statistics within the regions mentioned above are similar, except for the complex of buildings and other small areas with a single tree, small road, etc. Large sections of the river bottom, for instance, can be classified as areas of independent, identically distributed (iid) targets. However, the building complex would need the clutter scattering statistics defined at a much finer spatial resolution. The right image in Figure 3.10 shows expected scattering intensity areas of the SAR image that have been hand classified to show areas with similar scattering statistics. The scattering statistics within these classified areas can be considered homogeneous; however, it is obvious that the entire scene is not entirely homogeneous in range or azimuth.

3.4.1 Fading Statistics

The differences between the classified image and the original image in Figure 3.10 are primarily due to fading statistics resulting in speckle in the SAR image. Fading statistics and speckle are important concepts when considering whether a SAR image, as represented by (3.5) provides a good estimate of the GMTI clutter spectrum, as represented by (2.35). In the second of two volumes on microwave remote sensing, Ulaby et al. [73] present the concepts and statistics of fading in Section 7-2 and the resulting speckle within an image in Section 8-7. The following discussion on fading draws heavily from Section 7-2.

Fading comes about because the path lengths, or equivalently the radial speeds, between the radar and various point scatterers in the illuminated area are different. In the case of a SAR image, one pixel or resolution cell, is large with respect to the wavelength of the radar's carrier frequency. This means *the target* represented by a resolution cell is actually a large collection of scatterers often represented by iid point scatterers. The radial speed differences between the radar and the individual scatterers in this large collection result in different frequencies with random initial phases, which results in a noise-like signal. Thus, the statistics for the fading signal are the same as those of noise.

If the scattering coefficient of the kth scatterer in a resolution cell is expressed as

$$\gamma_k e^{j(\omega t+\theta_k)} \triangleq \gamma_k e^{j\varphi_k}, \tag{3.22}$$

where $\gamma_k$is its magnitude, and $\varphi_k = (\omega t + \theta_k)$ is the instantaneous frequency. A collection of N_r scatterers within a resolution cell would then result in a sum of N_r

scattering coefficients

$$\gamma = \sum_{k=1}^{N_r} \gamma_k e^{j\varphi_k}. \tag{3.23}$$

γ may also be expressed in terms of an envelope magnitude $|\gamma|$ and a phase angle φ by adding up the randomly phased phasors as a random walk:

$$\gamma = |\gamma|\, e^{j\varphi}. \tag{3.24}$$

It is evident that the real and imaginary parts of γ may be expressed, respectively, as

$$\gamma_r = |\gamma|\, cos\, \varphi = \sum_{k=1}^{N_r} \gamma_k \cos\, \varphi_k, \tag{3.25}$$

and

$$\gamma_i = |\gamma| \sin\, \varphi = \sum_{k=1}^{N_r} \gamma_k \sin\, \varphi_k. \tag{3.26}$$

If the number of scatterers is large, the central limit theorem may be invoked. Then γ_r and γ_i may be assumed to be Gaussian distributed with means

$$E\left\{\gamma_r\right\} = \sum_{k=1}^{N_r} E\left\{\gamma_k \cos\, \varphi_k\right\}, \tag{3.27}$$

and

$$E\left\{\gamma_i\right\} = \sum_{k=1}^{N_r} E\left\{\gamma_k \sin\, \varphi_k\right\}. \tag{3.28}$$

The randomly phased scatterers γ_k and φ_k are assumed to be independent random variables with φ_k uniformly distributed over $[0,\ 2\pi)$. These assumptions result in

$$E\left\{\gamma_r\right\} = \sum_{k=1}^{N_r} \left[E\left\{\gamma_k\right\} \cdot \int_0^{2\pi} \cos\, \varphi_k\, d\varphi_k \right] = 0. \tag{3.29}$$

Similarly,

$$E\{\gamma_i\} = 0. \tag{3.30}$$

Ulaby [73] states it can also be shown that $E\{\gamma_r \gamma_i\} = 0$, implying the real and imaginary parts of the sum are uncorrelated, which implies independence for Gaussian random variables. He also shows that the envelope magnitude $|\gamma|$ is then Rayleigh distributed with a mean value of

$$E|\gamma| = \sqrt{\frac{\pi}{2}}\,\sigma \tag{3.31}$$

where σ is the standard deviation of the individual real and imaginary components of the phasor sum. Recognizing that $|\gamma|^2 = \gamma_r^2 + \gamma_i^2$, given that the real and imaginary parts of the scattering coefficient are Gaussian, the distribution of $|\gamma|^2$ is exponential and the second moment of the envelope is

$$E|\gamma|^2 = 2\sigma^2, \tag{3.32}$$

which leads to

$$S_{eq} = \frac{E|\gamma|}{E|\gamma|^2 + E|\gamma|} = 3.66, \quad \text{or } 5.6 \text{ dB}. \tag{3.33}$$

where Ulaby [73] calls S_{eq} the *inherent* SNR of a Rayleigh-fading signal. In other words, even without additive noise, the best SNR possible in the presence of Rayleigh fading is 5.6 dB. The only way to increase the SNR is to add multiple independent fading samples together.

The fading statistics of the observed signal returned from an extended target represented by a resolution cell (one pixel) result in the random fluctuations in the simulated SAR image of Figure 3.10. The SAR image is composed of magnitudes of the

estimate of the scattering coefficient $|\hat{\gamma}|$ for each pixel. These values are exponentially distributed resulting in *speckle* in the SAR image. The field regions in Figure 1.2 are prime examples of speckle–the bright and dim variations from pixel-to-pixel–which is the equivalent to uncertainty in the spectrum of the scattering function.

Speckle, as a result of fading statistics in the scattering coefficients are precisely why single-look SAR images are not good estimates of the clutter spectrum, i.e. $|\hat{\gamma}_i|^2 \neq E\,|\gamma_i|^2$. However, the estimate of the expected values improve as multiple independent estimates are incoherently averaged, which is referred to as multilook SAR. The accuracy of the estimation is referred to as radiometric resolution; therefore, the radiometric resolution of the SAR image increases as more independent estimates of the clutter spectrum (using GMTI nomenclature) are incoherently averaged.

3.4.2 Scattering Function Heterogeneity

As shown in Figure 3.10, clutter statistics can be very heterogeneous in range and azimuth. Knowing whether or not the clutter is homogeneous is advantageous, because approaches to mitigating heterogeneous clutter exist—some even use SAR-based estimates of the clutter spectrum, such as in Gurram and Goodman [18]. However, without a priori knowledge of the expected clutter spectrum, the variation of the spectrum from pixel-to-pixel is completely unknown. Speckle further complicates the issue, because it adds randomness to pixel-to-pixel clutter statistics potentially resulting in homogeneous clutter appearing to be heterogeneous. The end result is a clutter spectrum that is difficult to classify into homogeneous regions.

Since the relative sizes of the homogeneous regions are unknown, it follows that the optimum spatial resolution of the estimate of the clutter spectrum for GMTI is unknown. Using too coarse or too fine of a resolution can result in a high false alarm

and/or a reduced probability of detection.

3.4.3 Measurement Degrees of Freedom

As discussed in the Introduction, SAR processors associate the received energy with azimuth location by the Doppler shift between slow-time measurements. However, GMTI processors associate Doppler with a moving target's relative velocity. Given that dichotomy, what happens to a moving target in a SAR image?

Figure 3.11 is a classic image which clearly illustrates how energy from scattered from a moving object is displaced in azimuth in a SAR image. In this case, the moving scatterer is a boat on a body of water. The wake is caused by the boat, but the boat is not at the apex of the wake. The velocity of the boat with respect to the Earth had a component in the direction the the radar contributing to the relative velocity of the boat with respect to the radar. This relative velocity added to the relative velocity of the boat due to its position on Earth. This added relative velocity translated into an additional Doppler offset that the SAR processor associated with an incorrect azimuth position.

Another measurement degree of freedom is necessary to determine the azimuth direction of a scatter, regardless of the associated Doppler shift. GMTI radars use multiple receive antennas in the along-track direction to unambiguously determine the change of phase with respect to spatial location. Figure 3.12 illustrates how the clutter subspace is linear with respect to Doppler and azimuth, but the azimuth location of a moving target can be isolated if both azimuth and Doppler are measurement degrees of freedom, as it is in GMTI.

SAR requires fine spatial resolution in range and azimuth; therefore, wide bandwidth and a long coherent processing interval (CPI) are needed. SAR inherently as-

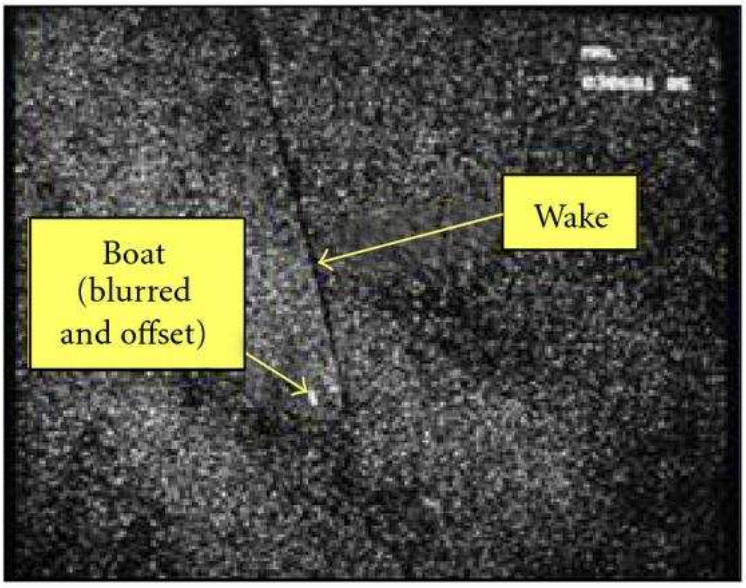

Figure 3.11. Boat off wake illustrating relative motion results in azimuth offset in SAR image (used with permission from Sandia National Laboratory)

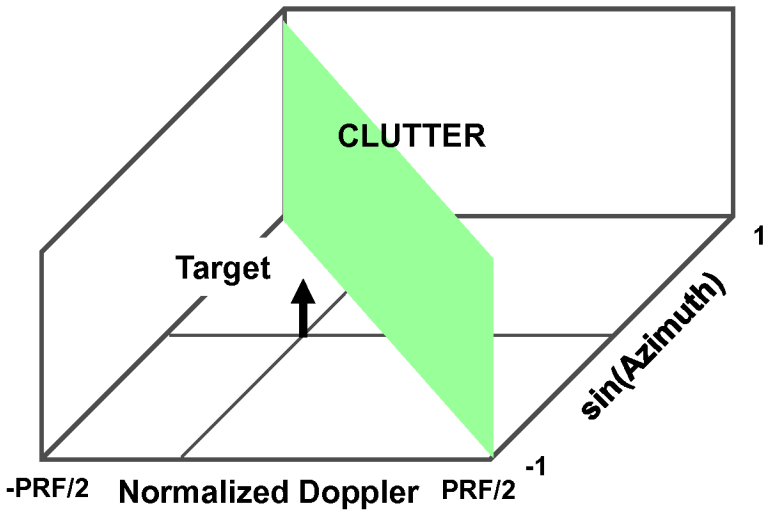

Figure 3.12. GMTI measurement degrees of freedom

sumes all the energy received is from nonmoving targets and maps the energy received into the image based on the phase change between received samples with respect to frequency (Doppler/azimuth) and phase change with respect to time (delay/range). For that reason, target motion with respect to ground results in the target being displaced and blurred in a SAR image, as illustrated by the boat appearing blurred and to the side of its wake in Figure 3.11 from a paper by Sanyal et al. [61].

GMTI exploits multiple apertures and the relative motion between moving targets and nonmoving targets (clutter) for detection. The multiple apertures add a spatial dimension to the received data, which equates to an extra degree of freedom to resolve the relative motion between moving targets and clutter.

The wide bandwidth and long CPI required for SAR is not necessary for GMTI; however, Jao et al. [74] observe that it may be beneficial in several aspects:

1. target detection at lower minimum detectable velocities,
2. robust adaptive processing to cancel strong ground clutter,
3. high sensitivity to detect weak targets,
4. flexible array requirement including sparser arrays, and
5. compatibility with SAR imaging applications.

Similarly, using multiple apertures for SAR imaging has advantages. Collecting SAR-quality data from multiple apertures results in oversampling the scene. Integrating the measurements from the multiple apertures may result in an image with the same spatial resolution as a single aperture SAR image with less speckle. This means an image with higher radiometric resolution may be gained without sacrificing spatial resolution.

The pulse repetition frequency (PRF) of the dual-mode radar system can be an area of contention. A pulse Doppler radar has range and Doppler ambiguities dependent on the PRF of the transmitted signal. The low PRF mode is unambiguous in range and ambiguous in Doppler, while the high PRF mode is unambiguous in Doppler but has range ambiguities. As Klemm [2] points out, the medium PRF mode is a compromise between the low PRF and high PRF modes and is often used in GMTI. There are methods to mitigate ambiguities that result from using medium PRF signals for SAR imaging that will not be specifically addressed by this research, such as staggered PRF and pulse coding.

Chapter 4

Multiple Look SAR Using Subapertured Eigensensors

Chapter 2 established that accurately estimating the clutter covariance matrix is a primary concern in GMTI. Chapter 3 drew a parallel between the clutter covariance matrix and an intensity-squared SAR image, with the difference being that an intensity-squared SAR image is one realization of the expected clutter covariance matrix. For simplicity, in this and following chapters, the term SAR image refers to an intensity-squared SAR image. This chapter shows that multilook SAR can better estimate the expected clutter covariance matrix, and presents a novel approach to calculate multilook SAR images from a single measurement vector.

This approach is presented by introducing multilook SAR as analogous to a power spectral estimation process that increases the radiometric resolution (estimation accuracy) of the spectral estimate in homogeneous scattering regions of the scene. A novel approach to partitioning, or subaperturing, the space-time radar data to produce the multilook SAR is presented. This approach includes transforming the measurement model into a domain of synthetic array sensor locations, called the eigensensor domain. After transforming, the measurements are subapertured in this new eigensensor domain. The result is a lower spatial resolution multilook SAR image with suppressed ambiguities as opposed to conventional subaperturing techniques.

4.1 Multilook SAR as Power Spectral Estimation

Multilook SAR images increase the radiometric resolution estimate of the expected clutter spectrum, as compared to the single-look SAR image. As discussed in Section 3.4.1, incoherently averaging multiple, independent estimates of the scattering coefficients of the scene reduces the speckle in a SAR image. Multilook SAR is an incoherent average of the scattering coefficients of the scene. The individual estimates of the scattering coefficients to be averaged are calculated from *subapertures* or partitions of the measurement vector. The term *subaperture* comes from antenna array theory, where the antenna array aperture is partitioned into groups of elements, and each group of the full array is treated as a separate, smaller array or subaperture. These subapertures have a smaller spatial extent, and therefore, a wider beamwidth. The wider beamwidth reduces the angular resolution as compared to the full aperture. Ideally, each subaperture provides an independent observation, or look, at the same region of space. These multiple looks allow finer radiometric resolution measurements, or estimation accuracy, at the expense of angular resolution.

Subaperturing long CPI, wideband, space-time data is complicated compared to subaperturing a one-dimensional or even a two-dimensional antenna array. Before discussing subaperturing space-time data, one-dimensional power spectral estimation (PSE) will be used to demonstrate the concept and effect of subaperturing for multilook estimation.

4.1.1 Power Spectral Estimation Math

Building on Fuhrmann's [14, 42] observation that estimating the spectrum of the clutter scattering function is foundational to mitigating the clutter in GMTI, PSE techniques will be used to illustrate how multilook SAR increases radiometric reso-

lution at the expense of spatial, or frequency, resolution. Here the Welch averaged PSE technique as presented in Chapter 12 of Proakis and Manolakis [75] will be used to estimate a one-dimensional expected power spectrum. Using progressively larger subapertures will demonstrate the effect of averaging power spectral estimates on radiometric and frequency resolutions of uniform (homogeneous) and nonuniform (heterogeneous) power spectra. As an aside, other PSE techniques exist, including more accurate parametric techniques. However, the Welch technique can easily incorporate the subapertured measurement approach used in this research.

Let an underlying process consist of independent, identically distributed (iid), zero-mean, complex Gaussian vectors with a diagonal covariance matrix

$$\boldsymbol{\gamma} \sim CN\left(0, \mathbf{R}_{\gamma}\right), \tag{4.1}$$

where the diagonal elements of the covariance matrix are considered to be the expected spectrum

$$\mathbf{R}_{\gamma} = \operatorname{diag}\left(E\left|\gamma_0\right|^2,\ E\left|\gamma_1\right|^2,\ \ldots,\ E\left|\gamma_{N_t-1}\right|^2\right), \tag{4.2}$$

where $\operatorname{diag}(\mathbf{v})$ denotes a diagonal matrix with the values $\mathbf{v}$ along the main diagonal. Let

$$\boldsymbol{\Gamma} = \left[E\left|\gamma_0\right|^2\ E\left|\gamma_1\right|^2\ \cdots\ E\left|\gamma_{N_t-1}\right|^2\right]^{\dagger} \tag{4.3}$$

be a vector of samples of the expected power spectrum $\gamma\left(f\right)$. Via the inverse discrete Fourier transform (DFT) of the spectral samples, a Nyquist-sampled temporal *received* vector is a noisy linear transformation of the underlying process:

$$\mathbf{d} = \mathbf{P}\boldsymbol{\gamma} + \mathbf{n},$$

where the noise is assumed to be complex, zero-mean, white-Gaussian, with known variance σ_n^2, i.e., $\mathbf{n} \sim CN\left(0, \sigma_n^2 \mathbf{I}\right)$, where $\mathbf{I}$ is an identity matrix, and $CN\left(\mu, \sigma^2 \mathbf{I}\right)$ describes a vector-valued, complex Gaussian (normal) random variable with mean μ and covariance matrix $\sigma^2 \mathbf{I}$. Then the measurement vector is distributed as

$$\mathbf{d} \sim CN\left(0, \mathbf{P}\mathbf{R}_\gamma \mathbf{P}^H + \sigma_n^2 \mathbf{I}\right). \tag{4.4}$$

The Welch method estimates the power spectrum by incoherently averaging the periodograms calculated from subapertures (partitions) of the temporal data. The periodogram is a normalized estimate of the power spectrum $\gamma\left(f\right)$. As a reminder, the periodogram for a continuous frequency f is defined as

$$P_{dd}(f) = \frac{1}{N}\left|\sum_{n=0}^{N-1} d(n) e^{-j2\pi f n}\right|^2 = \frac{1}{N}\left|X(f)\right|^2, \tag{4.5}$$

where $X(f)$ is the discrete-time Fourier transform (DTFT) of the data vector $\mathbf{d}$.

To subaperture the data, the N-point data sequence is partitioned into L_s subapertures of length M_s. The elements of each subaperture are then

$$d_i\left(m\right) = d\left(m + iD\right) \quad i = 0,\, 1, \ldots, L_s - 1 \quad m = 0, 1, \ldots, M_s - 1, \tag{4.6}$$

where D determines the number of duplicated elements in each subaperture, or equivalently the amount of *slide* in a sliding window. The element $x(iD)$ is the first element of the i^{th} subaperture. If $D = M_s$ the data in each subaperture do not overlap and all the elements in each data subaperture are unique. The periodograms for each data

subaperture are calculated as

$$\tilde{P}_{d_i d_i}(f) = \frac{1}{M_s U} \left| \sum_{m=0}^{M_s-1} d_i(m) w(m) e^{-j2\pi f m} \right|^2 \quad i = 0, 1, ..., L-1. \tag{4.7}$$

The scalar U is a normalization factor for the power in the window function $w(n)$, and is defined as

$$U = \frac{1}{M_s} \sum_{n=0}^{M_s-1} w^2(n). \tag{4.8}$$

This averaged, continuous periodogram is related to the discrete estimate of the expected power spectrum by

$$\hat{\Gamma}_{d_i}(f) = M_s \, \tilde{P}_{d_i d_i}(f). \tag{4.9}$$

The periodogram for each subaperture of the data is then incoherently averaged for the Welch averaged, or *multilook* periodogram:

$$P_{dd}^{(M)}(f) = \frac{1}{L_s} \sum_{i=0}^{L_s-1} \tilde{P}_{d_i d_i}^{(M)}(f). \tag{4.10}$$

As noted in Proakis [75], the Welch PSE is a biased estimator. This could be an issue when the subapertures are not independent, as will be the case for oversampled measurements.

4.1.2 Incremental Multiresolution Spectral Estimates

Returning to the one-dimensional, linear system and PSE in Section 4.1.1, given a measurement vector $\mathbf{d}$ uniformly sampled in time, the discrete-time Fourier spectrum is

$$\gamma(f) = \sum_{n=0}^{N_s-1} d_n e^{-j2\pi f n}. \tag{4.11}$$

The estimated spectrum for $M_s = 1$ (single-element subapertures) is then

$$\gamma_n^{(1)}(f) = d_n e^{-j2\pi fn} \quad n = 0,\ 1,\ ...,\ N_s - 1, \tag{4.12}$$

where the superscript $(\cdot)^M$ denotes the number of temporal elements used to estimate the complex spectrum. Similarly, assuming nonoverlapping subapertures, the estimated spectrum for $M_s = 2$ is

$$\gamma_n^{(2)}(f) = \frac{1}{\sqrt{2}} \left(d_n e^{-j2\pi fn} + d_{n+1} e^{-j2\pi f(n+1)} \right). \tag{4.13}$$

Recognizing the relationship between $\gamma_n^{(1)}$, $\gamma_{n+1}^{(1)}$, and $\gamma_n^{(2)}$, leads to

$$\gamma_n^{(2)}(f) = \frac{1}{\sqrt{2}} \left(\gamma_n^{(1)}(f) + \gamma_{n+1}^{(1)}(f) \right). \tag{4.14}$$

This relationship is continued as subaperture size increases by a factor of two:

$$\gamma_n^{(m)}(f) = \frac{1}{\sqrt{m}} \sum_{i=n}^{n+m} d_i e^{-j2\pi fi} = \frac{1}{\sqrt{m}} \sum_{i=n}^{n+m} \gamma_i^{(1)}(f) \tag{4.15}$$

Assuming N_s is a factor of two, the full-aperture spectral estimate is identical to the spectral estimate computed using the building-block technique just described.

The hope is that this building-block approach to finer spatial resolution using lower resolution estimates is that the lowest resolution estimates of the scattering coefficients in the radar model may be calculated, then used to estimate finer resolution estimates of the same scattering coefficients. Thus, the matrix inversions required to estimate the scattering coefficients may not have to be accomplished for each new resolution of the multilook SAR image.

4.1.3 Power Spectral Estimation and Heterogeneous Spectra

The number of subapertures L_s and the resulting incoherently averaged periodogram, or equivalently the estimated power spectrum $\hat{\Gamma}$, directly affect the variance of the estimate. The expected power spectrum for a zero-mean, white-Gaussian noise process is uniform for all frequencies. Because the measurements for this process are iid, the best spectral estimate for this process would result from incoherently averaging the spectral estimates from each individual measurement. In one dimension, this incoherent average is a multilook periodogram generated with one-element subapertures.

Figure 4.1 illustrates the differences in the power spectral estimates for the number of subapertures, for a given measurement vector. The one-element subaperture best estimates the expected power spectrum of the white-Gaussian noise process, in fact, the one-element estimate overlaps the expected power spectrum in the second plot in Figure 4.1. As the number of subapertures increases, the estimated power spectrum has more variance, and thus more error in homogeneous spectral regions. The full-aperture estimate best estimates the power spectrum of the statistical realization of the expected power spectrum. The realization is not the same as the expected spectrum because of the limited number of measurements; in this case 2048 measurements were used. Notice the difference in the ordinates' scales in Figure 4.1.

When the expected power spectrum is not uniform, as represented by the expected power spectra in Figure 4.2, more measurements are needed in each subaperture. The effect of the subaperture size on the power spectral estimate can be clearly seen in Figure 4.3, which is a zoomed-in version of data shown in Figure 4.2. Three multilook estimates and the full-aperture estimates are compared to the expected power spectrum from about 4.4 to 4.95 radians. The eight-element subaperture smooths the

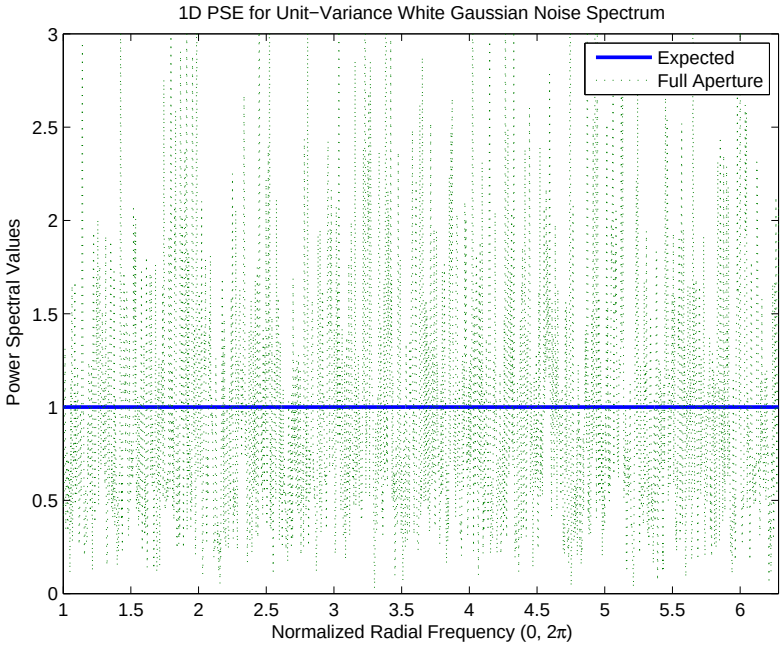

(a)

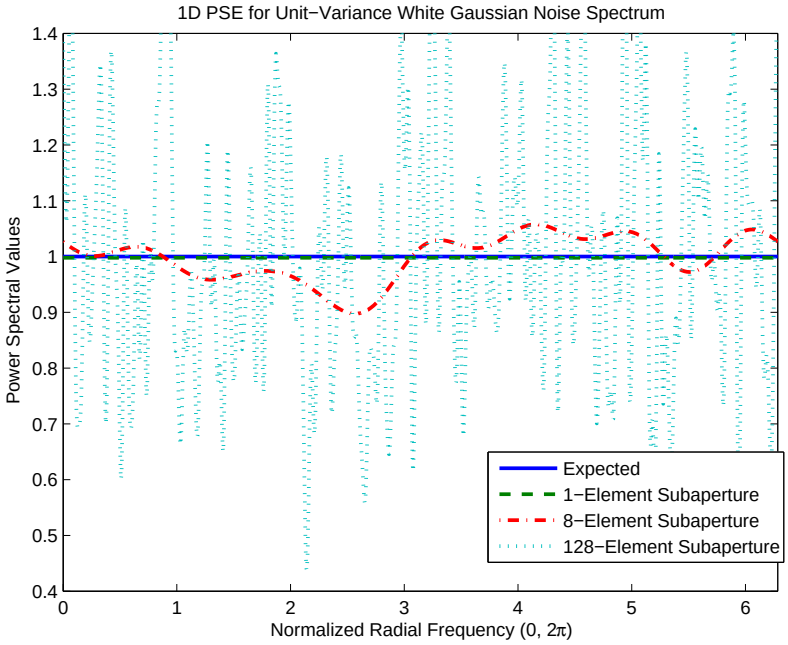

(b)

Figure 4.1. One-dimensional PSE of unit-variance, white-Gaussian noise, (a) expected power spectrum and full-aperture PSE (b) multilook PSE

transition region near 4.7 radians excessively, while the full-aperture estimate better tracks the transition but has a high variance in the flat region. Thus, the 128-element subaperture results in higher spectral resolution at the expense of lower estimation accuracy, which is equivalent to higher variation in areas where the expected spectrum is uniform.

This analysis confirms the observation of (2.36), which can be restated as the expected power spectrum is not equal to the power spectrum of a time (and/or band) limited realization of that expected power spectrum. One can also conclude that there is no *one-size-fits-all* approach to subaperturing for multilook power spectral estimation.

4.1.4 Subaperturing Space-Time Data

To create multilook SAR from one measurement vector, the vector must be partitioned into subapertures. The subapertures for one-dimensional, uniformly sampled data are simply sequential partitions of time over which the measurements were collected. The steering vectors for uniformly, Nyquist-sampled temporal measurements have Vandermonde form, as found in the discrete Fourier transform matrix, and are orthogonal. Take, for example, 16 data samples uniformly collected in time. Partitioning the measurement vector into four subapertures would best be accomplished by taking four sequential measurements for each subaperture. This simple case is

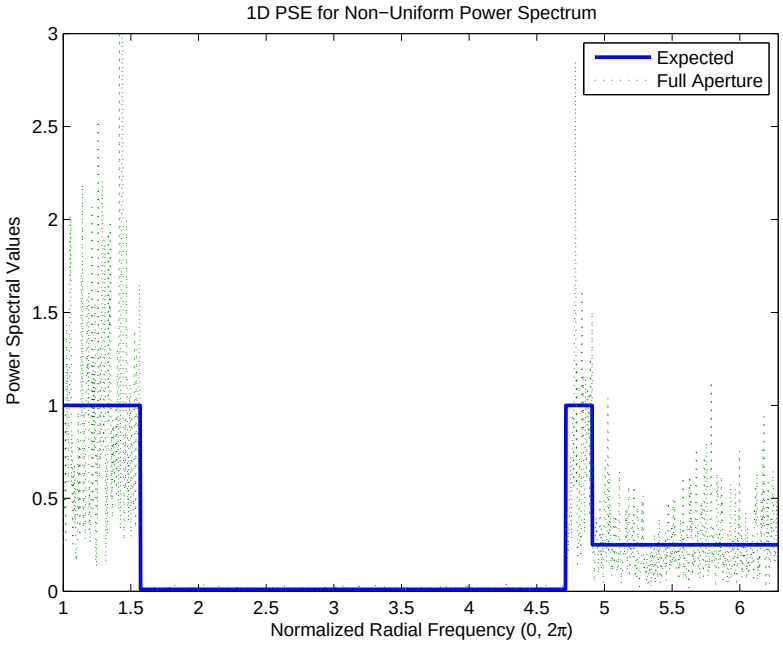

(a)

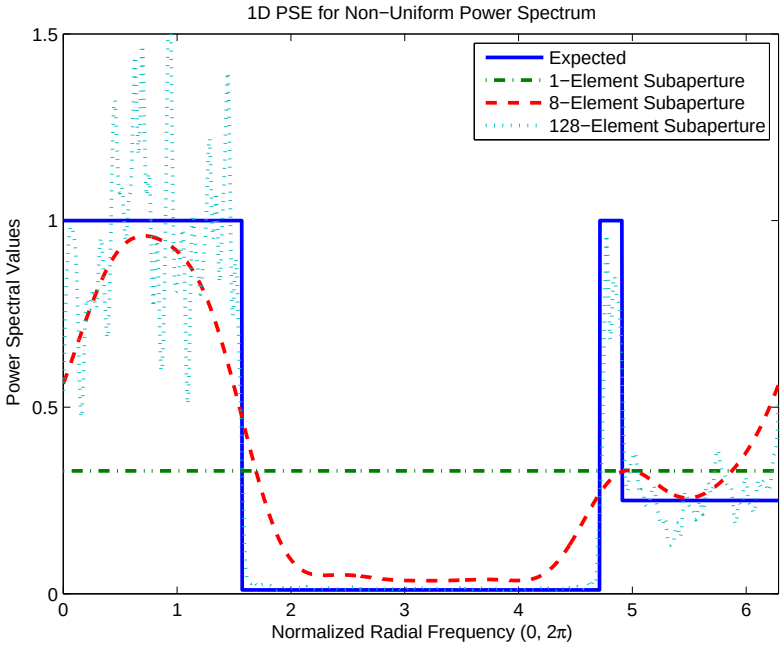

(b)

Figure 4.2. One-dimensional PSE for nonuniform power spectrum, (a) expected power spectrum and full-aperture PSE, (b) multilook PSE

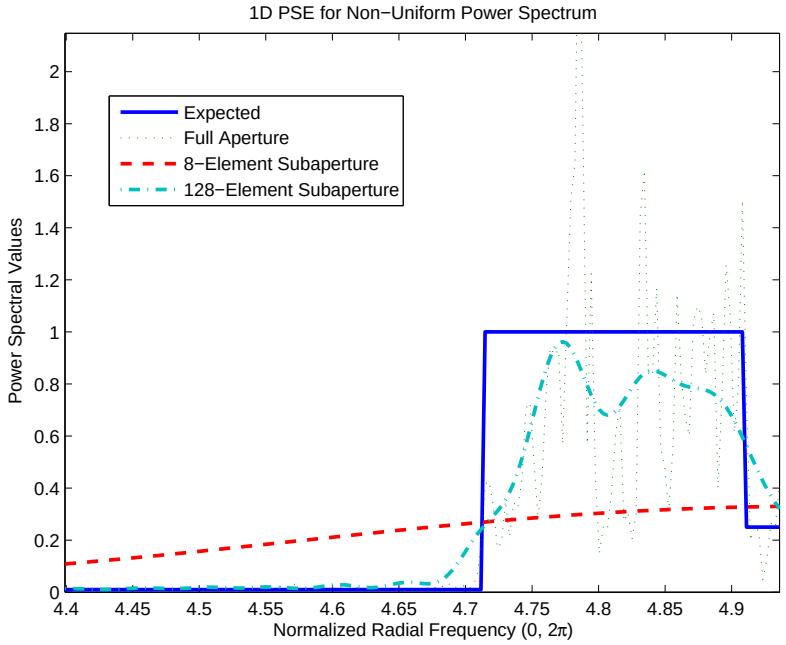

Figure 4.3. Subaperture size effect on spectral transition region (close-up of one-dimensional PSE for nonuniform power spectrum)

shown below:

$$\begin{aligned}\mathbf{d} &= [d_1\ d_2\ d_3\ \cdots\ d_{16}]^\dagger \\ &= \begin{bmatrix} \mathbf{d}_1 \\ \mathbf{d}_2 \\ \mathbf{d}_3 \\ \mathbf{d}_4 \end{bmatrix},\end{aligned}$$

where

$$\begin{aligned}\mathbf{d}_1 &= [d_1\ d_2\ d_3\ d_4\ ]^\dagger \quad \mathbf{d}_3 = [d_9\ d_{10}\ d_{11}\ d_{12}]^\dagger \\ \mathbf{d}_2 &= [d_5\ d_6\ d_7\ d_8]^\dagger \quad \mathbf{d}_4 = [d_{13}\ d_{14}\ d_{15}\ d_{16}]^\dagger .\end{aligned} \tag{4.16}$$

Similarly, the array manifold must be subapertured in the time dimension:

$$\mathbf{P} = \begin{bmatrix} \boldsymbol{\rho}_{1,1} & \boldsymbol{\rho}_{1,2} & \cdots & \boldsymbol{\rho}_{1,16} \\ \boldsymbol{\rho}_{2,1} & \boldsymbol{\rho}_{2,2} & & \boldsymbol{\rho}_{2,16} \\ \vdots & & \ddots & \vdots \\ \boldsymbol{\rho}_{16,1} & \cdots & & \boldsymbol{\rho}_{16,16} \end{bmatrix} = \begin{bmatrix} \mathbf{P}_1 \\ \mathbf{P}_2 \\ \mathbf{P}_3 \\ \mathbf{P}_4 \end{bmatrix}, \tag{4.17}$$

where

$$\mathbf{P}_1 = \begin{bmatrix} \rho_{0,0} & \rho_{0,1} & \cdots & \rho_{0,15} \\ \rho_{1,0} & \rho_{1,1} & \cdots & \rho_{1,15} \\ \rho_{2,0} & \rho_{2,1} & \cdots & \rho_{2,15} \\ \rho_{3,0} & \rho_{3,1} & \cdots & \rho_{3,15} \end{bmatrix} \quad \cdots \quad \mathbf{P}_4 = \begin{bmatrix} \rho_{12,0} & \rho_{12,1} & \cdots & \rho_{12,15} \\ \rho_{13,0} & \rho_{13,1} & \cdots & \rho_{13,15} \\ \rho_{14,0} & \rho_{14,1} & \cdots & \rho_{14,15} \\ \rho_{15,0} & \rho_{15,1} & \cdots & \rho_{15,15} \end{bmatrix}. \tag{4.18}$$

An image for each subaperture can then be computed, in this case, resulting in four lower resolution images. These images may be incoherently averaged to produce one multilook SAR image with finer radiometric resolution over homogeneous scattering regions (less speckle) at the expense of lower spatial resolution (image detail).

4.1.5 Extension to Multilook Imaging

The one-dimensional PSE example may be extended to two dimensions to conceptually demonstrate multilook SAR imaging. The image in Figure 4.4 is the expected SAR image analogous to the one-dimensional expected power spectra in Figure 4.1. The following multilook SAR demonstration parallels the one-dimensional Welch PSE demonstration.

Figure 4.5 contains a full-aperture intensity SAR image estimated using all the elements in the measurement vector in the lower left, and three multilook SAR im-

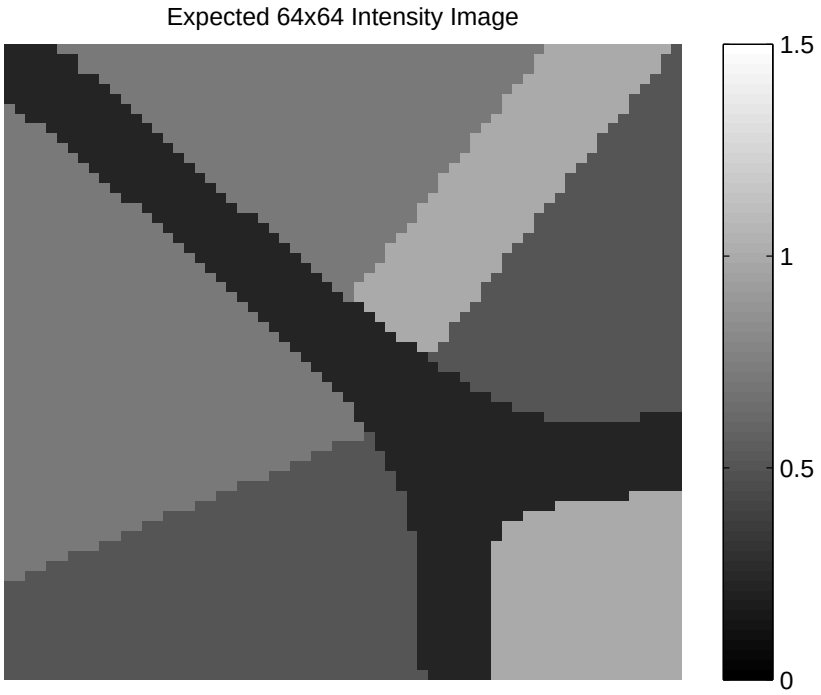

Figure 4.4. Expected intensity SAR image for a synthetic scene

ages generated using subapertures of three different sizes. The difference in speckle between the images is obvious. Fewer subapertures clearly reduce speckle, but the image is blurred potentially beyond recognition in the top two images of Figure 4.5.

The collage in Figure 4.6 visually demonstrates multiple resolutions of the same image using different subaperture sizes. The images in the right column of Figure 4.6 are the incoherent averages of the single-look images on the left, and the 1x1, 4x4, 16x16 subapertured multilook images and the full-aperture image are the same as the images in Figure 4.5. Each image from the individual subapertures in Figure 4.6 is a spectral estimate using only one subaperture of the data. Each row of images corresponds to one subaperture size, such as the second row, which consists of images from individual 2x2 subapertures. In this example, the data is simulated using only a

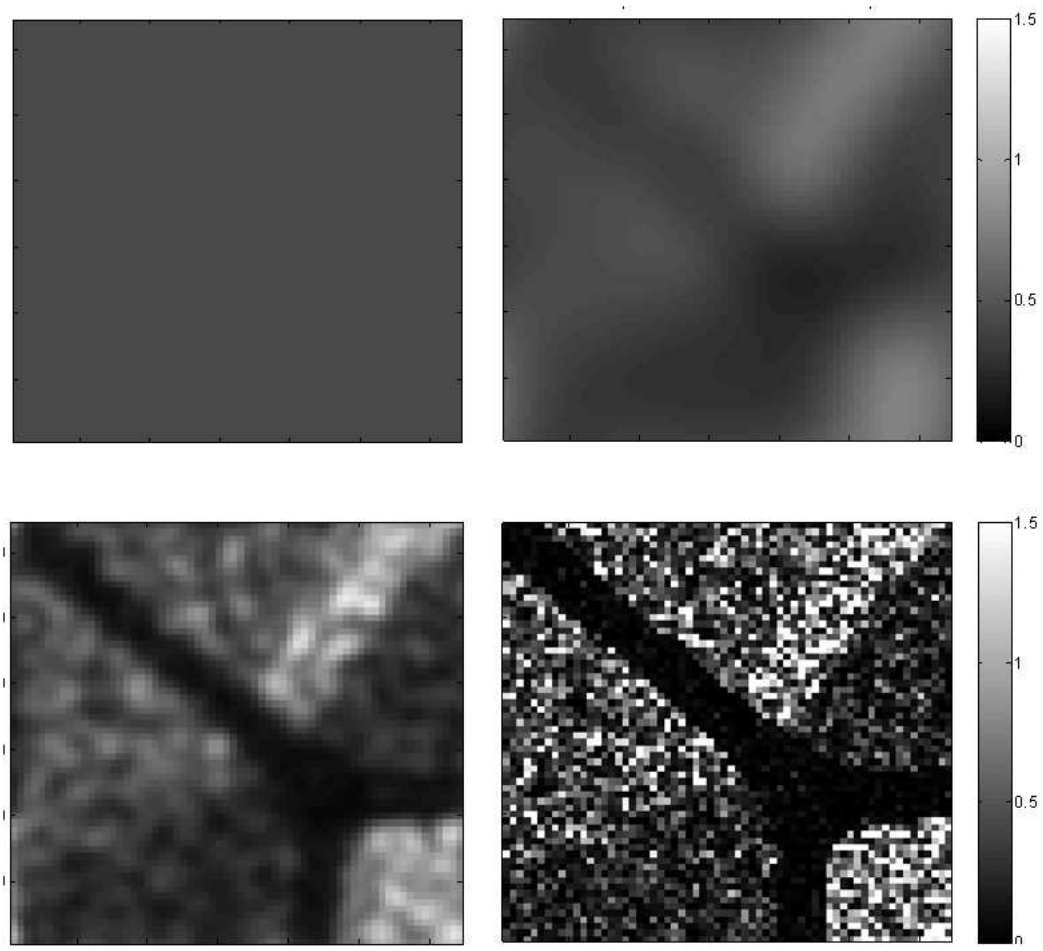

Figure 4.5. Multiple spatial resolutions of one realization of 256x256 intensity image

single receive antenna, so the subapertures are based on slow-time and fast-time divisions of the simulated SAR data. Similar to the one-dimensional PSE images, these multilook SAR images demonstrate the effect incoherent averaging of independent looks has on reducing the speckle at the expense of spatial (or spectral) resolution.

The full-aperture (64x64) SAR image has the finest spatial resolution, and it can be computed using the full data vector or by coherently combining lower resolution spectral estimates. This coherent combining process is also illustrated conceptually in Figure 4.6. For the 64x64 resolution cell scene in this example, there are 64^2 data

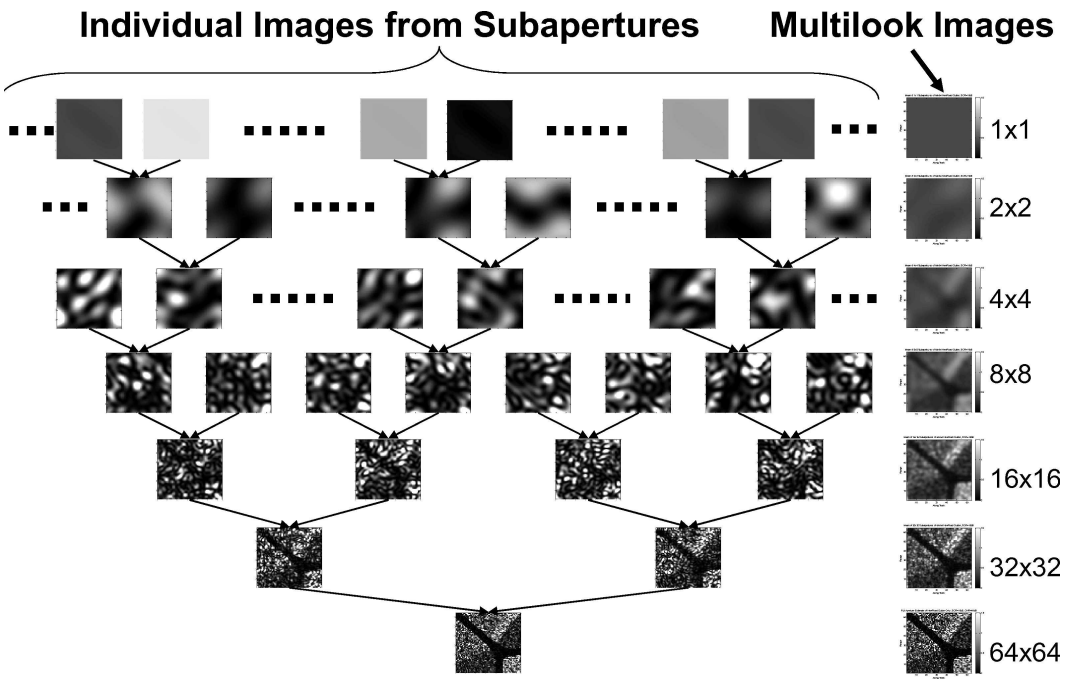

Figure 4.6. Dyadically increasing spatial resolutions

elements in the vector **d**, which translates into 4096 images created from 1x1 (single element) subapertures of the data. The 2x2 subaperture images could be computed from the complex spectra estimated using single element subapertures. This concept was demonstrated in Section 3.1.2 with Fourier analysis in one dimension.

4.2 Subaperturing Using Eigensensors

In general, space-time data may not be uniformly sampled in space and/or time. Rather than the temporal example given in Section 4.1.1, the phase of the space-time radar response at a receiver for a given scatterer varies with time, frequency, and location of the receiver. Thus, the data will be sampled over five dimensions; range, along-track, elevation, fast-time, and slow-time time. For convenience of presenting the multilook SAR approach, the Fourier transform of the radar model is computed with respect to fast time, resulting in the five dimensions of range, along-track, eleva-

tion, fast-frequency, and slow-time. Partitioning measurements collected over these five dimensions into subapertures is not simple. As in array theory, the ambiguity function and resolution of each subaperture depend on the interrelationships of the elements within the subaperture.

In antenna array theory, the beamwidth of a subarray depends on the spatial separation between the two antenna elements that are the farthest apart. The characteristics of each subarray's sidelobes depend on the distance between adjacent elements. Subaperturing space-time data has the same relationship; therefore, care must be exercised in when subaperturing the data for multilook SAR.

Curlander and McDonough [34] discuss subaperturing data in the Doppler (slow-time) domain for multilook SAR. However, they only consider SAR measurements collected from a single aperture. On the other hand, in Section 2.2 of Goodman's dissertation [37] and a subsequent paper with Stiles [76], synthetic sensors they call eigensensors are developed as a way to represent five-dimensional data in two dimensions. They rigorously develop the eigensensors as a method to determine a radar system's resolution and ambiguity function. Their general radar model allows for sparsely populated, nonuniform, three-dimensional antenna array and a wide range of look geometries.

4.2.1 Eigensensor Math

Using Goodman and Stiles' eigensensor concept, subapertures of the data necessary for multilook SAR may be based on two-dimensional synthetic sensor parameters. The goal is to have a well-balanced ambiguity function and resolution in each subaperture resulting in better multilook SAR images for each spatial resolution than would occur via traditional subaperturing techniques. As a reminder, subaperturing

is just a way to partition the measurements for multilook SAR. Subaperturing itself performs no operations on the data.

The following discussion follows Goodman and Stiles' [37,76] development of synthetic sensors they call eigensensors. The actual five-dimensional sensor parameters are three-dimensional space, fast frequency, and slow time. Here it is important to note that the notation fast frequency refers to the Fourier transform of the phase history data with respect to the fast-time sampling period. The vector $\mathbf{s}$ is then the five-by-one vector of sensor parameters $\mathbf{s} = [\mathbf{r}^\dagger \ \omega \ t]^\dagger$, and $\mathbf{r}$ is the location in three-dimensional space of a receiver at $t = 0$ and is defined as $\mathbf{r} = [r_x \, r_y \, r_z]^\dagger$. Goodman and Stiles rationalize that since only two independent variables are necessary to define the location of a stationary scatterer on a two-dimensional plane, (location in along track and range for MTI and SAR), it is reasonable to assume two spatial sensor dimensions are sufficient to represent radar measurements. A two-by-five transformation matrix $\mathbf{\Lambda}_s$ is then developed based on first-order Taylor series expansions around the sensor parameters, $\mathbf{s}$. In terms of partial derivatives, $\mathbf{\Lambda}_s$ for the sidelooking case is given by

$$\mathbf{\Lambda}_s = \left[\begin{array}{ccccc} \dfrac{\partial^2}{\partial x \partial r_x} & \dfrac{\partial^2}{\partial x \partial r_y} & \dfrac{\partial^2}{\partial x \partial r_z} & \dfrac{\partial^2}{\partial x \partial \omega} & \dfrac{\partial^2}{\partial x \partial t} \\ \dfrac{\partial^2}{\partial y \partial r_x} & \dfrac{\partial^2}{\partial y \partial r_y} & \dfrac{\partial^2}{\partial y \partial r_z} & \dfrac{\partial^2}{\partial y \partial \omega} & \dfrac{\partial^2}{\partial y \partial t} \end{array} \right] \mathbf{\Psi} \Bigg|_{\mathbf{x}_0, \mathbf{s}_0}, \tag{4.19}$$

where $\mathbf{\Psi}$ is the phase of the space-time radar response vector for a given resolution cell and sensor parameters $\mathbf{s}$, $\mathbf{x}_0$. The vector $\mathbf{x}_0$ is the plane perpendicular to the boresight of the antenna, and $\mathbf{s}_0$ is the set of sensor parameters around which the expansion is performed, such that $\mathbf{x}_0 = [x_0 \ y_0 \ -h]^\dagger$, and $\mathbf{s}_0 = [0 \ 0 \ 0 \ \omega_0 \ 0]^\dagger$. Evaluating $\mathbf{\Lambda}_s$ at $\mathbf{x}_0$

and $\mathbf{s}_0$, the sensor transformation matrix becomes

$$\mathbf{\Lambda}_s = \frac{\omega_0}{c}\begin{bmatrix} \dfrac{-\left(h^2+y_0^2\right)}{R_0^3} & \dfrac{x_0 y_0}{R_0^3} & \dfrac{-x_0 h}{R_0^3} & \dfrac{2x_0}{\omega_0 R_0} & \dfrac{-2v\left(h^2+y_0^2\right)}{R_0^3} \\ \dfrac{x_0 y_0}{R_0^3} & \dfrac{-\left(h^2+x_0^2\right)}{R_0^3} & \dfrac{-y_0 h}{R_0^3} & \dfrac{2y_0}{\omega_0 R_0} & \dfrac{2v x_0 y_0}{R_0^3} \end{bmatrix} \tag{4.20}$$

where $R_0 = \sqrt{h^2 + x_0^2 + y_0^2}$ is the distance from the center of the radar aperture to the center of the imaged scene $\mathbf{x}_0$. The along-track velocity of the radar platform is v, the height above the earth is h, the along-track dimension is x, the range dimension is y, the fast-frequency sampling interval of the transmitted and received signals is ω_0 , and c is the velocity of the transmitted signal in freespace.

For the sidelooking case assumed in this research, $x_0 = 0$, and $R_0 = \sqrt{h^2 + y_0^2}$. $\mathbf{\Lambda}_s$ becomes

$$\mathbf{\Lambda}_s = \frac{\omega_0}{c}\begin{bmatrix} \dfrac{-1}{R_0} & 0 & 0 & 0 & \dfrac{-2v}{R_0} \\ 0 & \dfrac{-h^2}{R_0^3} & \dfrac{-y_0 h}{R_0^3} & \dfrac{2y_0}{\omega_0 R_0} & 0 \end{bmatrix}. \tag{4.21}$$

The singular value decomposition (SVD) of the sidelooking sensor transformation matrix can be taken to yield:

$$\mathbf{\Lambda}_s = \mathbf{U}\mathbf{S}\mathbf{V}^{\dagger}, \tag{4.22}$$

where the SVD matrices are:

$$\mathbf{U} = [\mathbf{u}_1\ \mathbf{u}_2]\ ,\ \mathbf{S} = \begin{bmatrix} \sigma_1 & 0 & 0 & 0 & 0 \\ 0 & \sigma_2 & 0 & 0 & 0 \end{bmatrix}\ ,\ \text{and}\ \mathbf{V} = \begin{bmatrix} \mathbf{v}_1 & \mathbf{v}_2 & \mathbf{v}_3 & \mathbf{v}_4 & \mathbf{v}_5 \end{bmatrix}. \tag{4.23}$$

Goodman [37] shows that only the first two column vectors of $\mathbf{V}$, $\mathbf{v}_1$, and $\mathbf{v}_2$, project the five sensor parameters into the two independent eigensensor dimensions.

Calculating the SVD of $\mathbf{\Lambda}_s$, the vectors $\mathbf{v}_1$ and $\mathbf{v}_2$ are

$$\mathbf{v}_1 = \begin{bmatrix} \dfrac{-1}{\sqrt{1+4v^2}} & 0 & 0 & 0 & \dfrac{-2v}{\sqrt{1+4v^2}} \end{bmatrix}^\dagger \tag{4.24}$$

and

$$\mathbf{v}_2 = \frac{1}{\sqrt{\dfrac{h^4+h^2y_0^2}{R_0^4}+\dfrac{4y_0^2}{\omega_0^2}}} \begin{bmatrix} 0 & \dfrac{-h^2}{R_0^2} & \dfrac{-hy_0}{R_0^2} & \dfrac{2y_0}{\omega_0} & 0 \end{bmatrix}^\dagger. \tag{4.25}$$

The location of the first eigensensor dimension is obtained by taking the inner product of $\mathbf{v}_1$ with the sensor parameter $\mathbf{\Delta s}$, and similarly, the second eigensensor dimension is a result of the inner product of $\mathbf{v}_2$ with the sensor parameter $\mathbf{\Delta s}$. Consequently, the coordinates of the eigensensors are given by $\alpha = \mathbf{v}_1^\dagger \mathbf{\Delta s}$ and $\beta = \mathbf{v}_2^\dagger \mathbf{\Delta s}$. Completing the inner products,

$$\alpha = \frac{-1}{\sqrt{1+4v^2}} \left(r_x + vt\right) \tag{4.26}$$

and

$$\beta = \frac{1}{\sqrt{\dfrac{h^4+h^2y_0^2}{R_0^4}+\dfrac{4y_0^2}{\omega_0^2}}} \left(-\frac{h^2 r_y}{R_0^2} - \frac{hy_0 r_z}{R_0^2} + \frac{2y_0\Delta\omega}{\omega_0}\right). \tag{4.27}$$

The parameter α depends on the along-track position of the receiver, the along-track velocity, and slow time, and is therefore called the effective along-track position of the synthetic sensor. The effective cross-track position of the sensor is given by the value of β because of its dependence on fast time and the receiver's position in height and cross track. Using these parameters, each measurement can be mapped into the two-dimensional coordinate system of effective along track and effective cross track for the synthetic array.

Figure 4.7 is a plot of the synthetic array sensor locations for a measurement vector of a radar model with 12 receive elements, each receiving 21 pulses and 17 fast-frequency samples per pulse. The 12 receive elements are in a planar array with four elements in along-track by three elements in cross-track. Figure 4.7 (b) also shows a close-up view of the center of the synthetic sensor array clearly showing the sensor locations for the all 12 receiver elements at $t = 0$ and $\Delta\omega = 0$.

In the eigensensor scenario presented in Figure 4.7, there is a distinct difference in the contributions of the spatial locations of the receivers in cross track and along track to the synthetic array locations. Because $r_x \approx vt$ in (4.26), there are clearly more unique along-track positions of the synthetic sensors than just the 21 locations due to the slow-time pulses. Observing the four marker styles in effective along track in Figure 4.7, it is hard to distinguish the 21 slow-time pulses for each along-track receiver location. In contrast, $-\frac{h^2 r_y}{R_0^2} + \frac{h y_0 r_z}{R_0^2} \ll \frac{2 y_0 \Delta\omega}{\omega_0}$ in (4.27), so the relative separation of the cross-track receiver locations in the synthetic array location is much smaller than the fast-frequency separation. Therefore, each apparent synthetic array location in Figure 4.7 effectively overlap for all three cross-track receiver elements for a given $\Delta\omega$, and effective along-track synthetic sensor location that cannot be distinguished at the resolution of the figure. This confirmed by the difference of six orders-of-magnitude between the scales of the ordinates of plots (a) and (b) of Figure 4.7.

4.2.2 Ambiguity and Resolution

Using the two eigensensor coordinates in place of the five-dimensional measurement parameters, the radar model may be reorganized into the two eigensensor dimensions. This reorganization enables easier subaperturing of SAR data for multilook

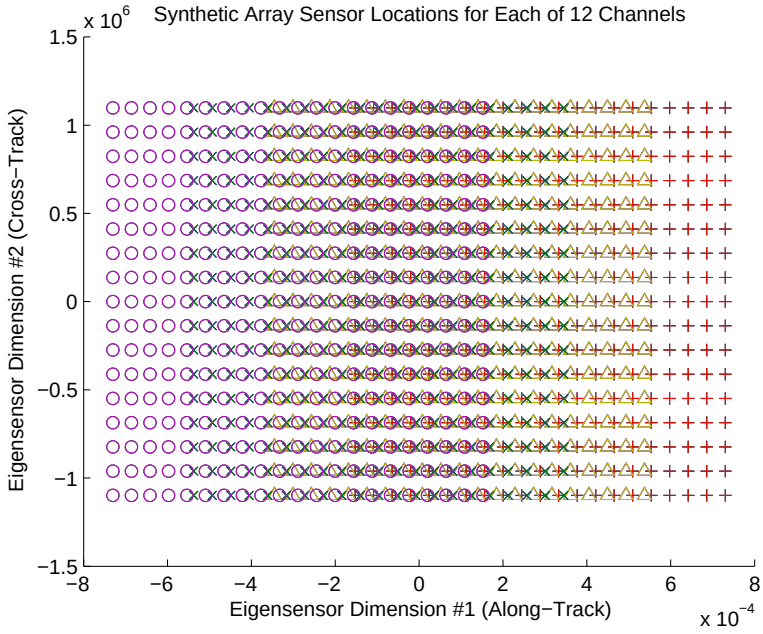

(a)

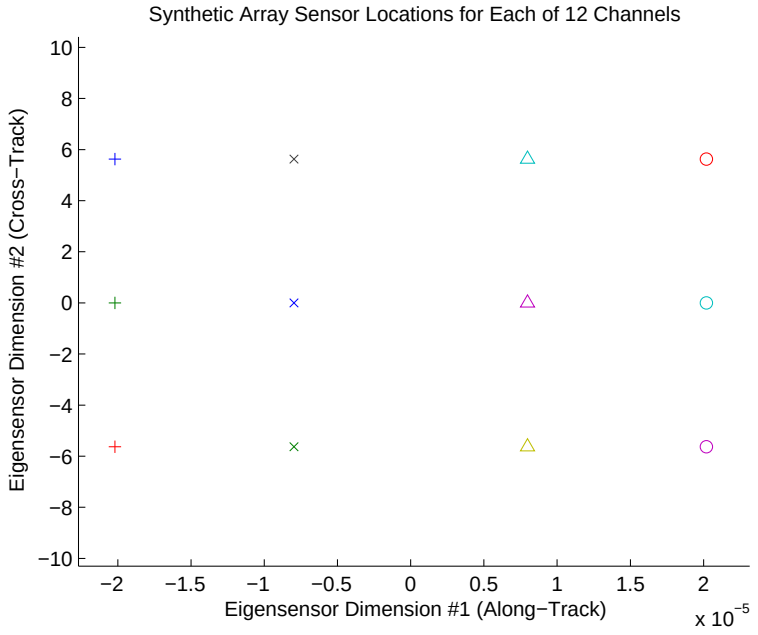

(b)

Figure 4.7. Synthetic array sensor locations for a receive array of 12 elements in a 4x3 planar array. The 4 distinct along-track receiver locations are denoted by the different symbols (a) full synthetic sensor array (b) close-up view showing effect of receiver location in 12-element planar receiver array

processing with the goal improving the ambiguity function as compared to other subaperturing techniques. Two conventional subaperturing approaches are mentioned in Section 6.5 of Cumming and Wong [77], and these approaches are presented and compared to the eigensensor subaperture approach.

Azimuth Subapertures SAR systems typically have better resolution in azimuth than range, so looks are most often taken from the azimuth spectrum using fixed bandwidth bandpass filters. The bandwidth of the bandpass filters depends on the desired azimuth resolution of the resulting multilook image. Cumming and Wong [77] detail azimuth look extraction, detection, and summation. The azimuth subaperturing technique used in this research is accomplished differently than in Cumming and Wong [77] with the same desired effect. The desired effect is better estimation accuracy, in the form of reduced speckle, at the expense of reduced azimuth resolution.

Azimuth subaperturing is accomplished by selecting all the measurements from sequential slow-time increments for each subaperture. Partitioning the measurements in slow-time increments shortens the timewidth of each subaperture, when compared to the full measurement vector. The decreased timewidth effectively increases the Doppler beamwidth reducing the Doppler resolution.

Each azimuth subaperture is then SAR processed, and all the resulting SAR images are incoherently averaged, as described in Section 4.1.5. For a single receive element, Figure 4.9 (a) shows where the synthetic array sensor locations are for four azimuth subapertures. Figure 4.9 (b) shows the ambiguity plot for 64 azimuth subapertures for a resolution cell near the center of a 32x32 scene. As expected, the near-center resolution cell is clearly ambiguous with the other resolution cells at the same azimuth, or along-track location.

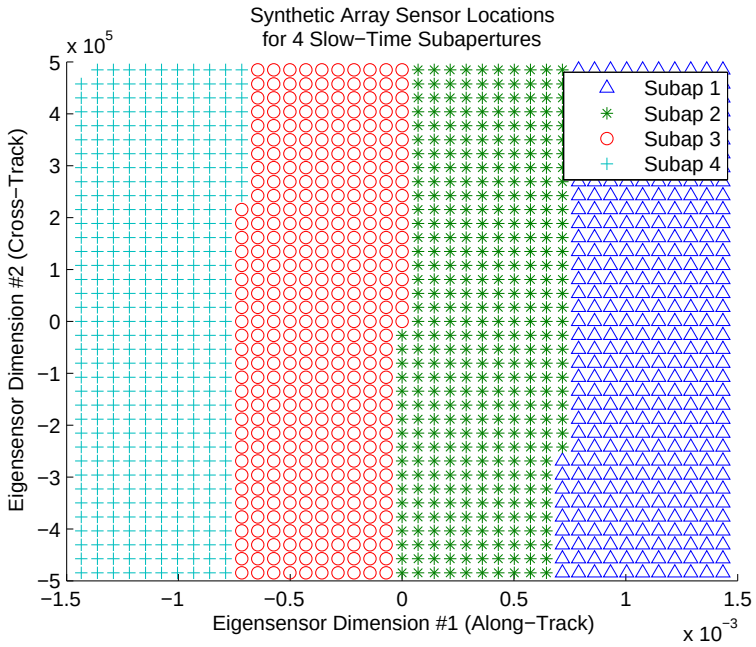

(a)

Figure 4.8. Synthetic sensor array locations for 4 azimuth subapertures

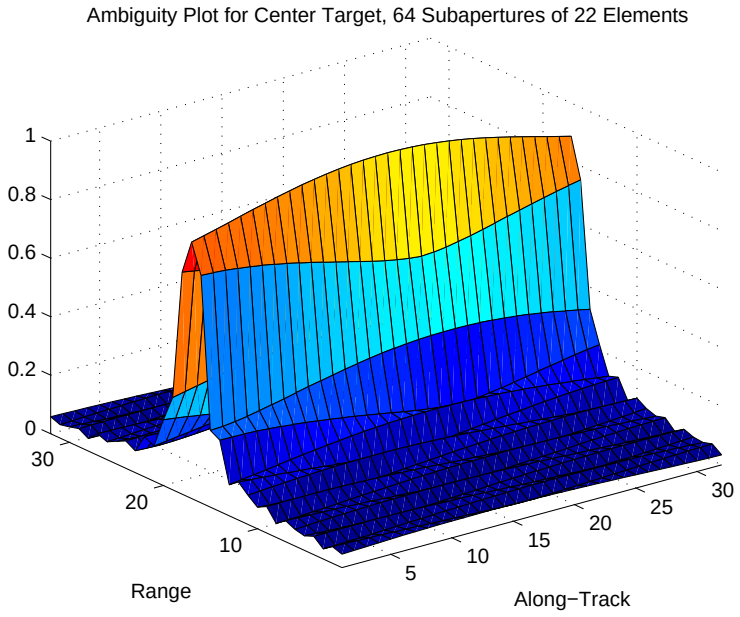

(a)

Figure 4.9. Azimuth subapertures (a) synthetic sensor array locations for 4 azimuth subapertures (b) ambiguity plot for 64 azimuth subapertures

Range Subapertures Similarly, the radar model may be subapertured in range by selecting the measurements for each subaperture based on fast-frequency sampling. Partitioning the measurements according to fast frequency reduces the fast-frequency bandwidth of each subaperture, as compared to the full measurement vector. The reduced fast-frequency bandwidth results in an increased range beamwidth and corresponding reduction in range resolution.

Figure 4.10 (a) shows where the synthetic array sensor locations are for four range subapertures. Figure 4.10 (b) shows the resulting ambiguity plot for the near-center resolution cell of the same 32x32 scene. As expected, the center resolution cell is highly ambiguous with the other resolution cells at the same cross-track location.

Eigensensor Subapertures The synthetic array sensor locations for four subapertures based on eigensensors are shown in Figure 4.11 (a) and ambiguity functions for the near-center target for 64 eigensensor-based subapertures is plotted in Figure 4.11 (b). These plots reveal that subapertures based on eigensensors are a hybrid of the azimuth and range subapertures. The eigensensor subapertures suppress ambiguities in azimuth that are evident in the azimuth subapertures ambiguity plot, and the ambiguities in range are suppressed, which are evident in the range subapertures ambiguity plot. Reducing the magnitudes of the ambiguities come at the expense of a wider mainlobe in the eigensensor subaperture ambiguity function, which results in decreased spatial resolution in the SAR intensity plot.

Subapertures based on the eigensensor locations effectively balance the reduction in slow-time timewidth and fast-frequency bandwidth for each subaperture, compared with azimuth and range subapertures. The resulting subaperture beamwidth is increased in Doppler and range, respectively, thereby reducing the spatial resolution, with respect to using the entire measurement vector.

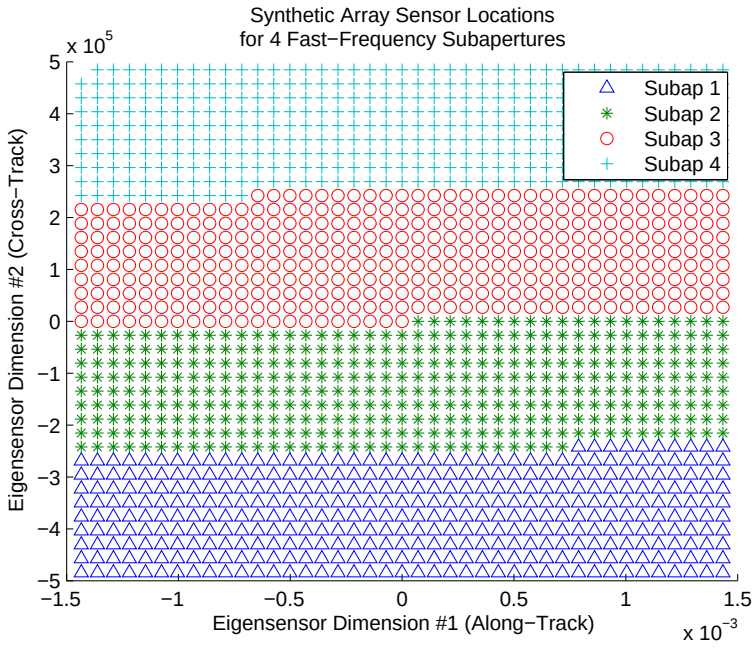

(a)

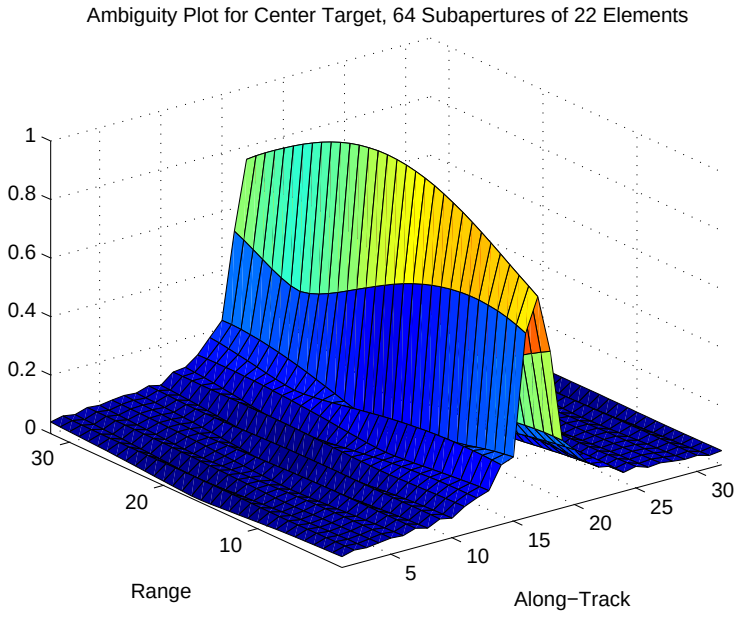

(b)

Figure 4.10. Azimuth subapertures (a) synthetic sensor array locations for 4 range subapertures (b) ambiguity plot for 64 range subapertures

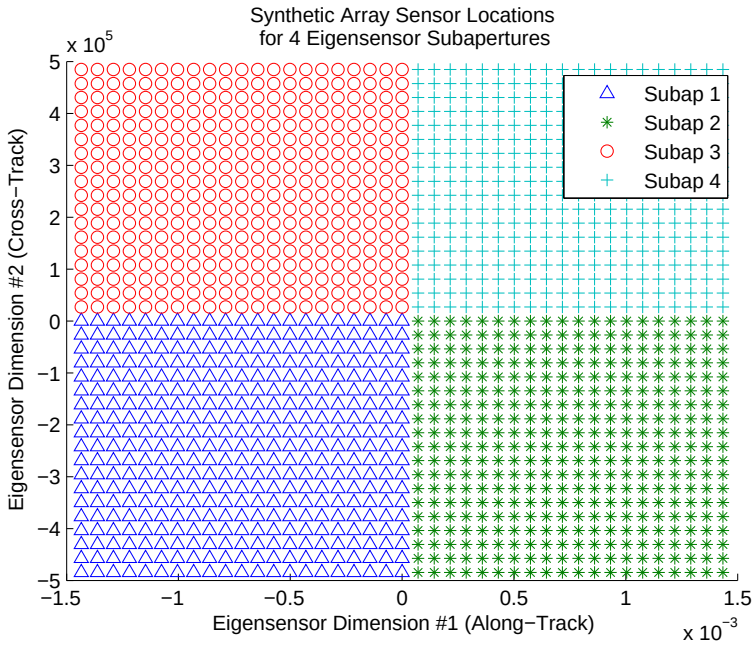

(a)

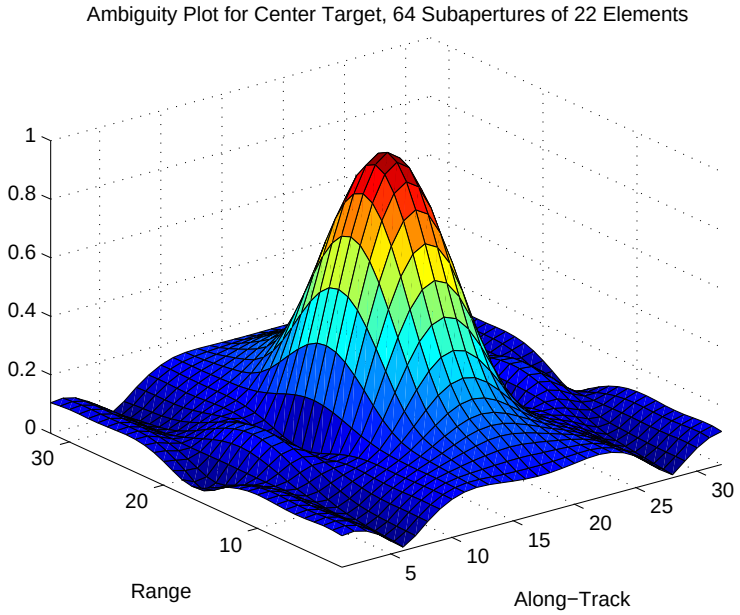

(b)

Figure 4.11. Eigensensor subapertures (a) synthetic sensor array locations for 4 eigensensor subapertures (b) ambiguity plot for 64 eigensensor subapertures

To further smooth the ambiguity function, the nonoverlapping rectangular subapertures in Figure 4.11 (a) may be redefined based on a normalized radius from the subaperture center. Figures 4.12 and 4.12 illustrate this circular eigensensor subaperture technique that will be used throughout the rest of this document.

An important observation is that a closely-spaced uniform receiver array results in redundant eigensensors. This becomes important in SAR imaging, because only one receiver is necessary to achieve the full, unambiguous resolution possible. The redundant measurements may be used to integrate out the effect of noise.

4.2.3 Under-Determined Estimation

Partitioning a measurement vector and corresponding array manifold into subapertures comes with a computional cost. If there are more unknowns (scattering coefficients to be estimated) than equations (measurements in a subaperture), then the system becomes underdetermined.

Recalling the space-time subaperture example in (4.16)–(4.18), we define the general subaperture equations to be

$$\mathbf{d} = \begin{bmatrix} \mathbf{d}_1 \\ \mathbf{d}_2 \\ \vdots \\ \mathbf{d}_{L_s} \end{bmatrix}, \quad \mathbf{P} = \begin{bmatrix} \mathbf{P}_1 \\ \mathbf{P}_2 \\ \vdots \\ \mathbf{P}_{L_s} \end{bmatrix}, \quad \mathbf{n} = \begin{bmatrix} \mathbf{n}_1 \\ \mathbf{n}_2 \\ \vdots \\ \mathbf{n}_{L_s} \end{bmatrix}, \tag{4.28}$$

where L_s is the number of subapertures. For a given subaperture l, the corresponding

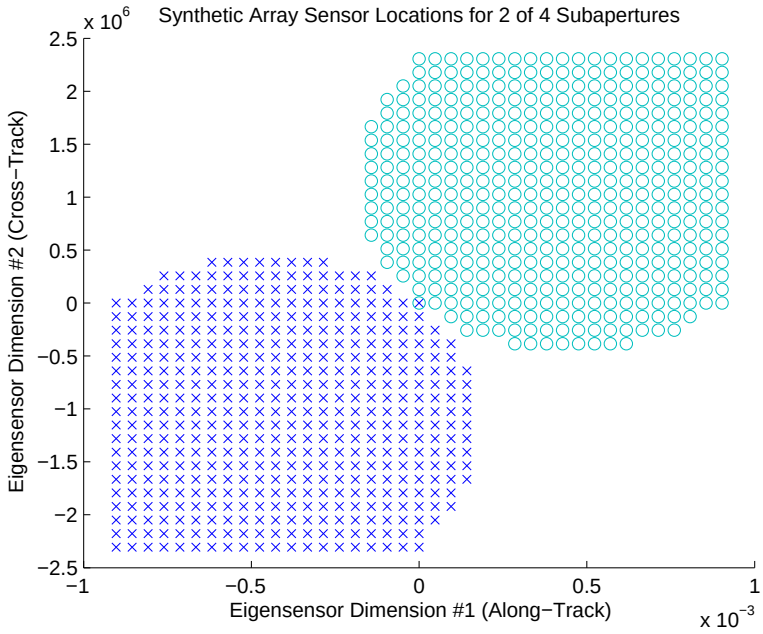

(a)

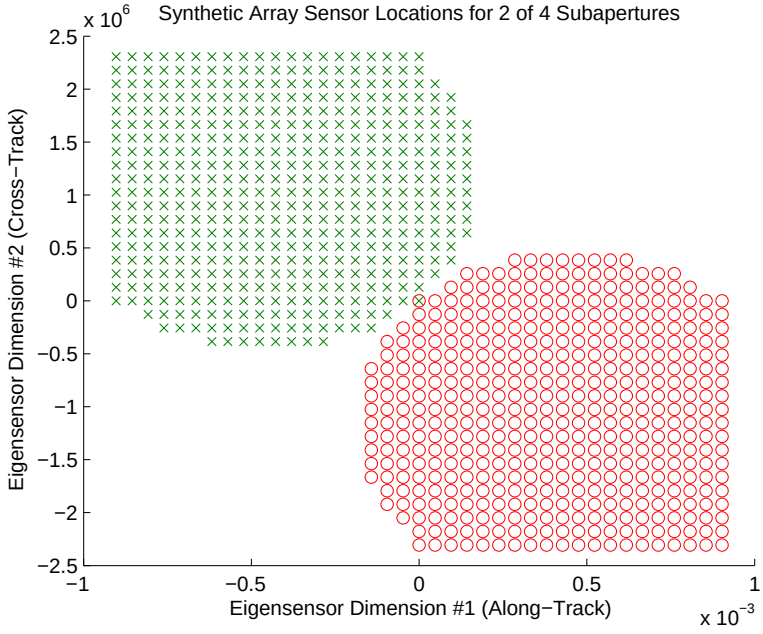

(b)

Figure 4.12. Synthetic sensor array locations (a) 2 of 4 circular eigensensor subapertures, (b) other 2 of 4 circular eigensensor subapertures

measurement vector, array manifold, and noise vector become

$$\mathbf{d}_l = \begin{bmatrix} d_1 \\ d_2 \\ \vdots \\ d_{M_s} \end{bmatrix}, \quad \mathbf{P}_l = \begin{bmatrix} \rho_{1,1} & \rho_{1,2} & \cdots & \rho_{1,N_t} \\ \rho_{2,1} & \rho_{2,2} & & \rho_{1,N_t} \\ \vdots & & \ddots & \vdots \\ \rho_{M_s,1} & \cdots & & \rho_{M_s,N_t} \end{bmatrix}, \quad \mathbf{n}_l = \begin{bmatrix} n_1 \\ n_2 \\ \vdots \\ n_{M_s} \end{bmatrix}, \tag{4.29}$$

where M_s is the number of measurements in a subaperture.

If $M_s < N_t$, then the system is under determined. Referring to the uniqueness theorem, Haykin [64], in Section 8.7 states that underdetermined systems have an infinite number of solutions. Specifically, this problem may be illustrated with the maximum likelihood estimator. Recall the maximum likelihood estimator (3.12), where the data covariance matrix is approximated as

$$\mathbf{R}_d = \mathbf{P}\mathbf{P}^{\mathbf{H}}. \tag{4.30}$$

According to the uniqueness theorem, a matrix $\mathbf{A}\mathbf{A}^H$ is invertible if and only if the matrix $\mathbf{A}$ has independent columns. A necessary, but not sufficient condition for $\mathbf{A}$ to have independent columns is $\mathbf{A}$ must have at least as many rows as columns. An under-determined, or ill-posed, matrix does not meet the uniqueness criteria, thus for small subaperture sizes when $M_s < N_t$, the multilook SAR problem is underdetermined.

There are many approaches to solving under-determined systems, including regularization and using different bases, such as wavelets and compressive sensing. Since $M_s < N_t$ for small subaperture sizes, representing the scattering scene with fewer than M_s values is desired. In theory, this problem is tailor-made for either wavelets or compressive sensing, as both attempt to represent a large data set with fewer

bases spanning the same subspace as the original data. However, the following discussions detail why these two classes of approaches are not the panacea hoped for, when applied to multiresolution, multilook SAR using a single complex measurement vector.

4.2.3.1 Wavelets and Filter Banks

As discussed in Section 3.3, wavelets and filter banks are extensively used in image compression. The multiple resolution structure of the DWT can be easily recognized. However, challenges arise when wavelets are applied to complex data. Specifically, when a lowpass filter is applied to zero-mean, complex Gaussian data, such as the scattering coefficient vector γ, the result approaches zero.

A tutorial by Selesnick, Baraniuk, and Kingsbury [78] describes the dual-tree complex wavelet transform (DT-$\mathbf{C}$WT) and its usefulness for applications including complex data. The multidimensional DT-$\mathbf{C}$WT is nearly shift-invariant, and directionally selective in two and higher dimensions. However, the DT-$\mathbb{C}$WT is four-times redundant, as compared to the DWT, for two-dimensional, complex data. Although the DT-$\mathbb{C}$WT is nonseparable, the redundancy may be thought of as two DWTs for each dimension of data, one DWT for the real part of the transform and one DWT for the imaginary part. Additionally, while the DT-$\mathbb{C}$WT approach results in perfect reconstruction, multiresolution is not practicable for zero-mean, complex Gaussian data. The random phase variation in the scattering coefficient matrix γ results in most of the information being represented by the fine scale filter coefficients. Therefore, only the finest spatial resolution filter bank results in a useful image reconstruction, which eliminates the desired reduction in computational complexity desired.

4.2.3.2 Compressive Sensing

Compressive sensing is an active research area, which attempts to capture and represent compressible signals at rates well below the Nyquist rate. The state vector is assumed (or known) to be sparse; and therefore, the signal is considered compressible. Baraniuk's lecture notes [79] and the references therein provide an overview of the compressive sensing concept. Baraniuk and Steeghs [80] apply compressive sensing to radar imaging with the purpose of eliminating the need for pulse compression at the receiver, and reducing the required analog-to-digital converter bandwidth.

Drawing from Baraniuk and Steeghs [80] and using the radar model description in (3.1), the signal $\mathbf{d}$ is sparsely respresentable if there exists a sparsity basis $\{\boldsymbol{\rho_i}\}$ that provides a K-sparse representation of $\mathbf{d}$; that is

$$\mathbf{d} = \sum_{i=1}^{N_t} \gamma_i \boldsymbol{\rho}_i = \sum_{k=1}^{K} \gamma(i_k) \boldsymbol{\rho}_k \tag{4.31}$$

where $\mathbf{d}$ is a linear combination of K basis vectors chosen from $\{\boldsymbol{\rho}_i\}$, and $\{i_k\}$ are the indices of those vectors. The scattering (weighting) coefficients $\{\gamma(i_k)\}$ then become the new state vector to be estimated, and all other γ_i are assumed to be zero. Compressive sensing then measures and encodes $M < N_t$ linear projections $y(m) = \langle \mathbf{d}, \boldsymbol{\phi}_m^T \rangle$, where $M = O(K \log(N_t/K))$. $O(\cdot)$ means on the order of, and $\langle \cdot, \cdot \rangle$ represents the inner product of two vectors. In matrix notation, the new measurement vector is

$$\mathbf{y} = \boldsymbol{\Phi}\mathbf{d}. \tag{4.32}$$

Baraniuk and Steeghs [80] state that even though $M < N_t$ and recovering the original measurement vector $\mathbf{d}$ from $\mathbf{y}$ is ill-posed, in general, if the matrix $\boldsymbol{\Phi}\mathbf{P}$ has the restricted isometry property, according to compressive sensing theory it is pos-

sible to recover the K largest γ_i's from $\mathbf{y}$. Candes and Tao [81] show that if a real signal is compressible, then it is possible to very accurately reconstruct that signal using a small number of random measurements by solving a simple linear program. Chen, Donoho, and Saunders [82] describe basis pursuit as a concept which solves $\min \|\boldsymbol{\alpha}\|_1$ such that $\boldsymbol{\Phi}\boldsymbol{\alpha} = \mathbf{s}$. Linear programs, such as simplex or interior methods are necessary to solve basis pursuit problems. Greedy algorithms, such as orthogonal matching pursuit (OMP) and variations of OMP, for example, [83–85], are also popular approaches to reconstructing compressible signals.

Most recently, Herman and Strohmer [86] show in some detail for a one-dimensional, single-pulse, farfield radar system, that under certain conditions compressed sensing radar can achieve better target resolution than classical radar. However, in addition to the computational burden presented by compressive sensing, the premise of compressive sensing does not match the needs of the multilook SAR problem presented in this chapter.

Compressive sensing assumes the state vector of a discrete, linear model is sparse. However, the premise of using multiple resolutions to estimate the expected clutter spectrum for GMTI is that the scattering statistics of the clutter scene are unknown. Using a low spatial resolution estimate presupposes that the scattering statistics have a high degree of uniformity throughout the scene. Rather than assuming only a few scatterers dominate the scene, as compressive sensing assumes, the scattering intensity (not the scattering coefficients themselves) may be represented by only a few values. Therefore, the set of bases representing the scattering function of the scene may not be reduced via compressive sensing.

4.2.3.3 Regularizing the Iterative Estimator

Regularizing a matrix, also called diagonal loading, eliminates singularities rendering the matrix invertible. As applied to the RLS estimator with unity exponential weighting factor (and the iterative MMSE) presented in 3.2, the term diagonal loading results from the regularization parameter $0 < \delta \leq 1$ being multiplied by an identity matrix and added to the data covariance matrix before the matrix inversion. Regularization is typically required in the RLS algorithm, because each iteration is inherently an under-determined system. However, the underlying assumption is that the underlying system is over determined. In other words, RLS assumes that the total amount of data observed by all the recursions are more than the number of unknowns. Including the regularization is equivalent to relaxing the high SNR assumption made by RLS or assuming a lower SNR (larger σ_n^2 in the case of iterative MMSE).

Given that small subapertures will contain less data than unknowns, an iterative process may be regularized more heavily to account for the underlying estimation problem being under determined. In the case of the iterative MMSE estimator, the regularized gain (3.9), would then be

$$\mathbf{G}_{k+1} = \mathbf{R}_{\hat{\gamma}_k}\mathbf{P}_{k+1}^H \left(\mathbf{P}_{k+1}\mathbf{R}_{\hat{\gamma}_k}\mathbf{P}_{k+1}^H + \mathbf{R}_n + \delta\mathbf{I}\right)^{-1}, \tag{4.33}$$

where the regularization factor is large ($\delta \approx 1$) due because of the under-determined underlying estimation problem.

4.2.4 Matched Filtering

The goal is multiple radiometric resolutions of the clutter covariance matrix estimate for the GMTI processor. Multilook SAR imagery has been determined to pro-

vide those estimates, at the expense of spatial resolution. Although a much smaller basis set via the DWT or compressive sensing would have been convenient, neither of those approaches are valid to achieve multilook SAR images at different resolutions, given one measurement vector. Therefore, two options remain, (i) estimate the entire scattering coefficient vector for each resolution, or (ii) estimate a subset of the scattering coefficient vector, where the size of the subset depends on the size of subapertures used to calculate the multilook SAR image.

Estimating the entire scattering coefficient vector $\boldsymbol{\gamma}$ for each subaperture is straightforward, although ill-posed for small subaperture sizes. As discussed in Section 3.2, the back projection method is a technique that is a further simplification of the iterative MMSE estimator (3.4), in that it assumes the nonGaussian interference, which is clutter in the case of the radar model, is uncorrelated. The matched filter is noniterative back projection. The data covariance matrix to be inverted in (3.4) is then an identity matrix and (3.4) reduces to (3.15), $\mathbf{W}_{MF} = \mathbf{P}$, which leads to the matched filter estimate:

$$\hat{\boldsymbol{\gamma}}_{MF} = \mathbf{P}^H \mathbf{d}. \tag{4.34}$$

Matched filtering is much simpler computationally than either MMSE or maximum likelihood, because only one Hermitian transpose is required as opposed to a multiple matrix operations, including a matrix inverse. While MMSE does, by definition, result in lower estimation errors for properly determined systems, underdetermined systems do not have the same MMSE guarantee. For that reason, and the radical difference in computation costs, multilook SAR images estimated using the back projection method, iterative MMSE, and RLS are compared in this research in Chapter 6.

Chapter 5

Multiple Resolution GMTI

The intent of this chapter is to provide rationale for and an approach to calculating and exploiting multiple GMTI detection coefficients from a single measurement vector. Each detection coefficient corresponds to a detection decision based on a minimum variance method (MVM) estimator using a different whitening filter. These whitening filters vary based on the spatial resolution of the estimated clutter spectrum in the form of a multilook, intensity-squared SAR image, as discussed in Chapter 4. The hypothesis is that using more than one resolution of the clutter spectrum to estimate the interference covariance matrix will improve GMTI performance, as compared to STAP using sample matrix inversion (SMI). SMI STAP is a popular GMTI approach that requires a large amount of secondary data and assumes the clutter statistics are homogeneous in range, which is often not a valid assumption.

There are many structured covariance matrix GMTI techniques, as addressed in Section 2.2.5, and many ways to calculate multiple resolutions of the SAR image. Chapter 4 presented an approach that balances the computational burden of calculating the multiple SAR image resolutions with estimation accuracy. For proof-of-concept purposes, the GMTI approach in this chapter is the MVM estimator presented in Section 2.2. Modifications to this technique, such as diagonal loading are possible and would likely be required for an operational system to mitigate errors in the radar response vectors, as noted by Guerci [40]. Those modifications are outside the scope

of this research.

The detection scheme is not the focus of this research, so a Bayesian threshold detector, as described in Chapter 6 of Kay [87] will be used to compare the proposed approach to STAP. A detection coefficient for each resolution of the multilook SAR image used to estimate the scattering covariance matrix will be placed in a vector. Since the optimum spatial resolution of the estimated clutter spectrum necessary to effectively mitigate its effect on the data is unknown, a simple fusion algorithm will be used to make the final detection decision.

5.1 Estimating the Interference Covariance Matrix

Recalling the optimum processor (2.23), Section 2.2 claimed that how the interference covariance matrix (2.24) is estimated separates the many approaches to GMTI. While that is a true statement, estimating the whitening filter, in the form of the inverse of the interference covariance matrix, is more important than estimating the interference covariance matrix itself. In other words, estimating the inverse is not the same as inverting the estimate.

This section compares how well sample matrix inversion (SMI) and the different approaches to estimating the interference covariance matrix presented in Chapter 4 estimate the inverse of the interference covariance matrix. The comparison is accomplished by analyzing the eigenspectra of the inverse of the clairvoyant interference covariance matrix and inverses of the estimated interference covariance matrices.

The eigenvectors of the inverse clairvoyant interference matrix are used for comparison purposes. In general, for any given matrix $\mathbf{A}$, the matrix of eigenvectors $\mathbf{V}$ and the matrix $\mathbf{D}$, which is a diagonal matrix with the eigenvalues along the diagonal,

of $\mathbf{A}$ are given by

$$\mathbf{A}\,\mathbf{V} = \mathbf{V}\,\mathbf{D}. \tag{5.1}$$

The eigenspectrum of another matrix $\mathbf{B}$ may be compared to the eigenspectrum of $\mathbf{A}$ for the subspace of $\mathbf{B}$ that is spanned by the eigenvectors of $\mathbf{A}$. This is accomplished by

$$\hat{\mathbf{D}} = \mathbf{V}^H\,\mathbf{B}\,\mathbf{V}, \tag{5.2}$$

where $\hat{\mathbf{D}}$ is a diagonal matrix with the eigenvalues of the subspace of $\mathbf{B}$ spanned by the eigenvectors of $\mathbf{A}$.

This approach to eigenanalysis can be used to compare clairvoyant and estimated interference covariance matrices and inverse interference covariance matrices. In these cases, $\mathbf{A}$ would be the clairvoyant matrix and $\mathbf{B}$ would be the estimated matrix.

5.1.1 Heterogeneous Clutter and the Interference Covariance Matrix

Two scenes with very different scattering eigenspectra are compared in Figure 5.1. For this comparison, $\mathbf{A}$ in (5.1) is the interference covariance matrix with the expected scattering spectrum composing the diagonal of the scattering covariance matrix $\mathbf{R}_\gamma$ in (2.32). The homogeneous, white-Gaussian scene and the road scene are quite different, by design. The resulting eigenspectra for both scenes are shown in Figure 5.1. As expected, the homogeneous scene has a flat spectrum due to the white-Gaussian noise (WGN) characteristics of the clutter scattering. The eigenspectrum of the road scene has more structure due to different scattering characteristics within the range-of-interest. As a note, the signal-to-clutter ratio (SCR) of the measurements for both scenes was 20 dB, thus the floor of both eigenspectra was not zero, which would correspond to an infinite SCR.

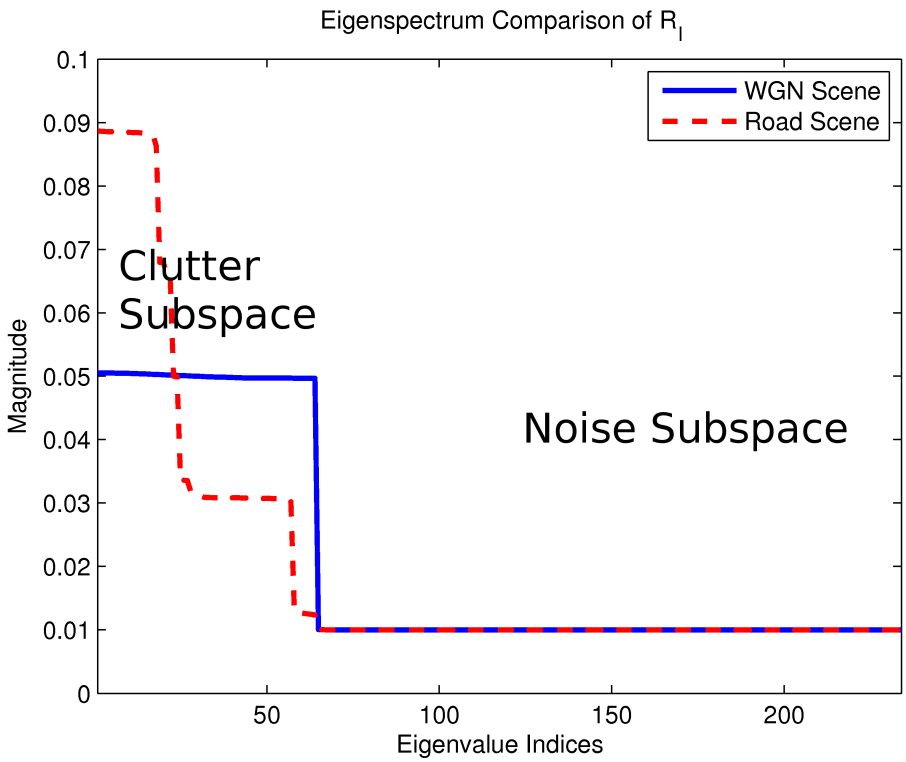

Figure 5.1. Eigenspectra of the expected clutter covariance matrices for range 13 of simulated homogeneous, white-Gaussian scene and simulated road scene

5.1.2 Moving Target and the Interference Covariance Estimate

A moving target whose velocity is low enough to be Doppler ambiguous with a clutter resolution cell is termed an *endoclutter* moving target, as opposed to an *exoclutter* moving target, which is not Doppler ambiguous with a resolution cell. In general, endoclutter targets are more difficult to detect than exoclutter targets, because their energy exists within the clutter subspace of a receiver. The existence of moving energy within the clutter subspace of the eigenspectrum is shown in Figure 5.2, which illustrates this concept using an endoclutter moving target in a homogeneous, unit-variance, white-Gaussian scene. The plots focus on the clutter subspace of the eigenspectra of clairvoyantly estimated $\mathbf{R}_I$ with and without a moving target of

three different magnitudes. Figure 5.2 illustrates the eigenspectrum of an endoclutter mover, as opposed to an exoclutter moving target, whose response would result in an eigenspectrum with nonzero eigenvalues (larger than the noise eigenvalues) in the noise subspace.

Figure 5.3 illustrates the same concept using an endoclutter moving target in the same homogeneous, unit-variance white-Gaussian scene, but the interference covariance matrix is estimated for three range bins. Consequently, the radar consists of three receivers, thus the three distinct peaks corresponding to the contribution of the moving target to the eigenspectrum via the three receivers. Ideally, by inverting the estimate of interference covariance matrix, the clutter subspace of the eigenspectrum will be suppressed leaving the energy of the moving target to be detected. This process is commonly called *whitening* the data. Figure 5.4 shows the whitened eigenspectrum of the measurements containing energy from the moving target.

5.2 Updating the Inverted Interference Covariance Matrix

Requiring the entire interference covariance matrix to be inverted for each new resolution estimate of the clutter spectrum could render the proposed multiresolution GMTI approach intractable for large problems with many resolutions to be used. However, because the scattering covariance matrix is assumed to be diagonal, the updating process can be simplified. Using a combination of singular value decomposition (SVD) and eigenanalysis, the inverted interference covariance may be updated directly using a few matrix multiplications and inverting the resulting diagonal matrix.

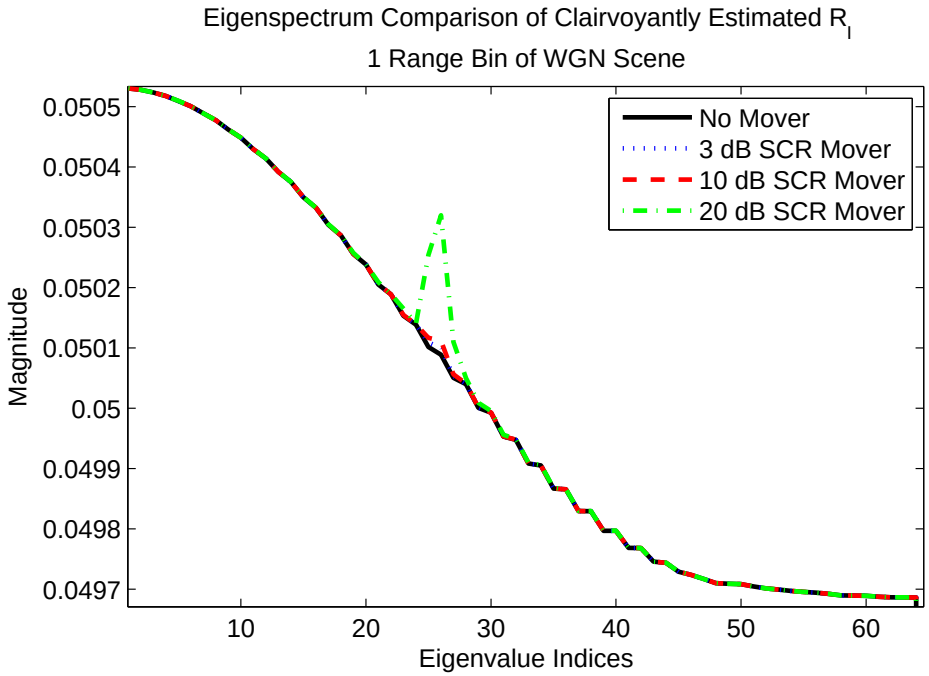

(a)

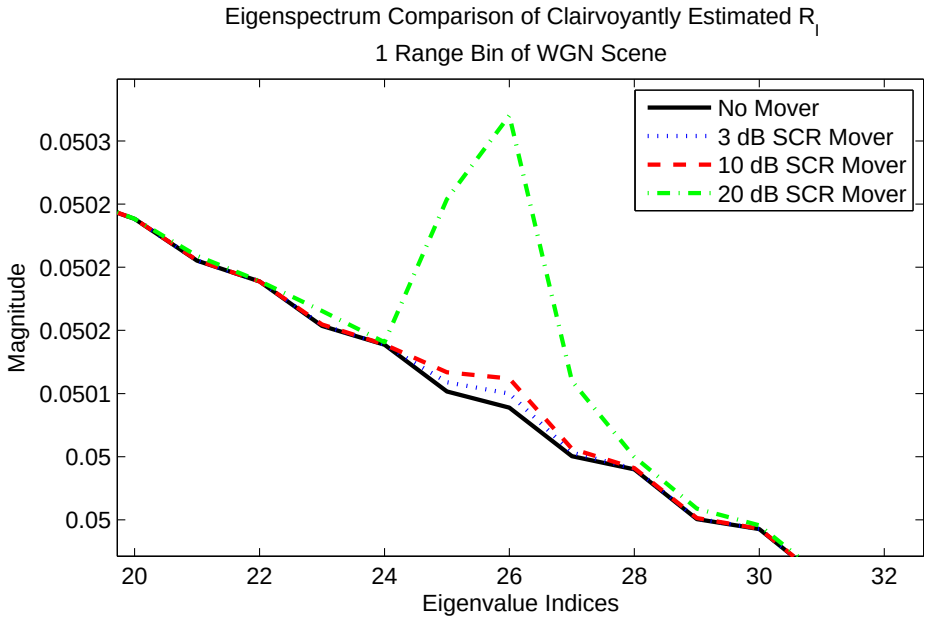

(b)

Figure 5.2. Comparison of eigenspectra for clairvoyantly estimated $\mathbf{R}_I$ with and without moving target in homogeneous, unit-variance scene, (a) eigenspectra of clutter subspace, (b) close-up of eigenspectra of clutter subspace

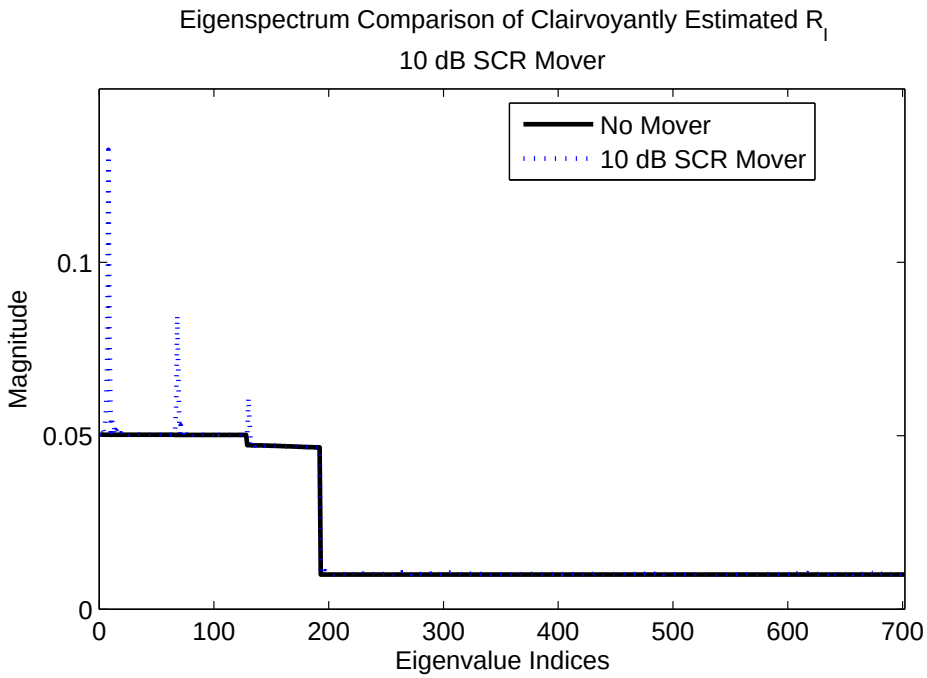

(a)

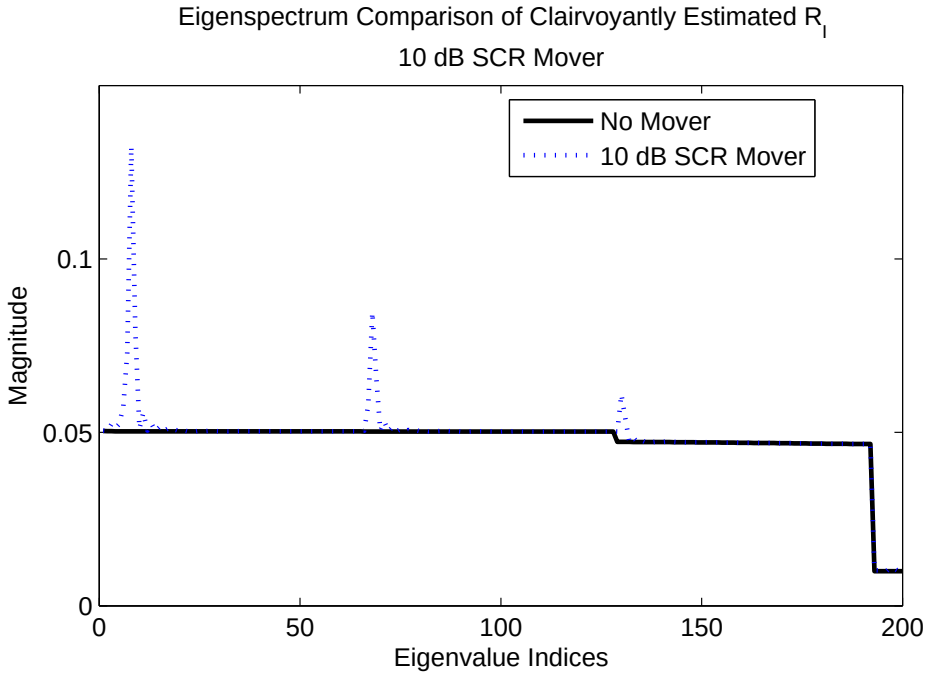

(b)

Figure 5.3. Comparison of eigenspectra for homogeneous, unit-variance scene with and without a 10 dB SCR moving target. (a) entire eigenspectra, (b) close-up of clutter subspace of eigenspectra

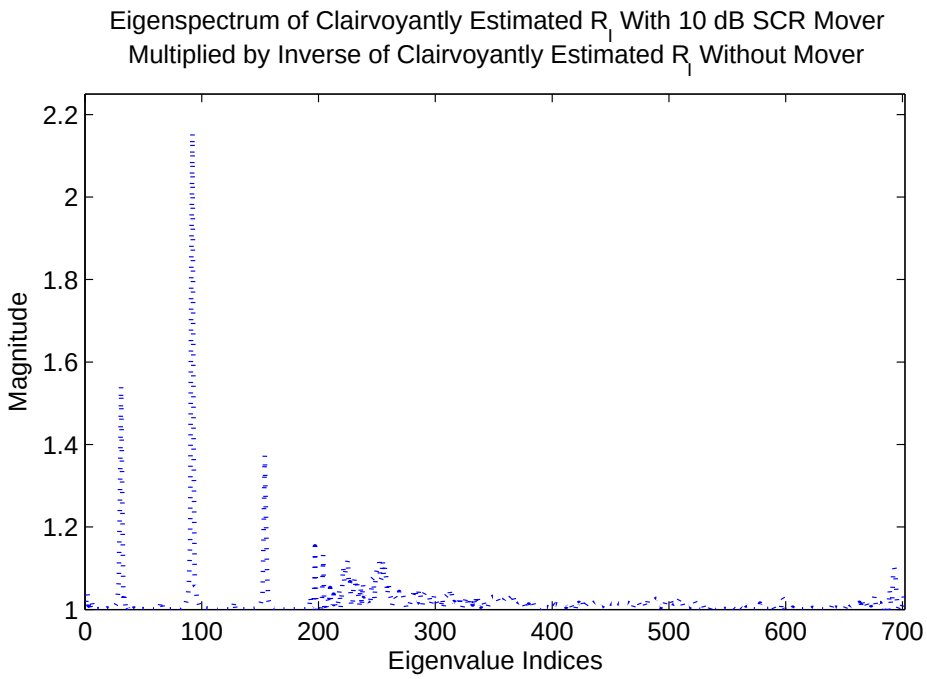

Figure 5.4. Eigenspectrum of clairvoyantly estimated covariance matrix with 10 dB SCR mover after whitening with clairvoyantly estimated interference only covariance matrix

Recalling (2.24) as the interference matrix,

$$\mathbf{R}_I = \mathbf{P}\mathbf{R}_\gamma\mathbf{P}^H + \mathbf{R}_n. \tag{5.3}$$

Taking the SVD of $\mathbf{P}$,

$$\mathbf{P} = \mathbf{U}\mathbf{S}\mathbf{V}^H \tag{5.4}$$

By definition, the SVD matrices $\mathbf{U}$ and $\mathbf{V}$ are unitary, and $\mathbf{S}$ is diagonal, though not square. Substituting (5.4) into (5.3), and grouping terms,

$$\begin{aligned}\mathbf{R}_I &= \mathbf{U}\mathbf{S}\mathbf{V}^H\mathbf{R}_\gamma\left(\mathbf{U}\mathbf{S}\mathbf{V}^H\right)^H + \mathbf{R}_n \\ &= \mathbf{U}\left(\mathbf{S}\mathbf{V}^H\mathbf{R}_\gamma\left(\mathbf{S}\mathbf{V}^H\right)^H\right)\mathbf{U}^H + \mathbf{R}_n\end{aligned} \tag{5.5}$$

Because $\mathbf{S}$ is diagonal, $\mathbf{S}\mathbf{V}^H\mathbf{R}_\gamma\left(\mathbf{S}\mathbf{V}^H\right)^H$ is also diagonal. Taking advantage of the noise covariance matrix being diagonal, it may be commuted inside what is now equivalent to the matrix of eigen values of the clutter covariance matrix, such that

$$\mathbf{R}_I = \mathbf{U}\left(\mathbf{S}\mathbf{V}^H\mathbf{R}_\gamma\left(\mathbf{S}\mathbf{V}^H\right)^H + \sigma_n^2\mathbf{I}\right)\mathbf{U}^H \tag{5.6}$$

For convenience, let $\mathbf{\Lambda}_I = \mathbf{S}\mathbf{V}^H\mathbf{R}_\gamma\left(\mathbf{S}\mathbf{V}^H\right)^H + \sigma_n^2\mathbf{I}$. Since $\mathbf{U}$ is unitary, inverting the interference covariance matrix simply requires taking the inverse of $\mathbf{\Lambda}_I$, a diagonal matrix, such that

$$\mathbf{R}_I^{-1} = \mathbf{U}\mathbf{\Lambda}_I^{-1}\mathbf{U}^H. \tag{5.7}$$

Using this approach to update the estimate of the clutter spectrum in GMTI, the only inverse required to update the inverted interference covariance matrix $\mathbf{R}_I^{-1}$ is inverting the updated $\mathbf{\Lambda}_I$, a diagonal matrix. However, the cost computing the singular value decomposition of $\mathbf{R}_I^{-1}$ is significant. Often the SVD approach only saves time when many different spatial resolutions of $\mathbf{R}_\gamma$ being used in the multiresolution GMTI processor.

5.3 Receiver Operating Characteristic Curves

Receiver operating characteristics (ROC) curves are commonly used to assess the quality of a communication or radar system. The curve is a function of the probability of false alarm (P_{FA}) and the probability of detection (P_D). Recalling the GMTI decision hypotheses (2.22), P_D is the probability that, given a target exists (H_1), that a target is declared;

$$P_D = P\left(H_1|H_1\right). \tag{5.8}$$

Similarly, P_{FA} is the probability that, given there is no target (H_0), a target is declared;

$$P_{FA} = P\left(H_1|H_0\right). \tag{5.9}$$

In an ideal system $P_{FA} = 0$, and $P_D = 1$. However, noise and clutter prevent ideal ROC, except for high signal-to-interference plus noise ratio (SINR) scenarios. Figure 5.5 shows an example ROC for a 64x64 homogeneous, unit-variance scene, 0 dB SCR scenario. The P_D and P_{FA} were calculated via 373 Monte Carlo simulations, as will be the ROC curves generated for Chapter 6.

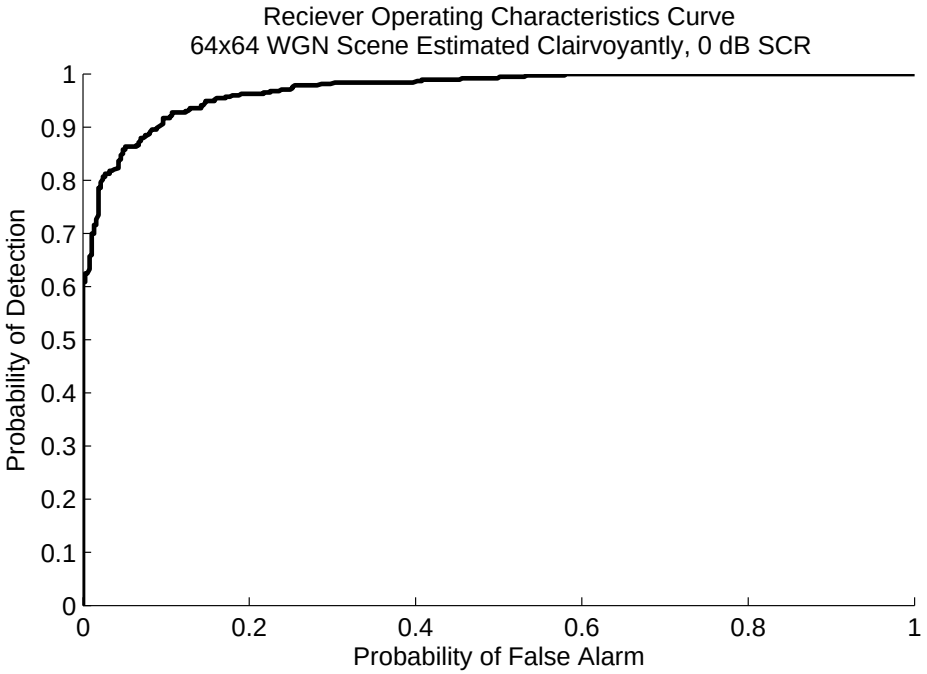

Figure 5.5. Example ROC curve for 373 Monte Carlo simulations of clairvoyantly estimated $\mathbf{R}_I$ for 64x64 WGN scene with 0 dB SCR

5.4 Accounting for Range-Spread Energy

This section discusses the advantage of using multiple range cells in the GMTI processor for both the optimum processor and SMI STAP. The return from a target

at a discrete range from the receiver is not limited to a discrete delay. Additionally, range walk occurs when moving targets cross range cell boundaries with the CPI. Accounting for range-spread energy and range walk in GMTI is possible at the cost of increased computational complexity by including multiple range cells in the GMTI processor. The target steering vector and beamformer must be calculated for the ranges-of-interest. Just as traditional SMI excises the target range-of-interest and guard ranges to account for range-spread energy, a robust detector should include the range-of-interest and the guard ranges where the moving target energy may be contained. Figure 5.6 shows an example of how moving target energy is spread over range cells for a scene with 64 range cells. Ideally, the curve would be an impulse function, yet even in this simple case of a moving point target, the concentration of energy is clearly spread over two range cells.

5.4.1 Optimal Processor for Multiple Range Cells

The optimum GMTI processor (2.23) is general enough, in form, to accommodate radar measurements, response vectors, and steering vectors of arbitrary length. In general, the entire measurement vector may be used; although, processing capabilities quickly become the limiting factor.

The size of the scattering covariance matrix (estimated by the SAR image) does not have a large impact on the performance of the GMTI processor, as long as is covers more ranges than the GMTI processor uses for matching. Figure 5.7 compares using three ranges in the matching filter to using a single range. The ROC curve resulting from using three ranges significantly outperforms the single range cases for both scenes. It is important to note that the ROC curves resulting from using three ranges are ideal for the three-decibel SCR scenario for both scenes.

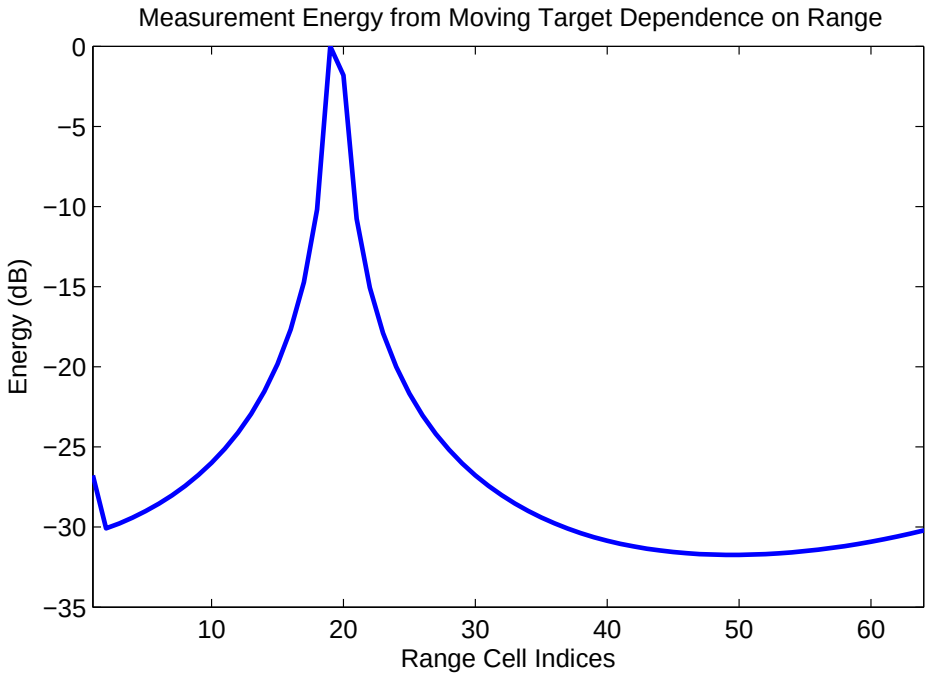

(a)

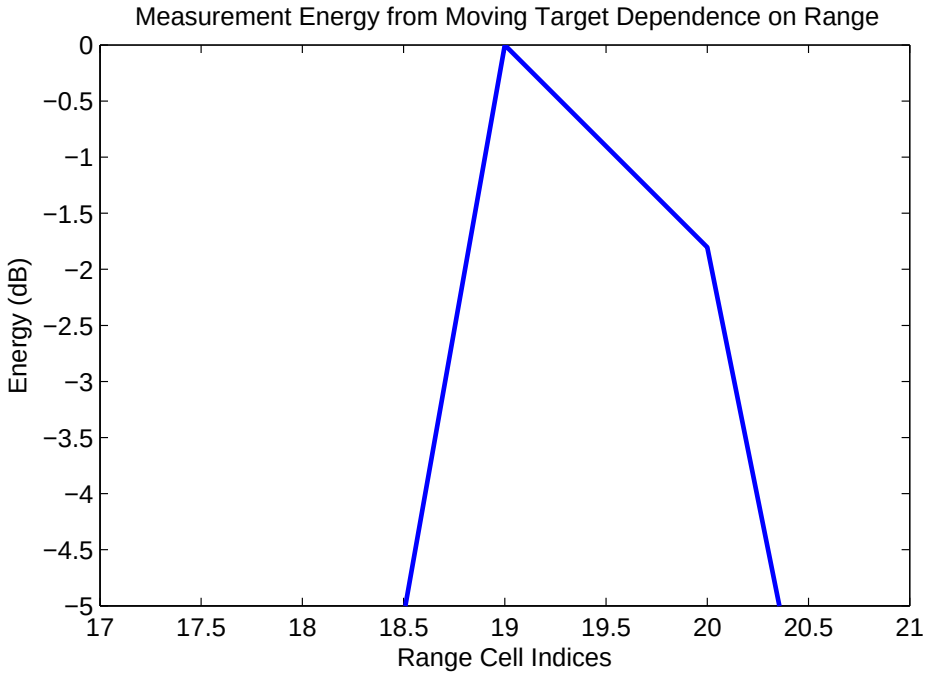

(b)

Figure 5.6. Squared absolute value of phase history measurements from moving target plotted against range cells for a 64 range cell scene (a) full 64 range cells (b) close-up of 5 range cells

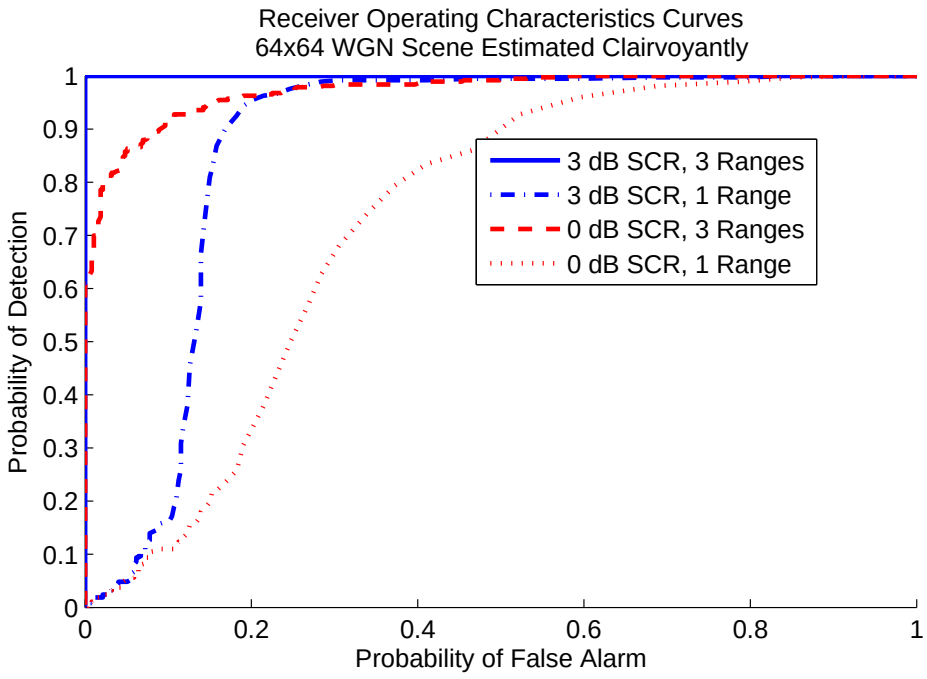

(a)

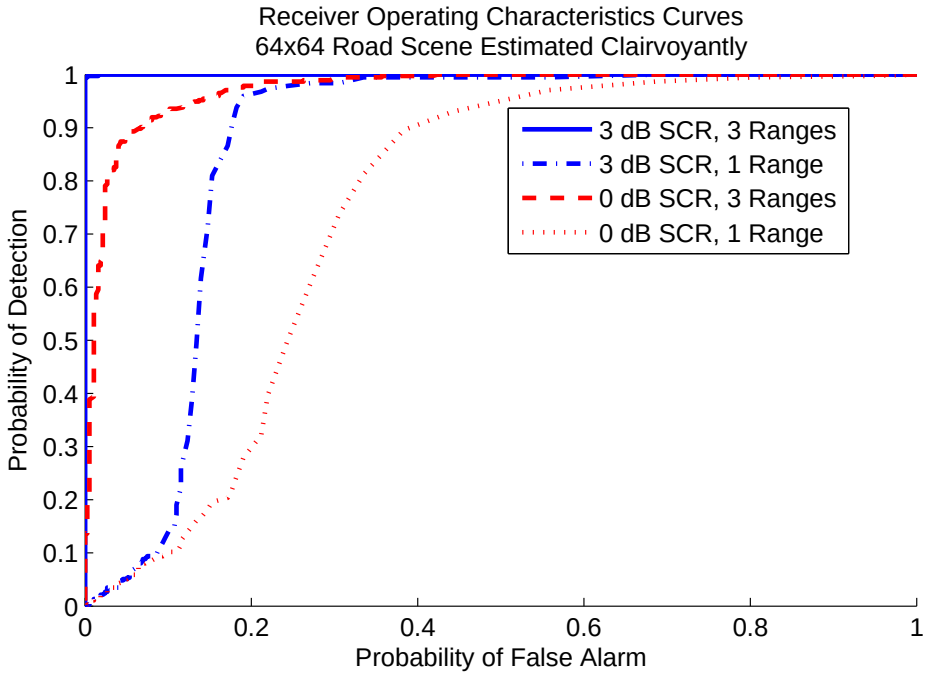

(b)

Figure 5.7. Comparison of ROC curves for the optimum GMTI processor using measurements from one and three range cells with 3 dB and 0 dB SCRs (a) homogeneous, unit-variance scene (b) simulated road scene. Note that the ROC curves for 3 dB SCR using 3 ranges are ideal.

5.4.2 SMI for Multiple Range Cells

While including multiple range cells in the whitening and matching portions of the optimum filter is straight-forward, SMI would require much more data to estimate the interference covariance matrix for three ranges. Recalling the description of SMI STAP in Section 2.2.4, the interference covariance matrix is estimated for one range. Implicitly, the scene is assumed to be homogeneous. The homogeneity assumption may be taken advantage of to estimate the interference covariance matrix for multiple ranges. The estimate of the interference covariance matrix $\hat{\mathbf{R}}_I$ from (2.45) may be *inflated* to further estimate the interference covariance matrix for multiple range cells. Specifically, this may be accomplished using a Kronecker product,

$$\hat{\mathbf{R}}_I^{(\lambda)} = \hat{\mathbf{R}}_I \otimes \mathbf{1}_\lambda, \tag{5.10}$$

where $\otimes$ is the Kronecker product operator, λ is the number of range cells for which to estimate the interference covariance matrix, and $\mathbf{1}_\lambda$ is a $\lambda \times \lambda$ matrix of ones.

Figure 5.8 exposes the limitation to using the inflated whitening filter to represent multiple ranges. SMI estimates the interference covariance matrix well for the homogeneous scene, as shown in Figure 5.8 (a). However, two-thirds of the clutter subspace corresponds to the scattering from the guard ranges. The inflated SMI estimate is limited in rank to a single-range estimate, thus the inflated estimate does not properly account for the unique eigenspectra from the guard ranges. This is illustrated by the null in the SMI eigenspectrum in Figure 5.8 (b). As a result, one would not expect SMI using three ranges to perform as well as the MVM GMTI processor using three ranges for even a homogeneous scene.

Using this inflated interference covariance estimate approach, the interference co-

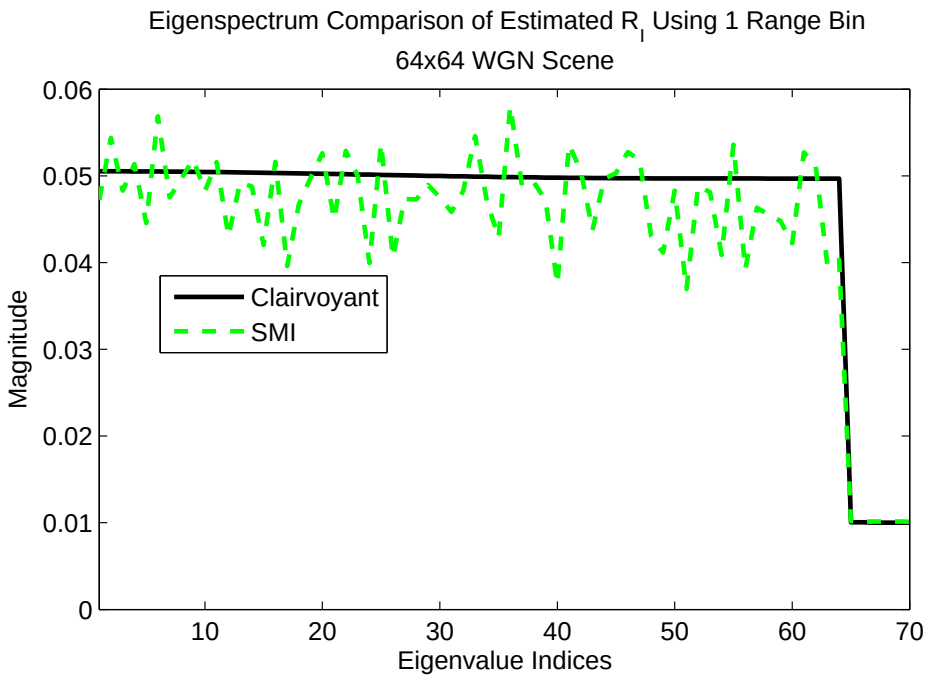

(a)

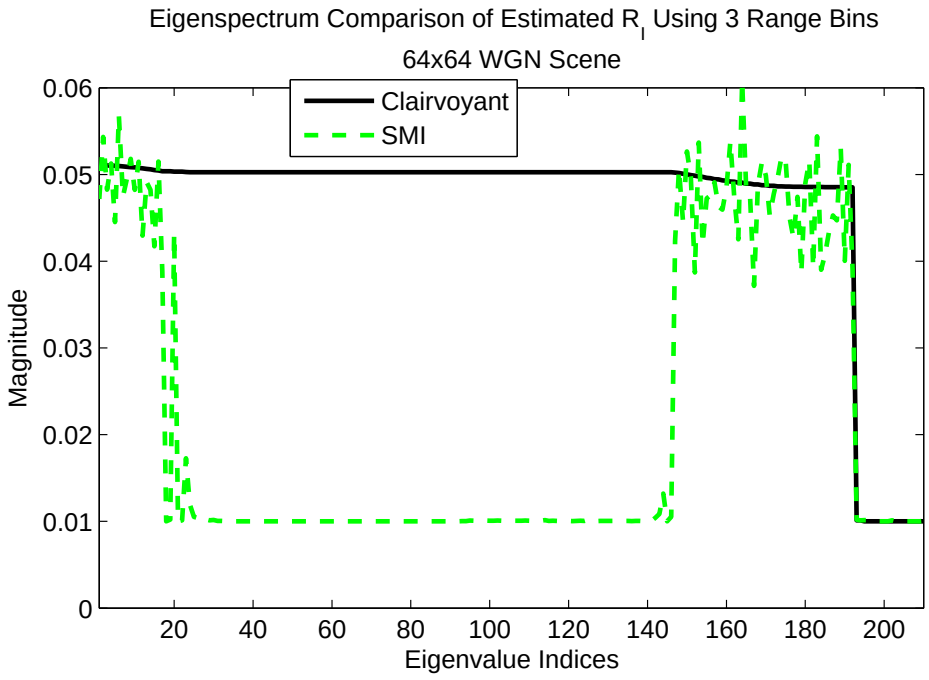

(b)

Figure 5.8. Comparison of eigenspectra for clairvoyant and SMI estimated covariance matrices of 64x64 homogeneous, unit-variance scene (a) $\mathbf{R}_I$ estimated for one range bin using SMI (b) $\mathbf{R}_I$ estimated for three range bins using SMI

variance matrix for three range cells was estimated using for two different scenes. Each scene was used as the background for a Monte Carlo simulation for two different moving target SCR scenarios. Figure 5.9 contains the ROC curves for these scenarios. Despite the rank limitation of the SMI whitening filter, the matching filter for three ranges does outperform that of the the single range. It is interesting to observe that the SMI performance using three ranges is similar to the optimum processor using one range in Figure 5.7.

5.5 Final Detection From Detection Vector

As stated at the beginning of the chapter, the detection algorithm is not the focus of this research, so a Bayesian threshold detector, as described in Chapter 6 of Kay [87] will be use. A detection coefficient resulting from using each resolution of the multilook SAR image to estimate the scattering covariance matrix will be placed in a vector, and a simple fusion algorithm will be used to make the final detection decision.

Given α resolutions of the clutter spectral estimate, the resulting detection coefficients δ_i may be organized into a vector,

$$\boldsymbol{\delta} = [\delta_1 \ \delta_2 \ \ldots \ \delta_\alpha]^\dagger , \tag{5.11}$$

where each detection coefficient is binary. Following the notation in (2.22),

$$\begin{aligned} \delta_{H_0} &= 0 \\ \delta_{H_1} &= 1. \end{aligned} \tag{5.12}$$

The simplest fusion algorithm arrives at a final detection decision using a voting

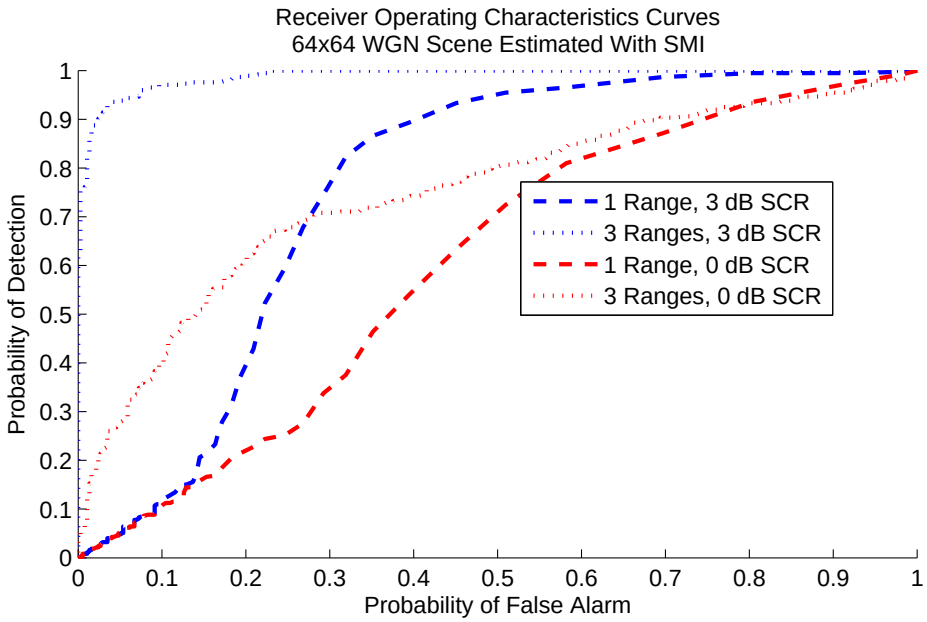

(a)

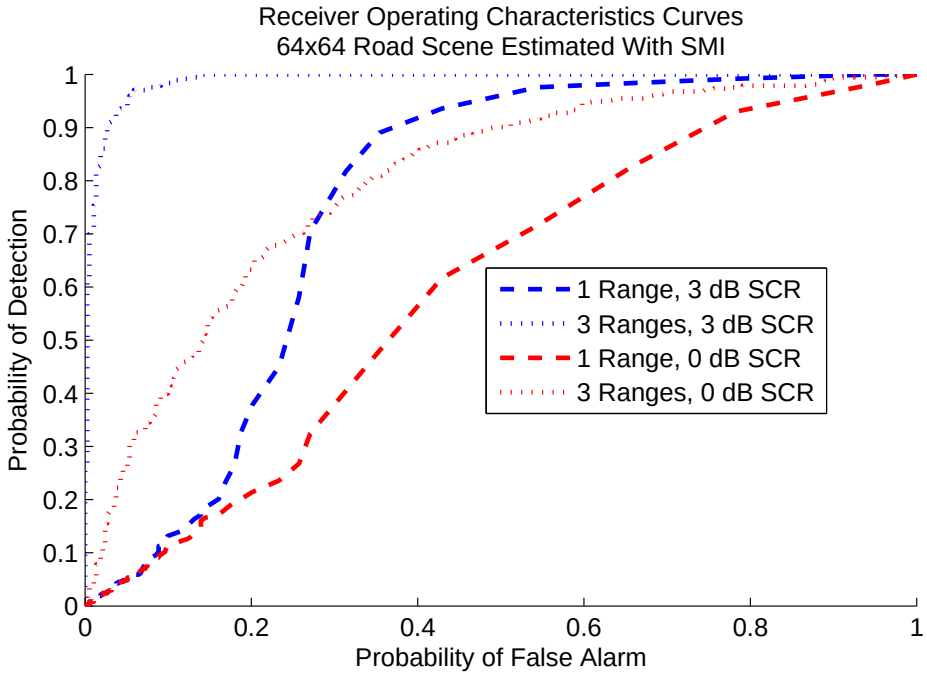

(b)

Figure 5.9. Comparison of ROC curves for the SMI STAP using measurements from one and three range cells with 3 dB and 0 dB SCRs (a) homogeneous, unit-variance scene (b) simulated road scene

scheme, which is a simple majority decision. An odd number of elements in the detection vector is required, and the final decision is based on the majority of the the results. Using a voting scheme for the final decision,

$$\Delta = \text{round}\left(\frac{1}{\alpha}\sum_{i=1}^{\alpha}\delta_i\right), \tag{5.13}$$

where, similar to (5.12), $\Delta_{H_0} = 0$, and $\Delta_{H_1} = 1$.

Another, slightly more complex fusion would be a consecutive scheme, which is a slight variation on the voting scheme. In addition to the requiring a majority, the a predetermined number of detection coefficients need to occur consecutively in the detection vector. However, due to its simplicity and the limited number of multilook SAR resolutions that will be used in this research, a voting scheme will be used in this research.

Chapter 6

Results

This chapter presents the results of the proof-of-concept approach to multiresolution GMTI presented in Chapter 5. The whitening filters for multiple resolutions of the clutter scattering spectrum are calculated two ways. First, the interference covariance matrix is estimated using multilook SAR images calculated from subapertures of the measurements, as covered in Chapter 4. Second, using the approach in Section 3.3, the same interference covariance matrix is estimated using multiple resolutions of the discrete wavelet transform (DWT) filter bank to smooth the full spatial resolution, single-look SAR image.

The multilook SAR and DWT approaches to estimating the interference covariance matrix are compared to the conventional sample matrix inverse (SMI) technique. SAR is an estimate of the scattering covariance matrix $\mathbf{R}_\gamma$ in (2.34), while SMI directly estimates the interference covariance matrix $\mathbf{R}_I$ via (2.45). Therefore, prior to presenting the receiver operating characteristic (ROC) curves for each approach, the SMI estimate of $\mathbf{R}_I$ is compared to the estimate of $\mathbf{R}_I$ using the SAR estimate of $\mathbf{R}_\gamma$ via (2.30). The comparison is performed through eigenanalysis of the estimates of $\mathbf{R}_I$ and $\mathbf{R}_I^{-1}$.

Finally, ROC curves for a simple fusion algorithm to determine the final detection decision from a vector of detection coefficients resulting from using each resolution of the multilook SAR image are presented.

6.1 Experimental Design

This research presents a proof-of-concept approach to demonstrating multiresolution GMTI. For that reason, the lack of suitable measured data, and the complications that arise from measured data, simulated long-PRI, wideband, long-CPI data were generated and processed. This section briefly describes the computational approach to simulating the radar model and the parameters for the Monte Carlo simulations used to calculate the receiver operating characteristics in later sections.

6.1.1 MATLAB Radar Model

The space-time data were generated using a MATLAB radar model presented in 2.1 and more comprehensively presented in a series of unpublished papers by Stiles [88–91]. The mathematics describe an arbitrary space-time transmit signal, target set, and space-time receive measurements. The received measurements are related to the target and transmit signal description via farfield radar response vectors. The result allows for a set of complex receiver samples that accurately reflect the phase history in the slow-time domain, and the Fourier transform of the phase history in the fast-time domain of an arbitrary space-time radar when illuminating an arbitrary and diverse target set.

Figure 6.1 shows the graphical user interface (GUI) to the MATLAB radar model. Following Stiles' mathematical description, the software model was designed to be general. The sizes of the transmit and the receive arrays, as well as the locations of the elements may be input directly within the GUI or loaded from a file. Likewise, the complex clutter scattering coefficients may be randomly generated with Gaussian or uniform PDFs or loaded from a file. The bandwidth, PRI, number of pulses, and target spacing (physical size of the resolution cells) may be chosen by the user,

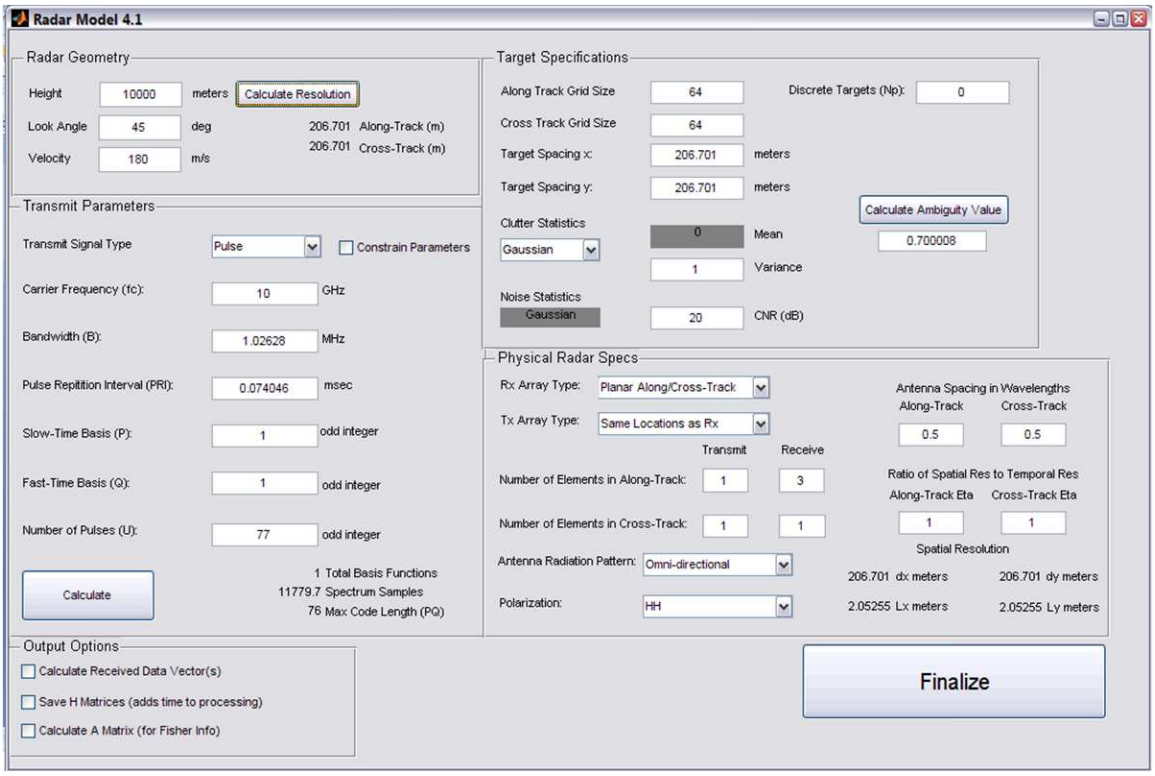

Figure 6.1. Graphical user interface for MATLAB radar model

or the model can calculate those values based on predetermined relationships. The output includes the data vector, array manifold, and noise vector, as well as all the constituent parameters that may be necessary in GMTI and SAR processing, such as positions of the array elements, stationary and moving target parameters, and clutter and noise statistics.

6.1.2 Monte Carlo Simulations

Radar Parameters Recalling the linear, discrete radar model (2.14) with $\boldsymbol{\varepsilon} = \mathbf{0}$, and explicitly calling out the clutter contribution and the contribution of a single moving target to the measurements leads to

$$\mathbf{d} = \mathbf{P}_C \boldsymbol{\gamma}_C + \boldsymbol{\rho}_t \gamma_t + \mathbf{n}. \tag{6.1}$$

For each Monte Carlo iteration, the clutter array manifold $\mathbf{P}_C$ and noise vector $\mathbf{n}$ were the same. The radar array consisted of one transmitter and a uniform linear array of three receivers separated by one-half wavelength of the transmitted center frequency. Table 6.1 contains the radar parameters for the Monte Carlo simulations. To be computationally feasible, the parameters are not operationally realistic (e.g., spatial resolution of 207 meters), but are included for completeness. The parameters were chosen such that the along-track and cross-track resolutions, dx and dy, respectively were equal.

Height	10 km	Scene Size	64x64
Look Angle	45deg	dx, dy	207 m
Velocity	180 m/s	SNR	20 dB
Frequency	10 GHz	PRI	73.1 μsec
Bandwidth	1.02 MHz	# Pulses	78
Samples/Pulse	75		

Table 6.1. Radar parameters for Monte Carlo simulations

These radar parameters resulted in 5850 measurements per receiver per CPI, the measurement vector $\mathbf{d}$ for one CPI was then 17 550 samples. The number of resolution cells, and thus scattering coefficients in γ, was 4096 resulting in a $17\,550 \times 4096$ array manifold $\mathbf{P}$.

Clutter Scenes Two scenes with very different eigenspectra, as defined by (2.30) and compared in Section 5.1 were used generate the complex scattering coefficient vector $\boldsymbol{\gamma}_C$. The first scene was a homogeneous, white-Gaussian scene with unit variance, which resulted in the complex scattering coefficient vector having a complex Gaussian distribution with zero-mean and unit variance, i.e., $\boldsymbol{\gamma}_C \sim CN(0, 1)$. The second scene was a structured clutter scene illustrated in Figure 3.10. In that scene, the variances changed between regions, but the scattering coefficients still had a com-

plex Gaussian distribution with zero mean, i.e., $\boldsymbol{\gamma}_{C_i} \sim CN(0, \sigma_i^2)$, where $\{i\}$ is the set of indices for the different regions in the scene. Figure 6.2 shows the statistical realizations for the clutter spectra used in the Monte Carlo simulations. The clutter spectra are in the form of intensity-squared, SAR images.

Moving Target Parameters The radar response vector for each iteration of the Monte Carlo simulation was generated with a random location within the illuminated scene and a random radial velocity to ensure the energy was endoclutter. Endoclutter is the more challenging case, since the moving target's radar response vector for one receiver is within the span of the clutter subspace for that same receiver. Figure 5.3 illustrates the eigenspectrum of an endoclutter mover, as opposed to an exoclutter moving target, whose response would result in an eigenspectrum with nonzero eigenvalues to the right of index 200.

A new moving target location for each iteration of the Monte Carlo simulation varied uniformly between the minimum and maximum ranges and cross ranges. The minimum and maximum ranges and cross ranges were set to be two range bins and cross-range bins, respectively, inside the edges of the scene. The radial velocity of the moving target was also randomly generated. To ensure each moving target's radial velocity resulted in endoclutter energy, the radial velocity was set to have a uniform distribution with a mean corresponding to just less than half the Doppler bandwidth, and the standard deviation equal to of half the mean, i.e., $v_t \sim \mathrm{U}(\mu_v, \sigma_v)$, where $\mu_v \lessapprox \frac{B_D \lambda}{4}$, where B_D is the Doppler bandwidth of the system, and λ is the wavelength of the center frequency of the transmitted waveform. Additionally, $\sigma_v \approx \mu_v/2$. The radial velocity of the target exceeded the Doppler resolution and was within the Doppler bandwidth of the system.

For the radar parameters in Table 6.1, the Doppler bandwidth $B_D = 12$ kHz,

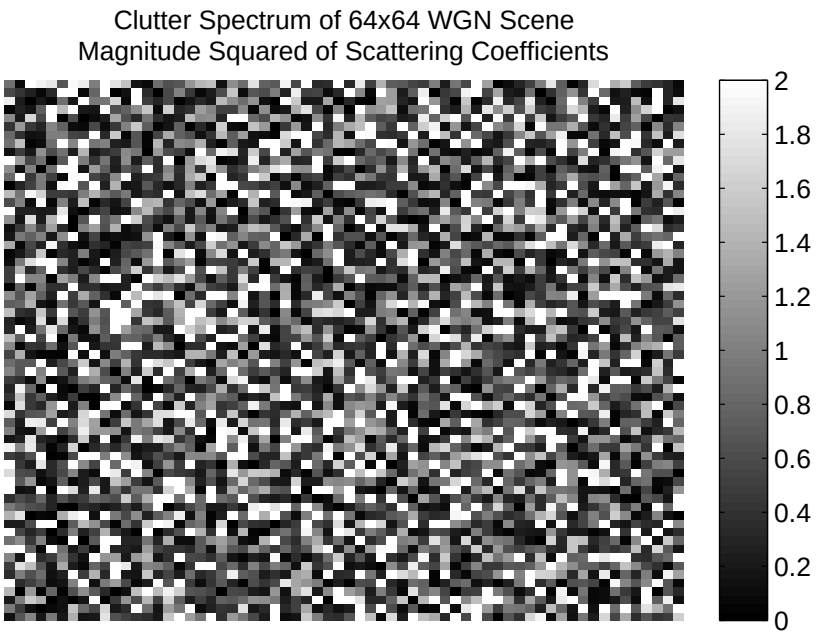

(a)

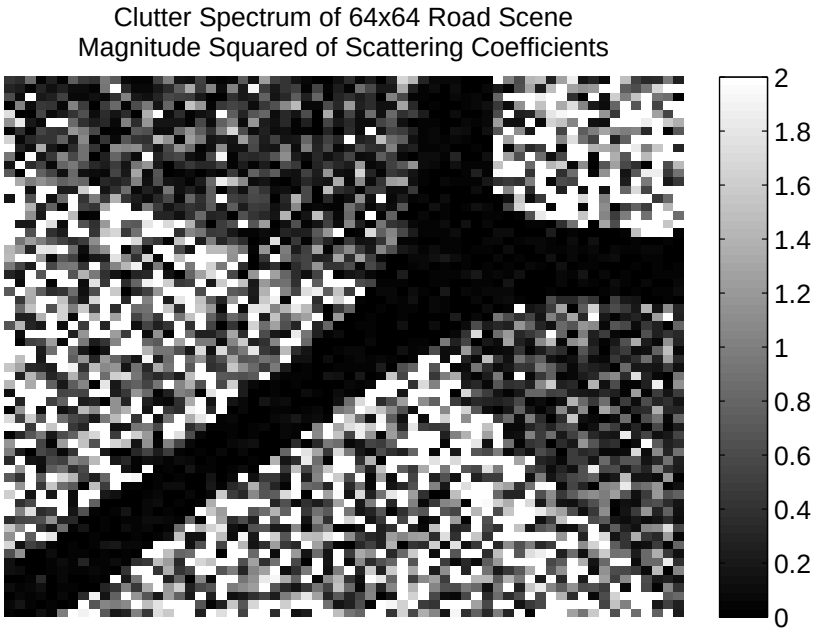

(b)

Figure 6.2. Intensity-squared realizations of 64x64 demonstration scenes (a) homogeneous, unit-variance, white-Gaussian scene (b) road scene

which leads to an unambiguous radial velocity for the radar of $v_{unambig} = \frac{B_D \lambda}{2} = \pm 90$ m/s. Then μ_v was set to be 40 m/s for moving targets behind broadside and -40 m/s for targets ahead of broadside. The standard deviation of the radial velocities for the moving target $\sigma_v = \frac{|\mu_v|}{4} = 10$ m/s. These values ensured all moving target energy was endoclutter.

The same moving target parameters were used for each iteration of the Monte Carlo simulation. Figure 6.3 contains a two-dimensional histogram of the physical locations and a one-dimensional histogram of the radial velocities of the moving targets.

6.2 GMTI Using Multilook SAR Images as Estimate of $\mathbf{R}_\gamma$

As presented in Chapters 4 and 5, multilook SAR may provide a computationally tractable approach to estimating the clutter spectra for GMTI. This section presents the results of investigating this hypothesis. First, the performance of the multilook SAR is presented, then the eigenspectra of the estimated interference covariance matrices using multilook SAR images is compared to those calculated clairvoyantly.

6.2.1 Multilook SAR Images

The following results are multilook SAR images generated using measurements from only one receiver. In general, the eigensensor approach to multilook SAR presented in Chapter 4 applies to arbitrarily-spaced receiver arrays. In fact, power of the eigensensor approach is seen when the receiver array is not uniformly spaced, as observed in Section 4.2.2. Assuming the scatterers are in the farfield, when using a closely-spaced, uniform linear array, the measurements from receiver-to-receiver only differ by a linear phase shift, dependent only on the interelement spacing. The lin-

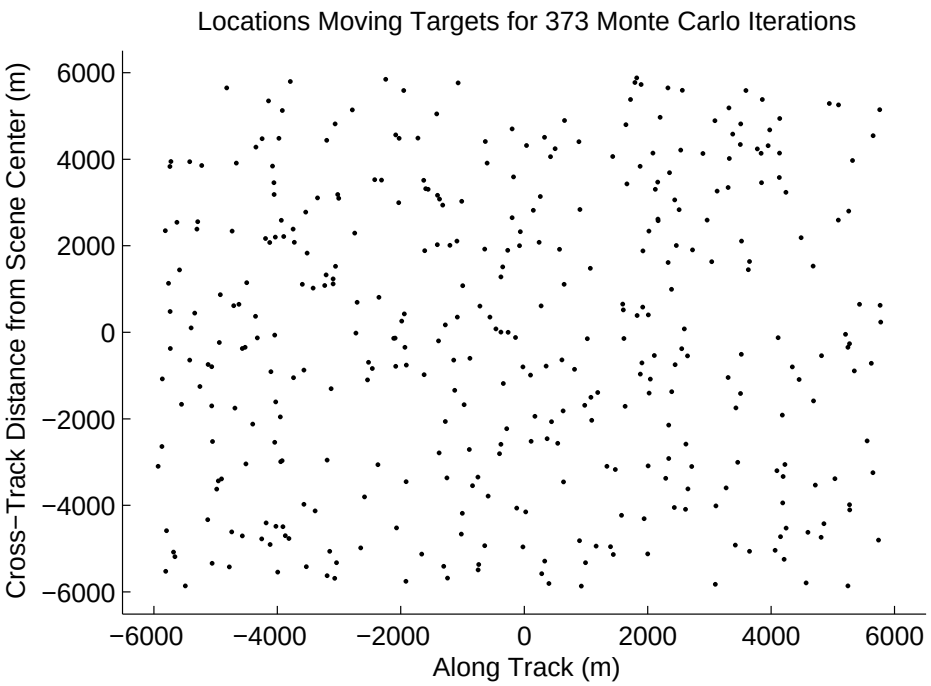

(a)

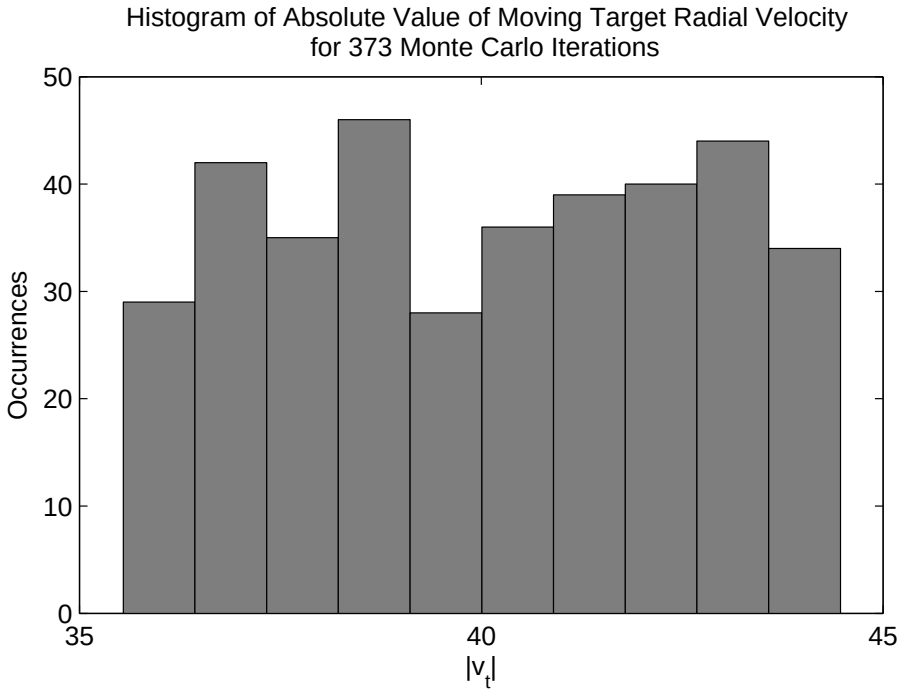

(b)

Figure 6.3. Histograms of the locations and radial velocities of the moving targets for each of 373 iterations of the Monte Carlo simulations (a) Locations within the 64x64 resolution cell scene (b) Radial velocities

ear phase shift results in the rows of the array manifold corresponding to different receivers being linearly dependent. Thus the row rank of the array manifold $\mathbf{P}$ is dependent on only one receiver. As discussed in Section 4.2.3, multilook SAR processing is an inherently under-determined process when using many looks.

For the radar parameters in Table 6.1 the measurement vector for one receiver was 5850 samples. The multilook SAR subapertures for were chosen to be square factors of two, such that 4, 256, and 1024 subapertures were used to calculate the multilook SAR images. These numbers of subapertures led to subaperture sizes of about 1500, 25, and 5 samples per subaperture, respectively. Since the number of scattering coefficients to be estimated was 4096, each of the subaperture sizes resulted an under-determined system. Including measurements from all receivers would result in an increase in the number of measurements per subaperture, without increasing the rank of the system or accuracy of the estimate.

The multilook SAR images in Figures 6.4 and 6.5 show multilook, intensity-squared SAR images with decreasing spatial resolution. The complex scattering coefficients were estimated using the matched filter in plot (a) and maximum likelihood in plot (b) of each figure. The measurements were from the homogeneous, unit-variance, white-Gaussian scene in Figure 6.2 (a) and contained no moving target. Similarly, Figures 6.6 and 6.7 show multilook, intensity-squared SAR images with decreasing spatial resolution. The measurements used to estimate these images were from the road scene in Figure 6.2 (b) with no moving target.

No effort to zero pad the subapertured data was made, resulting in the *picture frame* effect on the images estimated with maximum likelihood. This effect and the effect of bias in both the matched-filter estimates and the maximum-likelihood estimates due to the Welch power spectrum estimate (PSE) technique are noticeable

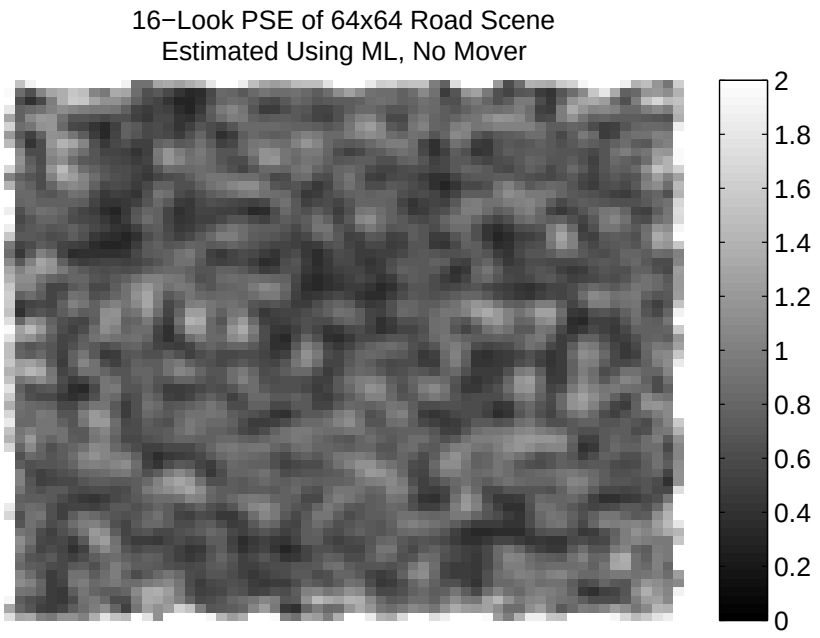

(a)

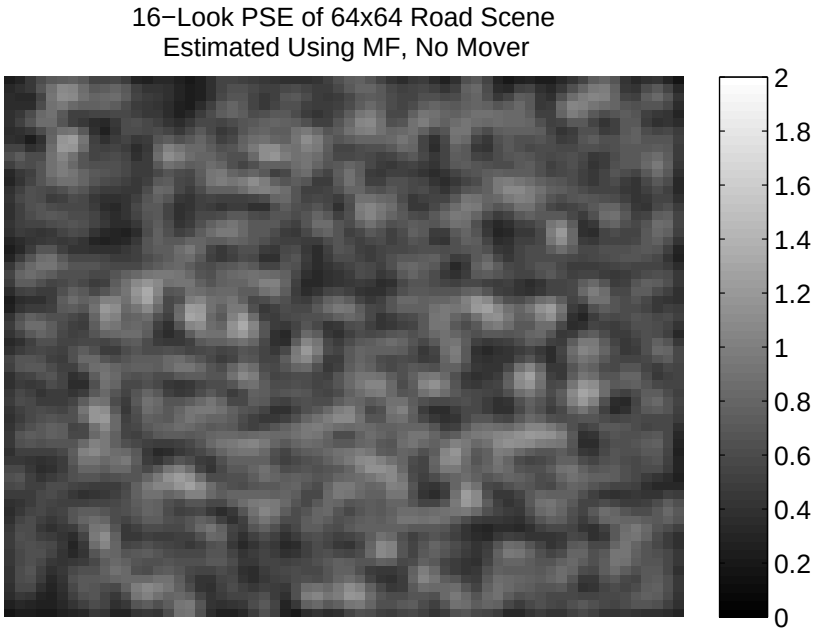

(b)

Figure 6.4. 16-look, 64x64 SAR image of homogeneous, unit-variance Gaussian scene (a) estimated using maximum likelihood (b) estimated using matched filter

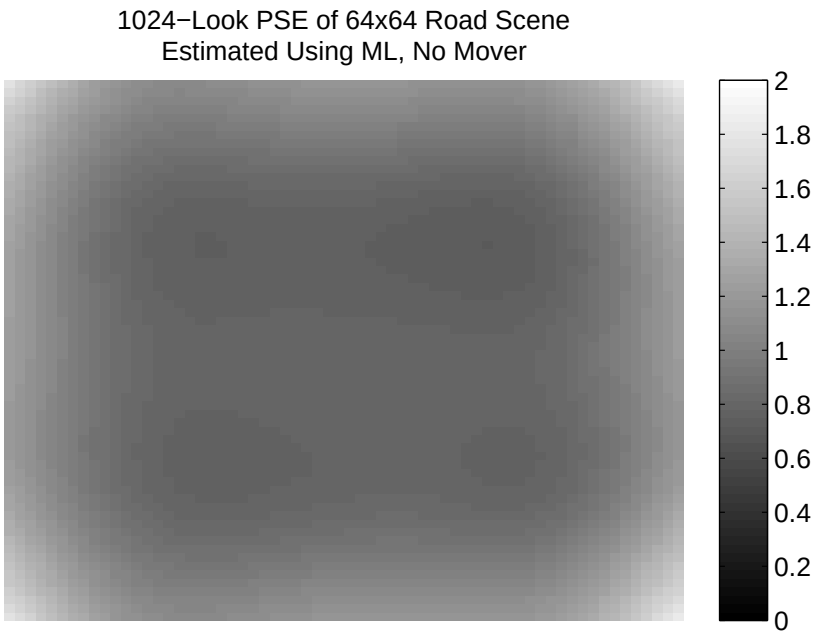

Figure 6.5. 1024-look, 64x64 SAR image of homogeneous, unit-variance Gaussian scene (a) estimated using maximum likelihood (b) estimated using matched filter

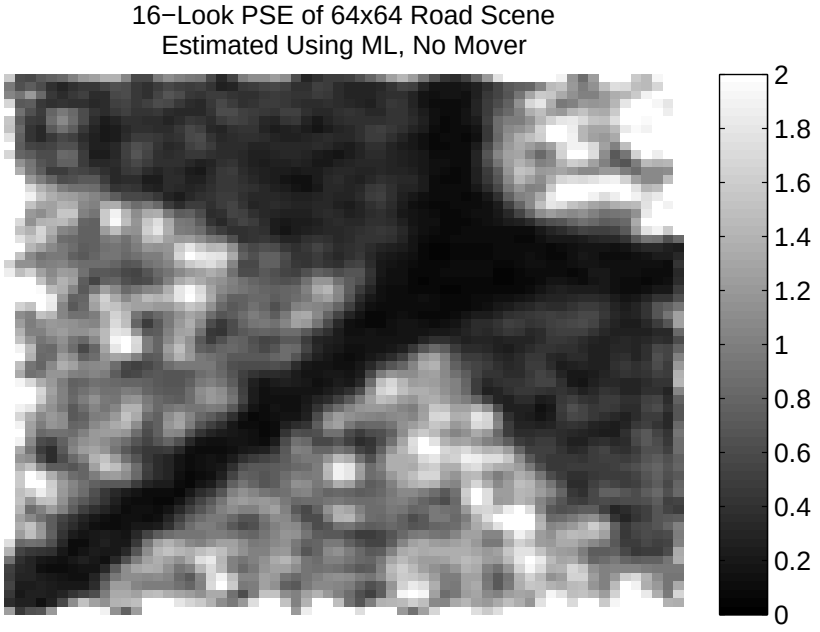

(a)

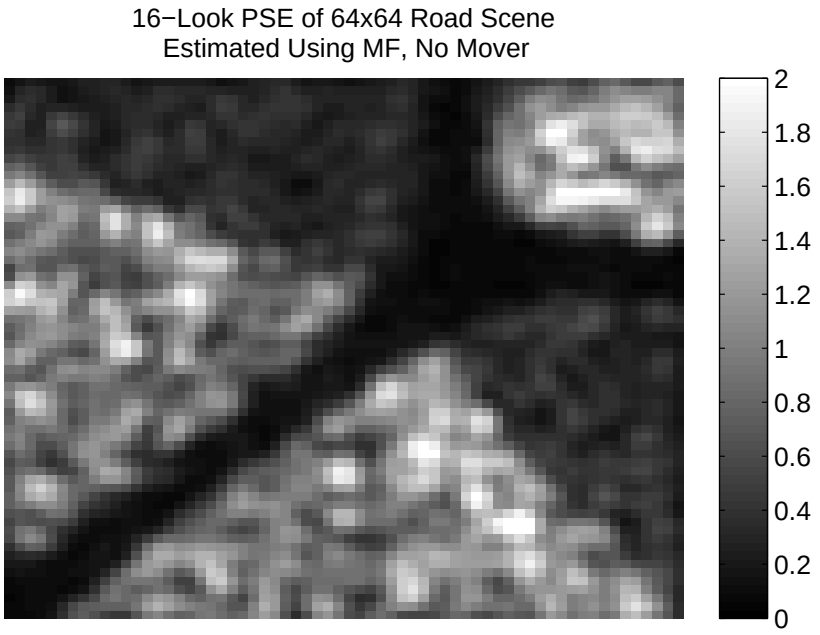

(b)

Figure 6.6. 16-look, 64x64 SAR image of simulated road scene (a) estimated using maximum likelihood, (b) estimated using matched filter

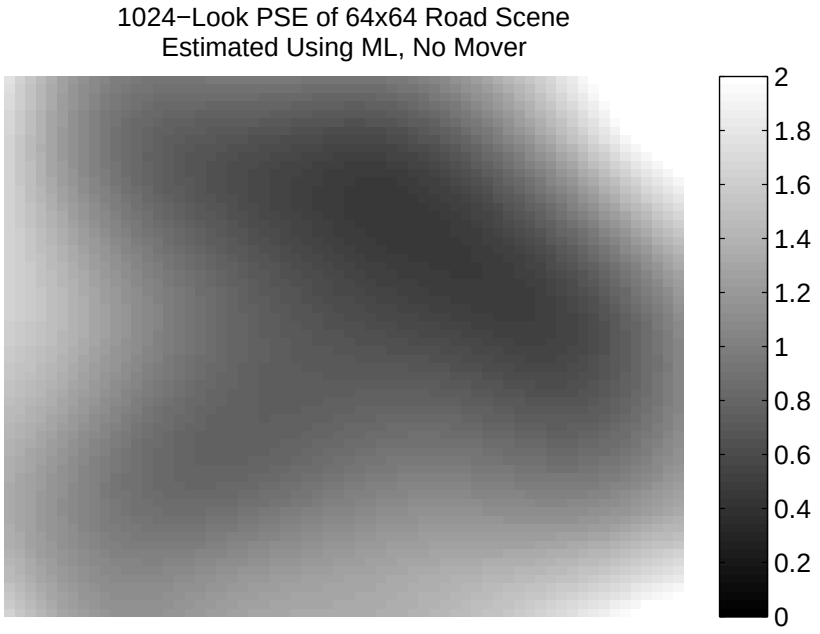

Figure 6.7. 1024-look, 64x64 SAR image of simulated road scene (a) estimated using maximum likelihood (b) estimated using matched filter

in the multilook SAR images in Figures 6.4 and 6.7.

6.2.2 Interference Covariance Matrix Estimates

The shortcomings of the Welch PSE technique discussed above are easily recognized in the one-dimensional eigenspectra of the estimates of the interference covariance matrices in Figure 6.8. The picture frame in the maximum-likelihood estimates result in spikes in the eigenspectra of the estimates of the interference covariance matrices and nulls in the whitening filters, as seen in Figure 6.9. The bias may be seen in the eigenanalyses of the interference covariance estimate using maximum likelihood in Figure 6.8 and its inverse in Figure 6.9. The bias appears even more pronounced in the matched filter estimates, as shown in Figure 6.9.

The bias in the interference covariance matrix estimates calculated from the multilook SAR images results in under-suppressed clutter in the whitening filter output. This is particularly true for the estimated whitening filters for the homogeneous scenes, as evidenced by Figures 6.9 (a) and 6.10 (a), although the maximum likelihood estimate bias is less than that of the matched filter. From these results, one would expect better GMTI performance from the multilook SAR images estimated using maximum likelihood than those estimated using the matched filter.

6.3 GMTI Using DWT-Smoothed SAR Images as Estimate of $\mathbf{R}_\gamma$

Smoothing SAR images by taking the low-scale filter outputs from a multistage Haar discrete wavelet transform (DWT) filter bank was discussed in Section 3.3. In Section 4.2.3.1, filter banks were determined unsuitable to provide a reduced basis set for the complex radar model because of the uniform random phase distribution of the radar response vectors and the scattering coefficients. However, filter banks are

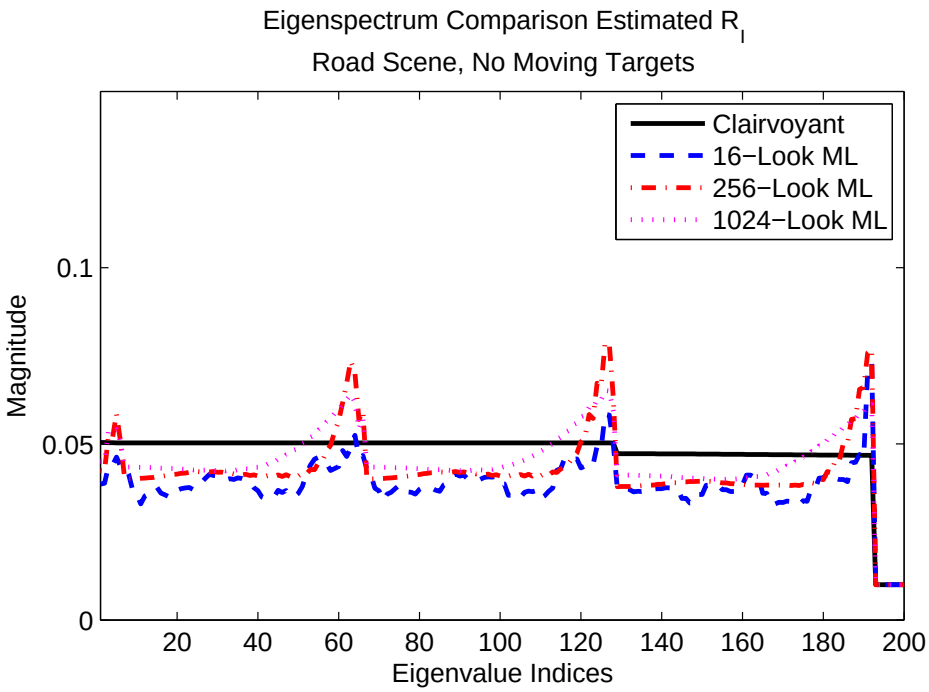

(a)

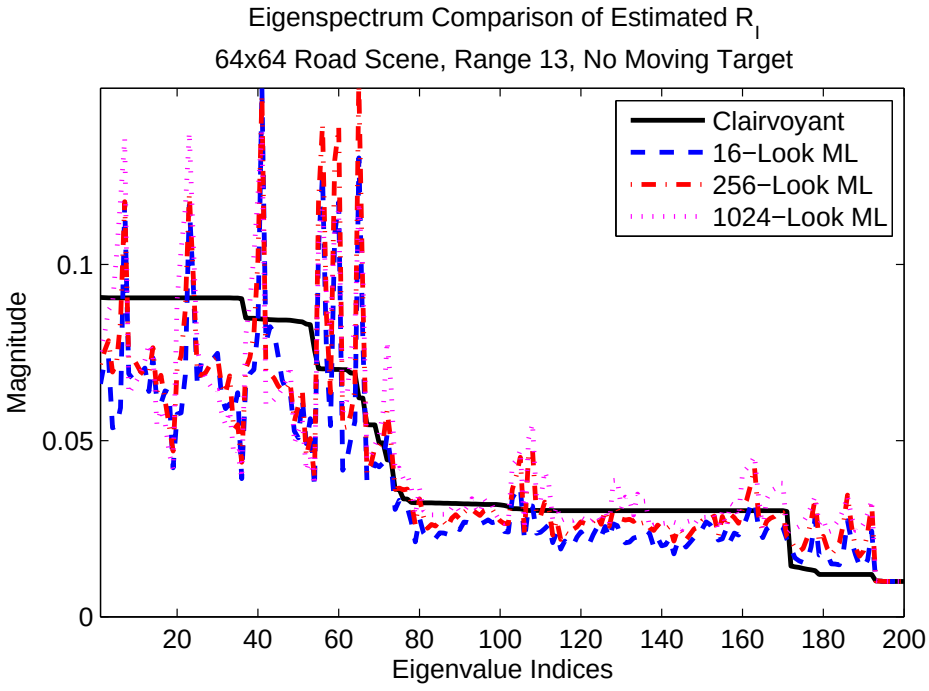

(b)

Figure 6.8. Close-up of the clutter subspace of the eigenspectra of the clairvoyant and ML estimated $\mathbf{R}_I$ (a) homogeneous, unit-variance scene (b) simulated road scene

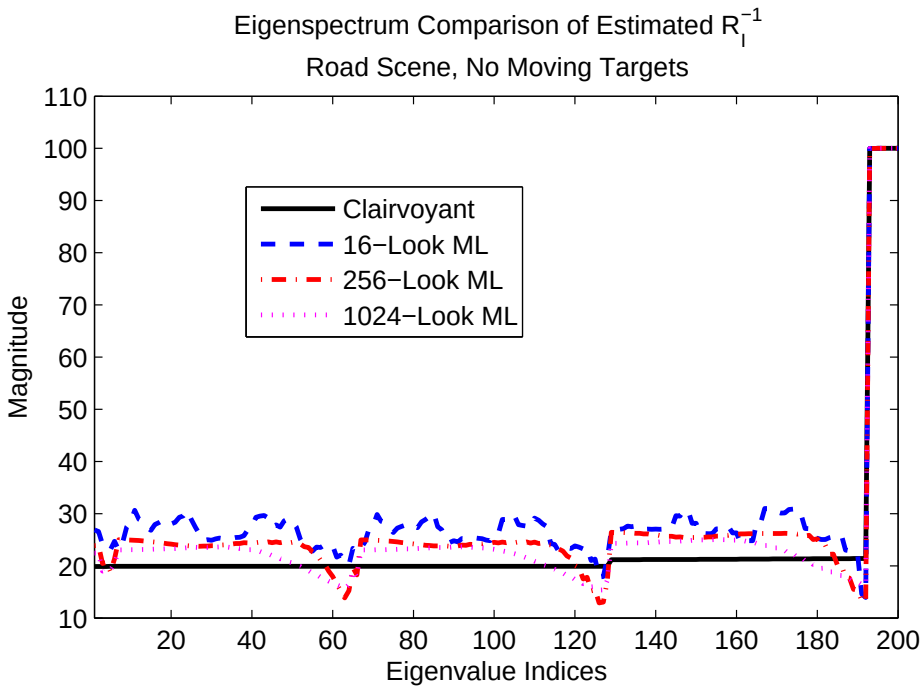

(a)

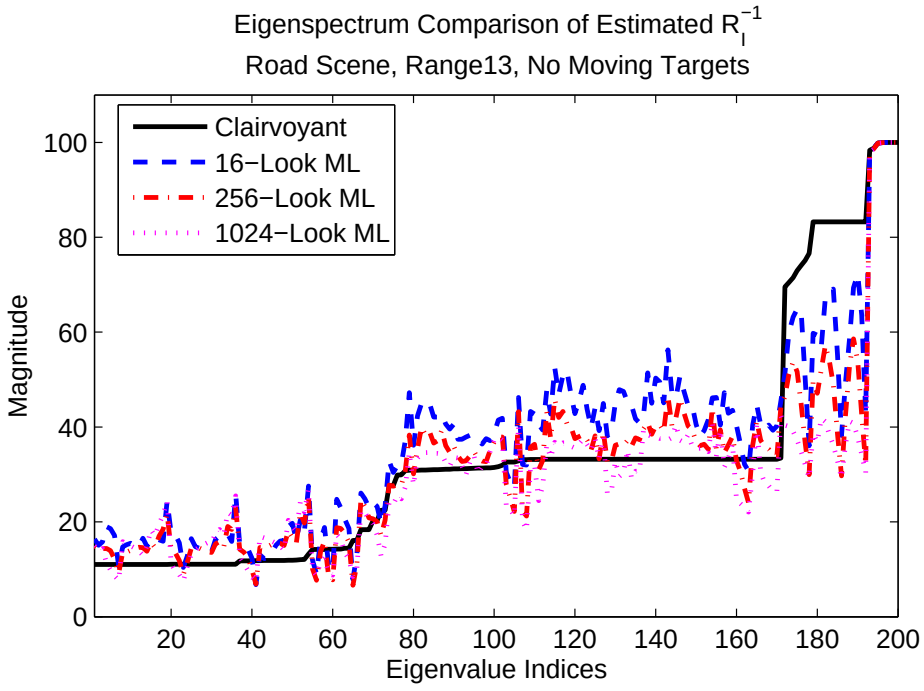

(b)

Figure 6.9. Close-up of the clutter subspace of the eigenspectra of the clairvoyant and ML estimated $\mathbf{R}_I^{-1}$ (a) homogeneous, unit-variance scene (b) simulated road scene

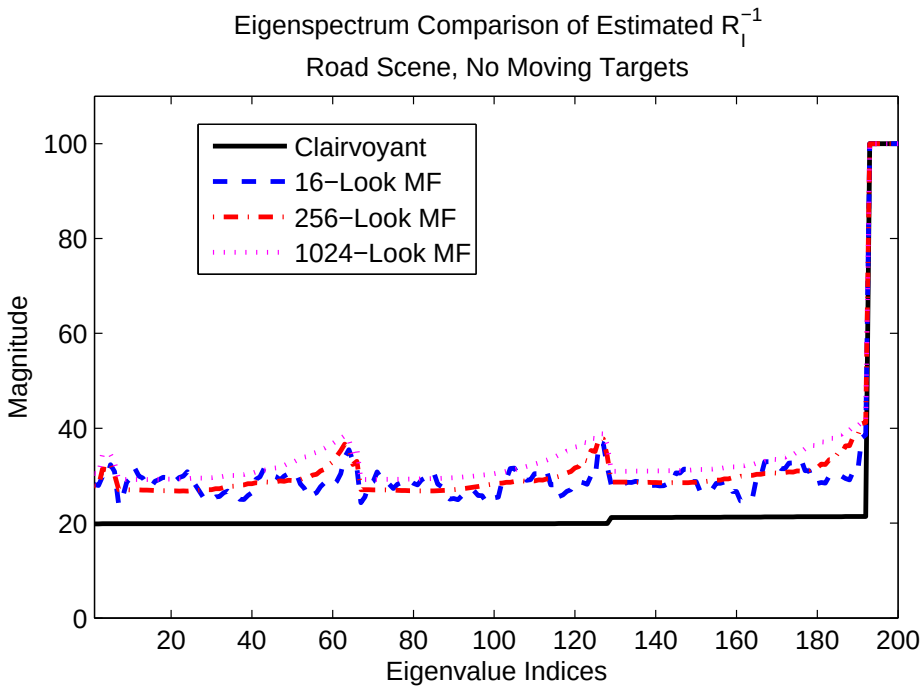

(a)

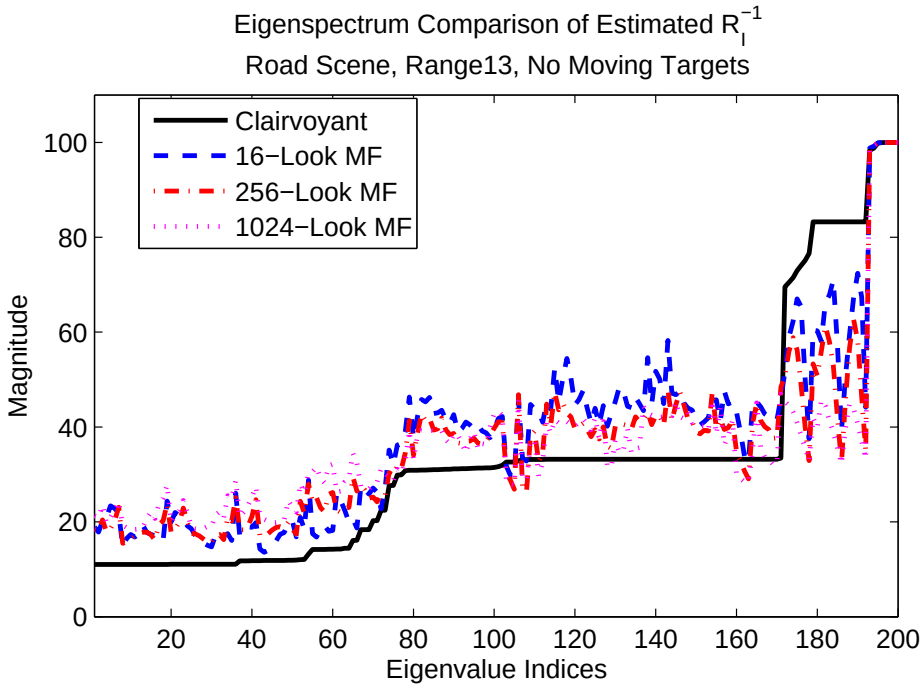

(b)

Figure 6.10. Close-up of the clutter subspace of the eigenspectra of the clairvoyant and MF estimated $\mathbf{R}_I^{-1}$ (a) homogeneous, unit-variance scene, (b) simulated road scene

widely used in image compression and smoothing.

Beginning with a full-resolution, single-look image, SAR images at multiple resolutions may be calculated, as shown in Figures 3.8 and 3.9. As shown in Figure 6.11, using these images in estimating the clutter spectrum in (2.30) result in good estimates of the inverse interference covariance matrix. These estimates of the inverse interference covariance matrix have less error than the estimates using multilook SAR, particularly for the homogeneous, unit-variance, white-Gaussian scene, as shown in Figure 6.11 (a).

Initially, one would think that a significant drawback to the DWT approach is the full-resolution image must first be calculated and then filtered. However, the Monte Carlo simulations to generate the multiple resolutions of the scattering spectra estimates in this research calculated the DWT-smoothed images much faster than the multilook SAR images. For the Monte Carlo simulations of 373 iterations, calculating the full-resolution, single-look SAR image and smoothing it with three different resolutions of DWT took around 14 minutes on a Quad Core, 3.0 GHz Xeon with 32 GB of RAM. The same scenario took almost 6.5 hours to estimate three different resolutions of multilook SAR images using the matched filter and 17 hours using maximum likelihood.

6.4 SMI Estimates of Interference Covariance Matrix

SMI STAP is computationally efficient compared to the proposed multiresolution GMTI approach. However, as discussed in Section 2.2.4, STAP using SMI assumes the scattering from the range-of-interest and the secondary ranges are homogeneous. This section demonstrates the effects of the homogeneous scattering assumption on estimating the interference covariance matrix for the same scenarios and radar pa-

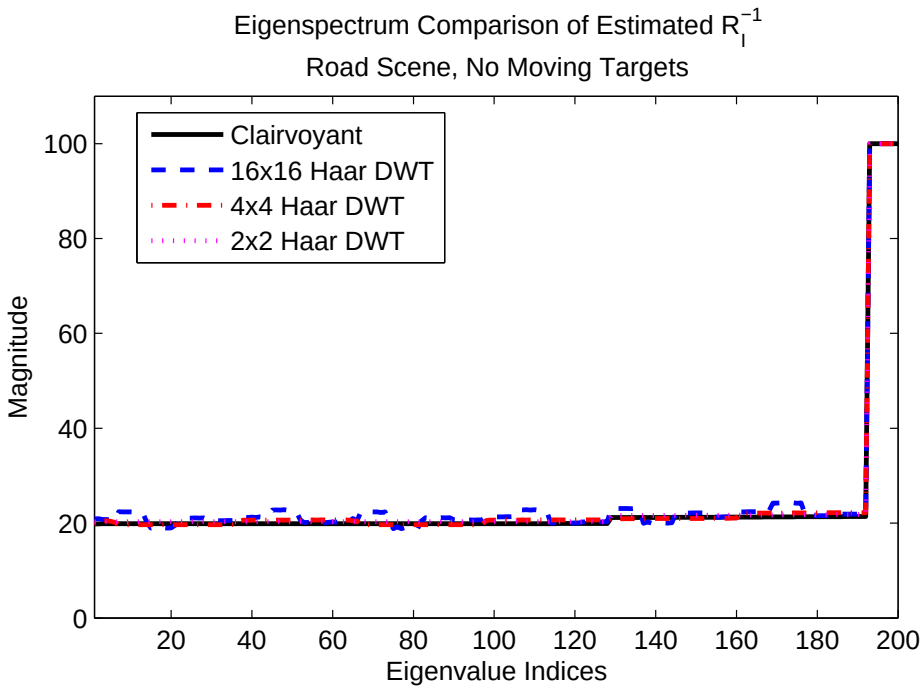

(a)

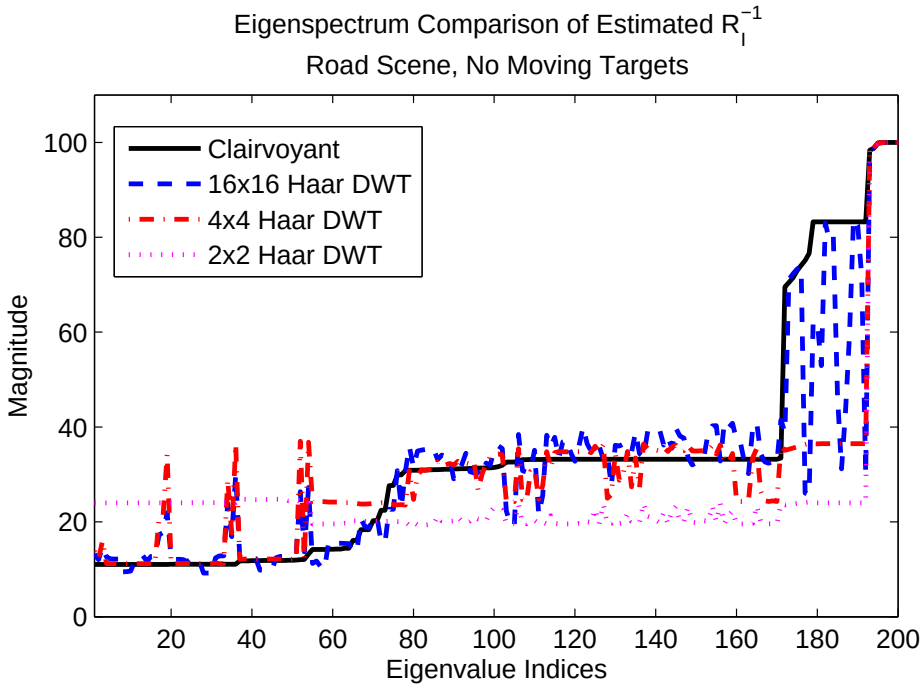

(b)

Figure 6.11. Comparison of eigenspectra for inverse covariance matrices estimated using back projection and intensity-squared image smoothed using multiple resolutions of Haar DWT

rameters presented in Section 6.1.

Section 5.4.2 discussed the impact of inflating the interference covariance matrix estimate for one range to represent three ranges in the whitening filter (2.23). Figure 5.8 compared eigenspectra for SMI estimated covariance matrices for one and three ranges, verifying that the rank of the whitening filter is not increased by inflating the estimate of $\mathbf{R}_I$ for one range to three ranges. Figures 6.12 and 6.13 show eigenanalyses of the inverse of the estimated interference covariance matrices for one and three range bins for a homogeneous scene and a heterogeneous scene (the road scene), respectively. These figures illustrate that the rank of the whitening filter for more than one range is limited to the rank of the whitening filter estimated for a single range. The subspace of the clutter not estimated by the single-range SMI estimate of $\mathbf{R}_I$ amounts to the clutter subspace of the two guard ranges, as defined in Section 2.2.4. The clutter energy from these guard ranges is not suppressed by the whitening filter and will likely degrade the GMTI performance. The plots in Figures 6.12 and 6.13 focus on the clutter subspace. Notice the difference in the eigenvalue indices between the single- and three-range estimates.

Figure 6.13 reinforces the observation in Section 2.2.4, that the eigenspectra of the SMI-estimated interference covariance matrices for structured clutter is spectrally white. Additionally, the eigenspectra may be biased by the measurements from the secondary ranges, this is especially evident in differences between the plots in Figure 2.11 and discussed in Section 2.2.4.

6.5 Effect of SAR Resolution on GMTI Performance

This chapter has demonstrated that using SAR images as estimates of the clutter spectrum in the in the optimum whitening filter can result in better estimates of the

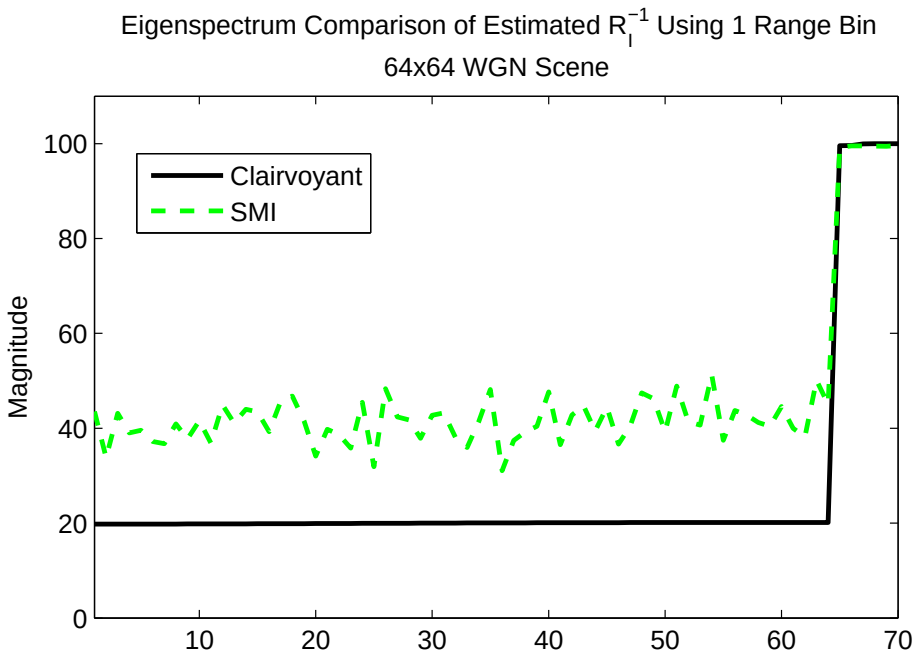

(a)

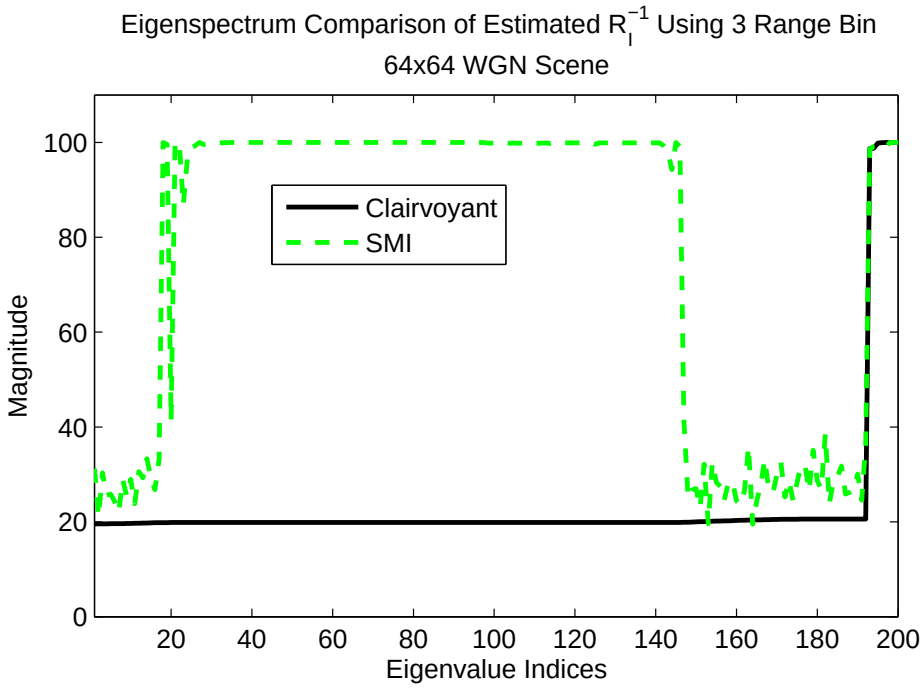

(b)

Figure 6.12. Eigenanalysis of road clutter subspace for homogeneous, unit-variance $\mathbf{R}_I^{-1}$ (a) estimated for one range bin (b) estimated for three range bins

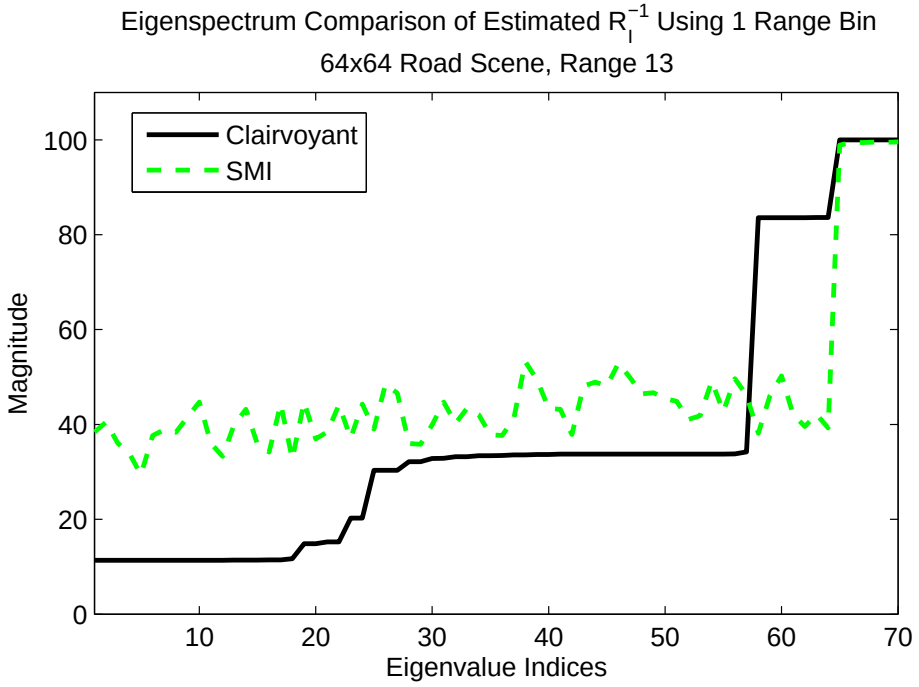

(a)

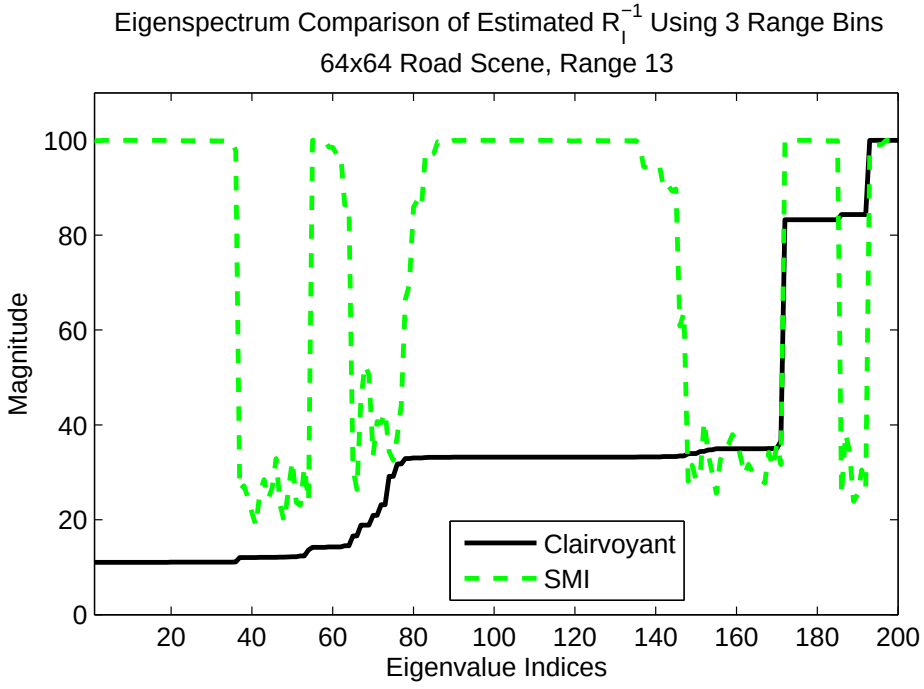

(b)

Figure 6.13. Eigenanalysis of road clutter subspace for SMI estimated $\mathbf{R}_I^{-1}$ (a) estimated for one range bin (b) estimated for three range bins

interference covariance matrix than the conventional SMI technique. This section discusses the ROC curves for moving targets with different scattering magnitudes, which is proportional to the radar cross section (RCS) of the moving target. As described in Section 6.1, the only differences between the scenarios in the following figures are the two scattering coefficient vectors $\boldsymbol{\gamma}$, one for the homogeneous, unit variance scene, and one for the simulated road scene; and the magnitude of the scattering coefficient of the moving target for each Monte Carlo run. The magnitude of the moving target's scattering coefficient is defined by the SCR of the scenario.

The ROC curves for GMTI using multilook SAR to estimate the scattering covariance matrix are included in Appendix A. It is significant to notice that the scenarios presented all have low SCR. The ROC curves were ideal in higher SCR scenarios for the MVM GMTI approach using SAR images, as they are ideal for the 3 dB SCR scenarios presented in Figures A.4 and A.5.

Figures 6.14-6.16 focus on the knee of the ROC curves for the zero decibel SCR scenario for both clutter scenes. Figure 6.14 compares the the ROC curves resulting from using maximum likelihood to estimate the multilook SAR images for the homogeneous scene in plot (a) and the road scene in plot (b). The GMTI performance in heterogeneous clutter in noticeably better than in the homogeneous clutter scenario. It also appears that the coarser spatial resolution multilook SAR estimate (1024-look SAR) resulted in slightly better performance in homogeneous scene than the finer spatial resolution multilook SAR estimates. The opposite is true for the road scene, which supports the original hypothesis that the desired spatial resolution estimate of the clutter spectrum depends on the expected spectrum–there is not a single spatial resolution that performs *best* for all scenarios.

In general, the matched filter estimate of the clutter spectrum resulted in lower

ROC curves than the maximum likelihood ROC curves, as seen by comparing Figures 6.14 and 6.15. Interestingly, the finer spatial resolution multilook SAR estimate (16-look SAR) resulted in better performance for both clutter scenes. Recalling Figure 6.10, the bias in the clutter spectrum of the inverse estimate of the interference covariance matrix was less for the finer spatial resolutions.

As expected from the analysis Figure 6.11, the DWT-smoothed, single-look SAR image resulted in ROC curves much closer to the ROC curve due to the clairvoyantly estimated interference covariance matrix. In fact, the results for the homogeneous scene appear to slightly outperform the clairvoyant estimator in Figure 6.11 (a). The effect of the clutter spectrum estimate is evident in the heterogeneous scene where the finer spatial resolution spectral estimate narrowly outperforms the coarser spatial resolution spectral estimate in Figure 6.11 (b). The middle spatial resolution estimate performed the worst of the three estimators, but it still outperformed all the multilook SAR estimators.

6.6 Multiresolution GMTI Performance

The hypothesis presented in the Introduction was that low-resolution SAR images would better estimate the clutter spectrum of homogeneous regions. Figures 6.17-6.20 are a series of plots comparing the ROCs of the different multiresolution GMTI approaches to each other and to SMI. In each figure, plot (a) shows the entire ROC for the clairvoyant GMTI processor, multiresolution GMTI processor using multilook SAR estimated via maximum likelihood, multiresolution GMTI processor using multilook SAR estimated via matched filter, multiresolution processor using multiple resolutions of DWT-smoothed SAR image, and SMI. Plot (b) in each figure is a close up of the same ROC curves in plot (a) of the same figure.

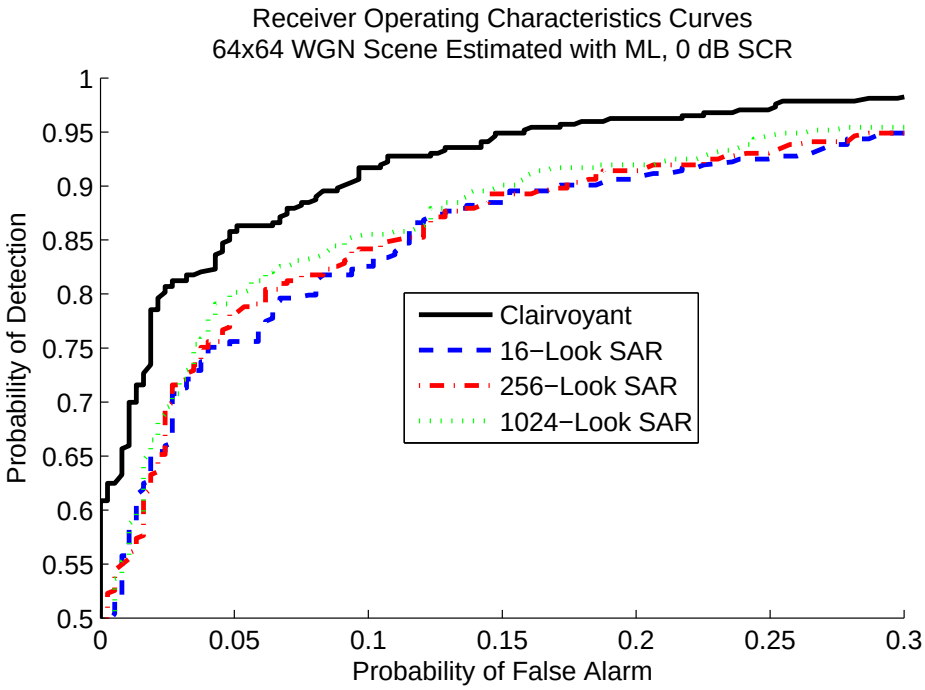

(a)

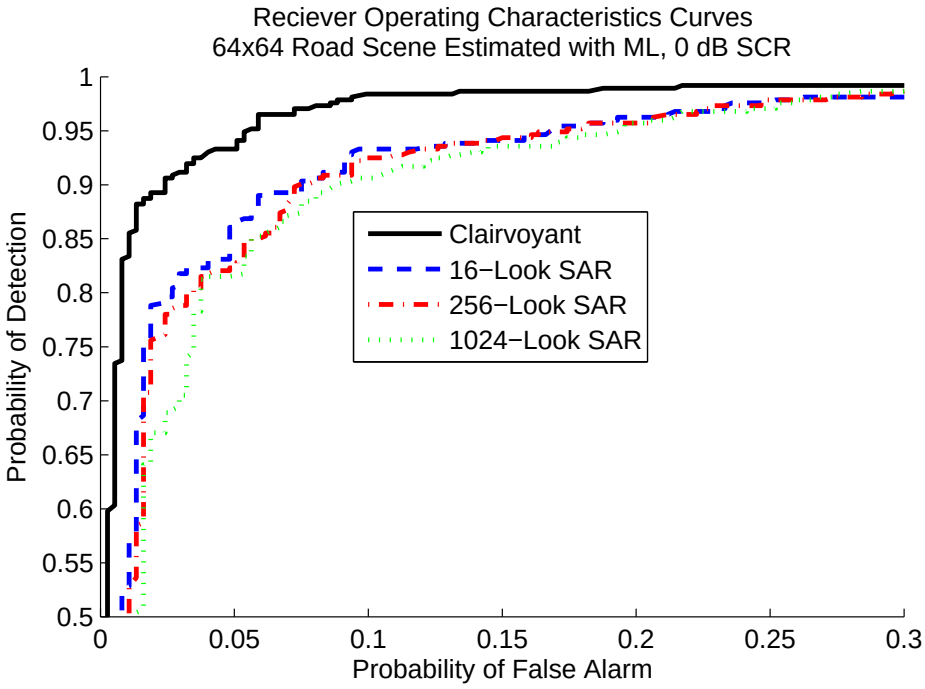

(b)

Figure 6.14. ROCs for MVM GMTI detector using ML to estimate multiple, multilook SAR images, SCR = 0 dB (a) homogeneous, unit-variance scene (b) road scene

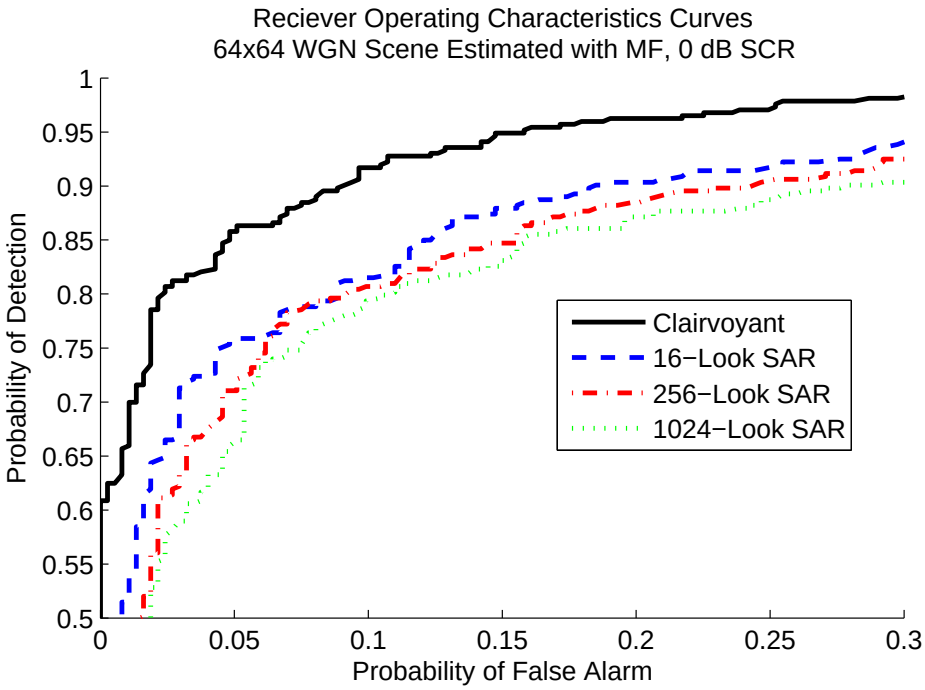

(a)

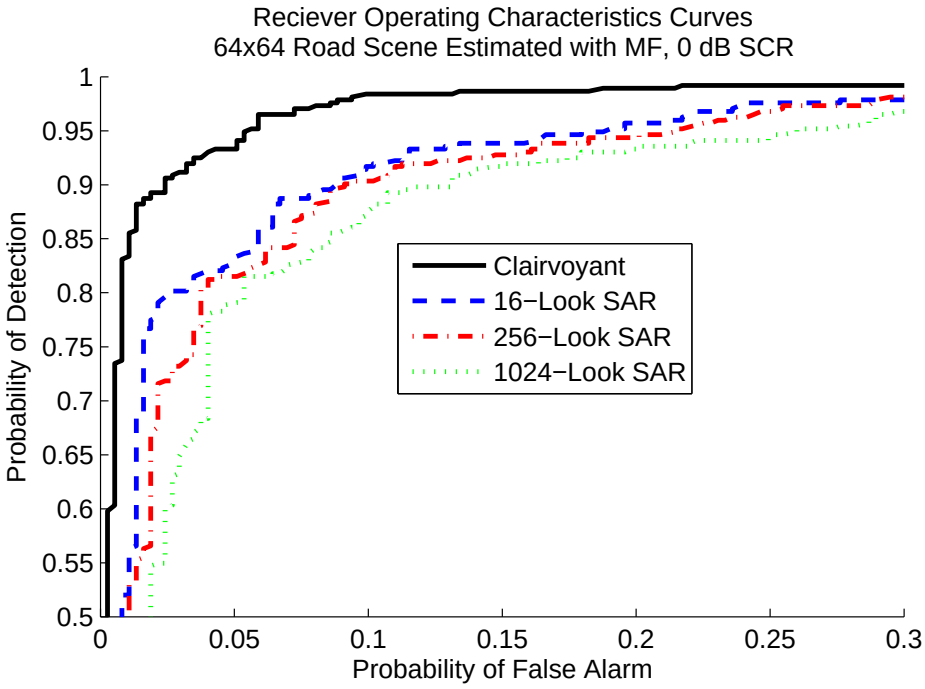

(b)

Figure 6.15. ROCs for MVM GMTI detector using MF to estimate multiple, multilook SAR images, SCR = 0 dB (a) homogeneous, unit-variance scene (b) road scene

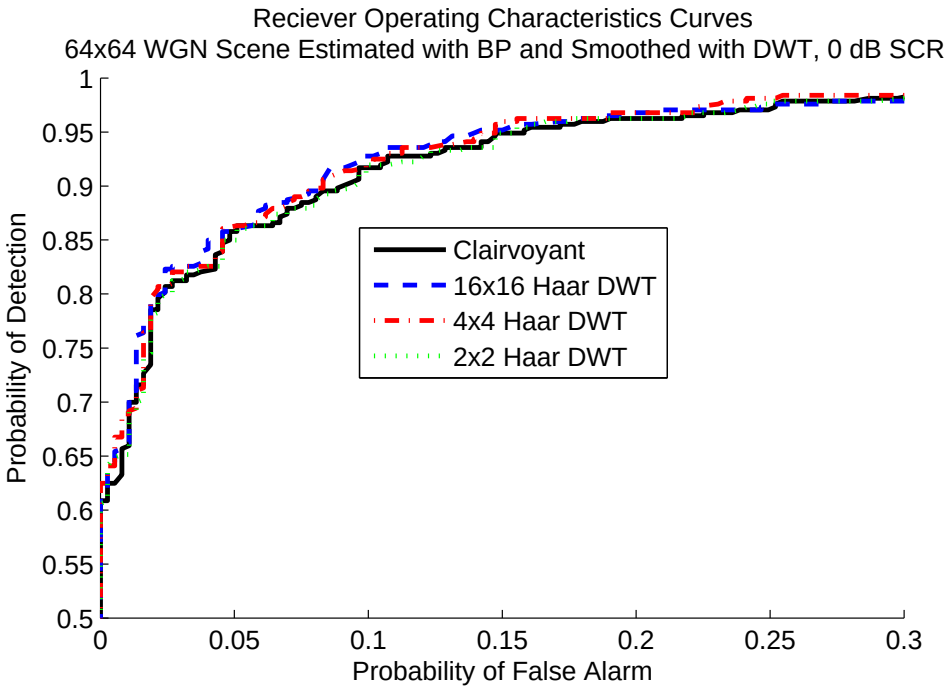

(a)

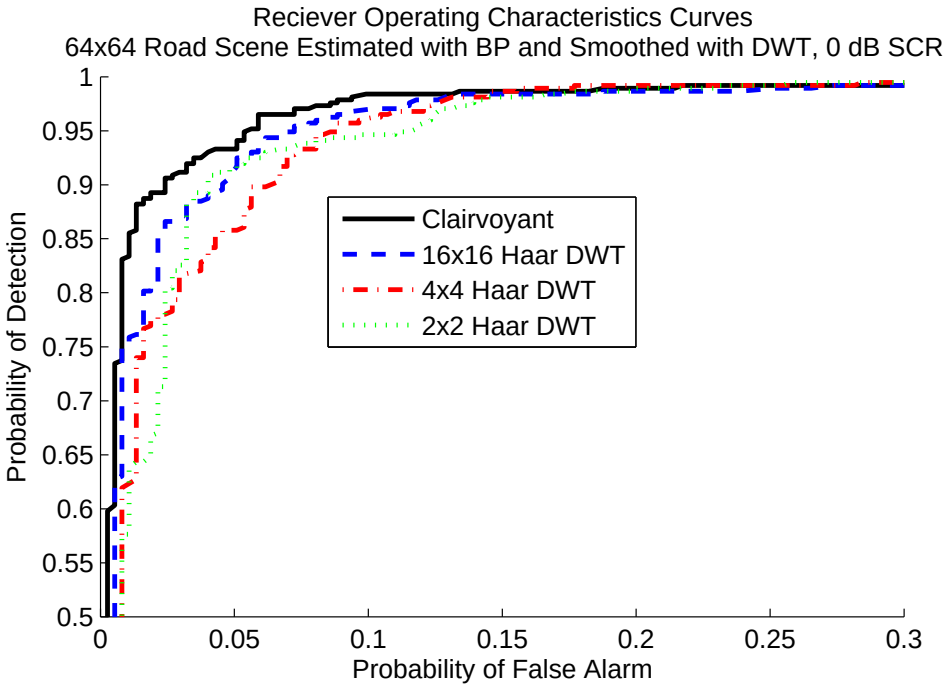

(b)

Figure 6.16. ROCs for MVM GMTI detector using DWT-smoothed SAR images, SCR = 0 dB (a) homogeneous, unit-variance scene (b) road scene

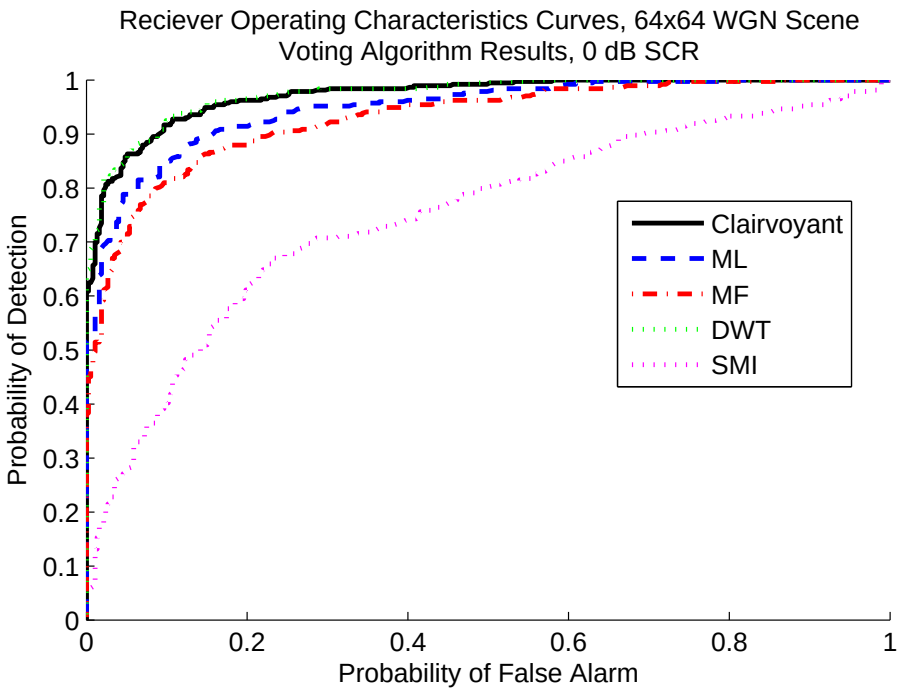

(a)

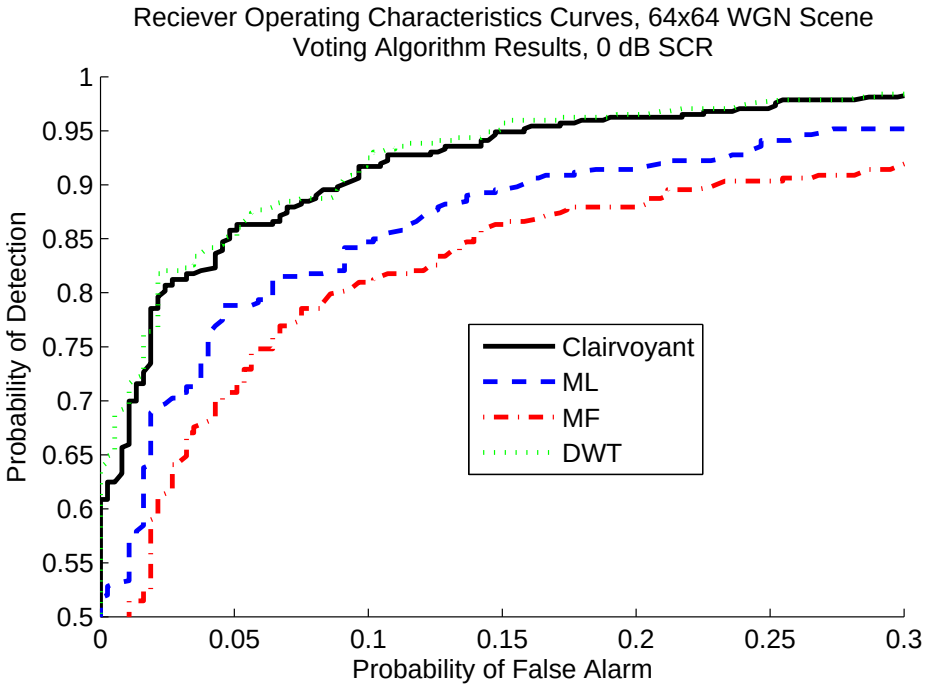

(b)

Figure 6.17. ROCs for MVM GMTI detector using voting fusion algorithm for WGN scene, SCR = 0 dB (a) fusion and SMI (b) close-up of fusion

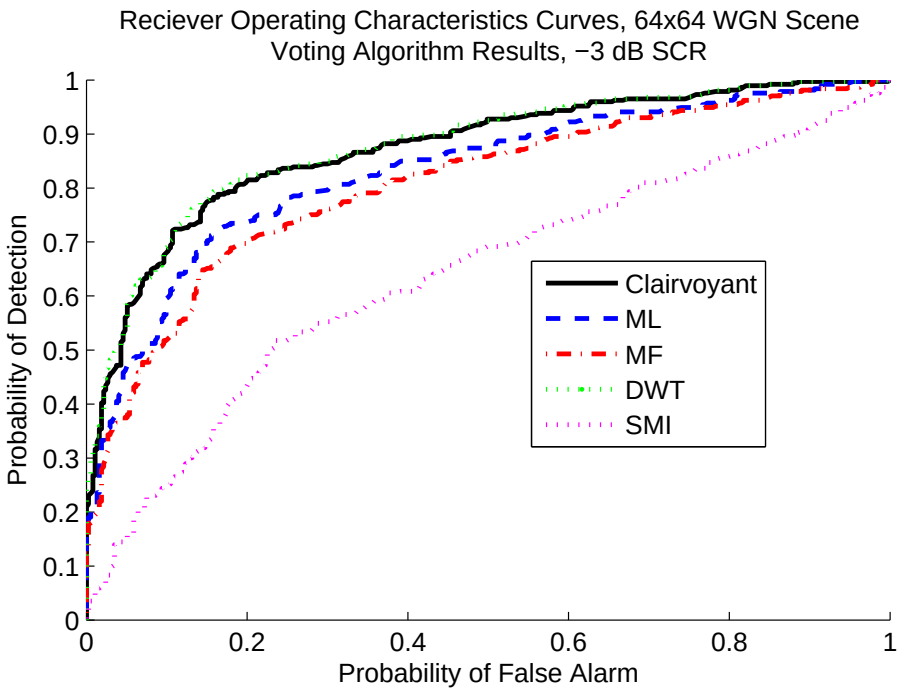

(a)

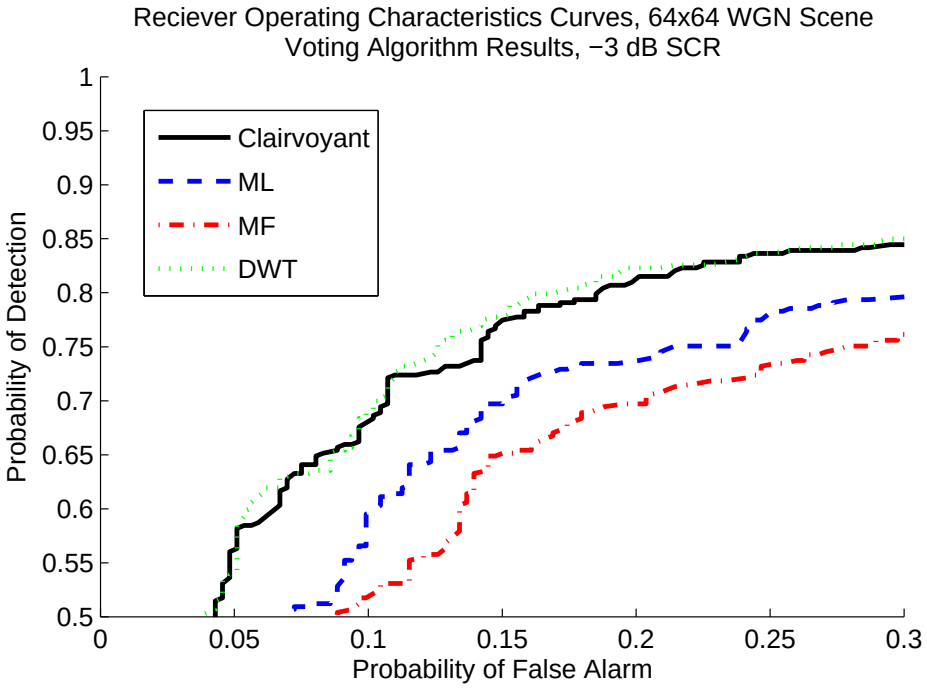

(b)

Figure 6.18. ROCs for MVM GMTI detector using voting fusion algorithm for WGN scene, SCR = -3 dB (a) fusion and SMI (b) close-up of fusion

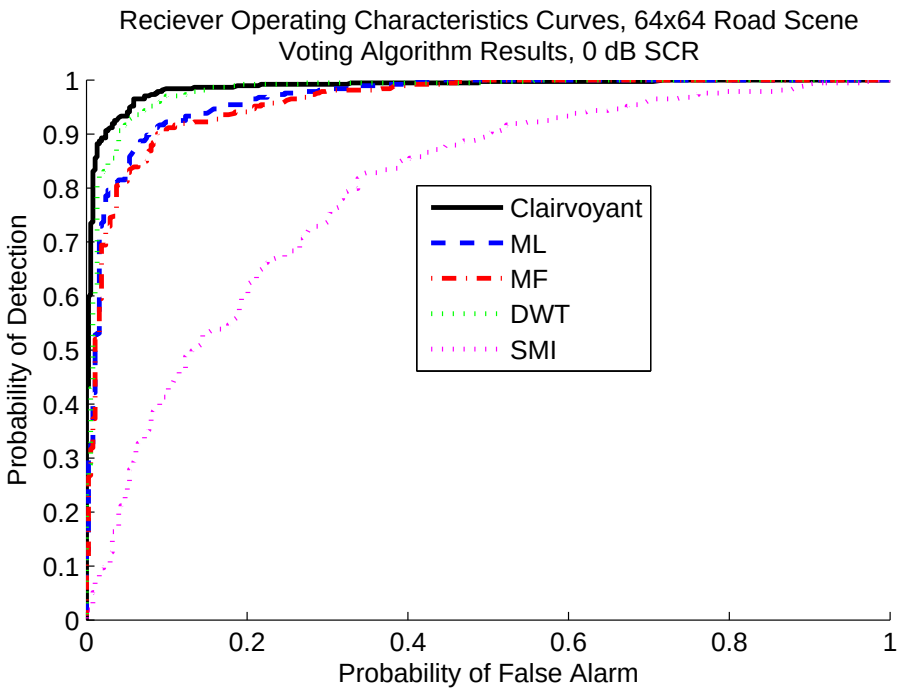

(a)

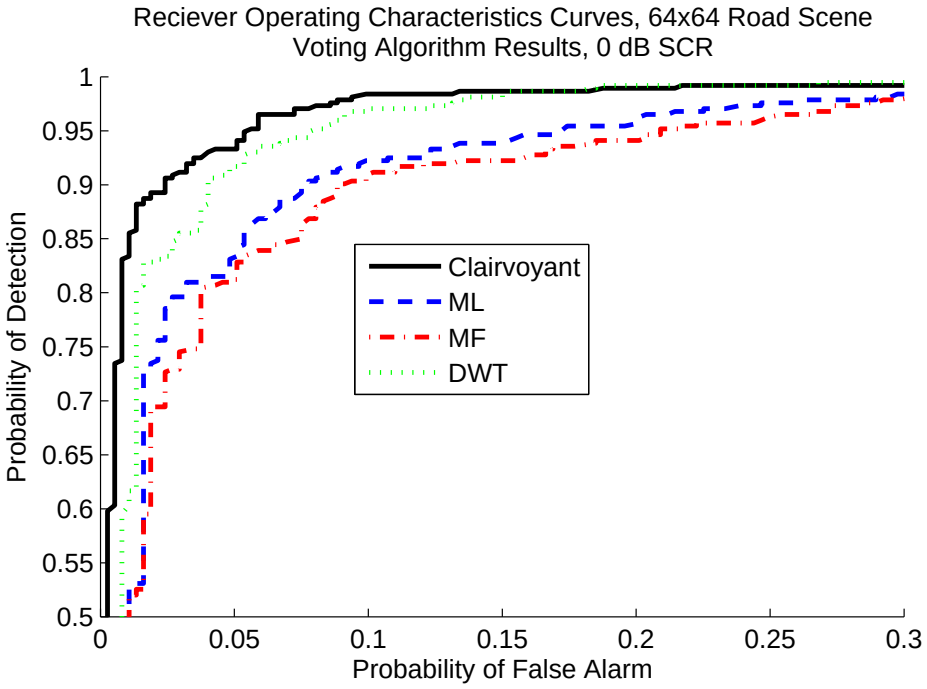

(b)

Figure 6.19. ROCs for MVM GMTI detector using voting fusion algorithm for road scene, SCR = 0 dB (a) fusion and SMI, (b) close-up of fusion

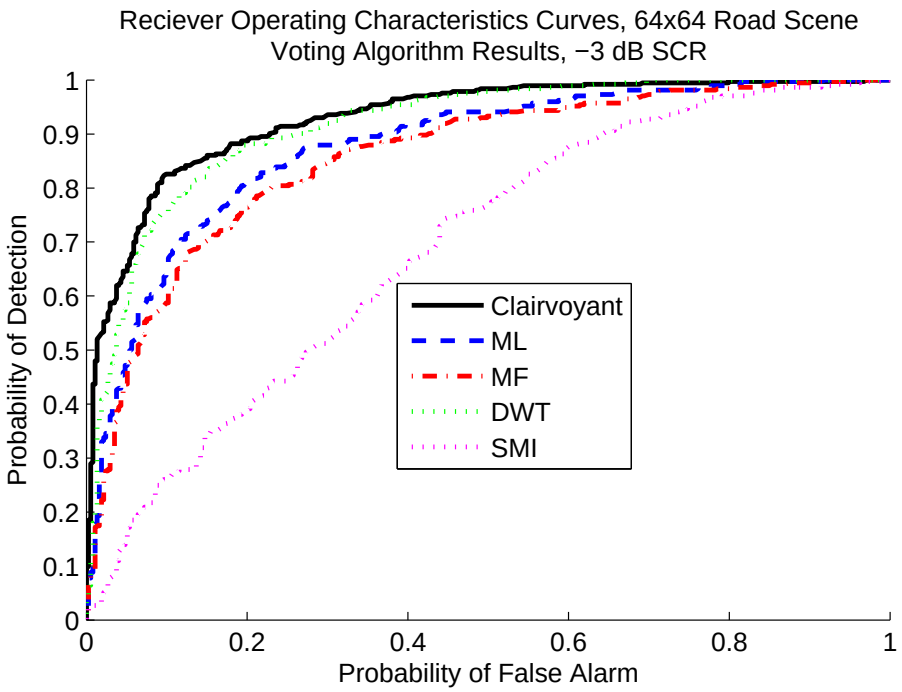

(a)

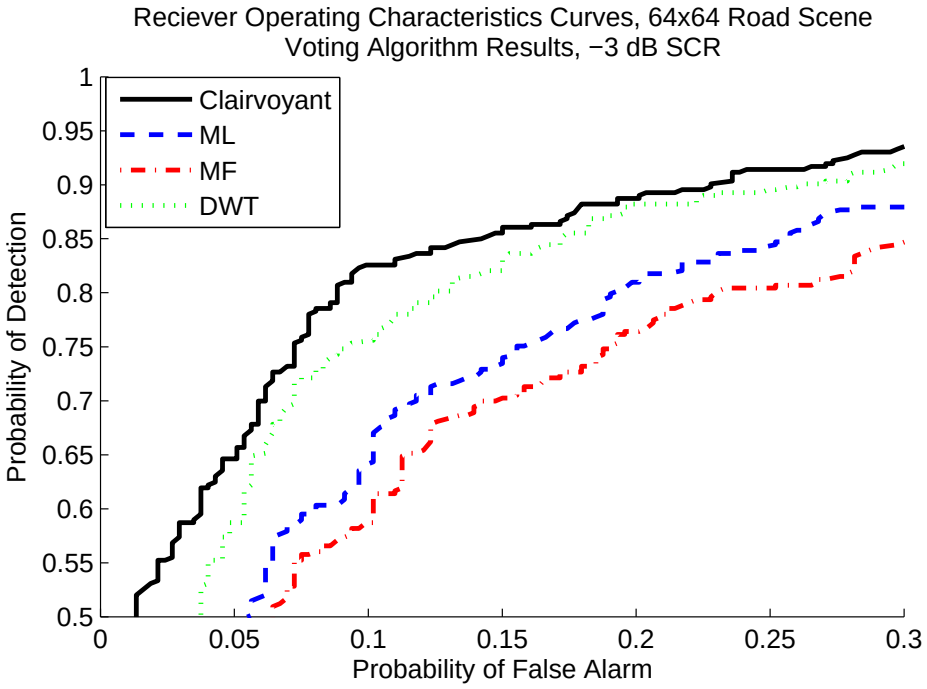

(b)

Figure 6.20. ROCs for MVM GMTI detector using voting fusion algorithm for road scene, SCR = -3 dB (a) fusion and SMI, (b) close-up of fusion

Chapter 7

Conclusions

The proposed approach to multiresolution ground moving target indication (GMTI) performs much better than conventional sample matrix inversion (SMI) space-time adaptive processing (STAP) at the expense of computational complexity. The multiresolution aspect of the multiresolution GMTI comes from multiple resolutions of an intensity-squared SAR image used to estimate the clutter scattering spectrum in the optimal GMTI processor (2.23).

Two approaches to calculating the different resolutions of the SAR image were investigated. The first approach used multilook SAR to increase the estimation accuracy of the clutter scattering spectrum at the expense of spatial resolution. The multilook SAR images were calculated from individual segments of the measurement vector partitioned using synthetic sensor locations. The size and number of the segments determined the spatial resolution and estimation accuracy of the images.

The second approach to calculating the different resolutions of the SAR image was smoothing a single-look SAR image using multiple stages of a Haar wavelet discrete wavelet transform (DWT). The DWT smoothed single-look SAR images better estimated the scattering covariance matrix than the multilook SAR images, and thus resulted in better GMTI performance. Additionally, the DWT smoothed image approach was more than an order-of-magnitude faster than the fastest multilook SAR approach investigated.

The multiresolution SAR approaches to estimating the clutter spectrum for the optimum GMTI processor is more computationally expensive than SMI. However, the approach produces much better receiver operating characteristics, as demonstrated in Chapter 6. One consolation to calculating multiple SAR images is that each image may be used in the GMTI whitening filter for potential targets at all ranges. SMI STAP estimates a new interference covariance matrix for every new range under test.

Finally, the multiresolution approach to GMTI is robust, in that it performs better than any single resolution GMTI processor for the homogeneous and heterogeneous scenarios investigated. However, the computational burden of calculating individual detection decisions for each clutter scattering spectral resolution must be considered prior to implementation.

Appendix A

ROC Curves From Multilook SAR GMTI

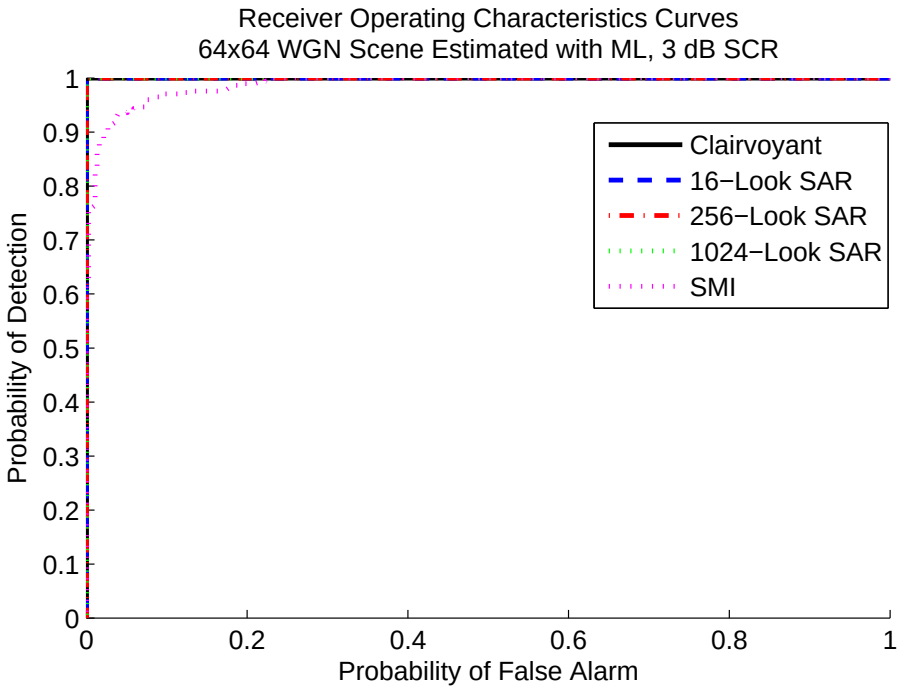

(a)

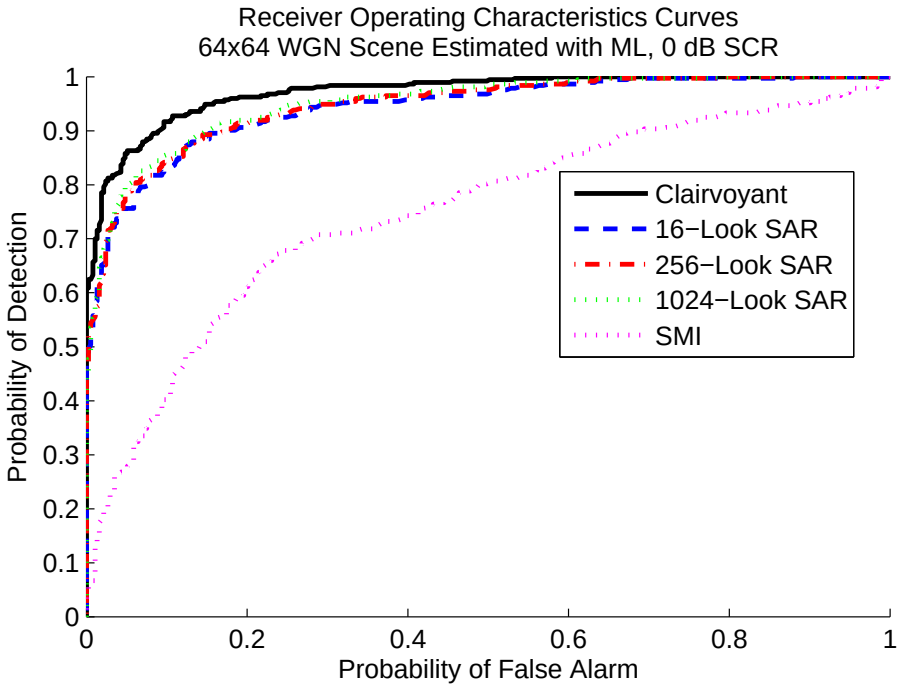

(b)

Figure A.1. ROCs for MVM GMTI detector using ML to estimate multiple multilook SAR images of homogeneous, unit-variance scene (a) SCR = 3 dB, (b) SCR = 0 dB. Note: All 3 dB SCR ML ROCs are ideal

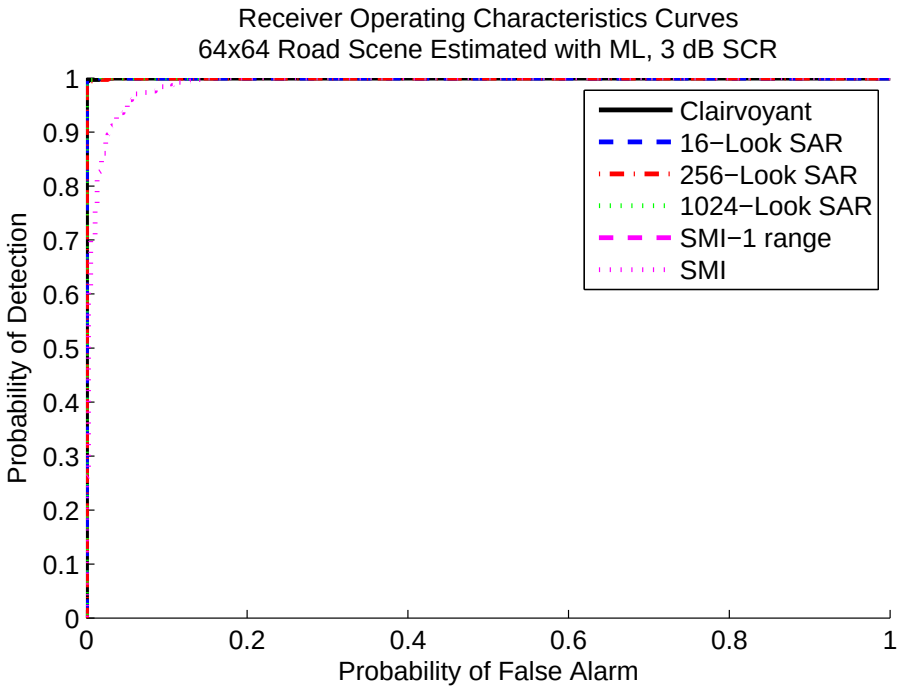

(a)

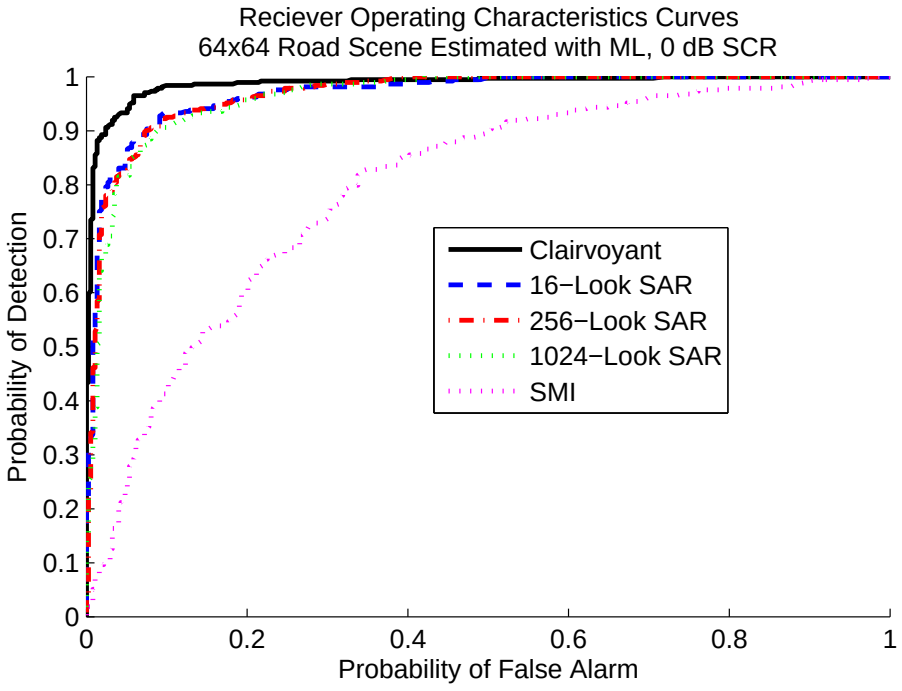

(b)

Figure A.2. ROCs for MVM GMTI detector using ML to estimate multiple multilook SAR images of road scene (a) SCR = 3 dB, (b) SCR = 0 dB. Note: All 3 dB SCR ML ROCs are ideal

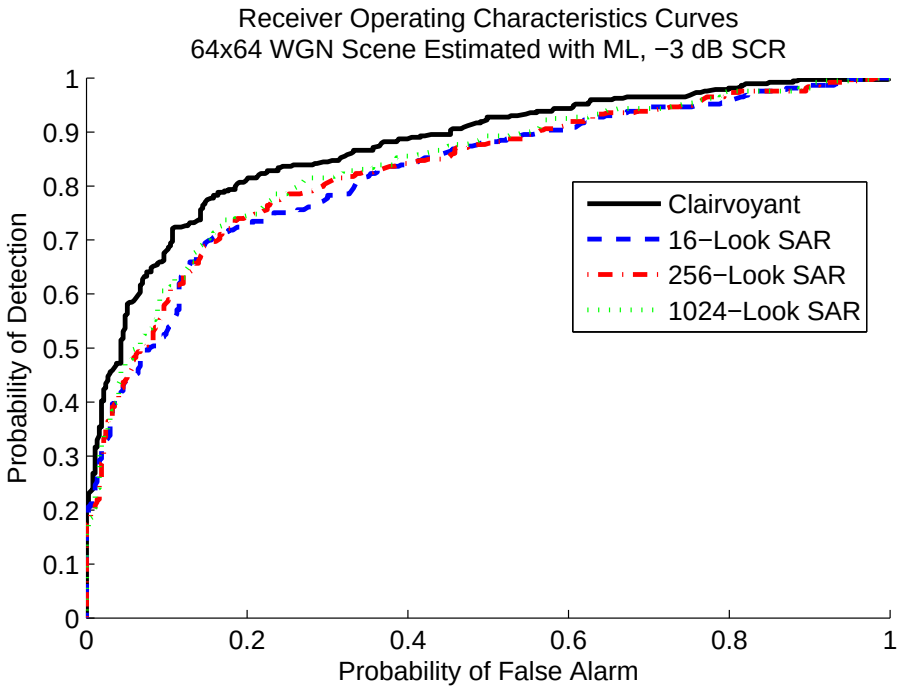

(a)

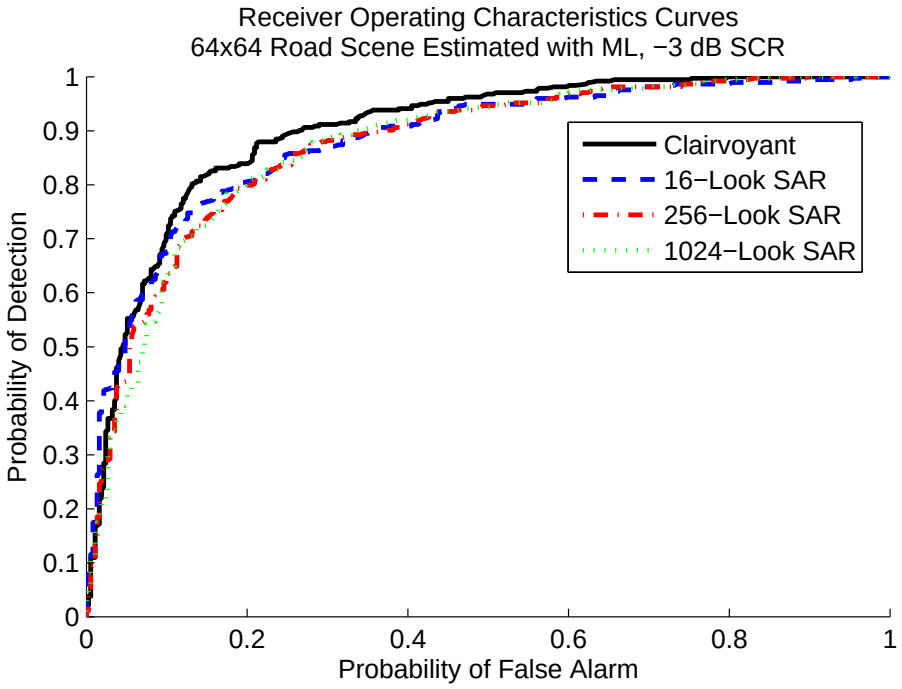

(b)

Figure A.3. ROCs for MVM GMTI detector using ML to estimate multiple multilook SAR images, SCR = -3 dB (a) WGN scene, (b) road scene

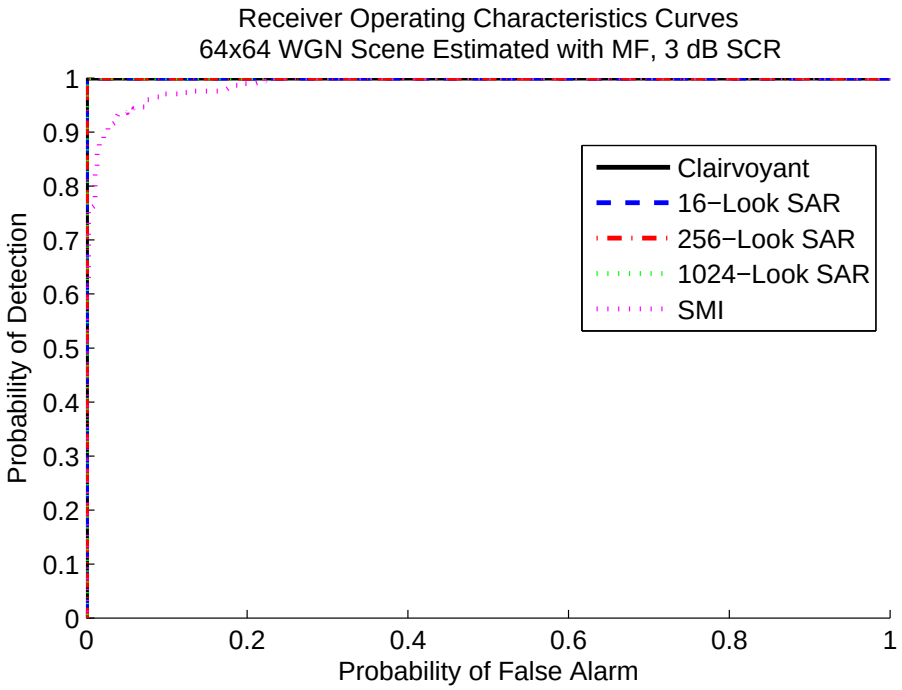

(a)

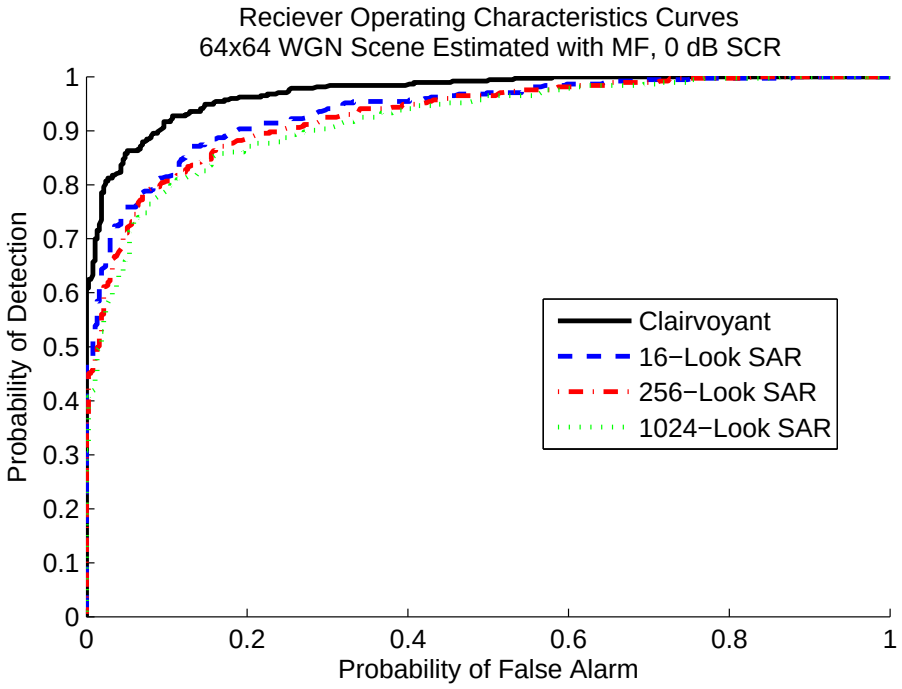

(b)

Figure A.4. ROCs for MVM GMTI detector using MF to estimate multiple multilook SAR images of homogeneous, unit-variance scene (a) SCR = 3 dB, (b) SCR = 0 dB. Note: All 3 dB SCR MF ROCs are ideal

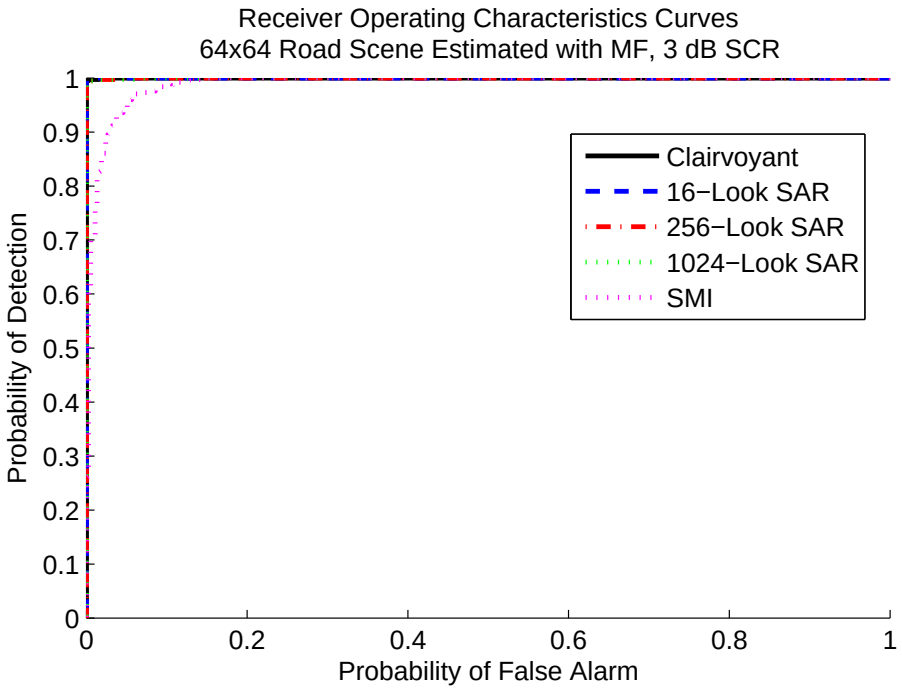

(a)

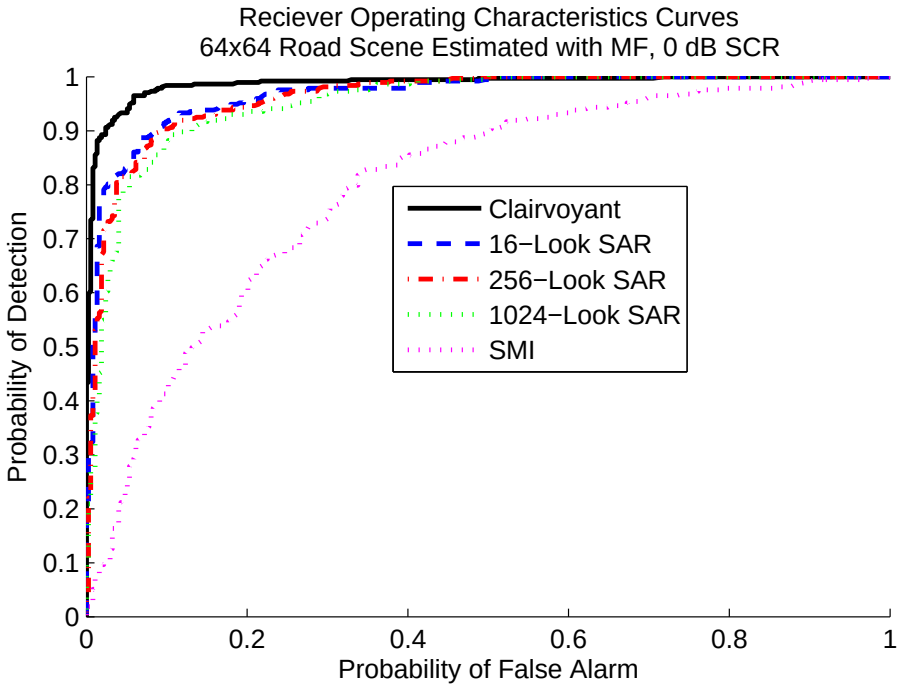

(b)

Figure A.5. ROCs for MVM GMTI detector using MF to estimate multiple multilook SAR images of road scene (a) SCR = 3 dB, (b) SCR = 0 dB. Note: All 3 dB SCR MF ROCs are ideal

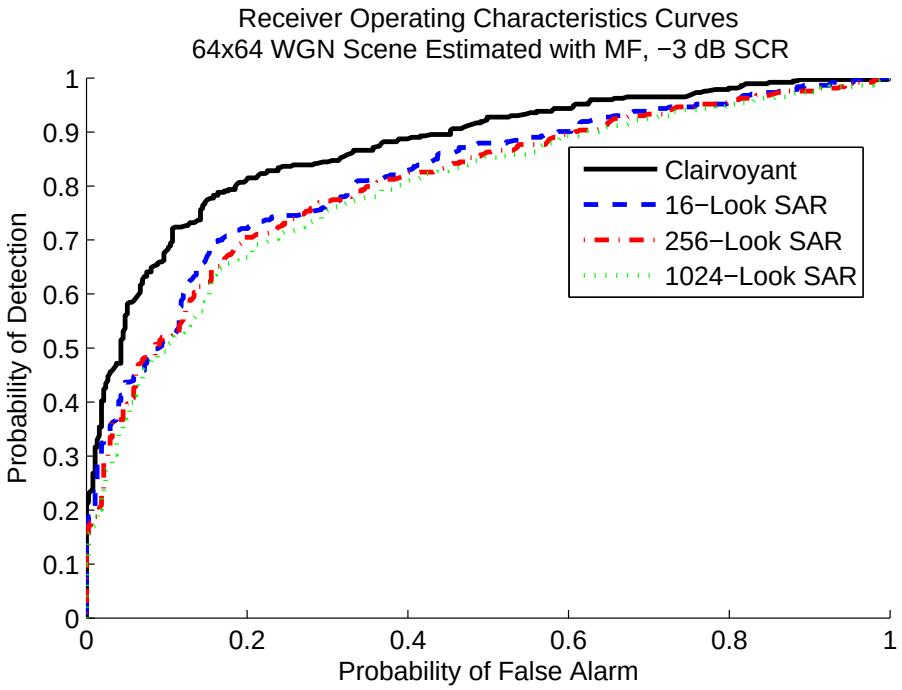

(a)

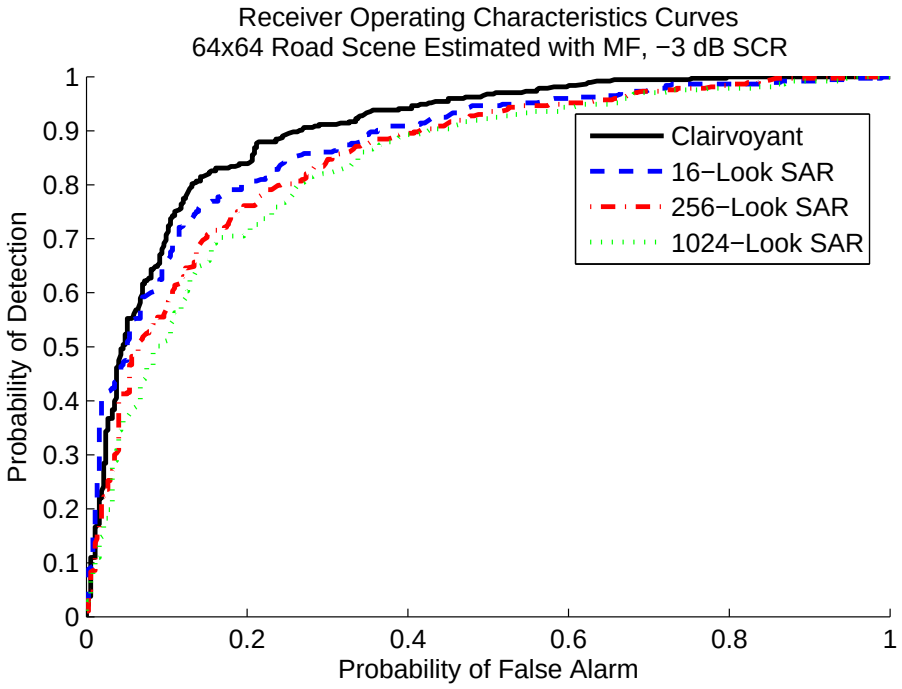

(b)

Figure A.6. ROCs for MVM GMTI detector using MF to estimate multiple multilook SAR images, SCR = -3 dB (a) WGN scene, (b) road scene

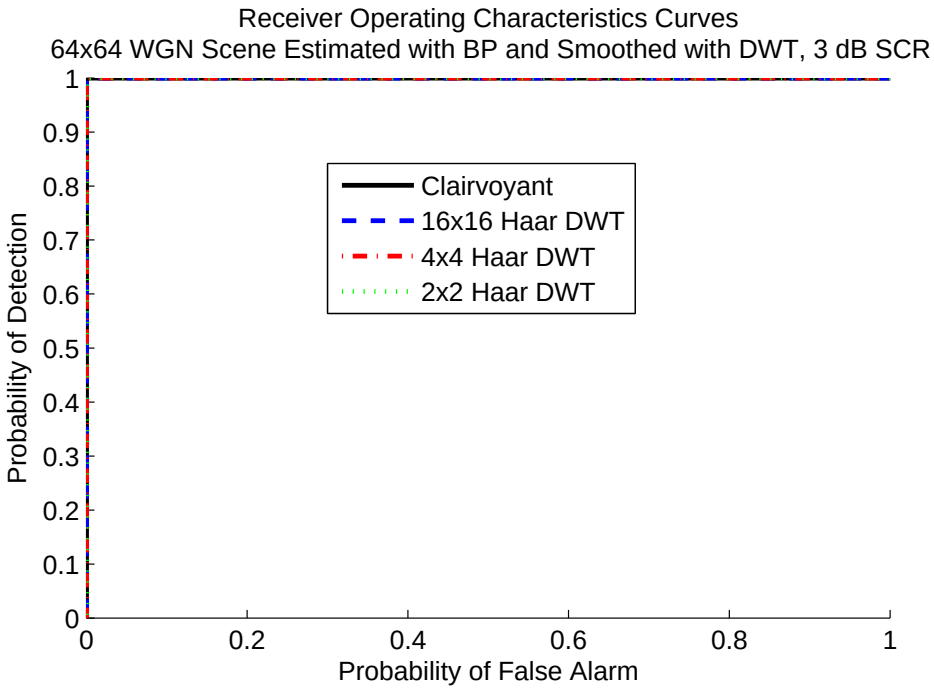

(a)

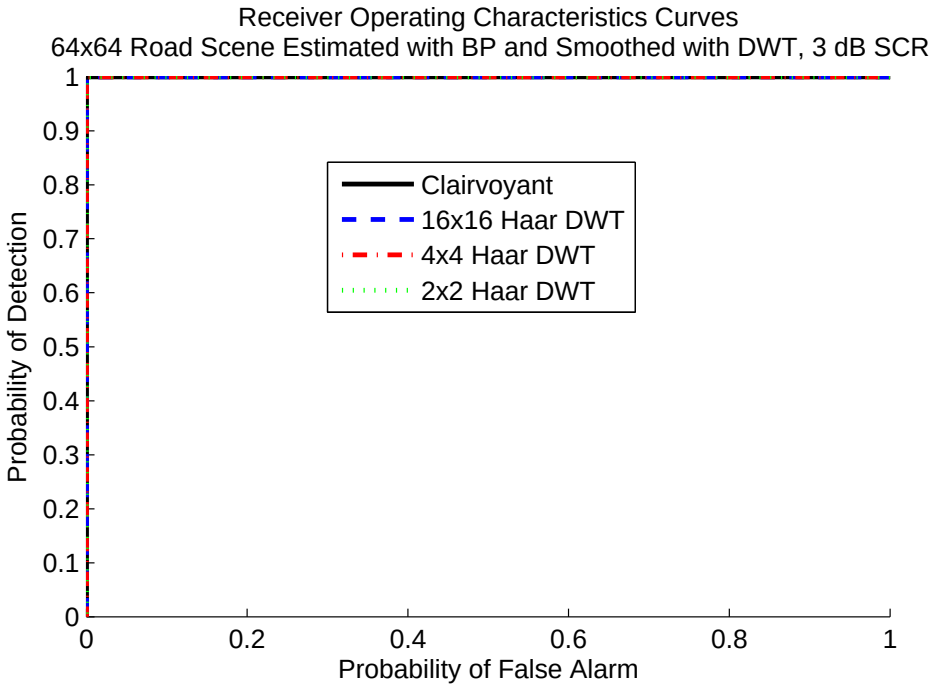

(b)

Figure A.7. ROCs for MVM GMTI detector using DWT-smoothed SAR images, SCR = 3 dB (a) WGN scene, (b) road scene. Note: All ROCs are ideal

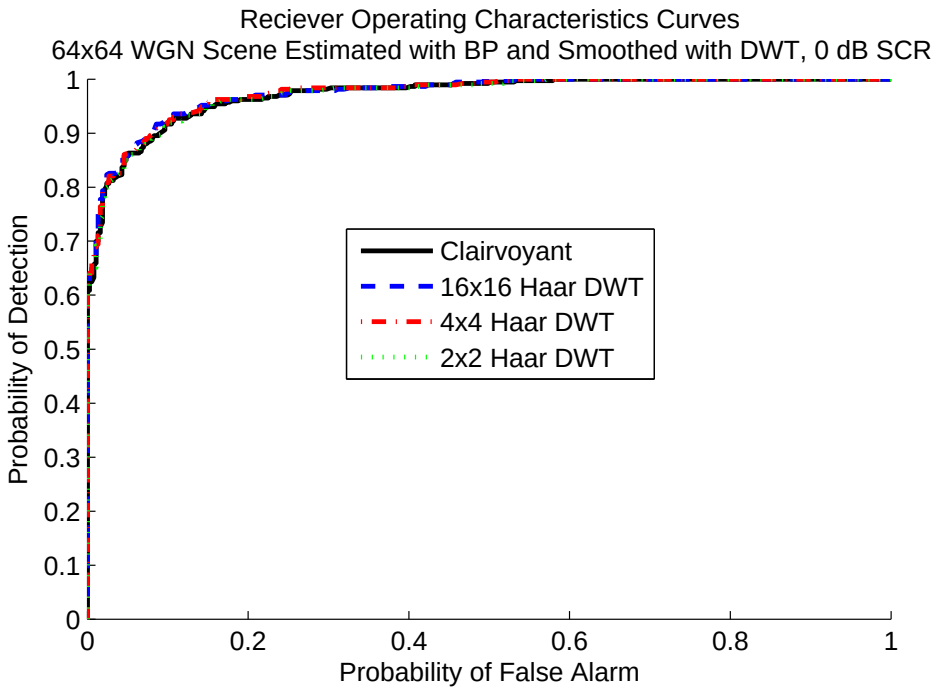

(a)

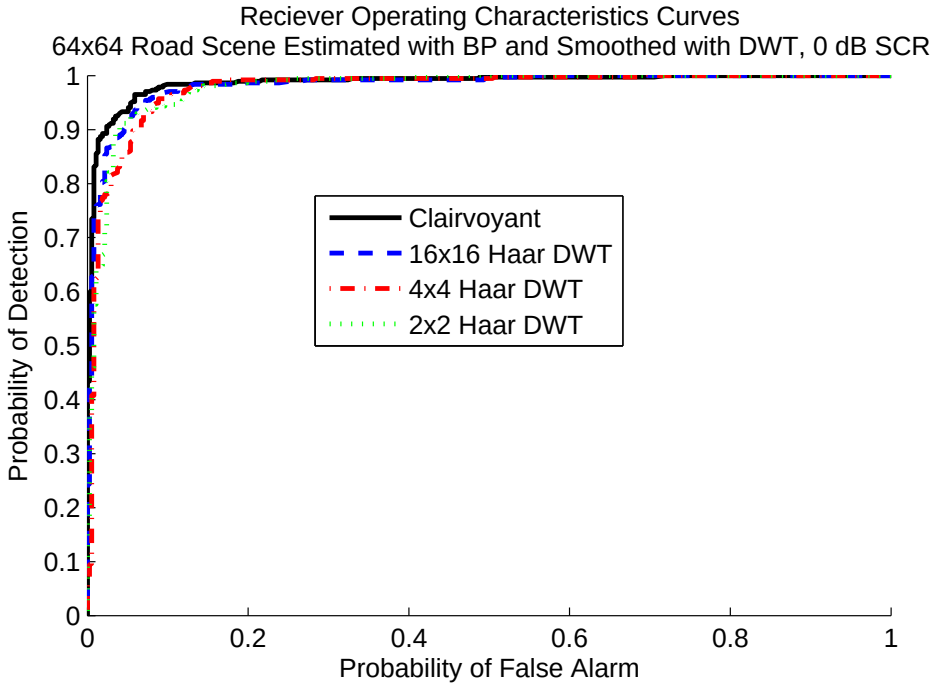

(b)

Figure A.8. ROCs for MVM GMTI detector using DWT-smoothed SAR images, SCR = 0 dB (a) WGN scene, (b) road scene

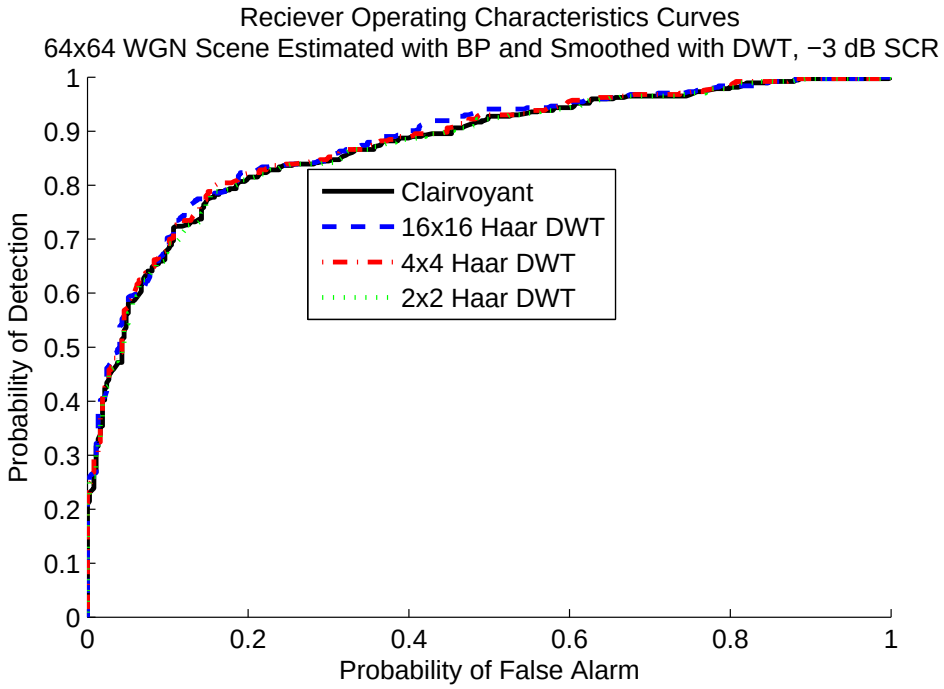

(a)

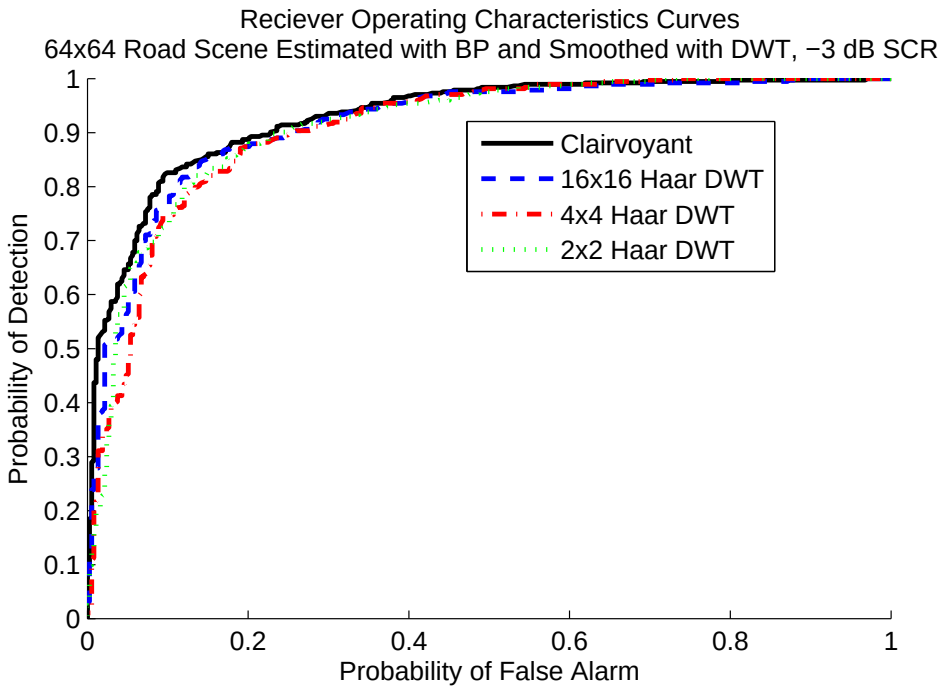

(b)

Figure A.9. ROCs for MVM GMTI detector using DWT-smoothed SAR images, SCR = -3 dB (a) WGN scene, (b) road scene

Appendix B

ROC Curves From Voting Algorithms

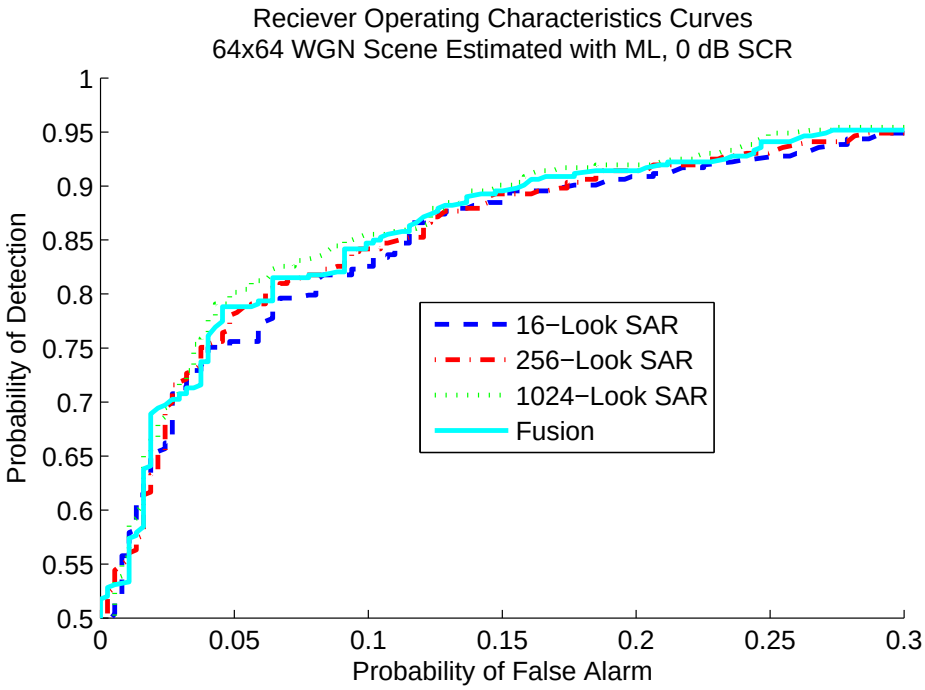

(a)

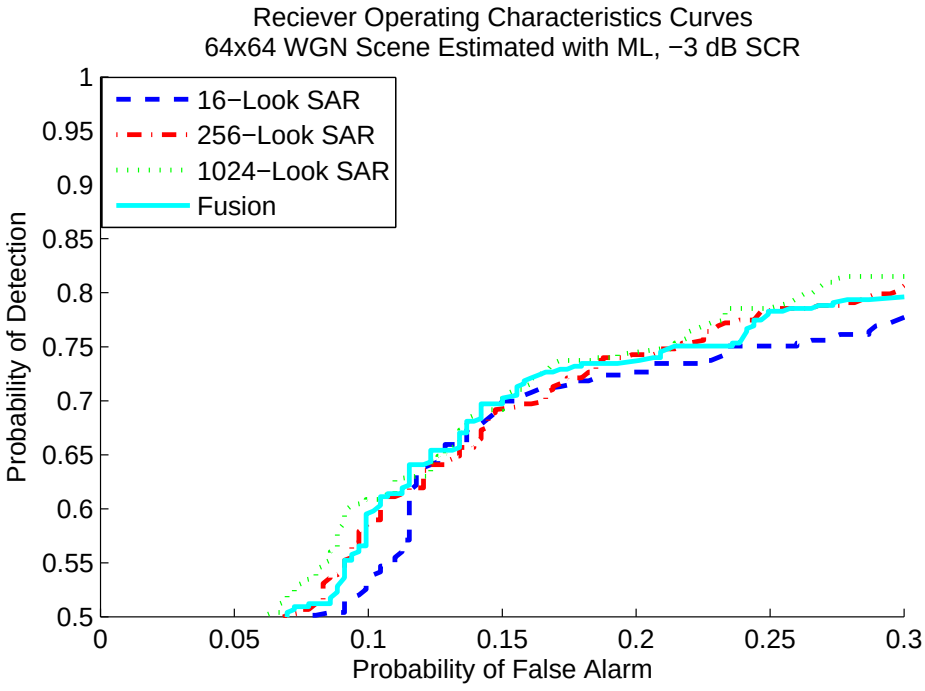

(b)

Figure B.1. ROCs for MVM GMTI detector using voting fusion algorithm and ML estimated multilook SAR images of homogeneous, unit-variance scene (a) SCR = 0 dB, (b) SCR = -3 dB

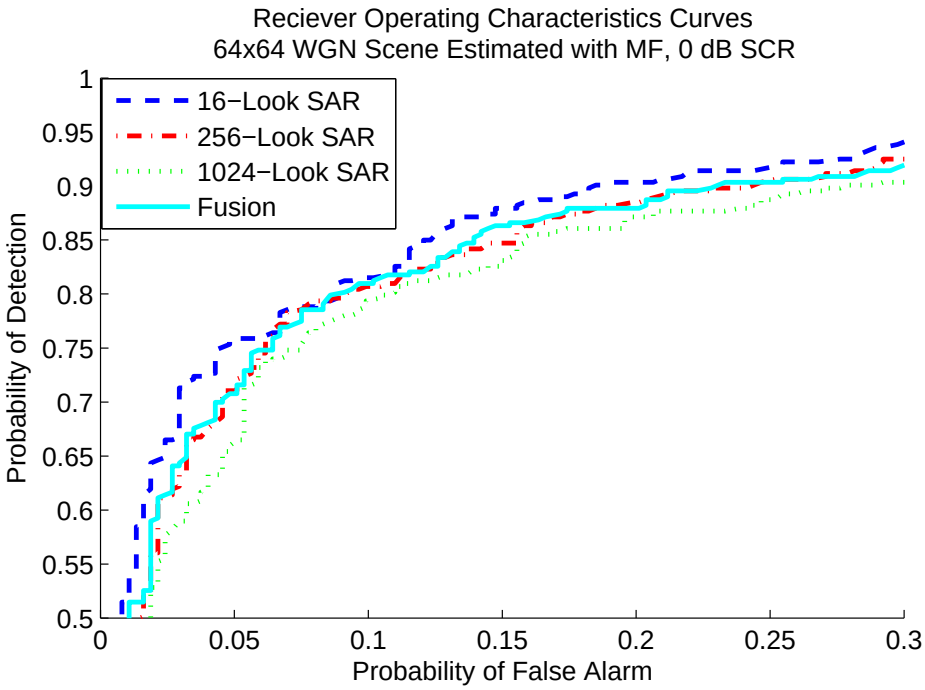

(a)

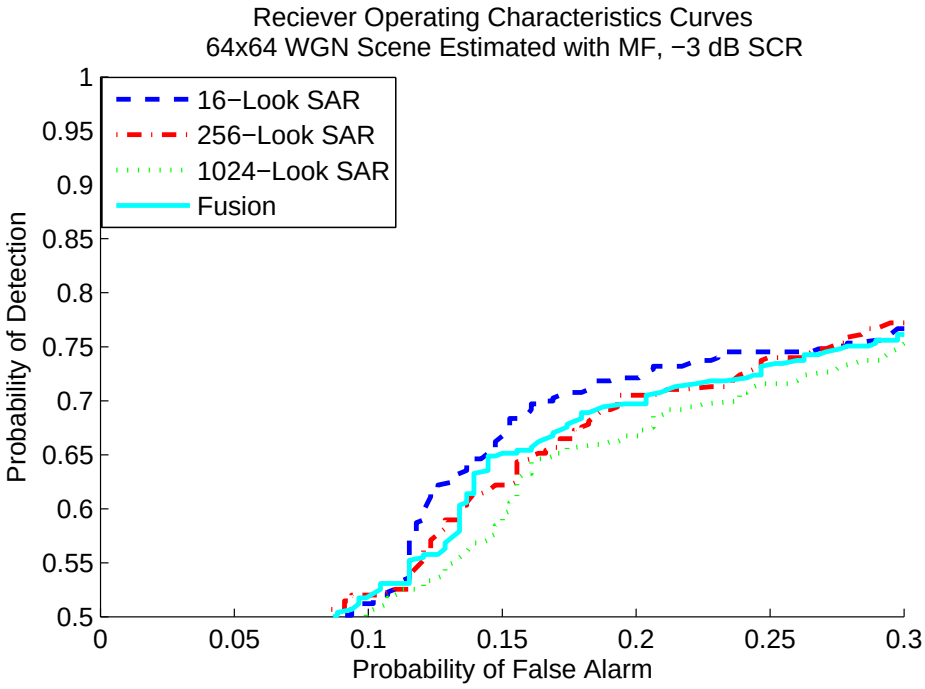

(b)

Figure B.2. ROCs for MVM GMTI detector using voting fusion algorithm and MF estimated multilook SAR images of homogeneous, unit-variance scene scene (a) SCR = 0 dB, (b) SCR = -3 dB

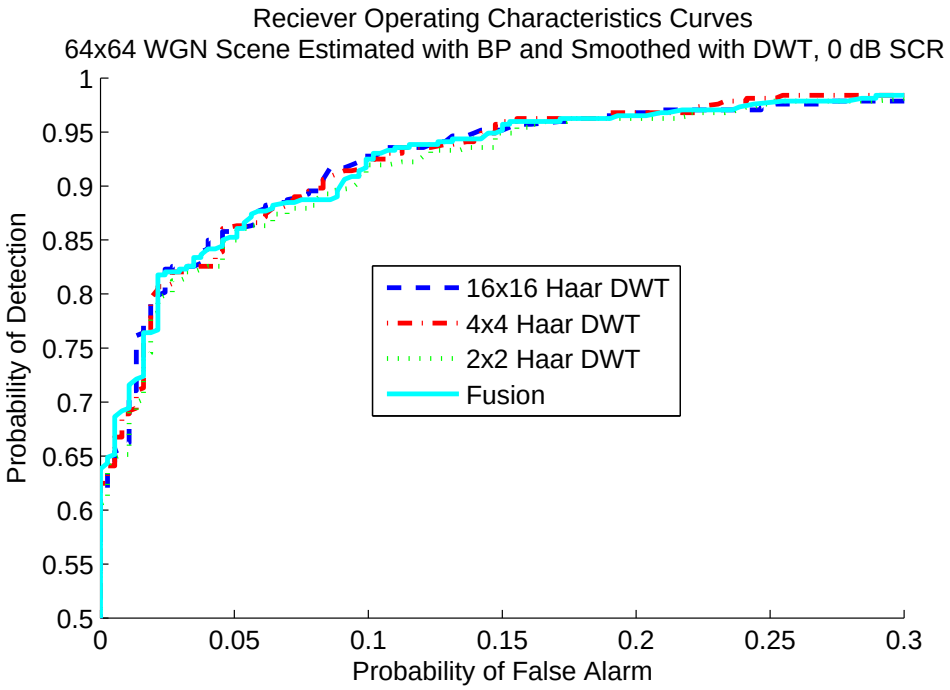

(a)

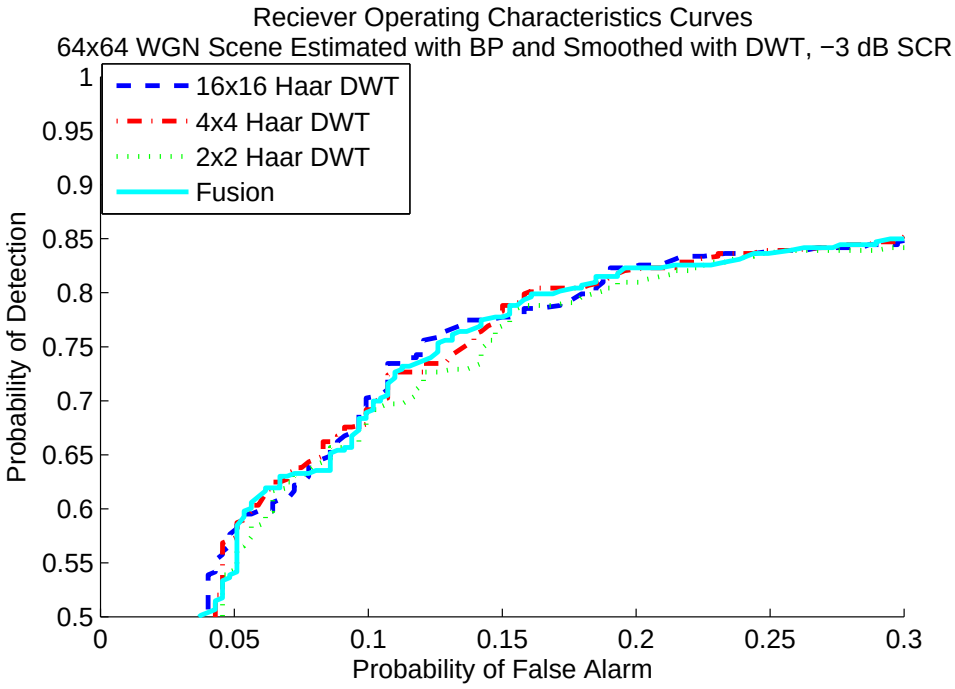

(b)

Figure B.3. ROCs for MVM GMTI detector using voting fusion algorithm and DWT-smoothed SAR images of homogeneous, unit-variance scene (a) SCR = 0 dB, (b) SCR = -3 dB

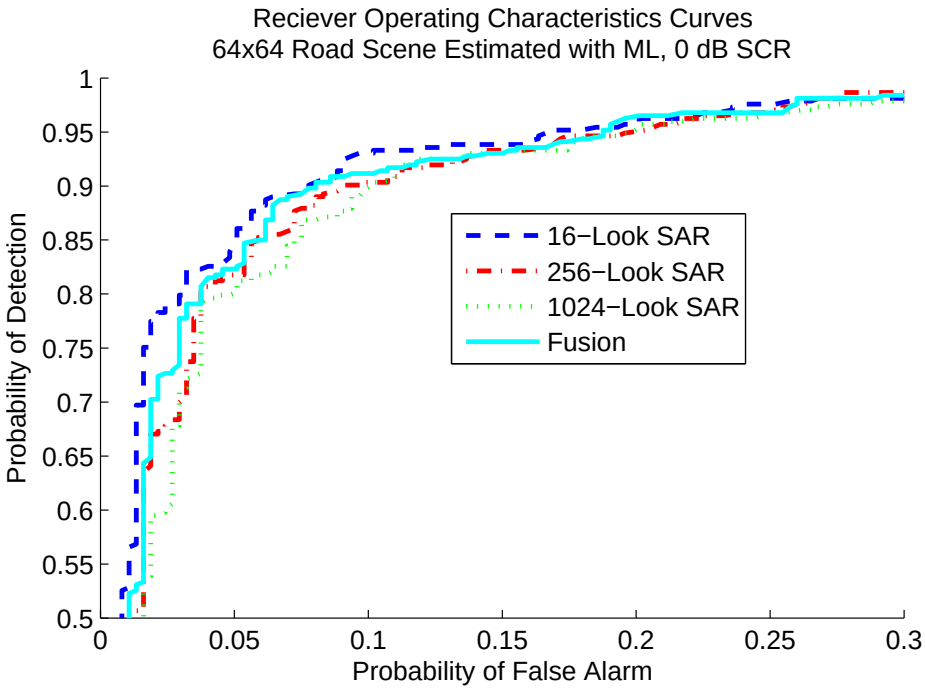

(a)

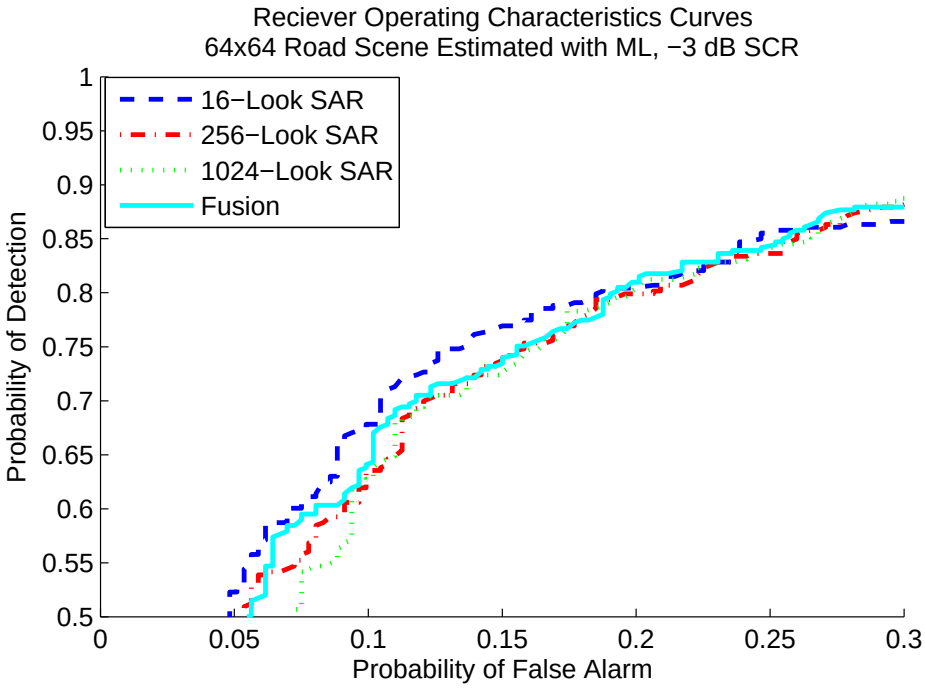

(b)

Figure B.4. ROCs for MVM GMTI detector using voting fusion algorithm and ML estimated multilook SAR images of road scene (a) SCR = 0 dB, (b) SCR = -3 dB

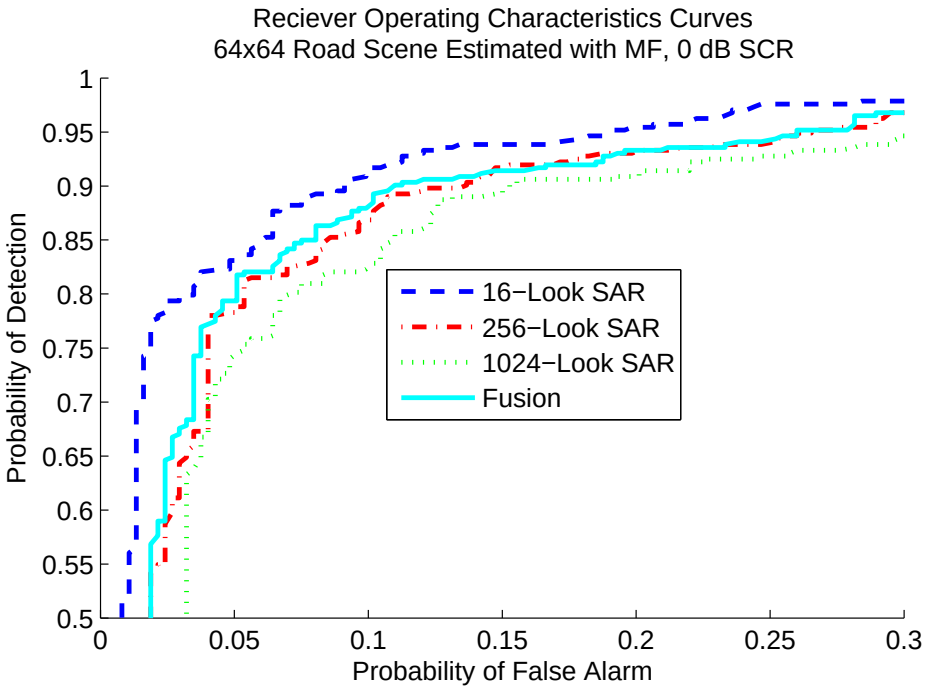

(a)

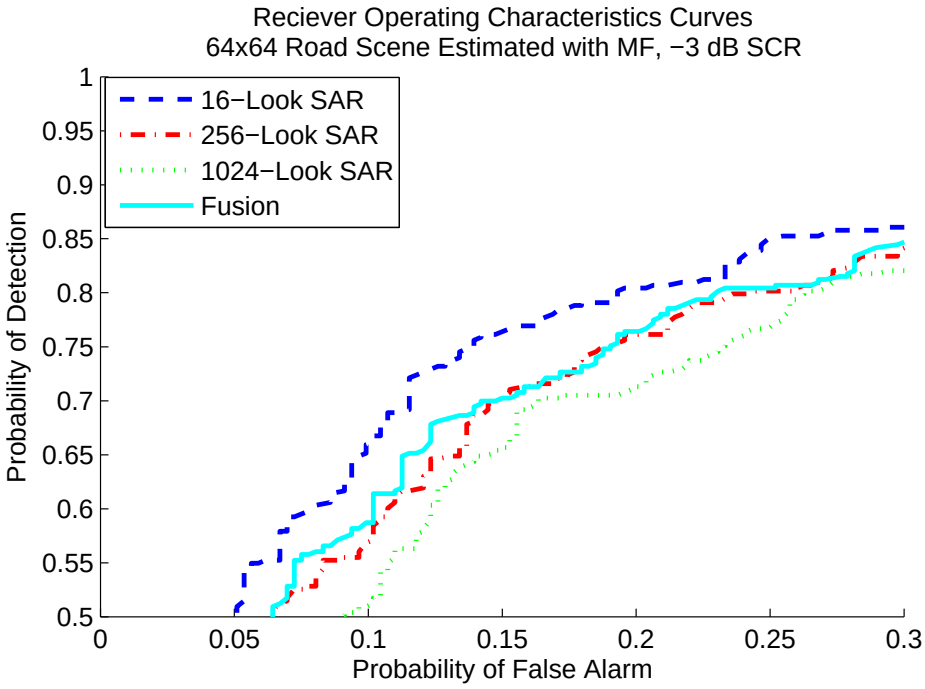

(b)

Figure B.5. ROCs for MVM GMTI detector using voting fusion algorithm and MF estimated multilook SAR images of road scene (a) SCR = 0 dB, (b) SCR = -3 dB

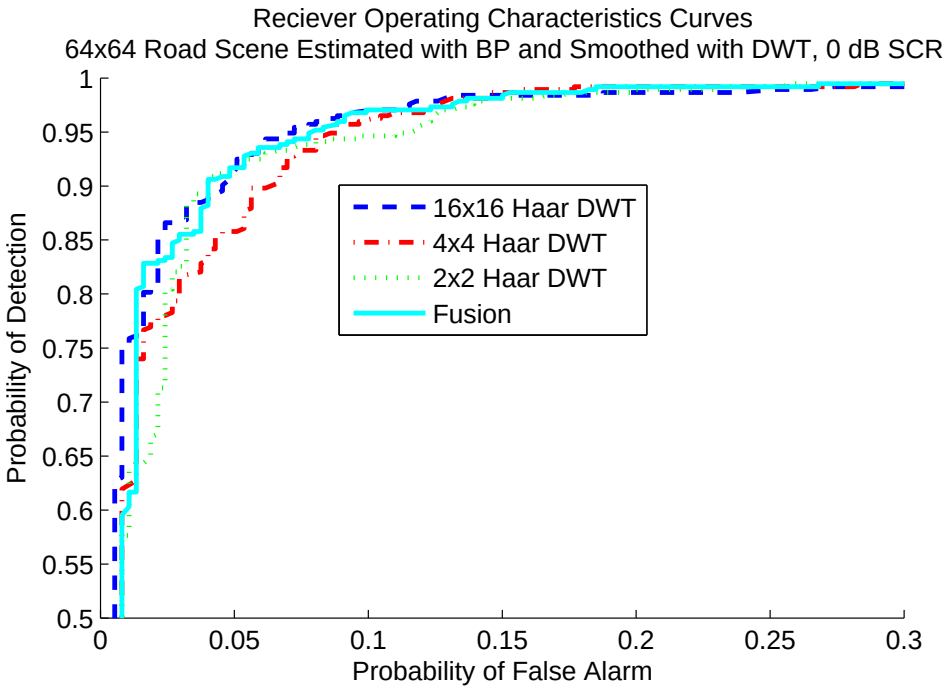

(a)

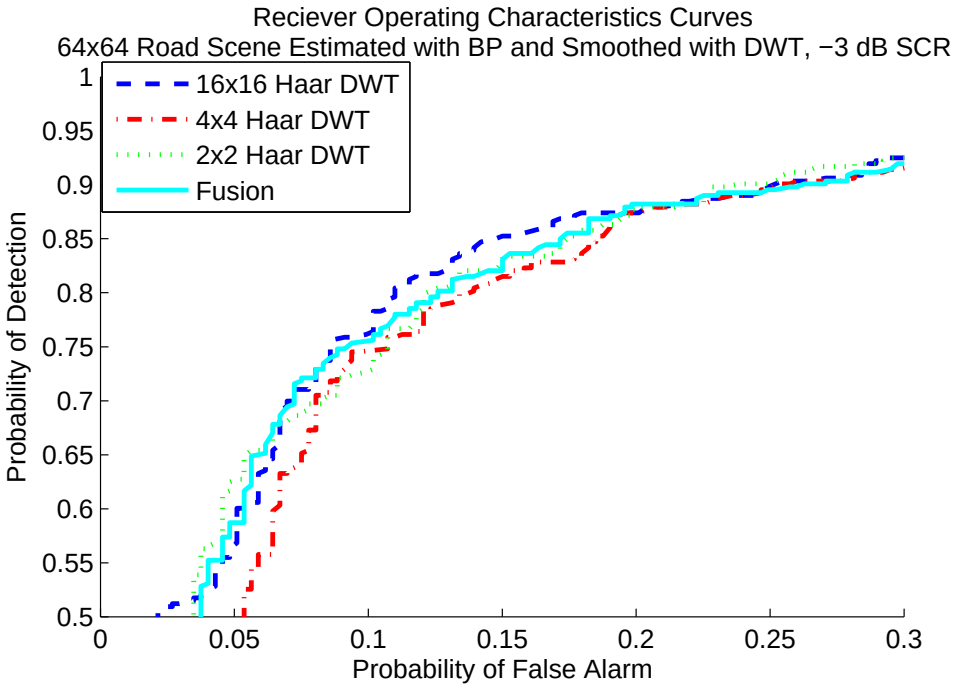

(b)

Figure B.6. ROCs for MVM GMTI detector using voting fusion algorithm and DWT-smoothed SAR images of road scene (a) SCR = 0 dB, (b) SCR = -3 dB

References

[1] J. B. McKinney, "Radar: A case history of an invention [the evolution of an innovation]," *IEEE Aerospace and Electronics Systems Magazine*, vol. 21, no. 8, p. 23, Aug. 2006.

[2] R. Klemm, *Principles of Space-Time Adaptive Processing*, 2nd ed., ser. IEE Radar, Sonar, Navigation and Avionics Series. London: The Institution of Electrical Engineers, 2002.

[3] S. Chiu and C. Livingstone, "A comparison of displaced phase centre antenna and along-track interferometry techniques for RADARSAT-2 ground moving target indication," *Canadian Journal of Remote Sensing*, vol. 31, no. 1, pp. 37–51, 2005.

[4] P. G. Richardson, "Analysis of the adaptive space time processing technique for airborne radar," *IEE Proceedings on Radar, Sonar, and Navigation*, vol. 141, no. 4, pp. 187–195, 1994.

[5] C. E. Muehe and M. Labitt, "Displaced-phase-center-antenna technique," *Lincoln Laboratory Journal*, vol. 12, no. 2, p. 16, 2000.

[6] A. Haimovich, "The eigencanceler: adaptive radar by eigenanalysis methods," *IEEE Transactions on Aerospace and Electronic Systems*, vol. 32, no. 2, pp. 532–542, 1996.

[7] A. M. Haimovich and M. Berin, "Eigenanalysis-based space-time adaptive radar: performance analysis," *IEEE Transactions on Aerospace and Electronic Systems*, vol. 33, no. 4, pp. 1170–1179, 1997.

[8] C. Lee and J. Lee, "Eigenanalysis interference cancelers with robust capabilities," *Signal Processing*, vol. 58, no. 2, pp. 193–202, APR 1997.

[9] M. Steiner and K. Gerlach, "Fast converging adaptive processor or a structured covariance matrix," *IEEE Transactions on Aerospace and Electronic Systems*, vol. 36, no. 4, pp. 1115–1126, 2000.

[10] L. E. Brennan and L. S. Reed, "Theory of adaptive radar," *IEEE Transactions on Aerospace and Electronic Systems*, vol. AES-9, no. 2, pp. 237–252, 1973.

[11] I. S. Reed, J. D. Mallett, and L. E. Brennan, "Rapid convergence rate in adaptive arrays," *IEEE Transactions on Aerospace and Electronic Systems*, vol. 10, no. 6, p. 11, 1974.

[12] W. L. Melvin, "Space-time adaptive radar performance in heterogeneous clutter," *IEEE Transactions on Aerospace and Electronic Systems*, vol. 36, no. 2, pp. 621–633, 2000.

[13] T. A. Barton and S. T. Smith, "Structured covariance estimation for space-time adaptive processing," in *IEEE International Conference on Acoustics, Speech, and Signal Processing*, vol. 5, 1997, pp. 3493–3496.

[14] D. R. Fuhrmann, L. A. Boggio, J. Maschmeyer, and R. Chamberlain, "Clutter scattering function estimation and ground moving target detection from multiple STAP datacubes," in *IEEE International Conference on Acoustics, Speech, and Signal Processing, Proceedings*, vol. 5, 2005, pp. v/593–v/596.

[15] M. Khanpour-Ardestani, R. S. Adve, and M. C. Wicks, "Pre-filtering for clutter rejection in beamspace STAP ," in *IEEE International Radar Conference*, 2005, pp. 709–713.

[16] S. D. Blunt, K. Gerlach, and M. Rangaswamy, "STAP using knowledge-aided covariance estimation and the FRACTA algorithm," *IEEE Transactions on Aerospace and Electronic Systems*, vol. 42, no. 3, pp. 1043–1057, 2006.

[17] K. Gerlach and M. L. Picciolo, "SINR improvement in airborne/spaceborne STAP radars using a priori platform knowledge," in *Sensor Array and Multichannel Signal Processing Workshop Proceedings, 2002*, 2002, pp. 548–552.

[18] P. Gurram and N. Goodman, "Spectral-domain covariance estimation with a priori knowledge," *IEEE Transactions on Aerospace and Electronic Systems*, vol. 42, no. 3, pp. 1010–1020, July 2006.

[19] J. S. Bergin, C. M. Teixeira, P. M. Techau, and J. R. Guerci, "Improved clutter mitigation performance using knowledge-aided space-time adaptive processing," *IEEE Transactions on Aerospace and Electronic Systems*, vol. 42, no. 3, pp. 997–1009, 2006.

[20] J. Hiemstra, M. Zoltowski, and J. Goldstein, "Recursive and knowledge-aided implementations of the multistage Wiener filter," in *Proceedings of the 2003 IEEE Radar Conference.*, May 2003, pp. 46–50.

[21] W. L. Melvin and G. A. Showman, "An approach to knowledge-aided covariance estimation," *IEEE Transactions on Aerospace and Electronic Systems*, vol. 42, no. 3, pp. 1021–1042, 2006.

[22] R. S. Adve, T. B. Hale, and M. C. Wicks, "Practical joint domain localised adaptive processing in homogeneous and nonhomogeneous environments. 1. homogeneous environments," *IEE Proceedings Radar, Sonar and Navigation*, vol. 147, no. 2, pp. 57–65, 2000.

[23] R. Adve, T. Hale, and M. Wicks, "Transform domain localized processing using measured steering vectors and non-homogeneity detection," in *1999 IEEE Radar Conference*, 1999, pp. 285–290.

[24] W. C. Ogle, H. N. Nguyen, M. A. Tinston, J. S. Goldstein, P. A. Zulch, and M. C. Wicks, "A multistage nonhomogeneity detector," in *Proceedings of the IEEE Radar Conference*, 2003, pp. 121–125.

[25] M. Rangaswamy, "Statistical analysis of the nonhomogeneity detector for non-Gaussian interference backgrounds," *IEEE Transactions on Signal Processing*, vol. 53, no. 6, pp. 2101–2111, 2005.

[26] R. Adve, T. Hale, and M. Wicks, "A two stage hybrid space-time adaptive processing algorithm," in *1999 IEEE Radar Conference*, 1999, pp. 279–284.

[27] R. S. Adve, T. B. Hale, and M. C. Wicks, "Practical joint domain localised adaptive processing in homogeneous and nonhomogeneous environments. 2. nonhomogeneous environments," *IEE Proceedings Radar, Sonar and Navigation*, vol. 147, no. 2, pp. 66–74, 2000.

[28] P. Antonik, H. Schuman, P. Li, W. Melvin, and M. Wicks, "Knowledge-based space-time adaptive processing," in *1997 IEEE National Radar Conference*, 1997, pp. 372–377.

[29] G. Capraro, A. Farina, H. Griffiths, and M. C. Wicks, "Knowledge-based radar signal and data processing," *IEEE Signal Processing Magazine*, vol. 1, pp. 18–30, 2006.

[30] M. J. Minardi, L. A. Gorham, and E. G. Zelnio, "Ground moving target detection and tracking based on generalized SAR processing and change detection," in *Algorithms for Synthetic Aperture Radar Imagery XII*, vol. 5808. SPIE - The International Society for Optical Engineering, 2005, pp. 156–165.

[31] M. J. Minardi and E. G. Zelnio, "Comparison of SAR based GMTI and standard GMTI in a dense target environment," in *Algorithms for Synthetic Aperture Radar Imagery XIII*, vol. 6237X. Orlando, FL: SPIE - The International Society for Optical Engineering, 2006, pp. 1–10.

[32] C. H. Gierull, "Statistical analysis of multilook SAR interferograms for CFAR detection of ground moving targets," *IEEE Transactions on Geoscience and Remote Sensing*, vol. 42, no. 4, pp. 691–701, 2004.

[33] E. Chapin and C. W. Chen, "GMTI along-track interferometry experiment," *IEEE Aerospace and Electronics Systems Magazine*, vol. 21, no. 3, pp. 15–20, 2006.

[34] J. C. Curlander and R. N. McDonough, *Synthetic Aperture Radar Systems and Signal Processing*, ser. Wiley Series In Remote Sensing. New York: John Wiley & Sons, Inc., 1991.

[35] G. Franceschetti and R. Lanari, *Synthetic Aperture Radar Processing*, ser. Electronic Engineering Systems Series. Boca Raton: CRC Press, 1999.

[36] M. I. Skolnik, *Radar Handbook*, 2nd ed. Boston, MA: McGraw Hill, 1990.

[37] N. A. Goodman, "SAR and MTI processing of sparse satellite clusters," Ph.D. dissertation, University of Kansas, 2002.

[38] J. Jenshak, "Transmit signal design for multistatic radar," Ph.D. dissertation, University of Kansas, 2009.

[39] J. Stiles, V. Sinha, and A. P. Nanda, "Space-time transmit signal construction for multi-mode radar," in *2006 IEEE Conference on Radar*, April 2006.

[40] J. R. Guerci, "Theory and application of covariance matrix tapers for robust adaptive beamforming," *IEEE Transactions on Signal Processing*, vol. 47, no. 4, pp. 977–985, 1999.

[41] K. Shanmugan and A. Breipohl, *Random Signals: Detection, Estimation, and Data Analysis*. John Wiley & Sons, 1988.

[42] D. R. Fuhrmann, "Structured covariance estimation: theory, application, and recent results," in *Fourth IEEE Workshop on Sensor Array and Multichannel Processing*, 2006, pp. 0–62.

[43] F. M. Staudaher, *Airborne MTI*. Boston, MA: McGraw-Hill, 1990.

[44] J. Ward, "Space-time adaptive processing for airborne radar," Lincoln Laboratory, Massachusetts Institute of Technology, Tech. Rep. ESC-TR-94-109, 1994.

[45] L. E. Brennan and F. M. Staudaher, "Subclutter visibility demonstation," Adaptive Sensors Incorporated, Tech. Rep. Technical Report RL-TR-92-21, March 1992.

[46] D. Slepian and H. Pollak, "Prolate spheroidal wave functions, Fourier analysis and uncertainty-I," *Bell Systems Technology Journal*, vol. 40, pp. 43–64, 1961.

[47] H. Landau and H. Pollak, "Prolate spheroidal wave functions, Fourier analysis and uncertainty-II," *Bell Systems Technology Journal*, vol. 40, pp. 65–84, 1961.

[48] ——, "Prolate spheroidal wave functions, fourier analysis and uncertainty-III," *Bell Systems Technology Journal*, vol. 41, pp. 1295–1336, 1962.

[49] J. S. Bergin, C. M. Teixeira, and P. M. Techau, "Multi-resolution signal processing techniques for airborne radar," in *2004 IEEE Radar Conference*, 2004, pp. 277–282.

[50] D. Sloper, D. Fenner, J. Arntz, and E. Fogle, "Multichannel airborne radar measurement (MCARM) flight test," Westinghouse Electronic Systems, Tech. Rep. Contract F30602-92-C-0161, April 1996 1996.

[51] P. Chen, "On testing the equality of covariance matrices under singularity," in *Report for AFOSR Summer Faculty Research Program.* Rome, NY: Rome Laboratory, 1994.

[52] J. R. Guerci and A. O. Steinhardt, "Multiresolution GMTI radar," in *Conference Record of the Thirty-Seventh Asilomar Conference on Signals, Systems and Computers, 2003.*, vol. 1, 2003, pp. 50–53 Vol.1.

[53] W. Choi, T. Sarkar, H. Wang, and E. Mokole, "Adaptive processing using real weights based on a direct data domain least squares approach," *IEEE Transactions on Antennas and Propagation*, vol. 54, no. 1, pp. 182–191, Jan. 2006.

[54] S. Burintramart and T. Sarkar, "Performance comparison between statistical-based and direct data domain STAP," in *Antennas and Propagation Society International Symposium 2006, IEEE*, July 2006, pp. 1421–1424.

[55] T. K. Sarkar, H. Wang, S. Park, R. Adve, J. Koh, K. Kim, Y. Zhang, M. Wicks, and R. Brown, "A deterministic least-squares approach to space-time adaptive processing STAP," *IEEE Transactions on Antennas and Propagation*, vol. 49, no. 1, pp. 91–103, Jan 2001.

[56] K. Gerlach, S. D. Blunt, and M. L. Picciolo, "Robust adaptive matched filtering using the FRACTA algorithm," *IEEE Transactions on Aerospace and Electronic Systems*, vol. 40, no. 3, pp. 929–945, 2004.

[57] B. D. Carlson, "Covariance matrix estimation errors and diagonal loading in adaptive arrays," *IEEE Transactions on Aerospace and Electronic Systems*, vol. 24, no. 4, pp. 397–401, 1988.

[58] M. C. Wicks, M. Rangaswamy, R. Adve, and T. B. Hale, "Space-time adaptive processing: a knowledge-based perspective for airborne radar," *IEEE Signal Processing Magazine*, vol. 23, no. 1, pp. 51–65, 2006.

[59] R. P. Perry, R. C. DiPietro, and R. L. Fante, "SAR imaging of moving targets," *IEEE Transactions on Aerospace and Electronic Systems*, vol. 35, no. 1, p. 12, 1999.

[60] ——, "Coherent integration with range migration using keystone formatting," in *2007 IEEE Radar Conference*, 2007, pp. 863–868.

[61] P. K. Sanyal, D. M. Zasada, and R. P. Perry, "Tracking moving ground targets from airborne SAR via keystoning and multiple phase center interferometry," in *2007 IEEE Radar Conference*, 2007, pp. 723–728.

[62] S. M. Kay, *Fundamentals of Statistical Signal Processing: Estimation Theory*, ser. Prentice Hall Signal Processing Series. Upper Saddle River, NJ: Prentice Hall, 1993, vol. 1.

[63] M. S. Grewal and A. P. Andrews, *Kalman Filtering: Theory and Practice Using MATLAB*, 2nd ed. New York: John Wiley & Sons, Inc., 2001.

[64] S. Haykin, *Adaptive Filter Theory*. Englewood Cliffs, NJ: Prentice Hall, 1996.

[65] H. L. Van Trees, *Optimum Array Processing*, ser. Detection, Estimation, and Modulation Theory. New York: John Wiley & Sons, Inc., 2002.

[66] T. K. Moon and W. C. Stirling, *Mathematical Methods and Algorithms for Signal Processing*. Upper Saddle River, NJ: Prentice Hall, 1999.

[67] J. M. Stiles, "Kalman filter," 2004, University of Kansas.

[68] M. Soumekh, *Synthetic Aperture Radar Signal Processing with MATLAB Algorithms*. New York, NY: John Wiley & Sons, Inc., 1999.

[69] G. Strang and T. Nguyen, *Wavelets and Filter Banks*. Wellesley, MA: Wellesley-Cambridge Press, 1996.

[70] G. Strang, "Wavelets," *American Scientist*, vol. 82, pp. 250–255, 1994.

[71] ——, "Wavelets and dilation equations: a brief introduction," *Siam Review*, vol. 31, no. 4, pp. 614–627, 1989.

[72] B. Hubbard, *The World According to Wavelets: The Story of a Mathematical Technique in the Making*, 2nd ed. Wellesley, MA: A K Peters, 1998.

[73] F. T. Ulaby, R. K. Moore, and A. K. Fung, *Microwave Remote Sensing–Active and Passive: Radar Remote Sensing and Surface Scattering and Emission Theory*, ser. Remote Sensing. Norwood, MA: Artech House, Inc., 1986, vol. 2.

[74] J. K. Jao, A. F. Yegulalp, and S. Ayasli, "Unified synthetic aperture space time adaptive radar (USASTAR) concept," Massachusetts Institute of Technology Lincoln Laboratory, Tech. Rep., 2004.

[75] J. G. Proakis and D. G. Manolakis, *Digital Signal Processing Principles, Algorithms, and Applications*, 2nd ed. New York, NY: Macmillan Publishing Company, 1992.

[76] N. Goodman and J. Stiles, "Resolution and synthetic aperture characterization of sparse radar arrays," *IEEE Transactions on Aerospace and Electronic Systems*, vol. 39, no. 3, pp. 921–935, July 2003.

[77] I. G. Cumming and F. H. Wong, *Digital Signal Processing of Synthetic Aperture Radar Data*. Artech House, 2005.

[78] I. W. Selesnick, R. G. Baraniuk, and N. C. Kingsbury, "The dual-tree complex wavelet transform," *IEEE Signal Processing Magazine*, vol. 22, no. 6, pp. 123–151, 2005.

[79] R. Baraniuk, "Compressive sensing [lecture notes]," *IEEE Signal Processing Magazine*, vol. 24, no. 4, pp. 118–121, July 2007.

[80] R. Baraniuk and P. Steeghs, "Compressive radar imaging," in *2007 IEEE Radar Conference*, April 2007, pp. 128–133.

[81] E. Candes and T. Tao, "Near-optimal signal recovery from random projections: Universal encoding strategies?" *IEEE Transactions on Information Theory*, vol. 52, no. 12, pp. 5406–5425, Dec. 2006.

[82] S. S. Chen, D. L. Donoho, and M. A. Saunders, "Atomic decomposition by basis pursuit," *SIAM Review*, vol. 43, no. 1, pp. 129–159, 2001.

[83] J. Tropp, "Greed is good: algorithmic results for sparse approximation," *IEEE Transactions on Information Theory*, vol. 50, no. 10, pp. 2231–2242, Oct. 2004.

[84] J. Tropp and A. Gilbert, "Signal recovery from random measurements via orthogonal matching pursuit," *IEEE Transactions on Information Theory*, vol. 53, no. 12, pp. 4655–4666, Dec. 2007.

[85] T. Do, L. Gan, N. Nguyen, and T. Tran, "Sparsity adaptive matching pursuit algorithm for practical compressed sensing," in *Signals, Systems and Computers, 2008 42nd Asilomar Conference on*, Oct. 2008, pp. 581–587.

[86] M. Herman and T. Strohmer, "High-resolution radar via compressed sensing," *IEEE Transactions on Signal Processing*, vol. 57, no. 6, pp. 2275–2284, June 2009.

[87] S. M. Kay, *Fundamentals of Statistical Signal Processing: Detection Theory*, ser. Prentice Hall Signal Processing Series. Upper Saddle River, NJ: Prentice Hall, 1993, vol. 2.

[88] J. M. Stiles, "Space-time radar transmission, target, and measurement model," 2004, University of Kansas.

[89] ——, "Model input parameters," 2004, University of Kansas.

[90] ——, “Transmit signal model, rev E,” University of Kansas.

[91] ——, “Determination of numeric model parameters,” 2004, University of Kansas.